CORA Cork Open Research Archive
Cartlann Taighde Oscailte Chorcaí

Title	Investigation of diffuse reflectance spectroscopy and acousto-optics for deep tissue imaging and diagnostics
Authors	Amissah, Michael
Publication date	2024
Original Citation	Amissah, M. 2024. Investigation of diffuse reflectance spectroscopy and acousto-optics for deep tissue imaging and diagnostics. PhD Thesis, University College Cork.
Type of publication	Doctoral thesis
Rights	© 2024, Michael Amissah. - https://creativecommons.org/licenses/by/4.0/
Download date	2026-11-03 10:07:31
Item downloaded from	https://hdl.handle.net/10468/17923



UCC
University College Cork, Ireland
Coláiste na hOllscoile Corcaigh

Ollscoil na hÉireann, Corcaigh

National University of Ireland, Cork



Investigation of Diffuse Reflectance Spectroscopy and Acousto-Optics for Deep Tissue Imaging and Diagnostics

Thesis presented by

Michael Amissah

for the degree of

Doctor of Philosophy

University College Cork

School of Physics

Head of School: Prof. Paul Callanan

Supervisor: Prof. Stefan Andersson-Engels

Co-Supervisor(s): Dr. Bryan Kelleher and Dr. Baptiste Jayet

2024





Funding
This project was funded by Research Ireland

No copyright
No part of this document has been submitted elsewhere for the award of Doctor of Philosophy degree except works done by collaboration.

Supervisors
Prof. Stefan Andersson-Engels
Dr. Bryan Kelleher
Dr. Baptiste Jayet

Publisher
Tyndall National Institute and University College Cork-School of Physics

DEDICATION

1. When you lose it all, find it all and keep living on.
2. Learn in confidence, teach in humility.

– Michael Amissah

1 Acknowledgements

Pursuing this PhD journey has been one of the most challenging yet rewarding experiences of my life, and it would not have been possible without the support and encouragement of many individuals. First and foremost, I extend my deepest gratitude to my supervisor, Prof. Stefan Andersson-Engels whose guidance, patience, and unwavering trust in my abilities have been the cornerstone of my academic and personal growth. Prof. Stefan's, expertise and insightful feedback have been invaluable, not just in shaping this thesis but in shaping my approach to research and critical thinking. I would also like to appreciate the immense contribution of my Co-supervisor, Dr. Bryan Kelleher and my PhD monitor, Dr. James O'Callaghan. Their contribution ranged from making time for all the scheduled report meetings, motivational comments for improvements in my works as well as creating a very friendly atmosphere for me during my works.

I am equally grateful to my Postdoc and personal teacher, Dr. Baptiste Jayet whose dedication to teaching and mentoring has profoundly influenced my journey. Baptiste's willingness to share his knowledge and experiences has enriched my understanding of our field, and his support has been a constant source of motivation. Baptiste, thank you for being not just a mentor, but a role model. I am also very thankful to Dr. Jacqeline E. Gunther for her immense contribution to my growth. I always called her my "acousto-optic" Mum in her presence and behind her back. I have always cherished the times we will be holding our markers to the white board in the lab to discuss concepts. I am also thankful to Dr. Sanathana Konugolu Venkata Sekar for his assistance in phantom making and optical characterisations.

To my colleague, Dr. Michael Raju, thank you for the brotherly talks we had, the discussions, and shared moments of PhD pressures and triumph. Your constant advice and your willingness to share with me your knowledge and experiences always implanted in me, a great hope for the future. I also thankful to Dr. Marcelo Saito Nogueira and Siddra Maryam for being great team-players during our experiments at Mercy Hospital in Cork city.

I am particularly grateful to Professor Samuel Yeboah Mensah, Professor Paul Kingsley Buah-Bassuah, Professor Benjamin Anderson, Professor Kofi Anane-Fenin all of the Laser and Fibre Optic Center of the University of Cape Coast (UCC) for all the opportunities, assistance and advice I received from them when I was studying at UCC and also, when I was working as a teaching assistant after my studies. I am also thankful to Professor Nana Ama Browne-Klutsey, the CEO of the Environmental Protection Agency of Ghana for all her inspirations, financial supports as well as her guidance in my life over the years.

I cannot express enough gratitude to my friends and family, whose love, encouragement, and faith in me have been unwavering. You have been my rock, reminding me of the world beyond academia, and providing a safe haven for me mentally, when the pressures of research seemed overwhelming. Your belief in me has been a source of strength and resilience, and I am profoundly grateful to each one of you. It will take me almost eternity to list all your names but I know I would definitely start with my mother, Grace Forson, my kid sister, Mercy Amissah, my cousin, Raymond Bruce and the blessed memory of

my father, Alfred John Amissah. This journey has also been a collective effort of all my uncles: Samuel, Benjamin and Emmanuel and my aunties: Mary and Sophia. I am also thankful to my friends who have now become brothers and fathers; Dr. Samuel Eshun, Dr. Patrick Essien, Mr. Herbert Prebi (CA), The Ofosu-Kissi brothers, Mr. Paul Oduro, Mr. Kofi Fofie, Nana Amoasi Rockson, Dr. Ebenezer Anohah, Mr. Kennedy Thompson and my other elderly friends of blessed memories; Mr. Sackey and Mr. Acheampong. My gratitude extends to their respective families. I cannot forget the well wishes of my grandmother of blessed memory, Agnes Apprey (Ekua Nfomaa). Thank you all for being a part of my PhD journey either directly or indirectly.

This thesis made use of LaTeX with `KOMA-Script` and the `kaobook` class for typesetting. The source code was obtained from: https://github.com/fmarotta/kaobook.

2 Declaration

This is to certify that the work I am submitting is my own and has not been submitted for another degree either at University College Cork or elsewhere except for works done in collaboration. All external references and sources are clearly acknowledged. I have read and understood the regulations of University College Cork concerning plagiarism and intellectual property.

Michael Amissah

3 Abstract

This dissertation explores two frontiers of optical technologies in biophotonics: diffuse reflectance spectroscopy (DRS) and acousto-optic interactions in tissues. The work capitalizes on the potential of DRS for objective surgical examinations of tissues, focusing on colorectal cancer (CRC) as a case study. It uses DRS as a tool for real-time surgical guidance, offering surgeons the unparalleled ability to distinguish between healthy and malignant tissues during operations. A total of over 2889 spectral data, spanning both visible and near-infrared wavelength ranges, were used in this study. These spectra were collected from excised tumors and tissue samples from 47 patients who underwent colorectal cancer surgeries. The wavelength response to the biochemical composition of CRC were explored using two different source to detector distances (SDD) or probes. The study with short-SDD probe yielded (93.5 ± 2.4)% sensitivity and (94.0 ± 1.7)% specificity whereas using long-SDD probe to sample deeper tissue layers yielded (96.1 ± 1.8)% sensitivity, (95.7 ± 0.6)% specificity.

Furthermore, the acousto-optic approach was employed for non-invasive sensing of optical changes in blood-mimicking fluids with varying viscosities in blood-mimicking fluids (acqeous glycerol) from 2 cP to 7 cP which covers the range of human blood viscosities. The acousto-optic signal and in effect, the modulation depth was found to have a negative correlation to increase in glycerol concentration of non scattering samples while there was a direct relationship with increased optical scattering. This was achieved by employing coherent light with digital heterodyne holography as an ultrasound-tagged light detection mechanism.

The holograhic detection of acousto-optic signal for studying tissue decorrelation times via flow dynamics was explored. The decorrelation times were found to decrease as flow speed increases. Insights gained from these studies are important for advancing understanding of fluid mechanics in deep tissue dimensions and could be useful in developing tools for non-invasive, in situ monitoring of blood viscosity changes during surgical operations, as well as for diagnosing blood coagulopathies.

4 List of Manuscripts for the thesis

This thesis is based on chapters that were developed from published works and other works under preparation for submission.

List of publications based on our study with Diffuse reflectance spectroscopy (DRS)

- Paper I: Nogueira, M.S., Maryam, S., Amissah, M., Killeen, S., Lu H., Lynch, N., O'Ríordáin, M.,& Andersson-Engels, S. Evaluation of wavelength ranges and tissue depth probed by diffuse reflectance spectroscopy for colorectal cancer detection. Sci Rep 11, 798 (2021). https://doi.org/10.1038/s41598-020-79517-2
  Contributed to the data acquisition protocols and software for spectral processing and writing, review and editing.

- Paper II: Nogueira, M. S., Raju, M., Gunther, J., Maryam, S., Amissah, M., Lu, H.,& Andersson-Engels, S. (2021). Tissue biomolecular and microstructure profiles in optical colorectal cancer delineation. Journal of Physics D: Applied Physics, 54(45), 454002. https://doi.org/10.1088/1361-6463/ac1137
  Contributed to the investigation, data curation and software.

- Paper III: Nogueira, M. S., Maryam, S., Amissah, M., McGuire, A. T., Spillane, C., Killeen, S.,& O'Ríordáin, M., & Andersson-Engels, S. (2022). Insights into biochemical sources and diffuse reflectance spectral features for colorectal cancer detection and localization. Cancers, 14(22), 5715. https://doi.org/10.3390/cancers14225715
  Contributed to the investigation and data curation.

- Paper IV: Nogueira, M. S., Maryam, S., Amissah, M., Killeen, S., O'Ríordáin, M., & Andersson-Engels, S.(2022). Diffuse reflectance spectroscopy for colorectal cancer surgical guidance: towards real-time tissue characterization and new biomarkers. Analyst. 2023 Dec 18;149(1):88-99. doi: 10.1039/d3an00261f. PMID: 37994161
  Contributed to the investigation and data curation.

Publication in preparation

- Amissah, M., Jayet, B., & Andersson-Engels, S. Observing acousto optic interaction in viscous fluids using digital holography for tagged light detection.
  Contributed to the conceptualisation, data acquisition protocols, writing, review and editing.

  Publication in preparation
- Amissah, M., Jayet, B., & Andersson-Engels, S. Distinguishing mechanical contrasts in biological phantoms via the acousto optic effect .
  Contributed to the conceptualisation, data acquisition protocols, writing, review and editing.

  Publication in preparation
- Amissah, M., Jayet, B., & Andersson-Engels, S. Determination of tissue decorrelation time using 4-phase shifting holography.
  Contributed to the conceptualisation, data acquisition protocols, writing, review and editing.

Contents

1 Acknowledgements v
2 Declaration vii
3 Abstract viii
4 List of Manuscripts for the thesis ix

Contents **xi**

1 Introduction **1**
1.1 Motivation 2
1.2 Recommendation for merging DRS and acousto-optics 4
1.3 Hypothesis of the work 5
1.4 Thesis structure 6

2 Optical properties of biological tissues **9**
2.1 The Poynting theorem 10
2.1.1 The time averaged Poynting vector 12
2.1.2 Propagation of scattered light 13
2.2 Diffusion regimes 15
2.3 Light propagation models 16
2.3.1 Radiative Transfer Equation 17
2.3.2 Fick's Law and The Diffusion Equation 18
2.4 Absorption 20
2.5 Scattering 23
2.6 Phase function 24

3 Background of diffuse reflectance spectroscopy **29**
3.1 The Kubelka-Munk theory 30
3.2 Instrumentation and experimental techniques 33

4 Ultrasound and tissue mechanics **37**
4.1 Mechanical waves in fluids 38
4.2 Acoustic impedance, reflection and transmission of ultrasound waves . . . 40
4.3 Impedance matching for acoustic coupling 41
4.4 Transducers and ultrasound fields 41

5 A review of acousto-optical tomography **45**
5.1 Theoretical background of acousto-optics 46
5.1.1 Raman-Nath and Bragg diffraction regimes 46

5.1.2 Brownian motion and ultrasound-induced movement of point-like scatterers in the acousto-optic signal . . . 49
5.1.3 Contributions of the refractive index change and displacement of scatterers to the acousto-optic signal . . . 52
5.2 Optical techniques in AOT . . . 55
5.2.1 Challenges in AOT signal detection . . . 55
5.2.2 Detection solutions . . . 56
5.2.3 Imaging and resolution solutions . . . 67
5.3 How multiple acoustic foci have been used in AOT . . . 69
5.4 Plane-Wave Ultrasound in AOT . . . 71

6 Diffuse reflectance spectroscopy for colorectal cancer surgical guidance 75
6.1 Background of colorectal cancer . . . 75
6.2 Material and Methods . . . 77
6.2.1 DRS systems . . . 78
6.2.2 Data collection and analysis . . . 79
6.3 Results of the publications associated with this work . . . 80
6.4 DRS in the AOT framework . . . 84

7 Acousto-optics with digital heterodyne holography 85
7.1 Theory . . . 86
7.1.1 2-Phase . . . 87
7.1.2 4-Phase . . . 87
7.2 Method . . . 88
7.3 Results . . . 92
7.3.1 Simulation . . . 92
7.3.2 Experiment . . . 93
7.4 Discussion . . . 96
7.5 Conclusion . . . 97

8 Viscosity contrast in blood mimicking fluids 99
8.1 Motivation . . . 99
8.2 The process of blood coagulation . . . 100
8.3 Coagulation measurement tools . . . 101
8.4 Material and method . . . 103
8.4.1 Samples . . . 103
8.4.2 Data acquisition . . . 104
8.4.3 Depth Scanning . . . 104
8.5 Results . . . 105
8.6 Discussion . . . 107
8.7 Conclusion . . . 110

9 Measurement of decorrelation time under flow conditions **111**
9.1 Introduction 111
9.2 Materials and methods 112
9.3 Results 112
9.4 Discussion and conclusion 114

10 Discussion and conclusion of the thesis **117**
10.1 Diffuse Reflectance Spectroscopy for Colorectal Cancer 117
10.2 Acousto-Optics and Digital Holography in decorrelation and Flow Monitoring 120
10.3 Conclusion 122

11 Personal reflections **125**

Bibliography **129**

Appendix **147**
1 Safety considerations of the use of light and ultrasound in medical solutions 223
1.1 Ultrasound Mechanical Index (MI) 223
1.2 Ultrasound Thermal Index (TI) 224
1.3 Maximum Permissible Exposure (MPE) for Lasers 225
1.4 Accessible Emission Limit (AEL) 225

List of Figures

1.1 The Electromagnetic Spectrum . . . 1
1.2 X-ray . . . 2
1.3 Various imaging modalities . . . 3

2.1 Light propagation scenarios in tissues . . . 9
2.2 The Poynting vector field . . . 10
2.3 Rotational invaraince of the Poynting vector . . . 13
2.4 Photon scattering regimes . . . 15
2.5 Radiative Transfer Equation . . . 17
2.6 Absorbed light . . . 20
2.7 The absorption spectra . . . 23
2.8 Scattered light . . . 23
2.9 Anisotropic scattering . . . 24
2.10 Isotropic scattering . . . 24
2.11 The Henyey-Greenstein's phase function . . . 25
2.12 Illustration of scattering mean free path (l_{sc}) and transport mean free path (l'_{sc}) 27

3.1 The Kubleka-Munk model . . . 31
3.2 Diffuse reflectance system components . . . 33
3.3 DRS reflectance spectra . . . 34

4.1 Tissue under mechanical force . . . 38
4.2 Snell's law . . . 40
4.3 Impedance matching . . . 41
4.4 Ultrasound transducer components . . . 42
4.5 The ultrasound pressure field . . . 42

5.1 Light-ultrasound interaction . . . 46
5.2 (a)Raman-Nath and (b)Bragg diffractions. . . . 47
5.3 Relative intensity of different diffraction orders with respect to the Raman-Nath regime. Inspired from[55]. . . . 49
5.4 Modulation depth variation with respect to changes ultrasound amplitude [50]. 52
5.5 A time domain representation of the autocorrelation function [60]. . . . 54
5.6 Confocal Fabry-Perot interferometry . . . 56
5.7 Spectral hole burning . . . 58
5.8 Optical phase conjugation . . . 61
5.9 Photorefractive-based detection of tagged photons . . . 64
5.10 Parallel speckle detection . . . 64
5.11 Comparison of ultrasound tagged photon detection methods . . . 66

5.12 Reflection mode configuration 73

6.1 Experimental set up for Diffuse reflectance spectroscopy 79
6.2 Resected colon 79
6.3 Boxplots of small and large probe results 82

7.1 Digital heterodyne holography for the selection of ultrasound shifted light. A coherent laser source is split into an reference beam and a sample beam by a beam splitter (BS 1). From mirror (M2), the sample beam goes through a diffuser that is attached to a container holding the block of agar fitted with a tube containing blood mimicking fluid. The tube is placed in the focus of the Ultrasound transducer (UT). Water is used to couple the ultrasound wave propagation. An aperture is placed close to the sample holder the emerging light is focused on a lens (Bi-convex, focal length=75 mm) placed 5 cm away together with a beam splitter (BS2) and a camera. The sample beam is modulated by AOM 1 at 80 MHz at its -1 order was directed unto the sample. The reference beam was created with the -1 order of AOM 2 and modulated at 8 500 012 500 MHz before being expanded by a beam expander (Plano-concave lens, $f = -30$ mm). This was then reflected on mirror M1 unto the camera through beam splitter BS2. 91
7.2 Electronic component connections. 91
7.3 Signal detection within the aperture using 2-phase holography where both the real and twin signals appear. 92
7.4 In the case of 4-phase detection, only the signal of interest can be extracted. . . 93
7.5 4-phase holographic detection with a decorrelation effect representing the appearance of the twin signal. 93
7.6 Image of the aperture and its conjugate. This shows the signal intensity from 390 to 600 on the camera dimension along the horizontal pixels, DX. The zero order term is located about 1000 while the twin signal is located from 1500 to 1610. . 94
7.7 This is a plot of the total pixel intensity values spatially across the pixels of the camera. 94
7.8 This show the types of signal to be acquired without the ultrasound waves and without frequency modulation of the light (heterodyne in green). When the the ultrasound is on, the untagged (blue) signal can be acquired and when the AOMs are tuned and with the ultrasound on, the tagged signal (red) could be acquired. 95

8.1 ultrasound scanning requirement 104
8.2 Locating the tube embedded in an agar block. The position of the tube is over the array of camera pixels. The pixel values from 320 to 710 on the DY axis show the position of the tube on the camera after holographic processing. Image **(a)** shows an empty tube while image **(b)** shows a the tube filled with Indian ink. Image **(c)** shows the contrast between the empty tube and the filled tube. . . . 105

8.3 The modulation depth of non scattering aqueous glycerol of varying concentrations showing a negative dependence. 106
8.4 A study of the modulation depth dependence on optical scattering and glycerol concentration. 106
8.5 An axial acquisition of 11 data locations at an interval of 5.1 mm were collected. This corresponded to a scanning range from 3.45 cm to 8.55 cm from the ultrasound transducer. The plot shows the mean and the associated standard error. 107

9.1 Decorrelation dependence on frequency 111
9.2 Using the siphoning principle to ensure different flow conditions: (a) fast flow condition ($3\,m\,s^{-1}$), (b) slow flow condition ($1.7\,m\,s^{-1}$). 112
9.3 Holographic signal of flowing milk (fluid). The black box represent the location of the tube embedded in the clear agar block. The signals above and below this box is out of the tube region. This is the mean of 200 images. 113
9.4 Fitting of the sum of the pixel values in the tube region to find the background signal of the camera. 113
9.5 Frequency scanned normalized ultrasound tagged signal for different flow conditions. The blue curve signifies the no flow condition which shows little broadening of the signal as compared to the slow flow and fast flow. For the decorrelation time calculated from half-with at half maximum (HWHM) of the tagged signal, then the time for no flow is 4.65 µs, it is 1.83 µs at $1.7\,m\,s^{-1}$ and at $3\,m\,s^{-1}$, it is less than 1.43 µs. 114

List of Tables

6.1 Patient Demographics and Tumor Characteristics. 78
6.2 Comparison of the classification performance of SVM classifiers for the dataset of the small SDD probe (n = 1363) containing reflectance values from 350 to 1919 nm. 83
6.3 Comparison of the classification performance of SVM classifiers for the dataset of the large SDD probe (n=1526) containing reflectance values from 350 to 1919 nm. 83
6.4 Performance metrics of each wavelength range analysed using the quadratic SVM classifier on the dataset of the small SDD probe. 83

1 Introduction

1.1 Motivation 2
1.2 Recommendation for merging DRS and acousto-optics 4
1.3 Hypothesis of the work 5
1.4 Thesis structure 6

The existence of the electromagnetic spectrum (EMS) as illustrated in Figure 1.1 has led up to the development of a wide range of sensory technologies, each of which has made unique contributions to the overall advancement in the quality of life that we now experience. This progress has enabled us to have higher living standards than ever before. In today's world, it is possible to discuss topics centred on technologies from aerial imaging to biological cell manipulation as well as the use of high-speed internet and augmented reality experiences all because of technological progress. Despite the progress, the journey of discovery continues, with light playing a key role. This thesis explores how light and sound waves are used in biology, aiming to push the boundaries of what we can diagnose and treat deep inside the body either surgically or non-invasively.

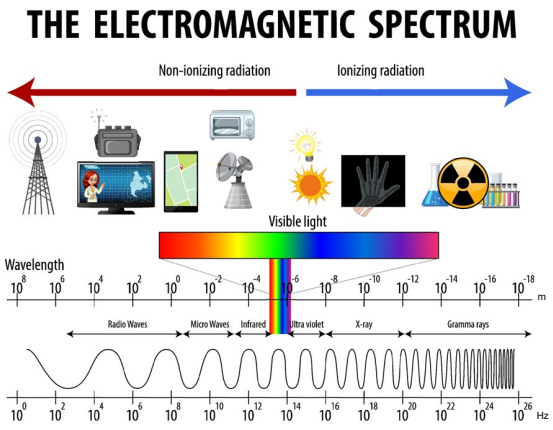


Figure 1.1: Electromagnetic spectrum comprises ionizing and non-ionizing radiations. Our human eyes serve as detectors which are receptive to the visible range of the electromagnetic spectrum. This is the very reason why we can see light in colours. The various regions have specific appliances that operate within such wavelengths.

When it comes to biological imaging, it was precipitated by the invention of X-rays in 1895 when the first interaction of an ionizing electromagnetic wave was observed in the human body by Wilhelm Conrad Röntgen. Following this precedence, various imaging modalities have been developed with each having its benefits and drawbacks. After the discovery of X-rays, even the unscientific people were fascinated. One of the earlier understanding of the potential use of X-rays was published in Life Magazine in 1896 (Figure 1.2 shows a cartoon depiction). Its applications to medical solutions progressed for a while without any thorough knowledge of

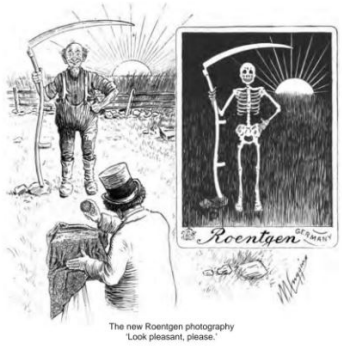


Figure 1.2: One of the earlier cartoons published to highlight the potential of X-rays. Image credit: originally published by Life Magazine, 1896 and found in https://books.google.ie/books?hl=en&lr=&id=QkssBgAAQBAJ&oi=fnd&pg=PR3&dq=radiography&ots=nj7-M_1xfM&sig=K-CqpiUyp2B-vnK9746cZeE8wFo&redir_esc=y#v=onepage&q=radiography&f=false

its adverse effects in the early stages. Other technologies that later evolved include ultrasound (US) imaging, computed tomography (CT), and magnetic resonance imaging (MRI) among others. This progression has been possible partly due to the sophisticated image processing algorithms and computing capacity we have today.

1.1 Motivation

The interaction of light within tissues or biological media is a complex phenomenon because of tissue heterogeneity. In the tissue environment, light can undergo scattering and absorption. The understanding of the dynamics of the light-tissue interaction has yielded to the development of several techniques for the study of tissue morphology, composition and functions. However, there remains a critical challenge when it comes to deep tissue optical imaging. The optical transmission window of 650 nm to 900 nm [1] has deeper tissue penetration ability because the absorption of light by water and haemoglobin is relatively small as compared to other wavelength ranges [2]. In spite of this penetration advantage, pure optical imaging and diagnostic systems are limited in optical sensitivity or resolution when considering deep tissue solutions[3]. This is because of the excessive light scattering within the tissue environment.

Light extinction in deep tissue poses a significant challenge for optical imaging because photons quickly lose their directional information due to scattering. In many materials, including biological tissues, variations in refractive index cause light to scatter strongly. The scattering strength is quantified by the scattering mean free path, l, which is the average distance that a photon travels between scattering events (i.e., $l = 1/\mu_s$, where μ_s is the scattering coefficient).

When a beam of light enters a scattering medium, a fraction of the light, known as ballistic light, is refracted with minimal scattering. However, its intensity decays exponentially with depth as energy is progressively converted into a diffuse glow of multiply scattered light. This diffuse component obscures the internal structure of the material if its thickness exceeds a few multiples of l. In fact, beyond a depth of roughly $5\times l$, over 99% of the light has been scattered multiple times. At such

depths, methods that rely on rejecting multiply scattered light such as optical coherence tomography (OCT) or multiphoton microscopy become ineffective because almost all of the signal is scrambled.

Thus, for samples thicker than about $5 \times l$, only photons that have undergone very few scattering events contribute effectively to image formation. As a result, imaging is primarily restricted to superficial or subsurface layers (as in microscopy within 0.5 mm to 1 mm), and the penetration depth of photons in conventional optical imaging systems is typically 0.5 mm to beyond 1 cm, indicating mesoscopic to macroscopic dimensions [4, 5].

Imaging modalities such as optical coherence tomography (OCT) [6, 7], diffuse optical tomography (DOT) [2], as well as confocal and multi-photon microscopy [8–10] offer high optical contrast and can be adapted for multi-modal imaging to provide complementary information in disease monitoring and progression. Moreover, the frontier of medical imaging is increasingly focused on developing non-ionizing and non-invasive techniques. In Figure 1.3, several imaging modalities are compared in terms of penetration depth and imaging resolution [11].

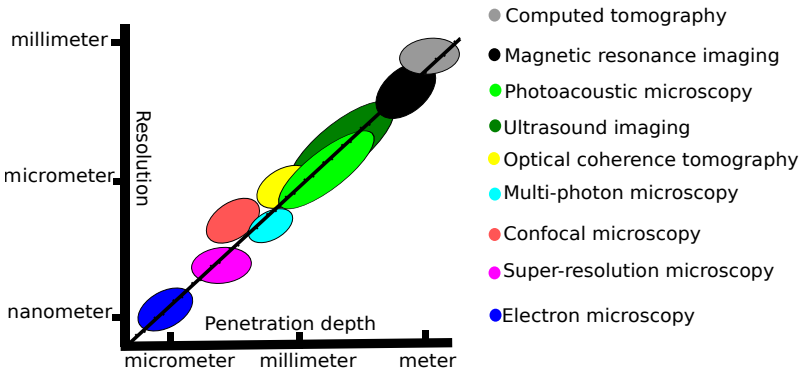


Figure 1.3: Resolution and penetration depth of various imaging modalities. This image was inspired from [11].

A non invasive and non-ionizing modality like Ultrasound (US) uses the wave characteristics such as velocity, attenuation and scattering to reveal mechanical variations in tissues. The scattering of ultrasonic wave in tissues is far less than the scattering of light in tissues. As a result, the spatial resolution of ultrasound imaging (~100 µm) is better than that of optical resolution in deep tissue imaging [12, 13]. The ultrasonic spatial resolution depends on the frequency of the ultrasound in the megahertz (MHz) range. The attenuation of the ultrasound wave in tissue is directly proportional to the frequency of the propagation wave. Due to the mechanical

response of tissues to US wave, imaging of blood flow and tissue motion has been possible. Adversely, pure US imaging does not provide molecular composition of tissues because it lacks sensitivity and cannot be used to monitor abnormal tissue structures and molecular sensitivity. To deal with this problem, vascular US imaging or contrast-enhanced ultrasound imaging has been explored using contrast agents [14]. Utilisation of such techniques would have to address toxicity of exogenous contrast agents among other considerations [15]. The technique of acousto optical imaging combines the advantages of light based and ultrasound based imaging to access deep tissue structures and to also have access to molecular responses from tissues. Much would be discussed about this later in Chapter 5 and Chapter 7.

1.2 Recommendation for merging DRS and acousto-optics

This thesis proposes that exploring the combination of Diffuse Reflectance Spectroscopy (DRS) and acousto-optic techniques presents a promising area of research in biophotonics, with the potential to significantly advance deep tissue diagnostics and therapeutics. The suggested approach would leverage the non-invasive and diagnostic capabilities of DRS, while benefiting from the enhanced depth penetration and improved resolution provided by acousto-optic methods that may require spectral hole filters. Although this thesis does not integrate the two techniques, it outlines key considerations for future studies aimed at combining these methodologies.

By addressing the challenges posed by light scattering and absorption in biological tissues, such a combined approach could lead to notable improvements in the precision and effectiveness of deep tissue imaging and disease diagnosis. This potential collaboration would not only increase the ability to access and analyse tissue structures at greater depths, previously unreachable with either technique alone, but also open new avenues for precise, non-invasive medical interventions. The integration of these techniques, though speculative at this stage, represents a valuable direction for further investigation in medical imaging and diagnostics.

1.3 Hypothesis of the work

The motivation behind this thesis highlights challenges and limitations inherent in current deep tissue optical imaging, diagnostics, and therapeutics. Because the study is based on two techniques, the hypothesis is sectioned for diffuse reflectance spectroscopy and that of acousto optic interactions within complex media.

Diffuse reflectance spectroscopy

- DRS could be used for tissue recognition or identification for efficient tumor margin excision during surgery.
- Various wavelength ranges could identify different biomarkers especially those associated with early tumor development.
- Coupled with machine learning, DRS could offer objective guidance to surgeons in accessing tissue integrity during diagnosis.

Acousto optic interaction

- Acousto-optic interaction within blood mimicking fluids could provide underlying understanding of deep tissue sensing of blood viscosity changes during coagulation.
- Because of the ultrasound response to various tissue stiffness, understanding acousto-optic signal intensity with respect to tissue stiffness could unveil structures for tumor detection while the light component could provide biomarker sensitivities.
- The holographic detection of ultrasound tagged light is sensitive to tissue decorrelation and could be used to explore acousto-optic signal integrity in flowing fluids to determine decorrelation times.

1.4 Thesis structure

The structure of the thesis is sectioned in two parts. Part 1 provides tutorials that lead to the understanding of the fundamental concepts within the framework of light transport in biological tissues as well as ultrasound propagation in materials. These tutorials would be useful in understanding the experiments concepts provided in Part 2 of the structure where in depth contributions in diffuse reflectance spectroscopy and acousto optics are presented in chapters.

PART 1

Chapter 2 delves into the mechanisms and theoretical frameworks underlying light transport in complex media, offering a comprehensive examination of the subject.

Chapter 3 explores the theory of Diffuse Reflectance Spectroscopy (DRS) and its instrumentation.

Chapter 4 looks at the properties of ultrasound wave propagation and its applications in materials.

Chapter 5 traces the development of acousto-optical imaging techniques, providing a historical context and highlighting technological advancements.

PART 2

Chapter 6 focuses on the application of Diffuse Reflectance Spectroscopy (DRS) for Colorectal cancer surgical guidance

Chapter 7 describes the principles of Digital heterodyne holography for acousto optic detection as well as the construction of an off-axis digital heterodyne holography setup

Chapter 8 investigates the viscosity contrast in blood mimicking fluids using the acousto optic concepts.

The thesis progresses in **Chapter 9** where the decorrelation time in holography is studied and in **Chapter 10**, the thesis is discussed and concluded in full scope. In **Chapter 11**, my personal reflections and recommendations for future research directions are provided.

PART 1

Optical properties of biological tissues

2

This section begins the PART 1 of the thesis where I provide tutorials based on universal understanding. In this chapter, the underlying principles and terms associated with light propagation in biological tissues are considered. The chapter discusses the considerations involved in light as an electromagnetic wave interacting with tissue particles. It builds foundation from the detailed works in [16] to explain light propagation in tissues.

The complex composition of biological tissues has a substantial effect on light transport within the tissue environments. According to their structure and function, tissues are classified as epithelial, connective, muscular, and nervous. Their composition and organisation of cells, extracellular matrix, and biomolecules determine their macroscopic optical properties. Chromophores such as haemoglobin and melanin, which absorb light strongly at specific wavelengths, result in varying degrees of absorption in various tissue layers. A typical description of light distribution in tissue is as demonstrated in Figure 2.1 where light could be transmitted, reflected, refracted or scattered.

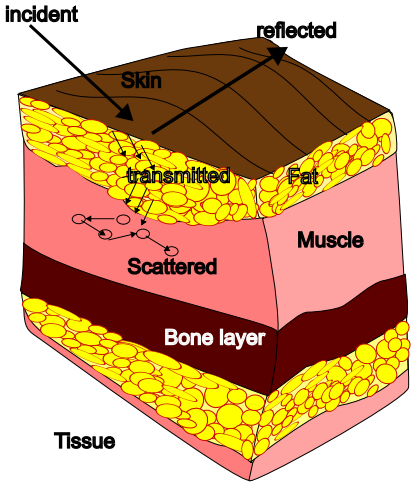


Figure 2.1: Light propagation scenarios in tissues.

The nature of the tissue structure is vital in determining the absorption, scattering, and transmission properties of light within tissue. For instance, the epithelial tissue, which lines the surfaces of organs and cavities, has densely packed cells and little extracellular matrix, which results in low scattering and high reflectance. Connective tissues, on the other

2.1 The Poynting theorem 10
2.1.1 The time averaged Poynting vector . . 12
2.1.2 Propagation of scattered light . . . 13
2.2 Diffusion regimes 15
2.3 Light propagation models 16
2.3.1 Radiative Transfer Equation 17
2.3.2 Fick's Law and The Diffusion Equation 18
2.4 Absorption 20
2.5 Scattering 23
2.6 Phase function . . . 24

hand, contain a greater proportion of extracellular matrix components such as collagen and elastin, which contributes to increased scattering and reduced transparency. In the discussions that follow, light is treated as an electromagnetic flow of energy to describe light absorption and scattering in relation to the Poynting vector.

2.1 The Poynting theorem

To understand the flow of light through tissues, emphasis would be drawn to the concept of the Poynting vector (represented here in this thesis as **S**). This vector illustrates the magnitude and direction of the energy flow in an electromagnetic wave. It specifically denotes the propagation direction of the wave, and its magnitude denotes the rate of energy transport per unit area that is perpendicular to the propagation direction. Hence, if we assume an illumination surface with area S and a normal to the surface as **s**, the quantity $\int_S \mathbf{S} \cdot \mathbf{s} dS$ could be measured to represent intensity. For example, a plot of the Poynting vector field is shown in Figure 2.2 and detailed explanations of it applications are treated by Mokhun et. al [17].

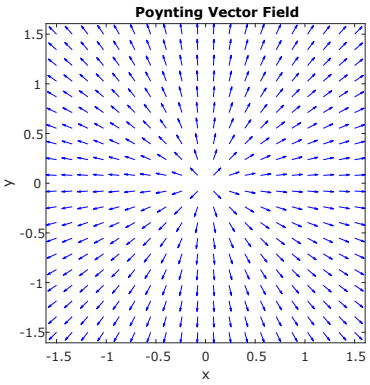


Figure 2.2: The Poynting vector field showing the flow of energy out of the page in the direction of $\hat{\mathbf{s}}$ where the vector is the direction of the cross product between the magnetic and electric fields.

If we assume an isotropic medium of properties having dielectric constant ε, electric field **E**, magnetic permeability μ and magnetic field vector **H** in the Maxwell's equation below, where c is the speed of light and **j** is the current density in the isotropic medium:

$$\nabla \times \mathbf{H} - \frac{\varepsilon \partial \mathbf{E}}{c \partial t} = \frac{4\pi \mathbf{j}}{c}, \tag{2.1}$$

$$\nabla \times \mathbf{E} + \frac{\mu \partial \mathbf{H}}{c \partial t} = 0, \tag{2.2}$$

By using Eqn. 2.1 and Eqn. 2.2 together with the vector identity:

$$\mathbf{E} \cdot (\nabla \times \mathbf{H}) - \mathbf{H} \cdot (\nabla \times \mathbf{E}) = -\nabla \cdot (\mathbf{E} \times \mathbf{H}), \tag{2.3}$$

We can arrive at:

$$\mathbf{E} \cdot (\nabla \times \mathbf{H}) - \mathbf{H} \cdot (\nabla \times \mathbf{E}) = \frac{4\pi}{c} \mathbf{j} \cdot \mathbf{E} + \frac{1}{c} \left(\varepsilon \mathbf{E} \cdot \frac{\partial \mathbf{E}}{\partial t} + \mu \mathbf{H} \cdot \frac{\partial \mathbf{H}}{\partial t} \right). \tag{2.4}$$

and this Eqn. 2.4 could then be rewritten as [18]:

$$\frac{1}{4\pi}\left(\varepsilon\mathbf{E}\cdot\frac{\partial\mathbf{E}}{\partial t}+\mu\mathbf{H}\cdot\frac{\partial\mathbf{H}}{\partial t}\right)+\mathbf{j}\cdot\mathbf{E}+\frac{c}{4\pi}\nabla\cdot(\mathbf{E}\times\mathbf{H})=0. \quad (2.5)$$

And isolating Eqn. 2.5 term by term, we can write the first term as:

$$\frac{1}{4\pi}\left(\varepsilon\mathbf{E}\cdot\frac{\partial\mathbf{E}}{\partial t}+\mu\mathbf{H}\cdot\frac{\partial\mathbf{H}}{\partial t}\right)=\frac{1}{8\pi}\frac{\partial}{\partial t}(\varepsilon\mathbf{E}^2+\mu\mathbf{H}^2) \quad (2.6)$$

where the energy density, W measured in $\mathrm{J\,cm^{-3}}$ is given as:

$$\frac{\partial W}{\partial t}=\frac{1}{8\pi}\frac{\partial}{\partial t}(\varepsilon\mathbf{E}^2+\mu\mathbf{H}^2). \quad (2.7)$$

The second term of Eqn. 2.5 defines the energy dissipation or absorbed energy (P_{abs}) per unit volume (V) in $\mathrm{W\,cm^{-3}}$ given as:

$$\mathbf{j}\cdot\mathbf{E}=\frac{dP_{abs}}{dV}. \quad (2.8)$$

By applying Ohm's law with harmonic time dependence, we can deduce from Eqn. 2.8 that:

$$\frac{dP_{abs}}{dV}=\omega\varepsilon^{(i)}(r)\mathbf{E}^2, \quad (2.9)$$

where ω is the frequency of the electromagnetic wave and $\varepsilon^{(i)}(r)$ is the imaginery component of permittivity at a positon r:

$$\varepsilon(r)=\varepsilon^{(r)}(r)+i\varepsilon^{(i)}(r). \quad (2.10)$$

Now with emphasis on the last term in Eqn. 2.5, we can write:

$$\frac{c}{4\pi}\nabla(\mathbf{E}\times\mathbf{H})=\nabla\cdot\mathbf{S}, \quad (2.11)$$

where $\mathbf{S}$ is the Poynting vector in $\mathrm{W\,cm^{-2}}$ given as:

$$\mathbf{S}=\frac{c}{4\pi}\mathbf{E}\times\mathbf{H} \quad (2.12)$$

By combining the individual terms of Eqn. 2.5 and for $\mathbf{E}$ and $\mathbf{H}$ being orthogonal, we arrive at the far field approximation (plane wave) of the Poynting theorem as:

$$\frac{\partial W}{\partial t}+\frac{dP_{abs}}{dV}+\nabla\cdot\mathbf{S}=0. \quad (2.13)$$

And therefore in a non-absorbing medium, we have $\nabla\cdot\langle\mathbf{S}\rangle=0$,

where $\left\langle \frac{\partial W}{\partial t} \right\rangle = 0$. Here, $\langle\rangle$ is used to denote the average quantities.

2.1.1 The time averaged Poynting vector

Considering that the period of electromagnetic waves, (T) and detection systems, $T^{'}$ are of different orders of magnitude, time average definition of the Poynting vector is relevant and is practically given as where $\Re$ denotes real term:

$$\langle \mathbf{S} \rangle = \frac{1}{2T'} \int_{-T'}^{T'} \frac{c}{4\pi} [\mathbf{E}_t(r,t) \times \mathbf{H}_t(r,t)] dt \simeq \frac{c}{8\pi} \Re\{\mathbf{E} \times \mathbf{H}^*\}, \tag{2.14}$$

where the magnetic and electric fields are defined respectively as: $\mathbf{H}_t(r,t) = \mathbf{H}\exp(-i\omega t)$ and $\mathbf{E}_t(r,t) = \mathbf{E}\exp(-i\omega t)$. Their unitary vector components are respectively defined as $\mathbf{H} = H\mathbf{h}$ and $\mathbf{E} = E\mathbf{e}$. For the mutual orthogonality of $\mathbf{H}$ and $\mathbf{E}$, we have $\sqrt{\mu}H = \sqrt{\varepsilon}E$ and for $c = n_0 c_0$ where $n_0 = \sqrt{\varepsilon\mu}$ is the refractive index and c_0 is the speed of light in a material. By using the vector identity: $\mathbf{A} \times \mathbf{B} = |A||B|sin\theta\hat{\mathbf{s}}$ and $\theta = \frac{\pi}{2}$, being the angle between the magnetic and electric fields, the time averaged Poynting vector could be written as:

$$\langle \mathbf{S} \rangle = \frac{\varepsilon c_0}{8\pi} |\mathbf{E}|^2 \hat{\mathbf{s}}, \tag{2.15}$$

and the density of the plane wave electromagnetic energy is given as:

$$\langle W \rangle = \frac{\varepsilon}{8\pi} |\mathbf{E}|^2 = \frac{\langle \mathbf{S} \rangle \cdot \hat{\mathbf{s}}}{c_0}. \tag{2.16}$$

With this approximation, the dissipative component as a result of the Joule's heat is written as:

$$\left\langle \frac{dP_{abs}}{dV} \right\rangle = \frac{\omega\varepsilon}{2} |\mathbf{E}|^2. \tag{2.17}$$

And by using Eqn. 2.15,

$$\left\langle \frac{dP_{abs}}{dV} \right\rangle = \frac{4\pi\omega\varepsilon^{(i)} \langle \mathbf{S} \rangle \cdot \hat{\mathbf{s}}}{\varepsilon c_0}. \tag{2.18}$$

The time average conservation of energy at a position $\mathbf{r}$ along the direction of $\hat{\mathbf{s}}$ could then be written as:

$$\frac{1}{c_0} \frac{\partial \langle \mathbf{S}(\mathbf{r}) \rangle \cdot \hat{\mathbf{s}}}{\partial t} + \left\langle \frac{dP_{abs}(\mathbf{r})}{dV} \right\rangle + \nabla \cdot \langle \mathbf{S}(\mathbf{r}) \rangle = 0. \tag{2.19}$$

Also, the rotational invariance of the Poynting vector ensures that the total power flow through a surface is independent of the orientation of the surface. As illustrated in Figure 2.3, assuming the Poynting vector in the direction, $\hat{\mathbf{s}}$ is rotated unto $\hat{\mathbf{s}}_j$, the electric and magnetic fields at each point on the surface will also rotate accordingly. However, because the Poynting vector is defined as a cross product of the electric and magnetic fields, it will also rotate in such a way that its direction remains perpendicular to the fields.Therefore, the component of the Poynting vector that is perpendicular to the surface remains constant under rotation, and this component represents the constant power flow through the surface.

For subtending the Poynting vector to an arbitrary direction of the Poynting vector, $\hat{\mathbf{s}}_j$:

$$\langle \mathbf{S}_j(\mathbf{r}) \rangle = S_j(\mathbf{r})\hat{\mathbf{s}}_j = S(\mathbf{r})(\hat{s} \cdot \hat{s}_j)\hat{\mathbf{s}}_j \tag{2.20}$$

and

$$\nabla \cdot \langle \mathbf{S}_j(\mathbf{r}) \rangle = \hat{\mathbf{s}}_j \cdot \nabla[S(\mathbf{r})(\hat{s} \cdot \hat{s}_j)] = \hat{\mathbf{s}}_j \cdot \nabla(\langle \mathbf{S}(\mathbf{r}) \rangle \cdot \hat{\mathbf{s}}_j) \tag{2.21}$$

Therefore the Poynting theorem could be fully written as:

$$\frac{1}{c_0}\frac{\partial \langle \mathbf{S}(r) \rangle \cdot \hat{\mathbf{s}}_j}{\partial t} + \left\langle \frac{dP_{abs}}{dV}(r) \right\rangle (\hat{\mathbf{s}} \cdot \hat{\mathbf{s}}_j) + \hat{\mathbf{s}}_j \cdot \nabla(\langle \mathbf{S}(r) \rangle \cdot \hat{\mathbf{s}}_j) = 0. \tag{2.22}$$

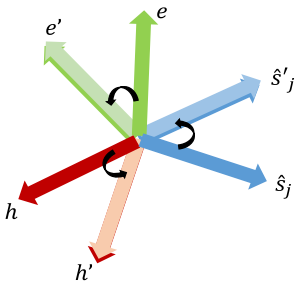


Figure 2.3: This shows the rotation of the direction of the Poynting vector, $\hat{\mathbf{s}}$ unto an arbitrary direction $\hat{\mathbf{s}}_j$. This was inspired from [16].

2.1.2 Propagation of scattered light

This section goes through the underlying equations that describe light intensity as a time averaged Poynting vector to define absorption, scattering, phase function and anisotropy in tissue. The first activity here is to calculate the scattering potential of a particle with a known refractive index $n(\mathbf{r})$. This refractive index is dependent on position $\mathbf{r}$. We can hereby assume a non-magnetic medium of volume V with no charges surrounded by a homogeneous refractive index n_0; Maxwell's equations can be used [16]:

$$\nabla \times \mathbf{H} = \frac{\varepsilon \partial \mathbf{E}}{c \partial t}, \tag{2.23}$$

$$\nabla \times \mathbf{E} = -\frac{\mu \partial \mathbf{H}}{c \partial t}, \tag{2.24}$$

By taking the curl of Eqn. 2.24, and substituting for $\nabla \times \mathbf{H}$ in Eqn. 2.23 we get:

$$\nabla \times \nabla \times \mathbf{E} = -\frac{\mu \partial(\nabla \times \mathbf{H})}{c\partial t}. \tag{2.25}$$

And using the fact that $\nabla \times \nabla \times \mathbf{E} = \nabla \cdot \nabla \mathbf{E} - \nabla^2 \mathbf{E}$, we can write that:

$$\nabla \cdot \nabla \mathbf{E} - \nabla^2 \mathbf{E} + \frac{\mu \varepsilon \partial^2 \mathbf{E}}{c^2 \partial t^2} = 0. \tag{2.26}$$

Here $\mathbf{E}(r,t) = \mathbf{E}(r) \exp -i(\omega t - k.r)$, $n^2 = \mu\varepsilon$ and $k^2 = \frac{n_0^2 \omega^2}{c^2}$, we can rewrite Eqn. 2.26 as:

$$\nabla \cdot \nabla \mathbf{E}(r,t) + k^2 \mathbf{E}(r,t) - k^2 \mathbf{E}(r,t) - \nabla^2 \mathbf{E}(r,t) + \frac{\mu \varepsilon \partial^2 \mathbf{E}(r,t)}{c^2 \partial t^2} = 0. \tag{2.27}$$

which could be simplified as:

$$\nabla^2 \mathbf{E}(\mathbf{r}) + k^2 \mathbf{E}(\mathbf{r}) = k^2 \mathbf{E}(\mathbf{r}) + \nabla \cdot \nabla \mathbf{E}(\mathbf{r}) - \frac{n^2(\mathbf{r}) \omega^2 \mathbf{E}(\mathbf{r})}{c^2} \tag{2.28}$$

and finally write:

$$\nabla^2 \mathbf{E}(\mathbf{r}) + k^2 \mathbf{E}(\mathbf{r}) = \underbrace{-k^2 \left(\frac{n^2(\mathbf{r})}{n_0^2} - 1 \right)}_{\mathrm{F}((\mathbf{r}))} \mathbf{E}(\mathbf{r}) + \nabla[\nabla \cdot \mathbf{E}(\mathbf{r})], \tag{2.29}$$

where the scattering potential is:

$$F(\mathbf{r}) = k^2 \left(\frac{n^2(\mathbf{r})}{n_0^2} - 1 \right) \tag{2.30}$$

and therefore; $F(\mathbf{r}) = \begin{cases} k^2 \left(\frac{n^2(\mathbf{r})}{n_0^2} - 1 \right), & \mathbf{r} \text{ in } V \\ 0, & \mathbf{r}\ out\ of\ V \end{cases}$

Considering that the source term in $\nabla[\nabla \cdot \mathbf{E}(\mathbf{r}]$ vanishes in Eqn. 2.29 for a situation where there is a slowly varying refractive index with position, the solution to Eqn. 2.29 will be the field:

$$\mathbf{E}(\mathbf{r}) = E^{in}(\mathbf{r}) + E^{sc}(\mathbf{r}), \tag{2.31}$$

where $E^{in}(\mathbf{r})$ and $E^{sc}(\mathbf{r})$ are the incident and scattered fields respectively.

With regards to far-field approximation, if we assume a

farther position $\mathbf{r}$ which is far greater than $\mathbf{r'}$, which is a position within a source region, we can write the scattered field as [16]:

$$E^{sc}(\mathbf{r}) = \int_V F(\mathbf{r'})E(\mathbf{r'})g(\mathbf{r},\mathbf{r'})d^3\mathbf{r'} \tag{2.32}$$

where $g(\mathbf{r},\mathbf{r'})$ is the Green's function;

$$g(\mathbf{r},\mathbf{r'}) \sim \frac{\exp(ikr)}{4\pi r}\exp(-ik\hat{\mathbf{s}}\cdot\mathbf{r'}). \tag{2.33}$$

For an incident monochromatic wave of amplitude $|E_0|$ and wave-vector $\mathbf{k}_i$ such that $\mathbf{k}_i = k\hat{\mathbf{s}}_0$ [16];

$$E^{inc}(\mathbf{r}) = |E_0|\exp(ik\hat{\mathbf{s}}_0\cdot\mathbf{r}) \tag{2.34}$$

and

$$E^{sc}(\mathbf{r}) = |E_0|f(\hat{\mathbf{s}},\hat{\mathbf{s}}_0)\frac{\exp(ikr)}{4\pi r}, \tag{2.35}$$

where $f(\hat{\mathbf{s}},\hat{\mathbf{s}}_0)$ is the scattering amplitude. This parameter can be arrived at by using Eqn. 2.32 and Eqn. 2.33 and it shows dependence on the scattering potential. The time averaged Poynting vector for the scattered field is then:

$$\langle\mathbf{S}^{(sc)}\rangle = |\langle S^{(inc)}\rangle|\frac{|f(\hat{\mathbf{s}},\hat{\mathbf{s}}_0)|^2}{r^2}\hat{\mathbf{s}}, \tag{2.36}$$

where the time averaged Poynting vector of the incident field is

$$\langle\mathbf{S}^{(inc)}\rangle = \frac{\varepsilon c_o}{8\pi}|E_0|^2\hat{\mathbf{s}}_0. \tag{2.37}$$

2.2 Diffusion regimes

When light is incident on a scattering medium, some of the photons do not scatter but exit the medium while maintaining their original direction, these are the ballistic photons that define the foundations of ballistic imaging. Apart from ballistic photons, other photons undergo single scattering and this type of photons account for activities in the single scattering regimes whereas photons that undergo multiple scattering form the basis for diffuse imaging and spectroscopy. These types of photons are illustrated in Figure 2.4.

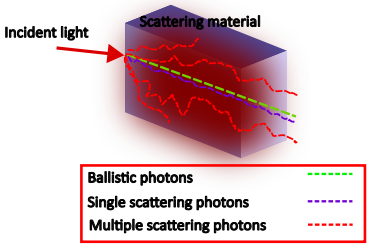


Figure 2.4: Photon scattering regimes.

Ballistic Photon Regime: The ballistic regime refers to the direct propagation of light without significant scattering or diffusion. In this regime, light travels along straight paths through relatively unobstructed regions of tissue. The scattered light does not contribute significantly to the overall distribution, and the transport of light is predominantly determined by unscattered or minimally scattered paths. The ballistic regime is relevant for short path lengths or low scattering densities.

Single Scattering Photon Regime: The single scattering regime occurs when light undergoes a single scattering event before exiting the medium. In this regime, all the scattered photons have an equal chance of going in every direction and the photon distribution becomes more diffuse compared to the ballistic regime.

Diffusive or Multiple Scattering Photon Regime: The diffusive regime is characterized by the dominance of multiple scattering events and the randomization of light propagation. In this regime, the scattered light undergoes a large number of scattering interactions, resulting in a highly scattered and isotropic distribution. The intensity of the scattered light decays exponentially with distance, following the diffusion equation. The diffusive regime is particularly relevant for a medium whose thickness is greater than the transport mean free path.

2.3 Light propagation models

The propagation of light through a medium with multiple scattering presents a complex situation for modelling, as it requires consideration of various parameters. For example, the scattering mean free path and the transport mean free path are integral to this. The scattering mean free path is the average distance a photon travels before being scattered while the transport mean free path, which takes into account the scattering and anisotropy, is the distance after which the photon path is random. These concepts will be illustrated later. Generally, the analytical theory or multiple scattering theory would be appropriate. This option has its foundations from Maxwell's equations but its rigorous nature in addressing practical problems has made it limited for practical reasons like computational complexities for complex tissue structures

[16, 19]. Therefore, the radiative transfer equation and its variations [20] have rather been widely used in the study of light propagation in multi-scattering media.

2.3.1 Radiative Transfer Equation

The Radiative Transfer Equation (RTE) is a fundamental equation derived from Maxwell's equations and used to model light propagation in various applications, such as biomedical optics, remote sensing, and atmospheric physics. The equation only looks at the propagation of the energy of the light and as a results, focuses on intensity as opposed to the electric field. Solving the RTE requires appropriate boundary conditions and often involves numerical methods to simulate light-tissue interactions accurately, especially in complex and heterogeneous tissues. Common techniques include Monte Carlo simulations, finite element methods, and discrete ordinate methods. The time-dependent RTE equation is generally given as [19]:

$$\begin{aligned}&\frac{1}{c}\frac{\partial}{\partial t}I(\vec{r},\hat{s},t)+\nabla\cdot[\hat{s}I(\vec{r},\hat{s},t)]+\mu_t I(\vec{r},\hat{s},t)\\&=\mu_s\int_{4\pi}p(\hat{s},\hat{s}')I(\vec{r},\hat{s}',t)d\Omega'+\varepsilon(\vec{r},\hat{s},t)\end{aligned}\tag{2.38}$$

where the steady-state version is given as [21]:

$$\nabla\cdot[\hat{s}I(\vec{r},\hat{s})]+\mu_t I(\vec{r},\hat{s})=\mu_s\int_{4\pi}p(\hat{s},\hat{s}')I(\vec{r},\hat{s}')d\Omega'+\varepsilon(\vec{r},\hat{s})\tag{2.39}$$

In Eqn. 2.38, $I(\vec{r},\hat{s},t)$ [W m^{-2} sr^{-1}] is the spectral radiance which is the average power in space and time ($\vec{r}$,t) through a unit area in the direction of the unit vector $\hat{s}$. The first term of the equation is a measure of the temporal change of the amount of photons that move in the direction of the unit vector $\hat{s}$, where c is the speed of light. While the second term is the net flux in the direction of the unit vector, the third term indicates the amount of energy influenced by absorption and scattering. The fourth term quantifies the energy from an arbitrary direction $\hat{s}'$ scattered into $\hat{s}$ and the last term ($\varepsilon(\vec{r},\hat{s},t)$) is the energy in $\hat{s}$ as a result of the source in the medium with a volume, V as shown in Figure 2.5.

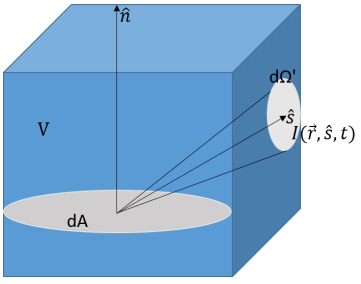


Figure 2.5: The spectral radiance from an area dA within a volume V. The spectral radiance is in the direction of the unit vector $\hat{s}$ with a solid angle $d\Omega'$.

In order to practically measure the spectral radiance, quantities such as the fluence $\Phi(\vec{r}, t)$ measured in $\mathrm{W\,m^{-2}}$ or the photon flux $\vec{J}(\vec{r}, t)$, also measured in $\mathrm{W\,m^{-2}}$ are considered. These are given by the respective equations as [19]:

$$\Phi(\vec{r}, t) = \int_{4\pi} I(\vec{r}, \hat{s}, t) d\Omega' \tag{2.40}$$

and

$$\vec{J}(\vec{r}, t) = \int_{4\pi} I(\vec{r}, \hat{s}, t) \hat{s} d\Omega' \tag{2.41}$$

The diffusion equation is an approximation of the radiative transfer equation (RTE) that can be used to model the transport of light in biological media. The RTE describes how the radiance of a light beam changes as it propagates through a medium that can absorb and scatter light. The diffusion equation simplifies the RTE by assuming that the medium is highly scattering (for example, human tissues where μ_a ranges from 0.03 to 1.6 $\mathrm{cm^{-1}}$ while μ_s', ranges from 1.2 to 40 $\mathrm{cm^{-1}}$ [22]) and isotropic, and that the diffuse flux vector is negligible over time [19]. The diffusion equation can be derived from the RTE by applying a Fick's law approximation and taking the first two moments of the angular dependence of the radiance. The diffusion equation can be solved analytically or numerically for various geometries and boundary conditions, and it can provide estimates of the fluence rate, intensity, and current density of light in biological tissues.

2.3.2 Fick's Law and The Diffusion Equation

Fick's law describes how photons diffuse through tissues, which are non-homogeneous media with varying optical properties. The law is efficient in its depiction of the initial interaction of light with biological tissues, characterized by absorption and scattering events that significantly alter the path and intensity of the light. In the diffusion approximation, the intensity is limited to the first and second terms of spherical harmonic expansion such that the time dependent and steady state equations are respectively given as:

$$I(\vec{r}, \hat{s}, t) = \frac{1}{4\pi}\Phi(\vec{r}, t) + \frac{3}{4\pi}\vec{J}(\vec{r}, t) \cdot \hat{s} \tag{2.42}$$

and

$$I(\vec{r},\hat{s}) = \frac{1}{4\pi}\Phi(\vec{r}) + \frac{3}{4\pi}\vec{J}(\vec{r})\cdot\hat{s}. \tag{2.43}$$

In order to arrive at the diffusion equation (DE), the RTE is integrated over all directions and the flux vector is defined in terms of the fluence rate and Fick's law could be applied [19]. Therefore,

$$\begin{aligned}&\int_{4\pi}\left(\frac{1}{c}\frac{\partial}{\partial t}I(\vec{r},\hat{s},t) + \nabla\cdot[\hat{s}I(\vec{r},\hat{s},t)] + \mu_t I(\vec{r},\hat{s},t)\right)\hat{s}\,d\Omega \\ &= \int_{4\pi}\left(\mu_s\int_{4\pi}p(\hat{s},\hat{s'})I(\vec{r},\hat{s'},t)d\Omega' + \varepsilon(\vec{r},\hat{s},t)\right)\hat{s}\,d\Omega\end{aligned} \tag{2.44}$$

By substituting Eqn. 2.42 into Eqn. 2.44 and performing the integration, we arrive at Fick's law by applying the conditions that $\int_{4\pi}\hat{s}[\hat{s}\cdot\nabla(\vec{A}\cdot\hat{s})]d\Omega = 0$ and $\int_{4\pi}(\hat{s}\cdot\vec{A})\hat{s}\,d\Omega = \frac{4\pi\vec{A}}{3}$. The explanation to these conditions are provided in the Appendix B of [19]. Fick's law is then given as:

$$\vec{J}(\vec{r},t) = -D\left[\nabla\Phi(\vec{r},t) - 3\int_{4\pi}\varepsilon(\vec{r},\hat{s},t)\hat{s}\,d\Omega\right] \tag{2.45}$$

and the steady state representation of this is given as;

$$\vec{J}(\vec{r}) = -D\left[\nabla\Phi(\vec{r}) - 3\int_{4\pi}\varepsilon(\vec{r},\hat{s})\hat{s}\,d\Omega\right] \tag{2.46}$$

In a situation where the source is isotropic, the source term component is non-applicable. Here, the diffusion coefficient, D is the given as $D = 1/3[\mu_a + \mu_s']$. The integral of the RTE yields [19]:

$$\frac{1}{c}\frac{\partial}{\partial t}\Phi(\vec{r},t) + \nabla\cdot\vec{J}(\vec{r},t) + \mu_a\Phi(\vec{r},t) = \int_{4\pi}\varepsilon(\vec{r},\hat{s},t)\hat{s}\,d\Omega \tag{2.47}$$

and by substituting Eqn. 2.45, we arrive at the diffusion equation which indicates the dependence of diffusivity of photons on absorption coefficient and reduced scattering

coefficient:

$$\frac{1}{c}\frac{\partial}{\partial t}\Phi(\vec{r},t) - \nabla\cdot D\left[\left(\nabla\Phi(\vec{r},t) - 3\int_{4\pi}\varepsilon(\vec{r},\hat{s},t)\hat{s}\,d\Omega\right)\right] + \mu_a\Phi(\vec{r},t) = \int_{4\pi}\varepsilon(\vec{r},\hat{s},t)\hat{s}\,d\Omega. \tag{2.48}$$

This equation can be rearranged to cater for a source term, $q_0(\vec{r},t)$ as;

$$\left[\frac{1}{c}\frac{\partial}{\partial t} - \nabla\cdot(D\nabla) + \mu_a\right]\Phi(\vec{r},t) = q_0(\vec{r},t), \tag{2.49}$$

where

$$q_0(\vec{r},t) = \int_{4\pi}\varepsilon(\vec{r},\hat{s},t)d\Omega - 3\nabla\cdot[D\int_{4\pi}\varepsilon(\vec{r},\hat{s},t)\hat{s}d\Omega] \tag{2.50}$$

and for an isotropic source, we can write that;

$$q_0(\vec{r},t) = \int_{4\pi}\varepsilon(\vec{r},\hat{s},t)d\Omega = 4\pi\varepsilon(\vec{r},t) \tag{2.51}$$

2.4 Absorption

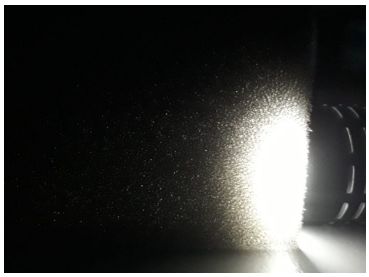


Figure 2.6: Light absorption in an absorbing medium.

When light interacts with biological tissues, it can be absorbed by various chromophores present in the tissue, including haemoglobin and melanin, as well as absorption by water. The absorption process involves the transfer of energy from the incident light to the absorbing molecules, leading to their excitation or promotion of electrons to higher energy levels. The absorption phenomenon is shown in Figure 2.6.

From Eqn. 2.17, we can write the absorbed light energy within a tissue volume as:

$$\overline{P}_{abs} = \int_V \left\langle \frac{dP_{abs}}{dV} \right\rangle dV = \frac{1}{2}\omega\int_V \varepsilon^{(i)}(\mathbf{r})|E(\mathbf{r})|^2 dV. \tag{2.52}$$

The absorption efficiency that relates the absorbed power to the incidence area, A is given as:

$$Q_a^{eff} = \frac{\overline{P}_{abs}}{\langle \mathbf{S}^{(inc)}\rangle A}. \tag{2.53}$$

By defining $k = \frac{\omega}{c_0}$, the absorption cross-section, σ_a is given as:

$$\sigma_a = \frac{\overline{P}_{abs}}{|\langle \mathbf{S}^{(inc)} \rangle|} = 4\pi k \int_V \frac{\varepsilon(i)(\mathbf{r})|E(\mathbf{r})|^2}{\varepsilon|E_0|^2} dV \tag{2.54}$$

The absorption coefficient is the average absorption cross-section per unit volume and for a homogeneous medium of particles (N) in a volume (V) having uniform radii and density ρ, we can write the absorption coefficient, μ_a in cm^{-1} as:

$$\mu_a = \frac{N}{V}\sigma_a, \tag{2.55}$$

where the term absorption mean free path (AMFP) is used to define the inverse of the absorption coefficient as $AMFP = \frac{1}{\mu_a}$.

For a homogeneous medium of thickness, L and assuming the flow of light energy at the surface ($z = 0$) to be $S^{(inc)}$ we can define the Beer-Lambert's Law and write the total energy measured at the thickness to be:

$$S = S^{(inc)} \exp(-\mu_a L) \tag{2.56}$$

Also, for a non-homogeneous situation where the absorption coefficient changes in an incremental portion (dz) along a direction, z summing up to the thickness, L of the medium or tissue:

$$S = S^{(inc)} \exp\left(-\int_0^L \mu_a(z) dz\right). \tag{2.57}$$

Tissue Chromophores

Tissue chromophores are molecules within biological tissues that absorb light at specific wavelengths, influencing the optical properties of tissues. These chromophores play important roles in a wide array of physiological functions and diagnostic procedures. Among the most significant tissue chromophores are melanin, water, oxyhaemoglobin, and haemoglobin, each with distinct absorption spectra and biological functions.

Melanin: the pigment melanin is responsible for the colour of human skin, hair, and eyes. It possesses a broad absorption spectrum that extends from ultraviolet (UV) to visible light. With decreasing wavelength, melanin absorption increases. It absorbs intensely in the UV spectrum and gradually decreases as it approaches the visible spectrum. The specific absorption properties of melanin depend on variables such as its concentration, type (eumelanin or pheomelanin), and the individual's skin.

Water: water is a major constituent of biological tissue and exhibits significant infrared (IR) absorption. In the near-infrared (NIR) region (between 700 nm and 1400 nm), water absorption is relatively low. However, water displays strong absorption bands in the mid-infrared (1400-3000 nm) spectrum. These absorption bands are the result of the vibrational modes of water molecules, specifically the bending and stretching vibrations of its molecular bonds.

Oxyhaemoglobin and haemoglobin: oxyhaemoglobin and haemoglobin are the oxygenated and deoxygenated forms of haemoglobin, respectively, which are responsible for transporting oxygen in blood. These chromophores exhibit characteristic absorption spectra due to their interaction with light and their oxygenation states. Oxyhaemoglobin absorbs light more strongly in the blue-green region (around 400-600 nm) and exhibits lower absorption in the red and near-infrared regions. As oxyhaemoglobin binds oxygen, its absorption spectrum shifts slightly towards longer wavelengths.

Haemoglobin, on the other hand, has a higher absorption in the red and near-infrared range (around 660-940 nm) compared to oxyhaemoglobin. This difference in absorption properties between oxyhaemoglobin and haemoglobin is the basis for various optical techniques, such as pulse oximetry, which utilize changes in blood oxygenation levels to measure physiological parameters.

The absorption of light energy by major tissue components are shown in Figure 2.7. It shows the relationship between the absorption of these chromophores and wavelength.

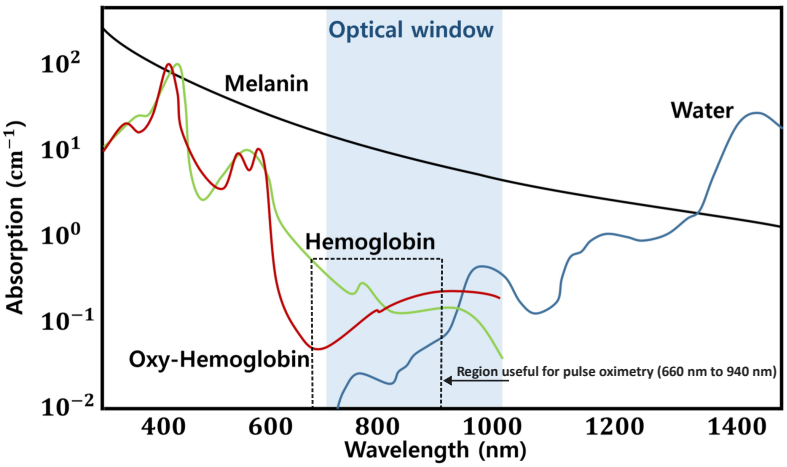


Figure 2.7: Wavelength dependence of optical absorption by chromophores in biological tissues. Inspired from [23].

2.5 Scattering

Scattering refers to the redirection of light rays as they interact with various structures and constituents within tissue. This scattering can occur due to differences in refractive index between tissue components, such as cells, organelles, and extracellular matrices. When light encounters these structural variations, it undergoes multiple interactions, resulting in a change in its direction. Scattering can be broadly classified into two types: elastic scattering (also known as Rayleigh scattering) and inelastic scattering (including Raman and fluorescence scattering). Elastic scattering occurs when the scattered light retains the same wavelength as the incident light. For example, Rayleigh scattering is responsible for the blue colour of the sky and the white appearance of clouds, where scattering of shorter wavelengths is more pronounced. Also, inelastic scattering, on the other hand involves a change in the wavelength of scattered light compared to the incident light. Raman scattering is a type of inelastic scattering that occurs when the scattered light undergoes a shift in energy, providing information about molecular vibrations and structure. Fluorescence scattering occurs when photons are absorbed by fluorophores in tissue and subsequently re-emitted at longer wavelengths. Figure 2.8 shows laser light diffused in an agar block.

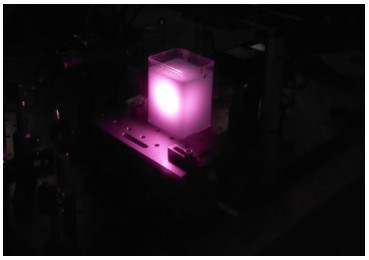


Figure 2.8: Light scattering in diffusive medium (agar block).

2.6 Phase function

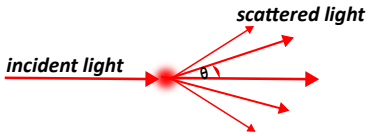


Figure 2.9: Anisotropic scattering of the incident light. For forward anisotropic scattering, $g = 1$.

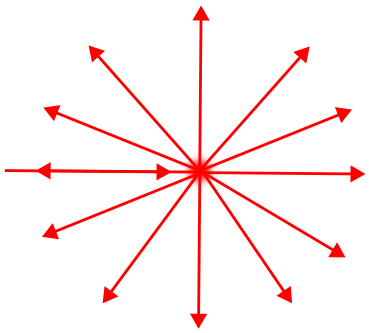


Figure 2.10: Isotropic scattering of the incident light. For isotropic scattering, $g = 0$.

The phase function represents the probability of light being scattered into different directions relative to the incident light direction. It provides information about the scattering characteristics of the tissue and is an important parameter in understanding and modelling light interaction with biological tissues. The diagram in Figure 2.9 shows the case of anisotropic scattering of the incident light, where θ is the angle of the scattered light.

When considering isotropic scattering, shown in Figure 2.10, the phase function is symmetric and uniform in all directions. In other words, isotropic scattering means that the scattered light is equally likely to be redirected in any direction. This is often a simplified assumption used in some theoretical models or simulations.

However, in reality, biological tissues exhibit more complex scattering behaviour with non-isotropic phase functions. The phase function can vary depending on the size, shape, and refractive index of the scattering particles or structures within the tissue. For example, in tissues containing highly ordered structures such as muscle fibres or collagen matrices, the phase function may exhibit preferential scattering in certain directions. This anisotropic behaviour can significantly affect the propagation and distribution of light within the tissue. The phase function is dependent on the scattering amplitude and is given by:

$$p(\hat{\mathbf{s}}, \hat{\mathbf{s}}_0) = \frac{1}{\sigma_{tot}} |f(\hat{\mathbf{s}}, \hat{\mathbf{s}}_0)|^2 \tag{2.58}$$

and the albedo, W_0 is given as:

$$W_0 = \int_{(4\pi)} p(\hat{\mathbf{s}}, \hat{\mathbf{s}}_0) d\Omega = \frac{\sigma_{sc}}{\sigma_{tot}} \tag{2.59}$$

Albedo refers to the fraction of incident light that is scattered by a medium or biological tissue. It represents the ratio of the scattered light intensity to the total incident light intensity. The albedo is a measure of the scattering efficiency of a medium or tissue, indicating how much of the incident light is redirected or scattered rather than absorbed or transmitted. This is a constant quantity that is equal to unity when we

are dealing with a purely non absorbing medium but it is realistically less than unity for tissue.

The Henyey-Greenstein's phase function is a widely used empirical phase function that approximates the scattering behaviour of biological tissues. It provides a more realistic representation of the angular distribution of scattered light compared to isotropic or Rayleigh scattering. Henyey-Greenstein's phase function is characterized by an anisotropic scattering pattern that can be adjusted using a parameter called the anisotropy factor (g). The average cosine of the angle subtended by the incident and scattering directions is defined as the anisotropy factor, g. The Henyey-Greenstein's phase function is given by:

$$p(\theta) = p(\hat{\mathbf{s}}, \hat{\mathbf{s}}_0) = p(\hat{\mathbf{s}} \cdot \hat{\mathbf{s}}_0) = \frac{1}{4\pi} \frac{W_0(1-g^2)}{(1+g^2-2g\hat{\mathbf{s}} \cdot \hat{\mathbf{s}_0})^{3/2}}, \quad (2.60)$$

where $p(\theta)$ is the phase function, θ is the scattering angle. The Figure 2.11 below shows the phase function in relation to the angle of scattering.

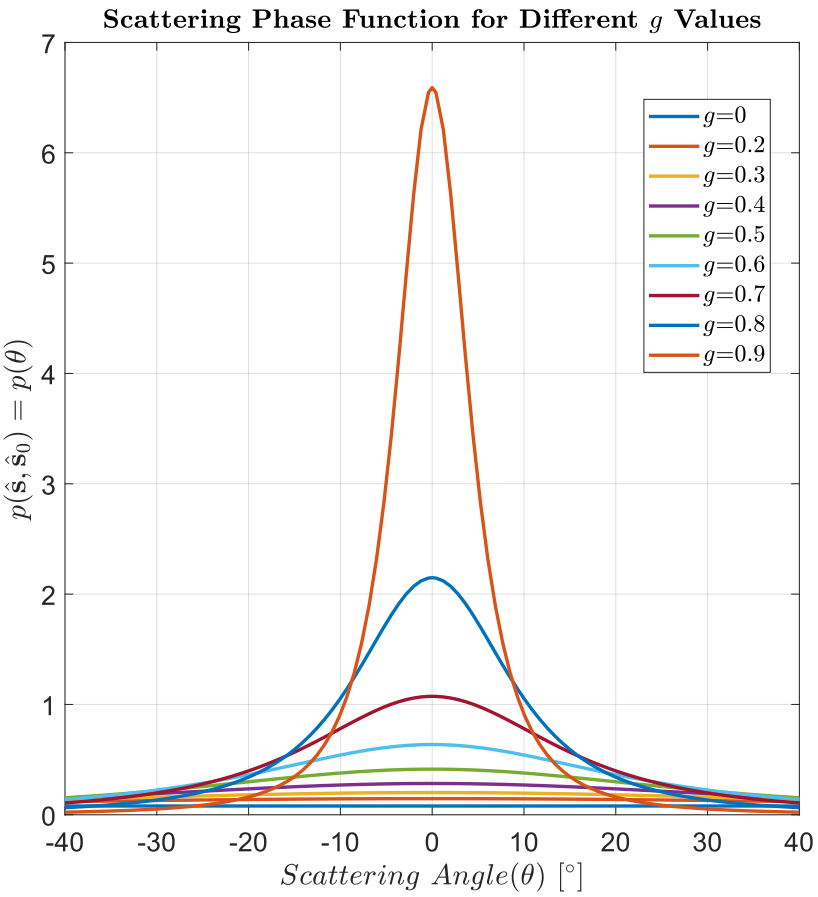


Figure 2.11: Relationship between scattering phase function and anisotropy. Typically for tissues, anisotropy that characterises scattering is 0.9. This shows the Henyey-Greenstein's phase function.

The value of g ranges from -1 to 1, with negative values

indicating backscattering dominance, positive values indicating forward scattering dominance, and $g = 0$, indicating isotropic scattering:

$$p(\hat{\mathbf{s}}, \hat{\mathbf{s}}_0) = \frac{W_0}{4\pi} \tag{2.61}$$

and Rayleigh's phase function is given by:

$$p(\hat{\mathbf{s}}, \hat{\mathbf{s}}_0) = p(\hat{\mathbf{s}} \cdot \hat{\mathbf{s}}_0) = \frac{3}{16\pi}(1 + (\hat{\mathbf{s}} \cdot \hat{\mathbf{s}}_0)^2)W_0 \tag{2.62}$$

The scattering efficiency could be defined in terms of the incident Poynting vector and the cross-sectional area, A where the scattered power is $\overline{P}_{sc}$:

$$Q_{sc}^{eff} = \frac{\overline{P}_{sc}}{\langle \mathbf{S}^{(inc)} \rangle A} \tag{2.63}$$

and the scattering cross-section σ_{sc} can be derived using the conversion equation, $\iiint_V (\nabla \cdot \mathbf{F})\, dV = \iint_S (\mathbf{F} \cdot \mathbf{n})\, dS$ to get:

$$\sigma_{sc} = \frac{\overline{P}_{sc}}{|\langle \mathbf{S}^{(inc)} \rangle|} = \int_V \frac{\nabla \cdot \langle S^{(sc)} \rangle}{|\langle \mathbf{S}^{(inc)}| \rangle} dV = \int_S \frac{\langle \mathbf{S}^{(sc)} \rangle \cdot \mathbf{n}}{|\langle \mathbf{S}^{(inc)} \rangle|} dS, \tag{2.64}$$

where the scattering is considered in a volume, V and $d\Omega = dS/r^2$, we get;

$$\sigma_{sc} = \int_{(4\pi)} |f(\hat{\mathbf{s}}, \hat{\mathbf{s}}_0)|^2 d\Omega. \tag{2.65}$$

With reference to Eqn. 2.55, we can write the scattering coefficient μ_s in (cm^{-1}) as:

$$\mu_s = N\sigma_{sc}, \tag{2.66}$$

and define the reduced scattering coefficient in (cm^{-1}), which accounts for the tissue anisotropy factor, g as, where N is the number of scattering particles per unit volume:

$$\mu_s^{'} = \mu_s(1 - g) \tag{2.67}$$

We can use these definitions to describe the scattering mean free path and transport mean free path, both measured in (cm) respectively as $l_{sc} = 1/\mu_s$ and $l'_{sc} = l_{sc}/(1 - g)$. These terms are illustrated in Figure 2.12. The scattering mean

free path refers to the average distance a photon travels in a medium before it undergoes a single scattering event and the transport mean free path is the average distance a particle travels in the medium before its direction of motion becomes randomized due to multiple scattering events. While the scattering mean free path measures the distance between individual scattering events, the transport mean free path accounts for the cumulative effect of many scattering events on the overall direction of the photon.

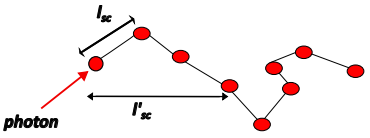


Figure 2.12: Illustration of scattering mean free path (l_{sc}) and transport mean free path (l'_{sc}).

The total extinction cross-section is given by:

$$\sigma_{tot} = \sigma_a + \sigma_{sc} \tag{2.68}$$

and the total extinction coefficient for number of particles per unit volume, N is given as;

$$\mu_{tot} = N\sigma_{tot}. \tag{2.69}$$

In conclusion, this chapter has provided a comprehensive overview of biological tissue optical properties and light interaction. It began with tissue structural and functional classification and how optical properties are influenced by cell, extracellular matrix, and biomolecule composition. It also used the Poynting theorem to explain light flow through tissues and highlighted the role of the Poynting vector in illustrating electromagnetic wave energy flow. This concept is essential for understanding light propagation in various directions with regards to anisotropy. Tissue structure also affects light absorption, scattering, and transmission. The chapter discussed how the ballistic, single scattering, and diffusive regimes of light propagation affect tissue light distribution. It continued to discuss light propagation models, focusing on the Radiative Transfer Equation (RTE) and light-tissue interactions. Fick's Law and the Diffusion Equation were explained to show their importance in light's diffusive transport through scattering media. These models predict light behaviour in complex biological environments and are crucial for non-invasive optical diagnostic and therapeutic studies.

Background of diffuse reflectance spectroscopy

3

3.1 The Kubelka-Munk theory 30
3.2 Instrumentation and experimental techniques 33

This chapter elaborates on the applications and underlying principles of Diffuse Reflectance Spectroscopy (DRS) within the realm of biological tissue analysis, following the fundamental of light propagation, presented in Chapter 2. Notably, it emphasizes the instrumental role of DRS in the non-invasive diagnosis and characterization of biological tissues, particularly through the lens of absorption and scattering phenomena. The application of DRS in detecting colorectal cancer within this thesis exemplifies its significant potential as a diagnostic tool in the field of biomedical optics.

DRS provides an option for the analysis of light interaction with tissues. It primarily relies on the fact that light undergoes partial absorption and scattering by tissue components. This interaction allows for the detailed characterization of the optical properties of tissues. The process requires light incident on biological tissue, thereby triggering a series of scattering and absorption events. Analysing the spectrum of light diffusely reflected from the tissue reveals the optical characteristics of the tissue. These are typically the absorption and scattering coefficients. These coefficients, influenced by the the composition of tissue, provide critical diagnostic information. The composition of a typical DRS system includes a light source, optical fibre and a spectrometer for spectrum analysis.

The clinical usefulness of DRS is highlighted through its capability for non-invasive differentiation of tissue types and identification of pathological alterations. Research works, including those by [24] and [25], have demonstrated the effectiveness of DRS in distinguishing between malignant and benign renal tissues and in characterizing myocardial infarction in vivo, respectively. Lin et al. [26] showcased the use of DRS in intraoperative guidance, differentiating paediatric brain tumors from normal tissue, with further advancements in intraoperative tumor surgery systems reported in subsequent studies [27]. Innovations by Yu et al. [28–30] have led to the development of fibre optic probes with real-time, self-calibration features, enhancing the clinical applications

of DRS. Theoretical contributions to the interpretation of DRS data, such as optical property extraction and Monte Carlo simulations, have been made by Ramanujam et al. [31, 32]. Moreover, DRS has gained prominence in the biomedical field, with studies like those by Volynskaya et al. [33] utilizing DRS alongside intrinsic fluorescence spectroscopy for breast tissue classification. Early system development efforts by Messerschmidt et al. [34, 35] provided a foundation for the technology. Works by Stelzle et al. [36, 37] into the use of DRS for tissue differentiation in oral and maxillofacial surgery highlight its potential in surgical settings. The extensive research across these studies illustrates the broad applications of DRS, underscoring its value in advancing non-invasive diagnostic methods.

An integral foundation of DRS could be based on the Kubelka-Munk (K-M) theory, a mathematical framework that simplifies the complex interplay of light absorption and scattering within a sample into quantifiable parameters. This model's ability to distinguish the intrinsic optical properties of materials from their reflectance spectra has facilitated groundbreaking research into a plethora of substances, including catalysts, minerals, polymers, and pharmaceuticals. Despite the inherent assumptions of the K-M theory, such as homogeneity and infinite thickness of samples, its applicability to a broad array of materials underlines its robustness and adaptability. The following section delves into the K-M theory.

3.1 The Kubelka-Munk theory

The Kubelka-Munk (K-M) theory provides an analogous quantification of the absorption and scattering of samples respectively denoted as K and S. This is actually not directly based on the discussion of μ_a and μ_s in Chapter 2. Here, these optical parameters are determined based on the configuration of transmittance and diffuse reflection. The theory is based on the assumption that the medium in question is homogeneous, isotropic and of semi-infinite thickness. This allows for the possible expression of the reflectance in terms of K and S. This theory models light-matter interaction with a two flux approach where the incident flux is forward propagating and the reflected flux is backward propagating as illustrated as I

and J respectively in Figure 3.1 [38]. It is hereby noted that the incident light traverses a fractional thickness dx where we have the forward and backward propagations respectively as $i(x)$ and $j(x)$. From the figure, R is the reflectance for example, of a tissue sample and considering that it is semi-infinitely thick, R_B signifies the reflectance from backing material [39].

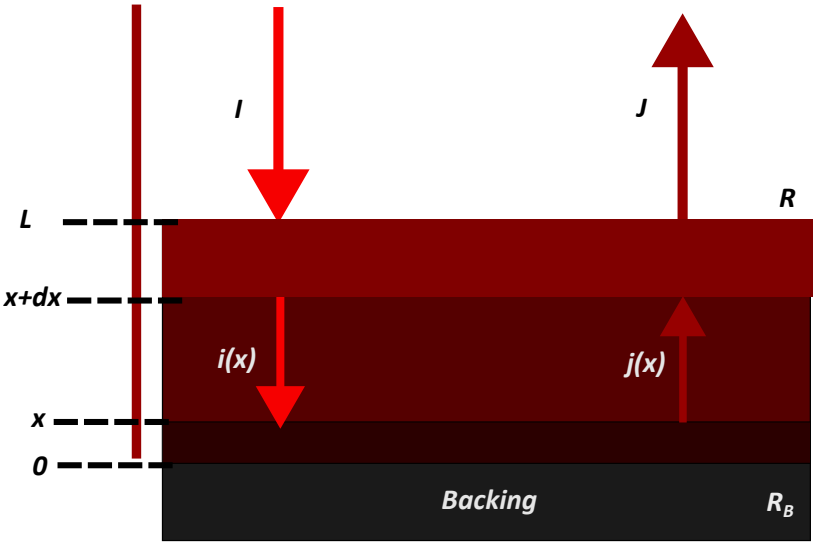


Figure 3.1: The Kubleka-Munk model of light-matter interaction.

We can hereby use sign conversions to write the fractional changes in th incident and the reflected fluxes within the fractional thickness respectively in the following equations:

$$\frac{-di}{i} = -Kdx - Sdx + S\left(\frac{j}{i}\right)dx \tag{3.1}$$

and

$$\frac{dj}{j} = -Kdx - Sdx + S\left(\frac{i}{j}\right)dx \tag{3.2}$$

By defining reflection as $r = j/i$, and summing these equations, we get:

$$\frac{dr}{r} = -2(K+S)dx + S\left(r + \frac{1}{r}\right)dx \tag{3.3}$$

From this, we can denote $a = \frac{K}{S} + 1$ and rearrange the equation with the purpose of integrating from reflectance of the backing material to the surface of the tissue sample, hence considering the full length, L:

$$\int_{R_B}^{R} \frac{dr}{r^2 - 2ar + 1} = SL \tag{3.4}$$

The solution to this is given by [38]:

$$\frac{1}{2\sqrt{(a^2-1)}} ln \left[\left(\frac{R - a - \sqrt{(a^2-1)}}{R - a + \sqrt{(a^2-1)}} \right) \left(\frac{R_B - a + \sqrt{(a^2-1)}}{R_B - a - \sqrt{(a^2-1)}} \right) \right] = SL \tag{3.5}$$

If we now consider the assumption that $L \rightarrow \infty$ then we can write:

$$R - a + \sqrt{(a^2-1)} = 0 \tag{3.6}$$

From this we can write the Kubelka-Munk function as:

$$F(R) = \frac{K}{S} = \frac{(1-R)^2}{2R} \tag{3.7}$$

The significance of this function is that the reflectance measured could be expressed in terms of the absorption and scattering of the material. This value of absolute reflectance, R is not measured practically and hence the relative reflectance, R_∞ is used and defined as:

$$R_\infty = \frac{R_{sample}}{R_{standard}}, \tag{3.8}$$

where R_∞ is the reflectance of an infinitely thick sample, R_{sample} and $R_{standard}$ are the respective reflectances of the sample and the reflection standard. The material for the reflection standard could be MgO or $BaSO_4$ [40].

3.2 Instrumentation and experimental techniques

The instrumentation of Diffuse reflectance spectroscopy generally comprises the broad-spectrum light source which can be a halogen lamp or white light emitting diode (LED) that operates over a range of wavelength. When appropriate, laser sources of specific wavelengths could be employed. These light sources are carried by fibre optic probes that could be used to access various depths of the sample under study through the source to detector separations. Integral to the instrumentation of DRS systems, is the spectrometer. The spectrometer analyses the wavelength distribution of the reflected light and in cases where spectral fingerprints of specific constituents of the sample is needed. The use of reflectance standards as mentioned above is important in the measurement of the actual sample reflectance. This is done by accounting for the reflectance of a pure white and pure black materials for signal corrections.

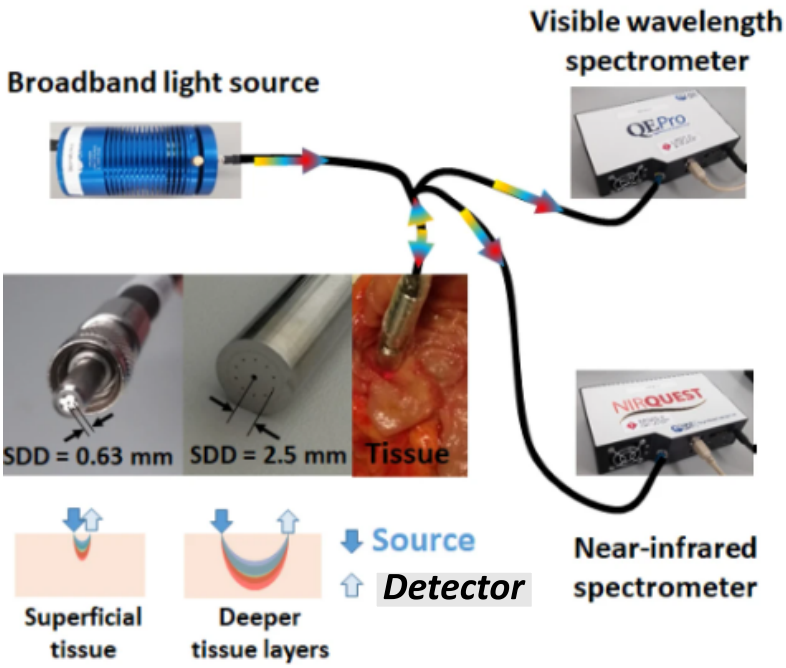


Figure 3.2: Diffuse reflectance system components. Inspierd from [41].

Typically, in experiments, the wavelength dependent reflectance of for example tissue sample, could be normalised by the reflectivity of the reflectance standard used it is calculated using [41]:

$$R(\lambda) = \frac{1}{Reflectivity} \frac{I_{sample}(\lambda) - I_{Background}(\lambda)}{R_{standard}(\lambda) - I_{Background}(\lambda)}. \quad (3.9)$$

The diagram in Figure 3.3 is a representation of the reflectance measured for both tumor and mucosal tissue. The image does not show significant differences in the NIR region but these differences could be classified using machine learning algorithms such as support vector machines (SVMs). This is one of the highlights of DRS with its sensitivity to the composition of chromophores in different tissues and as a result, presents a possibility for tissue classification.

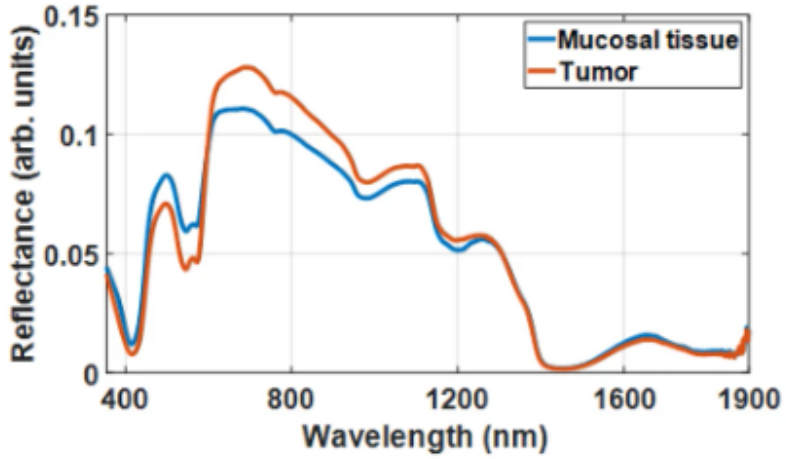


Figure 3.3: The reflectance spectra of mucosal tissue and tumor. Inspired form [41].

Generally in DRS, several conditions can influence the reflectance measured. These conditions can be the specular reflection that is superimposed on the diffuse reflection. Also, type of adsorbent, particle size and moisture can affect the reflectance [40]. Additionally, the concept of probe pressure in Diffuse Reflectance Spectroscopy (DRS) explores how the force exerted by the fibre-optic probe against tissue sample influences the spectral measurements obtained. This aspect is crucial because DRS measurements are sensitive to the micro-environment within tissue, including blood content, tissue morphology, and optical properties, all of which can be altered by applying pressure.

The study by Lim et al. investigated probe pressure effects on human skin via DRS and fluorescence measurements. It highlighted that short-term (< 2 s) application of light probe pressure affects physiological properties extracted from the

measurements by less than ±10%, with diagnostically significant physiological properties affected by less than ±5% [42]. The study reveals that absorption decreases with site-specific variations, suggesting blood is pressured out of the sampled volume, affecting the spectral measurements. This underlines that while minimal and short-applied pressure may introduce negligible distortions, long-term (> 30 s) and large pressures can significantly distort the spectra, necessitating careful consideration of probe pressure in clinical and research settings.

Furthermore, the work by Hennessy et al. looked into how probe geometry and optical properties affect the sampling depth in DRS, employing computational and experimental approaches. The study used Monte Carlo simulations to model light transport, examining the effects of probe design and optical properties on the depth of tissue sampled by the collected light [43]. This study highlights the importance of the design of the fibre-optic probe, specifically the source-detector separation and the optical properties of the probe, in determining the effectiveness of light collection and the extent of tissue examined. Consequently, these factors have a direct impact on the precision and reliability of DRS measurements.

The investigation of sampling depth, taking into account probe geometry and optical properties, highlights the potential for optimizing various probe designs for specific diagnostic applications. This can be achieved by adjusting the distance between the probe and target, or the distance between the source and detector, while also considering the optical characteristics of the tissue. This method allows for the creation of probes that are tailored to specific applications, thereby improving the diagnostic capabilities of DRS by ensuring that measurements precisely correspond to the characteristics of the target tissue [43].

While being useful in diffuse reflectance spectroscopy, the Kubelka-Munk model has several limitations that limit its applicability and accuracy. First, it assumes that medium scattering is isotropic and homogeneous, which is rare in real-world samples where scattering properties vary spatially and directionally. The model assumes a semi-infinite sample thickness and ignores sample boundaries and surface reflections, which can significantly affect measured reflectance in thin or highly reflective samples. Kubelka-Munk theory

also simplifies light-sample interaction by considering only two fluxes moving in opposite directions, without taking into account, the complex multi-directional scattering that occurs in practice. In summary, this chapter has used the Kubelka-Munk model to explain the concept of DRS while highlighting how DRS has been used in various applications especially for cancer studies and tissue characterization. The chapter explained the instrumental configuration in DRS while laying grounds for an overview of the experimental process. This section of the thesis is structured to provide foundational understanding to the DRS experiment conducted in Chapter 6.

Ultrasound and tissue mechanics

4

4.1 Mechanical waves in fluids 38
4.2 Acoustic impedance, reflection and transmission of ultrasound waves 40
4.3 Impedance matching for acoustic coupling 41
4.4 Transducers and ultrasound fields . . 41

This chapter provides an in-depth examination of the characteristics of ultrasound wave fundamentals in the field of bio-imaging. The purpose of this is to emphasize the basic operations of conventional ultrasound application with the aim of providing a framework for understanding the acousto-optic technique employed in the experiments described in this thesis.

Ultrasound waves oscillate at higher frequencies than the human audible range, which is 20 Hz to 20 kHz. Ultrasound imaging resolution is determined by the ultrasound wavelength, which is link to the frequency by the speed of sound in the imaged medium. The amplitude, which indicates how far tissue particles can move, influences the intensity of the ultrasound signal. Also, the speed of sound, (v_a) is important to how ultrasonic waves travel and is related to tissue characteristics. Changes in the composition, density, and elasticity of biological tissues alter this speed of sound, thereby influencing how well images are formed from various types of tissue. The speed, which is determined by the bulk modulus k or Young's modulus E and density ρ, is critical for properly interpreting ultrasound signals.

When ultrasound waves travel through tissues, a number of phenomena could be observed including reflection, refraction and scattering. Scattering for example, which is due to the presence of small tissue structures, has an effect on the quality of images and offers insights into the tissue microstructure. In ultrasound, the reflection, transmission, and absorption of ultrasound waves are all based on a phenomenon known as acoustic impedance Z, which is the product of tissue density and the speed of sound. Reflection is caused by differences in acoustic impedance at tissue interfaces, which contribute to the creation of echoes that are necessary for image reconstruction. Also, the attenuation coefficient, α, helps in determining the depth of penetration and the clarity of the image.

In addition, ultrasound waves can cause both thermal and non-thermal effects in biological tissues. The process of absorbing ultrasound energy is a fundamental aspect of thermal

phenomena, which has the potential to lead to a rise in temperature. Non-thermal effects, such as cavitation and acoustic streaming, offer alternative approaches for diagnostic and therapeutic purposes. In order to guarantee the safety of ultrasound procedures, it is important to achieve a balance between these effects. The rest of the chapter will discuss in depth, the enumerated quantities and phenomena.

4.1 Mechanical waves in fluids

Ultrasound waves in fluids are longitudinal waves, characterised by displacement of the medium in the same direction as the wave propagation. Compressibility, β of a material is defined as the relative change in volume, V that occurs in response to a change in pressure, P at constant temperature, T. Mathematically, it is expressed as:

$$\beta = -\frac{1}{V}\left(\frac{\partial V}{\partial P}\right)_T . \tag{4.1}$$

In the following development, the relationship between the speed of sound and the material property is derived to describe the mechanical characterisation of the fluid. When pressure, ΔP is applied to a fluid element as illustrated in Figure 4.1, the downward force $\mathbf{F}_{down}$ goes through a displacement Ψ to cause a pressure gradient as a result of $\mathbf{F}_{up}$ which is due to the corresponding pressure described by Taylor's series expansion along the z-axis as $\Delta P + \frac{\partial \Delta P}{\partial z} dz$. Similarly, the down displacement is not the same as the up displacement as seen in $\Psi + \frac{\partial \Psi}{\partial z} dz$. An in depth description of the phenomenon is in [44].

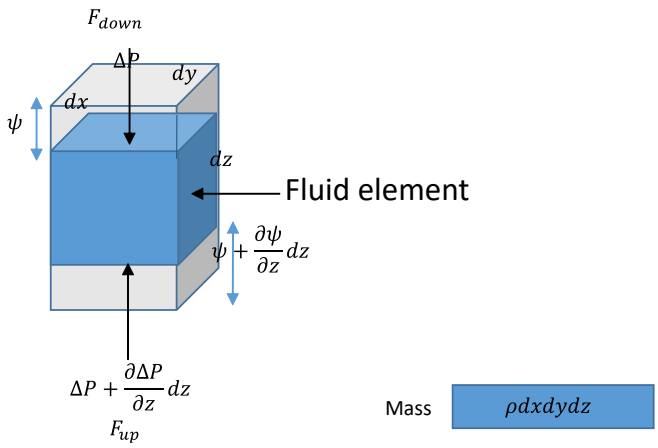


Figure 4.1: Pressed tissue sample undergoing mechanical deformation.

For a material density ρ, the mass of the sample could be written as $\rho dxdydz$. For the sake of simplicity, let us say $\Delta P = P$ is the applied pressure, we can the write $\mathbf{F}_{up} = P.dx.dy$ and $\mathbf{F}_{down} = \left(P + \frac{\partial P}{\partial z}dz\right).dx.dy$. The change in force Δf_z is then given as;

$$\Delta f_z = F_{down} - F_{up}. \tag{4.2}$$

Therefore,

$$\Delta f_z = -\frac{\partial P}{\partial z}dxdydz \tag{4.3}$$

Since the displacement is Ψ, it implies that Δf_z could be written in terms of mass and acceleration;

$$\Delta f_z = \rho dxdydz\frac{\partial^2\Psi}{\partial^2 t} \tag{4.4}$$

As a result, by equating Eqn. 4.3 and Eqn. 4.4 we have:

$$-\frac{\partial P}{\partial z} = \rho\frac{\partial^2\Psi}{\partial^2 t} \tag{4.5}$$

Also, from Eqn. 4.1, the compressibility and its relation to a fractional change in volume of fluid in a container, implies that

$$\frac{\Delta V}{V} = \frac{dxdy(\Psi + \frac{\partial\Psi}{\partial z}dz - \Psi)}{dxdydz} = \frac{\partial\Psi}{\partial z} \tag{4.6}$$

From Eqn. 4.1, it could be inferred that

$$\frac{\Delta V}{V} = -\Delta P\beta \tag{4.7}$$

and for an applied pressure P, we can use Eqn. 4.6 and Eqn. 4.7 to write;

$$-\frac{\partial P}{\partial z}\beta = \frac{\partial^2\Psi}{\partial^2 z} \tag{4.8}$$

Using Eqn. 4.5,

$$\frac{\partial^2\Psi}{\partial^2 z} = \rho\beta\frac{\partial^2\Psi}{\partial^2 t} \tag{4.9}$$

This is the wave equation where $1/v_a^2 = \rho\beta$ and for fluid element, the acoustic speed is dependent on the compressibility and therefore:

$$v_a = \sqrt{\beta\rho} \tag{4.10}$$

4.2 Acoustic impedance, reflection and transmission of ultrasound waves

The amount of an ultrasound wave that is reflected or transmitted at a boundary between two materials is determined by the acoustic impedance of the boundary. The relationship between the acoustic intensity, I_a and the impedance, Z is such that;

$$I_a = \frac{P^2}{2Z} \tag{4.11}$$

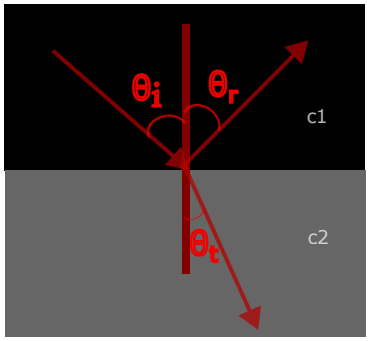


Figure 4.2: Snell's law depiction of ultrasound waves at the interface of two media.

The concept of acoustic impedance brings to mind the phenomenon that defines Snell's law of wave propagation across boundaries of different properties as illustrated in Figure 4.2. In here, if we assume two acoustic materials of respective speeds; $c1$ and $c2$ then the angle of wave incidence, θ_i and that of the transmitted wave, θ_t are related to the speeds by:

$$\frac{c_1}{\sin\theta_i} = \frac{c_2}{\sin\theta_t} \tag{4.12}$$

and in case of reflection, the reflected angle θ_r requires that;

$$\frac{c_1}{\sin\theta_i} = \frac{c_1}{\sin\theta_r} \tag{4.13}$$

In terms of pressure and intensity, we could define reflectance and transmission coefficients. The incidence pressure, P_i is related to both the reflected pressure, P_r and transmitted pressure, P_t as $P_i + P_r = P_t$ where the reflection and transmission coefficients are respectively given as;

$$R = \left(\frac{P_r}{P_i}\right)^2 = \left(\frac{Z_2\cos\theta_i - Z_1\cos\theta_t}{Z_2\cos\theta_i + Z_1\cos\theta_t}\right)^2 \tag{4.14}$$

and

$$T = \left(\frac{P_t}{P_i}\right)^2 = \frac{4Z_1Z_2\cos^2\theta_i}{(Z_2\cos\theta_i + Z_1\cos\theta_t)^2} \tag{4.15}$$

For perpendicular incidence,

$$R = \left(\frac{P_r}{P_i}\right)^2 = \frac{(Z_2 - Z_1)^2}{(Z_2 + Z_1)^2} \tag{4.16}$$

and

$$T = \left(\frac{P_r}{P_i}\right)^2 = \frac{4Z_1Z_2}{(Z_2 + Z_1)^2}. \tag{4.17}$$

4.3 Impedance matching for acoustic coupling

In ultrasound imaging, the impedance of the ultrasound transducer and the skin should be matched using ultrasound gel or water as shown in Figure 4.3. This is primarily because ultrasound waves are highly reflected in air and as a result, do not propagate to tissues without a coupling layer. Typical coupling efficiencies of medical coupling agents is over 90% because acoustic impedance of these agents are closely related to that of human tissues of 1.33 $MRayl$ to 1.6 $MRayl$. Practically, the transmission coefficient in an imaging scenario is given as [44, 45]:

$$T = \frac{4Z_1Z_3}{(Z_3 + Z_1)^2\cos^2(k_2L) + \left(Z_2 + \frac{Z_1Z_3}{Z_2}\right)^2\sin^2(k_2L)}. \tag{4.18}$$

In cases where the coupling layer is either thick or thin ($L = n\lambda/2$ or $L \ll \frac{\lambda}{4}$ respectively), the sin term becomes negligible and the cos term becomes 1 where k_2 is the wave number in the coupling layer. Hence, the transmission coefficient becomes independent of the impedance of the coupling layer and it is given as:

$$T = \frac{4Z_1Z_3}{(Z_3 + Z_1)^2}. \tag{4.19}$$

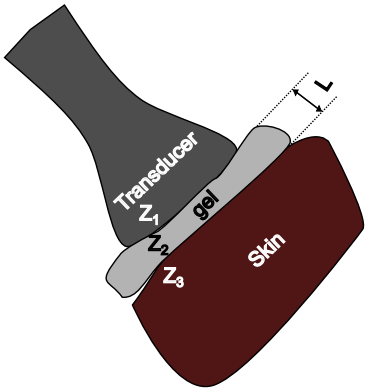


Figure 4.3: Impedance matching requirement for ultrasound imaging. The thickness of the gel is independent of the transmission coefficient of the wave that gets to the skin. For thick and thin layers (L), $L = n\lambda/2$ and $L \ll \frac{\lambda}{4}$ respectively, where n is an integer [44].

4.4 Transducers and ultrasound fields

It is possible to observe the piezoelectric effect in materials such as lead zirconate titanate (PZT), which, when subjected to an electrical voltage, undergoes a change in shape, resulting in the production of sound waves. Conversely, when these materials are subjected to mechanical vibrations brought on by incoming sound waves, they generate an electrical voltage. This dual capability is utilised in ultrasound imaging by employing the transducer to both transmit high-frequency sound waves into the body and to receive the echoes that

are reflected back from the internal tissues of the body. This piezoelectric material is typically used in the construction of a transducer. It is sandwiched between an absorbing layer at the back and an impedance matching layer at the front of the device. The absorbing layer is employed to prevent the piezoelectric material from reverberating. On the other hand, the impedance layer is designed to optimise the ultrasonic wave for propagation into materials [44]. This configuration is depicted in a cylindrical transducer, as shown in Figure 4.4. The acoustic lens works in the manner as lenses operate in optics.

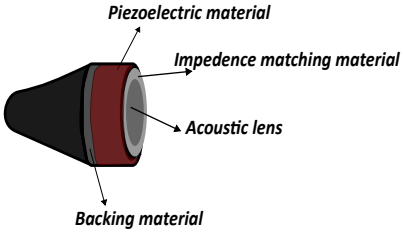


Figure 4.4: Parts of a cylindrical transducer.

The design of ultrasound transducers varies to cater to different imaging needs. Transducers come in various shapes and sizes, with the choice depending on the specific application, such as abdominal, cardiac, or intravascular imaging. The frequency of the sound waves used in ultrasound also plays a critical role in determining both the resolution and penetration depth of the imaging. Higher frequencies produce higher resolution images but have a shallower penetration depth, making them suitable for imaging superficial body structures. Conversely, lower frequencies penetrate deeper but at the expense of image resolution, making them ideal for imaging deeper structures.

Another important aspect of ultrasound transducer technology is the array design, which includes linear, phased, and curved arrays. These designs influence the focusing and steering of the ultrasound beam, thereby affecting the quality and dimensions of the acquired images. Phased array transducers, for instance, are capable of electronically steering the beam, allowing for rapid imaging of moving organs, such as the heart.

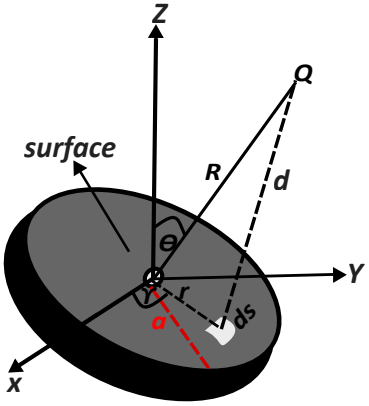


Figure 4.5: Ultrasound propagation by a cylindrical ultrasound transducer. Inspired from [44].

Now, we can use Huygen's principle to consider the acoustic pressure field $P_s(r)$ with amplitude A_0. This field is from a fractional area, ds of the disc-shaped transducer surface to an arbitrary distance, R, as shown in Figure 4.5 as:

$$P_s(r) = A_0 \frac{\exp^{j(\omega t - kr)}\, ds}{R}, \tag{4.20}$$

where ω, t, R and k are the angular frequency, time, distance from the transducer surface and wave vector respectively.

If we now want the total pressure field from the cylindrical transducer at a tissue position, Q, we would integrate the

field with respect to the differential element $ds = rd\Upsilon \cdot dr$, for the entire pressure over the area of the transducer as:

$$P = A_0 \cdot \int_{r=0}^{a} \int_{0}^{2\pi} \frac{\exp^{j(\omega t - kd)} \cdot r d\Upsilon \cdot dr}{d}. \tag{4.21}$$

Here, the distance R in Eqn. 4.20 is replaced by d because we are considering the propagation from the differential element. The radius of the transducer is a and the distance for the centre of the transducer to the location of the differential element is r.

By following the full derivation in [44], we can use Bessels functions to write the overall field subtended by R and θ at an acoustic far field as:

$$P(R, \theta) = [\pi a^2 \cdot A_0] \left[\frac{\exp^{j(\omega t - k \cdot R)}}{R} \right] \cdot \left[\frac{2 \cdot J_1 ka \sin\theta}{ka \sin\theta} \right]. \tag{4.22}$$

If we separate the terms of Eqn. 4.22, the first term controls the amplitude of the pressure field while the second term describes the extinction of the pressure field with distance, R. The third term is the directivity function which describes the amplitude of the pressure field as a function of the azimuth.

In conclusion, this chapter has provided a look into the fundamental aspects of ultrasound and its interaction with biological tissues, which is essential to the study of acousto-optical interaction in tissue samples as treated in the PART 2 of this thesis. By exploring the mechanical waves in fluids and solids, the chapter showed how acoustic impedance plays a role in the reflection, transmission, and absorption of ultrasound waves. The principle of impedance matching for acoustic coupling has also been addressed. It also discussed the design and functionality of transducers and how these tools are precisely engineered to generate and receive ultrasound waves.

A review of acousto-optical tomography

5

This chapter provides a review of the techniques of acousto-optical tomography. It presents the various optical configurations as well as highlighting the ultrasound engineering used in AOT setups. It specifically looks at the progress of the acousto-optical technology to its current state of the art. Also, the theoretical explanations of how light interact with ultrasound in a scattering medium is approached through various mechanisms such as the displacement of scatterers and changes in refractive index.

The acousto-optic effect, which is the interaction between acoustic waves and optical waves was first predicted by Brillouin in 1922 [46] and a decade after, experimental works were conducted by Lucas and Biquard in France [47] as well as Debye and Sears in the United States [48]. Quite recently (in the 1990s), the acousto-optic effect has been explored for biological imaging.

The underlying principle of AOT is based on the acousto-optic effect where a beam of coherent light traversing an acoustic focus gets modulated in frequency and the amount of frequency-shifted photons (tagged photons) is extracted using sensitive detection systems and image reconstruction tools. In other words, the light going through tissue sample is modulated by the US wave at the focus of the transducer. The light-ultrasound interaction within the tissue matrix is caused by the variation of refractive index locally within and around the focal region. Also, the US wave pressure causes the displacement of scatterers up to a few nanometres [49]. The refractive index modulation and displacement of scatterers consequently modulate the phase of the light emerging out of the acoustic focus. The light illumination and the US wave can be orthogonally positioned in the medium under study as shown in Figure 5.1. This tagging of the light by the ultrasound wave generates sidebands that are close to the wavelength of the incident laser. The separation between a sideband and the incident wavelength is 10^{-5} nm at the same MHz frequency.

5.1 Theoretical background of acousto-optics 46
5.1.1 Raman-Nath and Bragg diffraction regimes 46
5.1.2 Brownian motion and ultrasound-induced movement of point-like scatterers in the acousto-optic signal 49
5.1.3 Contributions of the refractive index change and displacement of scatterers to the acousto-optic signal 52
5.2 Optical techniques in AOT 55
5.2.1 Challenges in AOT signal detection . . 55
5.2.2 Detection solutions 56
5.2.3 Imaging and resolution solutions . . . 67
5.3 How multiple acoustic foci have been used in AOT 69
5.4 Plane-Wave Ultrasound in AOT . . . 71

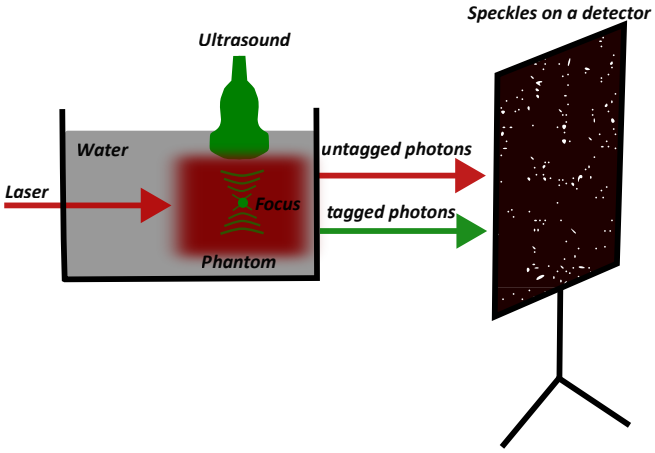


Figure 5.1: A coherent laser propagates through an ultrasound focus and the emerging light constitutes ultrasound-tagged photons and photons of the laser frequency.

5.1 Theoretical background of acousto-optics

One of the first theoretical explanation of the principles of AOT was developed by Leutz and Maret [50]. They modelled the ultrasound effect on the dynamic scattering of light in disordered homogeneous media in a transmission geometry. They assumed that by considering that the scattering mean free path was much greater than the acoustic wavelength. Later on, Wang [51, 52] presented an analytical and Monte Carlo modelling of ultrasound modulation of multiply scattered light. Both results were consistent with each other. In the local region of insonification within scattering media, the mechanisms of acousto-optical interaction have been attributed to changes in the refractive index and the displacement of scatterers. Additionally, the contribution of the Doppler effect to this interaction has been extensively studied, distinguishing its effects in both clear and scattering media. These theoretical considerations are discussed in detail in the following sections.

5.1.1 Raman-Nath and Bragg diffraction regimes

The acousto-optic effect in a medium with homogeneous optical properties is subject to Raman-Nath diffraction. This phenomenon accounts for the shifting of the light frequency by the ultrasound frequency thereby generating side-bands that depend on the ultrasound frequency [53]. These side-bands are actually integer multiples of the acoustic frequency.

Huang et al. [54] have recently utilized Monte Carlo (MC) simulation to study this and the ultrasound tagging efficiency in AOT. They redefined tagging efficiency by dividing the power of the tagged light by the sum of the power of light tagged within the acoustic focus as well as untagged light within the focus.

To understand what happens when light interacts with ultrasound in a clear medium, the two diffraction phenomena: Raman-Nath and Bragg diffractions are discussed. This section is treated with the understanding provided in [55, 56]. These are the Raman-Nath and Bragg diffractions as shown in Figure 5.2 (a) and (b) respectively.

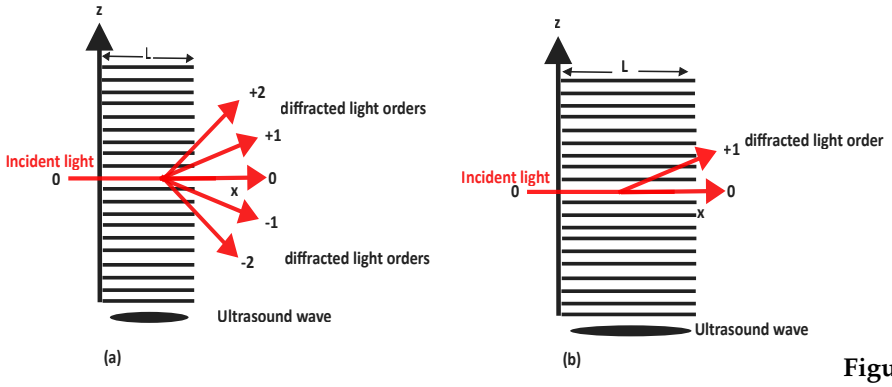


Figure 5.2: (a)Raman-Nath and (b)Bragg diffractions.

This acousto-optic interaction induces a moving refractive index change in the direction of the acoustic wave (z) as:

$$n(z,t) = n_0 + \Delta n \sin(\omega_a t - k_a z) \tag{5.1}$$

where n_o is the equilibrium refractive index and Δn is the change in the refractive index as a result of the acoustic strain, ω_a is the acoustic frequency and $k_a = \frac{2\pi}{\Lambda}$ is the acoustic wave vector (with acoustic wavelength, Λ).

When considering Raman-Nath diffraction regime, the primary interest is in the weak interaction between light and ultrasound as well as the small width L, of the interaction grating (at lower frequencies: MHz). On the other hand, the Bragg diffraction occurs when this width is large enough and the acousto-optic interaction is intense (at higher frequencies: MHz to GHz). In this case, there is a single diffraction order. In the case of the Raman-Nath diffraction, the width is considered small enough to generate a thin moving phase

grating which creates a phase change given by:

$$\Delta\phi = \left(\frac{2\pi}{\lambda_0}\right) n(z,t)L = \phi_0 + \phi_1 \sin(\omega_a t - k_a z) \tag{5.2}$$

where λ_0 is the free space optical wavelength and $\phi_0 = \left(\frac{2\pi}{\lambda_0}\right) n_0 L$ and $\phi_1 = \left(\frac{2\pi}{\lambda_0}\right) \Delta n L$ are the phase without the acoustic strain and with acoustic strain respectively.

The width, L defines the type of diffraction based on these conditions: $Diffraction = \begin{cases} L \ll \frac{k}{k_a^2}, & Raman - Nath \\ L \gg \frac{k}{k_a^2}, & Bragg \end{cases}$

here, $k_a = \frac{2\pi}{\Lambda}$ and $k = \frac{2\pi n_0}{\lambda_0}$.

We can consider the transmitted field as a result of the light-ultrasound interaction as:

$$\begin{aligned} E_t = {} & E_0 J_0(\phi_1) e^{j(\omega t - \phi_0)} \\ & - E_0 J_1(\phi_1) \left[e^{j[(\omega+\Omega)t - Kz - \phi_0]} - e^{j[(\omega-\Omega)t + Kz - \phi_0]} \right] \\ & + E_0 J_2(\phi_1) \left[e^{j[(\omega+2\Omega)t - 2Kz - \phi_0]} + e^{j[(\omega-2\Omega)t + 2Kz - \phi_0]} \right] \\ & \pm higher\ order\ terms \end{aligned} \tag{5.3}$$

When considering the thickness, this could be rewritten as [55, 56]:

$$\begin{aligned} E_t = {} & E_0 J_0(\phi_1) e^{j[\omega t - k(x-L) - \phi_0]} \\ & - E_0 J_1(\phi_1) e^{j[(\omega+\Omega)t - k_1^+(x-L) - Kz - \phi_0]} \\ & + E_0 J_1(\phi_1) e^{j[(\omega-\Omega)t - k_1^-(x-L) + Kz - \phi_0]} \\ & + E_0 J_2(\phi_1) e^{j[(\omega+2\Omega)t - k_2^+(x-L) - 2Kz - \phi_0]} \\ & + E_0 J_2(\phi_1) e^{j[(\omega-2\Omega)t - k_2^-(x-L) + 2Kz - \phi_0]} \pm higher\ order\ terms, \end{aligned} \tag{5.4}$$

where k_1^+ and k_1^- are wave-vectors for positive and negative first orders respectively. Similarly, k_2^+ and k_2^- are wave-vectors for positive and negative second orders respectively. The term J_n is the Bessel function of the first kind (where n is the various diffraction orders).

The respective intensities of the positive order and the negative order are I_n and I_{-n}. It can be stated that $I_n = I_{-n}$ can the be related to the $J_n^2(\phi_n) = J_{-n}^2(\phi_{-n})$. The relative intensity of as a result of the Raman-Nath diffraction is shown in Figure 5.3.

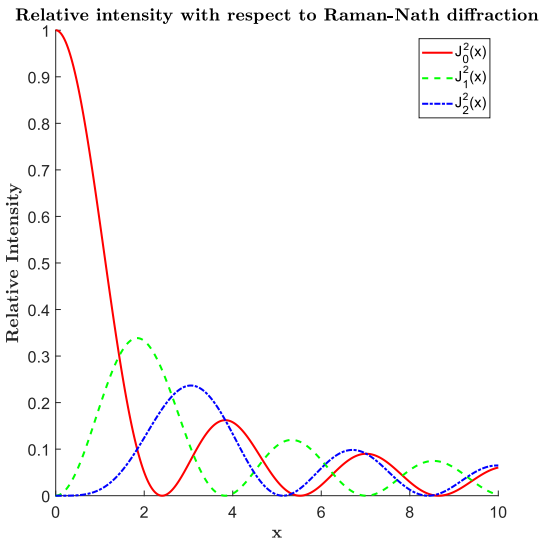


Figure 5.3: Relative intensity of different diffraction orders with respect to the Raman-Nath regime. Inspired from[55].

5.1.2 Brownian motion and ultrasound-induced movement of point-like scatterers in the acousto-optic signal

One of the earlier consideration of the theory of acousto-optic interaction was presented by Leutz and Maret [50], who modelled the acousto-optic interaction in a multiple scattering medium composed of scatterers that undergo Brownian motion as well as ultrasound-induced motion. If it is assumed that the scattering mean free path, $l > \lambda_0$, where λ_0 is the wavelength of the light and for a path length $s > l$, then the autocorrelation function $G_1(t)$ of the scattered electric field component is given as:

$$G_1(t) = \int_l^\infty P(s) \left\langle E_s(0) E_s^*(t) \right\rangle_B \left\langle E_s(0) E_s^*(t) \right\rangle_U ds, \qquad (5.5)$$

where the electric fields are averaged over time t and $P(s)$ and E_s are the probability density function of s and the electric field of the scattered light in path-length s respectively. The subscripts B and U denote Brownian and ultrasound contribution respectively to the autocorrelation function.

Now considering Brownian motion with the single particle relaxation time [57, 58], $\tau_0 = 1/D\mathbf{k}_0^2$, where D is the particle diffusion constant and $\mathbf{k}_0$ is the light wave vector, we can write the Brownian motion component and the ultrasound components respectively as [50]:

$$\langle E_s(0)E_s^*(t)\rangle_B = \exp\left(\frac{-2ts}{\tau_0 l}\right) \tag{5.6}$$

and

$$\langle E_s(0)E_s^*(t)\rangle_U = \left\langle \exp[-i\Sigma_{j=1}^{N}\Delta\phi_j(t)]\right\rangle, \tag{5.7}$$

where the number of scatterers $N = s/l$ and the temporal phase shift $\Delta\phi_j(t)$ is characterized by the optical wave vector $\mathbf{k}_j$ at the j^{th} scattering event. The ultrasonic wave has an amplitude A, frequency ω_a and the acoustic wave vector $\mathbf{k}_a$. The temporal phase shift is as a result of the change in distances between consecutive scatterings at points, $\mathbf{r}_j$ and $\mathbf{r}_{(j+1)}$. These two points define the ultrasonic induced distance as:

$$\Delta\mathbf{r}_{j+1,j}(t) = (\mathbf{r}_j + A\sin[\mathbf{k}_a.\mathbf{r}_j - \omega_a t]) - (\mathbf{r}_{j+1} + A\sin[\mathbf{k}_a.\mathbf{r}_{j+1} - \omega_a t]) \tag{5.8}$$

The temporal phase shift could now be written as [50]:

$$\Sigma_{j=1}^{N}\Delta\phi_j(t) = \Sigma_{j=1}^{N}\mathbf{k}_j[\Delta\mathbf{r}_{j+1,j(t)} - \Delta\mathbf{r}_{j+1,j(0)}] \tag{5.9}$$

The variable $\Delta\phi_j(t)$ has a Gaussian distribution with a variance $\left\langle \Delta\phi_j^2(t)\right\rangle$ and for ultrasound-induced displacement smaller than the wavelength of light, we can arrive at this approximation for the ultrasound component of the electric field as [50]:

$$\langle E_s(0)E_s^*(t)\rangle_U \simeq \exp\left(\frac{-s\left\langle \Delta\phi_j^2(t)\right\rangle}{2l}\right) \tag{5.10}$$

The term $\left\langle \Delta\phi_j^2(t)\right\rangle$ is averaged over θ_j and $\mathbf{k}_a.\mathbf{r}_j$ where θ_j is the angle between the acoustic and optical wave vectors and for point-like scatterers, θ_j and r_j are independent. Therefore [50];

$$\left\langle \Delta\phi_j^2(t)\right\rangle = (4k_0A)^2\sin^2\frac{(\omega_a t)}{2} \times \left\langle \sin^2\left[\mathbf{k}_a.r_j - \frac{(\omega_a t)}{2}\right]\right\rangle_{r_j} \times \left\langle \sin^2\left(\frac{k_a l}{2}\cos\theta_j\right)\cos^2\theta_j\right\rangle_{\theta_j}, \tag{5.11}$$

which could be written as:

$$\left\langle \Delta\phi_j^2(t) \right\rangle = (4k_0A)^2[1-\cos(\omega_a t)]\alpha \tag{5.12}$$

where k_a is the amplitude of the acoustic wave vector $\mathbf{k}_a$ and k_0 is the amplitude of the optical wave vector in vacuum. The parameter α is defined as:

$$\alpha = \frac{1}{6} - \frac{\cos[k_a l]}{(k_a l)^2} + \frac{\sin[k_a l]}{(k_a l)^3} - \frac{\sin[k_a l]}{(2k_a l)} \tag{5.13}$$

Therefore, Eqn. 5.10 could be written as:

$$\langle E_s(0)E_s^*(t)\rangle_U \simeq \exp\left(\frac{-2s(k_0A)^2}{l}[1-\cos(\omega_a t)\alpha]\right) \tag{5.14}$$

Hence, the total autocorrelation function from both the Brownian and ultrasonic induced motion could be written as:

$$G_1(t) = \int_l^\infty P(s)\exp\left[\left(\frac{-2s}{l}\right)\left(\frac{t}{\tau_0} + (k_0A)^2[1-\cos(\omega_a t)]\alpha\right)\right] ds. \tag{5.15}$$

By using the Wiener–Khinchin Theorem, the intensity spectrum can be calculated for light with frequency $n\omega_a$ as:

$$I_n(n\omega_a) = \frac{1}{T}\int_0^T \cos(n\omega_a t)G_1(t)dt, \tag{5.16}$$

where $T = \frac{2}{\omega_a}$ is the ultrasound period.

By assuming an infinite slab with thickness, L, being illuminated by a uniform light source from one side, the transmitted field correlation function is given by [59]:

$$G_1(t) = \frac{\sqrt{6\left(\frac{L}{l}\right)^2\left(\frac{t}{\tau_0} + (k_0A)^2\left[1-\cos(\omega_a t)\right]\alpha\right)}}{\sinh\sqrt{6\left(\frac{L}{l}\right)^2\left(\frac{t}{\tau_0} + (k_0A)^2\left[1-\cos(\omega_a t)\right]\alpha\right)}} \tag{5.17}$$

For an intensity without ultrasound applied, $I_n(n\omega_a) = I_0$ and experimental measurements could be characterised by

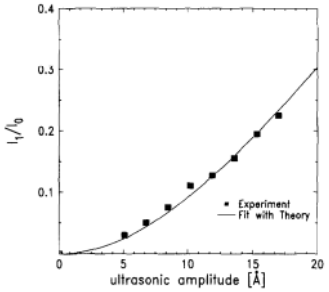


Figure 5.4: Modulation depth variation with respect to changes ultrasound amplitude [50].

the modulation depth, M as:

$$M = \frac{I_n(n\omega_a)}{I_0} \tag{5.18}$$

The plots in Figure 5.4, shows the ultrasound amplitude effect on modulation depth.

5.1.3 Contributions of the refractive index change and displacement of scatterers to the acousto-optic signal

In this scenario presented by Wang [51], the optical phase change is decomposed into that which is due to refractive index and displacement of scatterers within a homogeneous medium. Where t and τ are two different time instances, these two mechanism could be incorporated in the electrical field as:

$$\langle E_s(t)E_s^*(t+\tau)\rangle = \left\langle \exp\left(-i\left[\sum_{j=1}^{s/l+1}\Delta\phi_{nj}(t,\tau) + \sum_{j=1}^{s/l}\Delta\phi_{dj}(t,\tau)\right]\right)\right\rangle, \tag{5.19}$$

which for phase variations less than unity, could be simplified as [51, 52];

$$\langle E_s(t)E_s^*(t+\tau)\rangle = \exp\left(\frac{-1}{2}\left\langle\left[\sum_{j=1}^{s/l+1}\Delta\phi_{nj}(t,\tau) + \sum_{j=1}^{s/l}\Delta\phi_{dj}(t,\tau)\right]^2\right\rangle\right), \tag{5.20}$$

where the variance of phase variation as a result of displacement of scatterers in the j^{th} free path is
$\Delta\phi_{dj} = \phi_{dj}(t+\tau) - \phi_{dj}(t)$ and similarly, that due to refractive index contribution is $\Delta\phi_{nj} = \phi_{nj}(t+\tau) - \phi_{nj}(t)$.

The phase due to refractive index at time, t is defined as:

$$\phi_{nj}(t) = \int_0^{l_j} k_0\Delta n(\mathbf{r}_{j-1}, s_j, \theta_j, t)\, ds_j, \tag{5.21}$$

where l_j is the length of the j^{th} free path and s_j is the direction along the path.

Also, the refractive index modulation is given as:

$$\Delta n(\mathbf{r}_{j-1}, s_j, \theta, t) = n_0 \eta k_a A \sin\left(\mathbf{k}_a \cdot \mathbf{r}_{j-1} + k_a s_j \times \cos\theta_j - \omega_a t\right), \tag{5.22}$$

By substituting Eqn. 5.22 into Eqn. 5.21, we get the phase modulation as a result of refractive index variations as:

$$\begin{aligned}\phi_{nj}(t) = 2n_0 k_0 \eta A \sin\big(&\mathbf{k}_a \cdot \mathbf{r}_{j-1} \\ &+ k_a l_j \cos\theta_j/2 - \omega_a t\big) \times \frac{\sin(k_a l_j \cos\theta_j/2)}{\cos\theta_j}\end{aligned} \tag{5.23}$$

where the background refractive index is n_0 and η quantifies the piezo-optic coefficient of the material. It defines the fractional change in refractive index of the material upon ultrasound pressure. Mathematically,

$$\eta = \frac{\partial n}{\partial p}\rho v_a^2, \tag{5.24}$$

here ρ and v_a are the density of the material and the acoustic velocity respectively.

The phase modulation due to the displacement of scatterers is given as:

$$\phi_{dj}(t) = -n_0 k_0(\hat{\mathbf{k}}_{j+1} - \hat{\mathbf{k}}_j) \cdot \mathbf{A} \sin(\mathbf{k}_a \cdot \mathbf{r}_j - \omega_a t), \tag{5.25}$$

here, **A** is the acoustic amplitude vector.

With these definitions, we can write the separate components as [51, 52]):

$$\left\langle \left[\sum_{j=1}^{s/l+1} \Delta\phi_{nj}(t,\tau) \right]^2 \right\rangle = \left(\frac{s}{l} + 1\right) (2n_0 k_0 A)^2 \delta_n \left(1 - \cos(\omega_a \tau)\right), \tag{5.26}$$

and

$$\left\langle \left[\sum_{j=1}^{s/l} \Delta\phi_{dj}(t,\tau) \right]^2 \right\rangle = \left(\frac{s}{l}\right) (2n_0 k_0 A)^2 \delta_d \left(1 - \cos(\omega_a \tau)\right). \tag{5.27}$$

Writing the autocorrelation function as:

$$G_1(\tau) = \int_0^\infty p(s)\langle E_s(t)E_s^*(t+\tau)\rangle \, ds, \tag{5.28}$$

we can then substitute the individual components to get:

$$G_1(\tau) = \int_0^\infty p(s) \exp\left(-\frac{2s}{l}(\delta_n + \delta_d)(n_0 k_0 A)^2 \left[1 - \cos(\omega_a \tau)\right]\right) ds \tag{5.29}$$

which could be solved as:

$$G_1(\tau) = \frac{\frac{L}{l}\sinh\left(\sqrt{\varepsilon\,(1-\cos(\omega_a\tau))}\right)}{\sinh\left(\frac{L}{l}\sqrt{\varepsilon\,(1-\cos(\omega_a\tau))}\right)}, \tag{5.30}$$

where

$$\varepsilon = 6(\delta_n + \delta_d)(n_0 k_0 A)^2. \tag{5.31}$$

There variables of the equation are defined as follows:

- δ_n: The contribution from the ultrasound-induced modulation of the index of refraction.
- δ_d: The contribution from the ultrasound-induced displacement of scatterers.
- n_0: The background (unperturbed) refractive index of the medium.
- k_0: The optical wave number in vacuum, defined by

  $$k_0 = \frac{2\pi}{\lambda},$$

  where λ is the optical wavelength. In the medium, the effective wave number is $n_0 k_0$.
- A: The amplitude of the ultrasonic displacement, which quantifies how far the scatterers (or the medium) are moved by the acoustic wave.

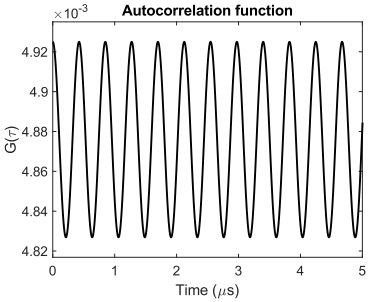


Figure 5.5: A time domain representation of the autocorrelation function [60].

For Rayleigh scatterers, the individual scatterers contribute individually to the field whereas the refractive index contribution is a cumulative of the individual paths. The time domain representation of the autocorrelation function is shown in Figure 5.5. The intensity could then be defined using Eqn. 5.16.

5.2 Optical techniques in AOT

The development of AOT has seen various instrumental configurations, primarily based on optical detection methods and ultrasound illumination techniques. Apart from the coherent laser source requirement in AOT, some groups have attempted incoherent illuminations[61] and acquisition of incoherent signals from chemiluminescent samples in phantoms[62, 63]. Using the acousto-optic effect, cerebral blood flow (CBF) studies have been conducted with ultrasound tagged near infrared spectroscopy (UT-NIRS). This has presented an avenue for non-invasive monitoring of changes in cerebral blood flow index (CFI) in the diagnosis of ischaemia or haemorrhage as a result of potential changes in brain perfusion[64]. Acousto-optic interaction has also been used to non-invasively measure blood glucose levels via characterisation of scattering coefficient of samples[65]. These are attempts to utilising the acousto-optic effect for clinical benefit but the actual benefit of acousto- optical imaging for in-vivo medical uses has to overcome some underlying challenges.

5.2.1 Challenges in AOT signal detection

Despite its potential, AOT faces several significant challenges that hinder its widespread application in clinical settings. One of the primary challenges is signal-to-noise ratio (SNR). In AOT, the light that is modulated by the ultrasound (which contains the useful imaging information) represents only a small fraction of the overall light transmitted through the tissue. As a result, separating this modulated light from the unmodulated background noise is difficult, especially in highly scattering media like biological tissues. Improving the sensitivity and detection techniques for these weak signals remains a key area of ongoing research.

Another major issue is resolution and imaging depth. While AOT benefits from the ability of ultrasound to penetrate deep into tissues, the optical component remains constrained by the high scattering nature of biological tissues. This scattering limits the depth at which optical signals can be detected and reduces resolution. Although advances like wavefront shaping and adaptive optics have improved light penetration,

overcoming this fundamental scattering limitation is still a significant challenge.

Speckle decorrelation, which refers to the loss in the coherent pattern of speckles over time is another factor that affects performance of AOT in real-time or in vivo imaging. Biological tissues, particularly in living organisms, undergo constant movement (due to factors like blood flow, respiration, or other physiological processes). These movements cause rapid decorrelation of both light and ultrasound signals, reducing the coherence necessary for accurate imaging [66]. The decorrelation time that makes acousto-optic imaging feasible lies within the range of 0.1 ms to 1 ms [67, 68].

Attempts to solve some of the challenges associated with AOT detection systems, has involved the use of long-cavity confocal Fabry-Perot interferometry (CFPI) shown in Figure 5.6 [67]. This method is immune to speckle decorrelation because the characteristics of the signal emerging out of the surface of the sample is preserved within the cavity [69]. Since the decorrelation of tissue is around 1 ms, it means such detection methods should be within or less than this time range. The CFPI scheme is limited in etendue (which is the product of the area and the solid angle of detection systems) but this could be addressed by using high-peak-power single frequency laser pulses and high frequency US waves [70, 71]. However, for in-vivo applications, sample illumination and signal detection should comply with the medical safety limits and moreover, the use of high frequency US wave would only limit deep tissue imaging.

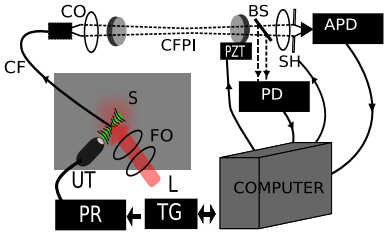


Figure 5.6: L=laser, TG= trigger generator, PR= pulser–receiver, UT= ultrasonic transducer, FO= focusing optics,
CF= collecting fibre, S= sample, CO= coupling optics, PZT=piezoelectric transducer, BS=beam splitter, SH= shutter, PD= photo-detector. Inspired from [67].

5.2.2 Detection solutions

Spectral hole burning

Quantum memory techniques utilizing rare earth crystals (RECs) have been an approach to detecting tagged photons. This is typically achieved through a process called spectral hole burning (SHB). Spectral hole burning makes use of optical pumping to "burn" holes or creates higher transmission in the in-homogeneously broadened absorption spectrum of a crystal, usually achieved at liquid helium temperatures. The technique of SHB does not rely on interferometry and

measures only the flux of ultrasound-tagged photons. The advantage of this method is that, it is not affected by speckle decorrelation since imaging is done in the time frame of light transport in the burnt hole of the absorption spectrum. Li et. al used spectral-hole burning as a front-end absorptive filter to extract one modulation sideband of ultrasound-modulated diffuse photons while blocking the DC and other sidebands [72]. The duration of spectral hole burning can vary depending on the material and conditions involved, but it is generally short-lived. It can last from milliseconds to a few seconds after the excitation source is removed. This type of spectral hole burning is temporary because the absorption profile typically relaxes back to its original state after the material returns to thermal equilibrium.

A variant of the hole burning technique is the persistent spectral hole burning (PSHB) which involves creating long-lived or persistent spectral holes in the absorption spectrum of a material. In PSHB, the spectral holes generated by optical or photochemical means can persist for extended periods of time, allowing for the storage and manipulation of optical information over longer time scales [73]. This has been applied to AOT and for example, the first AOT imaging using a filter based on PSHB in Tm:YAG was achieved by applying a magnetic field on the crystal maintained at 2 K [74]. The use of a magnetic field in PSHB is essential for creating, stabilizing, and preserving the spectral holes by influencing the spin states of the absorbing atoms or ions. The first in vivo AOT measurements is demonstrated by Nilsson et. al [73]. Thai et al. [75], have explored in vivo imaging using $Tm^{3+} : YAG$ crystal. In the study, indocyanine green (ICG) solution was injected intramuscularly and intravenously as an optical absorber in mice and its effects were observed in the muscle and liver in PSHB-based AOT images.

Typically, to create a spectral hole in this absorption band, a pump light of a narrow band with high intensity irradiates the crystal and the molecules that are in resonance with light of resonance wavelength (λ_L) become excited to higher energy states thereby creating a hole in the absorption profile of the crystal [76–78]. The frequency or wavelength of this narrow pump can be carefully selected to match that of the ultrasound tagged photons such that the crystal becomes transparent to this specific tagged light frequency or wavelength and absorbs untagged and background light. When the laser

line-width, typically in the sub-megahertz range, is reached, the crystal turns transparent at λ_L (laser wavelength), while wavelengths outside of this line-width are absorbed. As a result, a transmission bandpass filter with a very narrow band and high contrast is produced. Therefore, the high intensity background unmodulated signal could be suppressed while the small side band of the ultrasound-modulated signal could be filtered as shown in Figure 5.7 [72, 79]. Li et al. developed a non-linear optical filter utilizing SHB effects to detect ultrasound tagged light. Their system was capable of wider etendue and larger processing of speckles in parallel. Their clinically suitable solution was eventually used to image 10 mm thick tissue-mimicking phantoms [72].

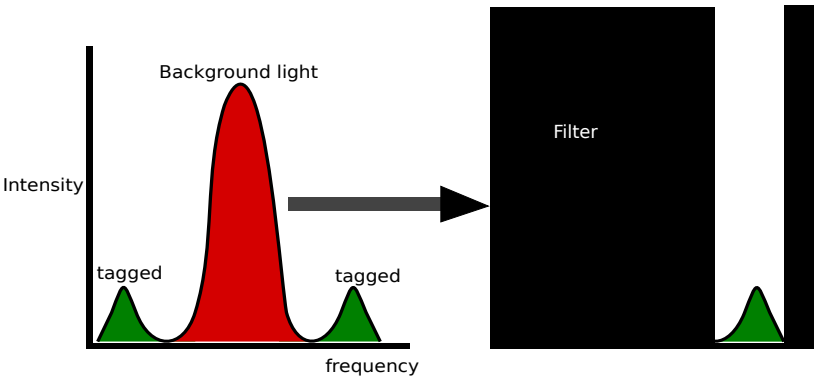


Figure 5.7: Spectral hole burning for filtering out tagged photon frequency. The wavelength shift between the background light and tagged light is 10^{-5} nm.

Another advantage of SHB is the slow light phenomenon that could also be achieved with these crystals. Slow light in spectral hole burning is achieved through the interaction of light with sharp spectral features burned into the material's absorption spectrum. In AOT, ultrasound-tagged light experiences modulation as it interacts with the medium, and when combined with SHB, this effect is amplified by the steep dispersion profile created near the spectral hole. This steep dispersion slows the group velocity of the light. The group velocity v_g of light, which determines how fast a light pulse propagates through the medium, can be expressed as:

$$v_g = \frac{c}{n + \omega \frac{dn}{d\omega}} \tag{5.32}$$

Where c is the speed of light in a vacuum ($3{\times}10^8$ m/s), n is the refractive index of the medium, ω is the angular frequency of light, and $\frac{dn}{d\omega}$ represents the change in the refractive index with respect to frequency.

In the presence of a spectral hole, the term $\frac{dn}{d\omega}$ becomes large due to the steep dispersion. This results in a significant reduction in the group velocity v_g, which causes the light to "slow down" as it passes through the medium. This phenomenon allows the ultrasound-tagged light to interact with the medium for a longer time, improving both the imaging resolution and sensitivity[74]. The factor $\frac{dn}{d\omega}$ is 10^4 within the transparent region and zero everywhere else within the crystal [80]. As a result, the group velocity of the ultrasound-tagged light lags behind the unmodulated background light in time. This time-gated approach is used to further suppress the unwanted signal.

The coherence of the energy levels in SHB materials such as rare-earth-doped crystals, like Tm:YAG or Pr:YSO, ensures that the spectral holes remain stable, thus preserving the slow light effect over longer periods. In AOT, this is an important effect needed for detecting weak ultrasound-tagged signals, as it allows the light to probe deeper tissue structures with greater efficiency. The reduced absorption near the spectral hole also ensures that more light is transmitted through the medium, which improves the signal-to-noise ratio (SNR) and enhances the overall imaging performance.

Phase conjugation

Another technique employed in AOT is the phase conjugation through the reversibility property of light propagation. This is used to increase the focusing efficiency of light in highly scattering materials. It literally employs a gain medium, photorefractive material or a spatial light modulator (SLM) to record the forward propagating phase of speckles and phase reverses it for backward propagation into the sample under study. In the pioneering work of Xu et al.[81], as illustrated in Figure 5.8, they explored time-reversed ultrasonically encoded (TRUE) optical focusing. This is a phase conjugation solution to the depth limitation of light in dense phantom environment where the ultrasound focus served as a guide star deep within the medium. This follows an interferometric setup where the light source is split into three different parts; sample beam and two reference beams where one of the reference beams is a conjugate that illuminates a holographic recording crystal after the interaction between the sample and the actual reference beam has been recorded in

the crystal. The intended signal could then be recorded by a photodetector. Using phase conjugation techniques, light focusing up to 16 mm round-trip in tissue-mimicking phantoms with optical extinction coefficient of $10\,\mathrm{mm}^{-1}$ has been possible [82]. Although photorefractive polymers allowed for a wider detection etendue, this couldn't be translated to clinical application due to their slow response time 5 s [83]. Also, $Nd:YVO_4$ (Neodymium-doped Yttrium Orthovanadate) has been used a gain medium to enhance acousto-optic signal detection by amplifying light and reducing sensitivity to speckle decorrelation [84]. Following the work of Xu et. al [81], Zhang et al. [85] in 2022, highlighted that traditional TRUE could be limited by the ultrasonic focusing area and pressure tagging efficiency, particularly in acoustically diverse media. They further indicated that iterative TRUE (iTRUE), could present high time requirement, limiting its use for in vivo applications. To address this issue, they proposed a technique known as time-reversed photoacoustic wave guided time-reversed ultrasonically encoded (TRPA-TRUE) optical focusing, which integrates accurate ultrasonic focusing through an acoustically heterogeneous medium guided by time-reversing photoacoustic (PA) signals and the ultrasound modulation of diffused coherent light with optical phase conjugation (OPC). Further activity within this regard has been the introduction of the acousto-optic transmission matrix technique (AOTM) [86]. This combines the principles of acousto-optics with the transmission matrix approach to enhance the ability to manipulate and focus light through strongly scattering materials.

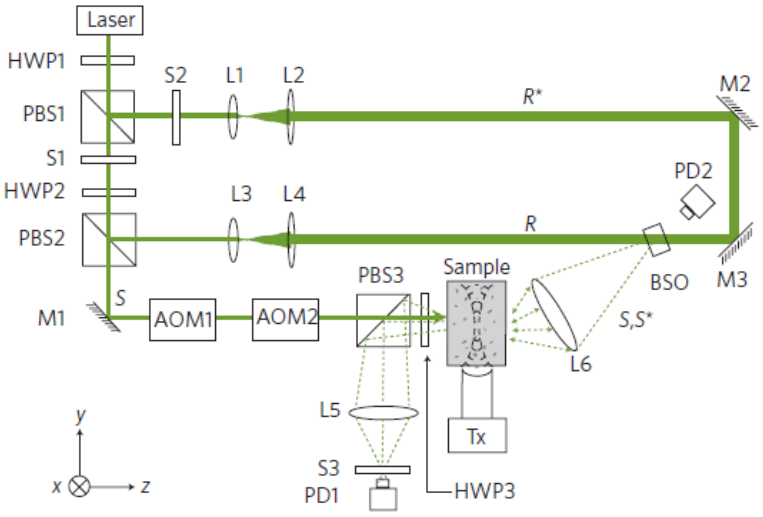


Figure 5.8: A hologram was recorded and read out during the time-reversal procedure. To record a hologram, shutter S1 was opened for 190 ms while shutters S2 and S3 were closed; to read the hologram, S1 was closed while shutters S2 and S3 were opened for 10 ms. HWPi= the ith half-wave plate; PBSi= the ith polarizing beam splitter; Si=ith shutter; Mi = ith mirror; AOMi = ith acousto-optic modulator; Li =ith lens; PDi = ith photodiode. R = reference beam; R* = conjugated reference beam; S = signal light; S* = time-reversed signal light. BSO, Bi_12SiO_20; Tx, ultrasonic transducer with f_a = 3.5 MHz centre frequency, focal length=38 mm, and focal width= 0.87 mm. Coordinates are as follows: x=sample scanning axis, y=acoustical axis, and z=optical axis. Copied from [81].

Photorefractive crystal based interferometry

In the quest to detect ultrasound-tagged light for systems capable of yielding higher detection etendue, other approaches have been employed using photorefractive crystals (PRCs) to record the phase and amplitude of the modulated signal emitted by the sample [87–89]. Some examples of these crystals are lithium niobate ($LiNbO_3$); barium titanate ($BaTiO_3$); potassium tantalate niobate (KTN); barium sodium niobate (SBN); bismuth silicon oxide (BSO); bismuth germanium oxide (BGO); tin hypothiodiphosphate (SPS); and gallium arsenide (GaAs).

Photorefractive effect occurs in materials with both electro-optic effect and photoconductivity, allowing non-uniform illumination of the material to be transformed into a spatial variation in the refractive index [90]. The principle of PRC based detection is such that reference and signal beams are made to interfere within the crystal. The experimental arrangement could be done so that either ultrasound tagged or untagged photons could be selected. Once, these two beams interfere in the crystal, a volume hologram is created in time. The process follows that, the areas of high intensity causes charge carries to be excited from the impurity sites

within the photorefractive material. The excited free electrons migrate through the crystal towards regions of low intensity due to internal electric field or gradient of the light intensity. This activity creates a non-uniform charge distribution, which results in spatially varying refractive index change. This then forms the volume hologram in the crystal. The reference beam maintains a consistent phase details and as result, it is reintroduced to the hologram in order to retrieve the signal required. A photodiode could then be used to extract the direct current (DC) component if the intensity emerging out of the crystal [91–93].

In the work done by Murray et. al [87] to scan for the optical contrast of buried inclusion within tissue phantom, they used the fundamental work of Huignard and Marrakchi [94] to assumed both signal and reference beams to be planar in order to derive the intensity that emerges out of the crystal as (where $\Re$ denotes real part):

$$I_{se} = e^{-\alpha L} I_{so} \left(|e^{\gamma L} - 1|^2 + 1 + 2\Re \left[(e^{\gamma L} - 1)^* e^{i\phi_a \sin(\omega_a t + \chi_r)} \right] \right). \tag{5.33}$$

In this equation, α represents the crystal absorption coefficient, while L denotes the length of the crystal. The gain coefficient γ is expressed as $\gamma = \gamma' + i\gamma''$, where γ' and γ'' are the real and imaginary parts of the gain, respectively. The term I_{so} indicates the intensity of the signal beam at the front surface of the crystal. The variables ω_a and ϕ_a correspond to the angular frequency and amplitude of the ultrasound-induced phase modulation, respectively, while χ_r is a constant influenced by the optical path. By rewriting Eq. (5.33) to include both DC and AC components, and focusing on the lowest-order terms from the Bessel function expansion, we derive the following result respectively for the DC and AC components [87]:

$$I_{se}^{DC} = e^{-\alpha L} I_{so} \left(\left| e^{\gamma L} - 1 \right|^2 + 1 + 2 \left[e^{\gamma' L} \cos(\gamma'' L) - 1 \right] J_0(\phi_a) \right), \tag{5.34}$$

$$I_{se}^{AC} = 4 e^{-\alpha L} I_{so} e^{\gamma' L} \sin(\gamma'' L) J_1(\phi_a) \sin(\omega_a t + \chi_r). \tag{5.35}$$

For reasons of acquiring signals not affected by incoherence, the DC component of the signal is typically detected

for acousto-optical imaging and sensing. Other ways of enhancing signal strength is to apply a high voltage ac bias to the photorefractive crystal. In [87], the reference beam is wavefront-matched hence, the phase modulation of the speckles interfering with the reference beam was converted into intensity of the signal. In AOT, the signal requires that the ultrasound effect is short with respect to the response time of the crystal. The response time is inversely related to the illumination intensity [95, 96].

In the instrumentation illustrated in Figure 5.9, the reference beam could be frequency-shifted to match the frequency of the speckle emanating from the sample as a result of ultrasonic and optical interaction. The laser source used had a wavelength of 1064 nm with a peak power of 100 mW and the photorefractive crystal used was Gallium Arsenide (GaAs). The experiment measured the SNR of different thicknesses (2 cm and 4 cm) of chicken breast. In the experiment, the interference flux in the crystal was 25 mW for a response time of 15 ms. The signal of interest is $\mathbf{E_A}\mathbf{E_R^*}$. With the re-illumination of the reference beam, $\mathbf{E_D}$ is created where $\mathbf{E_D} \cong \eta\langle\mathbf{E_A}\rangle_\tau$. Here, η is the efficiency factor that depends on the electro-optic constant of the photorefractive crystal and $\langle\rangle_\tau$ indicates time averaging [88].

In order to achieve imaging parameters within the decorrelation times of biological samples, the PRC could be chemically tuned so that their response times are just small enough not to be affected by speckle decorrelation in the image processing. However, finding the correct material with a fast response time and working in the correct wavelength range is complicated. AOT based experiments involving tellurium-doped tin thiohypodiphosphate crystal ($Sn_2P_2S_6 : Te$) have been conducted [97]. The response time of the crystal was 100 ms at 790 nm with a gain of 9 cm^{-1} for an intensity of 0.9 W cm^{-2}. In addition to this, other PRC based works demonstrated by Suzuki et. al [98] and Lai et. al [99] have been improved with respect to detection etendue [60].

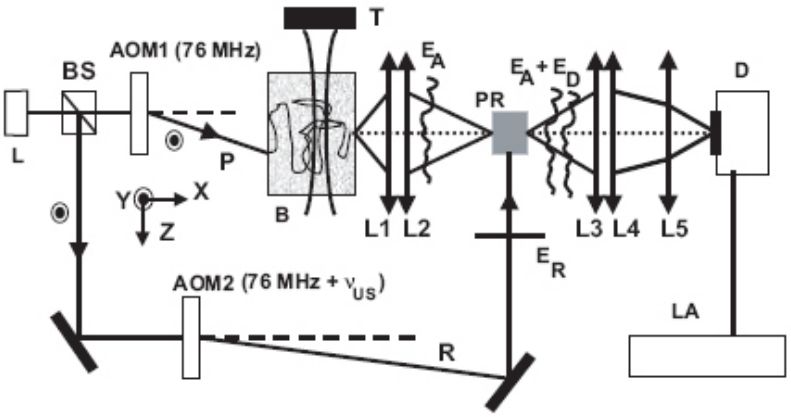


Figure 5.9: L:light source, BS:splits the laser beam into a probe(P) and a reference(R) beam, T: US piezo-transducer. AOM1,2: Acousto-optic modulators, E_A, E_D: fields associated to the speckle wavefronts. E_R: reference field. L1-L5 : wide aperture NA=1 aspherical lenses. B: chicken breast. PR: GaAs photorefractive crystal. LA: Lock-in amplifier. D: silicon photodetector ($S = 4.9\,\mathrm{mm}^2$). Copied from [88].

Speckle contrast

The use of single detection scheme in AOT was one of the first experiments demonstrated [50, 100]. When using single detection approach, the interest lies on a single speckle grain. Because a single speckle grain is as a result of coherent scattering, the effect of random phase variation could be controlled by averaging. However, the signal strength delivered by a single speckle grain is limited and the detection etendue is also small. In the context of AOT, a parameter in favour of detection etendue would be to have a charged-coupled device (CCD) camera whose pixels would independently detect the ultrasound tagged photons. And thus, in the experiment developed by Lévêque et al. [101] shown if Figure 5.10, a parallel speckle detection with a source-synchronised lock-in technique was used to acquire images in 1D. The SNR limitation was addressed by averaging the signals from all the CCD pixels.

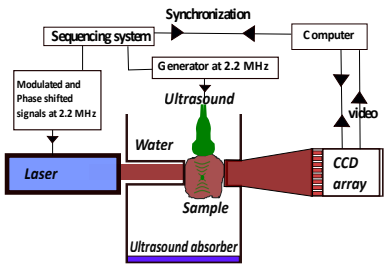


Figure 5.10: An ultrasound transducer modulates the speckles created by the laser beam within the sample. Instead of using a single optical detector, which combines the signals from many speckle grains, the CCD camera and parallel lock-in detection are used to record the full modulation of the speckle. Inspired from [101].

The study by Li et. al [102] makes use of this speckle recording technique to allow for the generation of two-dimensional ()2D images of biological samples as thick as 25 mm. They demonstrated that the use of low laser intensity (approximately 24 mW) in conjunction with ultrasonic waves enhances the contrast of the images, making it possible to detect optical inhomogeneities within the tissue. A significant finding of their work is the improvement in image contrast when using the speckle-contrast detection method compared to traditional parallel detection techniques. The contrasts for both unmodulated and modulated speckles are respectively C_b and C_m and respectively given as:

$$C_b = \frac{\left(\langle I_b^2 \rangle - \langle I_b \rangle^2\right)^{1/2}}{\langle I_b \rangle}, \tag{5.36}$$

and

$$C_m = \frac{\left(\langle I_m^2 \rangle - \langle I_m \rangle^2\right)^{1/2}}{\langle I_m \rangle}, \tag{5.37}$$

where I_b and I_m are the unmodulated light and modulated light intensities.

The acousto-optical signal collected by speckle contrast C is given by:

$$C = \frac{\sigma}{\langle \bar{I} \rangle} = \frac{C_b}{1 + M} \tag{5.38}$$

where σ is the variance of the intensity and $\langle I \rangle$ is the mean intensity. Here, M is the modulation depth defined as:

$$M = \frac{\langle I_m \rangle}{\langle I_b \rangle}. \tag{5.39}$$

Li et. al [102] highlight the simplicity of the setup and the efficiency of the speckle-contrast detection method, which requires fewer components than traditional methods. This makes the technique not only effective but also easier to implement in practical applications.

In concluding this section, the detection of acousto-optic signal has gone through several techniques. Bengtsson et al.[103], have done a comprehensive study on the performance, advantages and disadvantages of major detection schemes used in AOT. They show a theoretical comparison of spectral hole burning, single-shot off-axis holography, speckle contrast, and photorefractive detection methods. Their results show that the penetration depth of the speckle contrast method is shallower but in the case of spectral hole burning filters, deep imaging could be feasible. The results further shows that digital off-axis holography and photorefractive detection could posses good contrast-to-noise ratio at significant depths as depicted in Figure 5.11. In a recent work by Liu et al. [104], acousto-optical studies was performed on human skull using single-shot off-axis holography. Ultrasound tagged photon detection mechanisms employed in AOT have undergone

changes since heterodyne detection was demonstrated (much would be said about this in Chapter 7) [105].

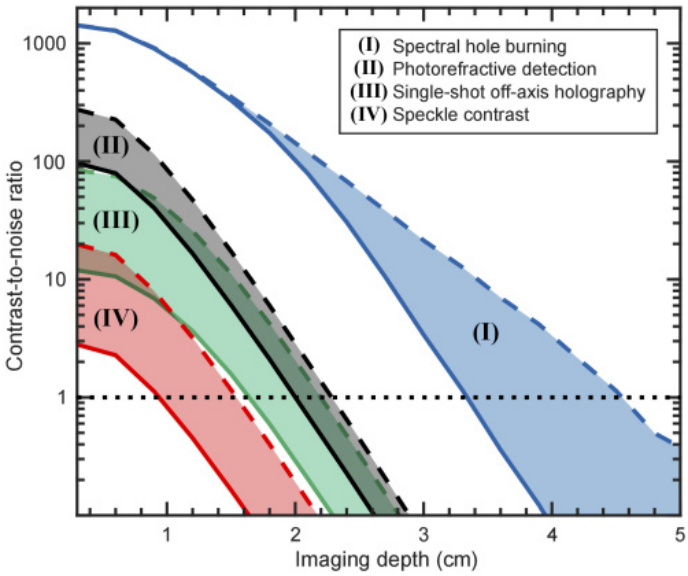


Figure 5.11: Contrast-to-noise ratio as a function of imaging depth (in cm) for four different imaging techniques. (I) Spectral hole burning, (II) Photorefractive detection, (III) Single-shot off-axis holography, and (IV) Speckle contrast are represented with distinct shaded regions. The dashed lines show the trend for each technique, with the contrast-to-noise ratio decreasing as imaging depth increases. The dotted horizontal line represents the threshold value of 1, indicating the minimum contrast-to-noise ratio required for effective imaging.. Copied from [103].

5.2.3 Imaging and resolution solutions

Early imaging attempts with acousto-optics was done by Marks et al. [100] who investigated the potential tagging of photons with an ultrasound frequency in order to study photon localisation within homogeneous turbid media using pulsed ultrasound waves. The configuration of the detection system was in the transmission mode with a PIN photodiode and a bandpass filter. In an effort to optimize the signal to noise ratio (SNR) at the time, continuous-wave US modulation of light was later used to acquire two dimensional (2D) images of objects buried within turbid media [106]. Experiments done by Wang and Ku demonstrated the possibility of using frequency-swept ultrasound-modulated tomography to acquire one dimensional (1D) images in the ballistic regime. Their mechanism was based on a single source photomultiplier tube (PMT) adapted for heterodyne detection[107]. Lesaffre et al. then introduced a technique referred to as Acousto-Optical Coherence Tomography (AOCT), which helped to obtain a millimetre resolution with continuous ultrasound and light beams by applying random phase jumps to ultrasound and light [108]. A self-adaptive holographic setup containing a photorefractive GaAs bulk crystal was used in the detection scheme.

In 2000, Yao et al. [109] combined frequency-swept ultrasound-modulation and the parallel detection scheme to obtain 2D images of objects buried within a biological tissue and to study the scalability of the spatial resolution along the ultrasonic axis. The study by Yao and Wang [110] utilised a low-power laser in a parallel detection scheme and a synchronous-illumination lock-in technique to acquire 2D images of 1.5 cm thick chicken breast with a white rubber inclusion. With regards to 2D imaging, the dependence of laser speckle contrast on ultrasound modulation has been studied by Li et al. [111]. Using the contrast of the emerging speckles, they were able to get a 2D image of a 25 mm thick sample with low power laser (about 24 m W). The variation of the speckle contrast is a measure of tissue inhomogeneity. The parallel speckle detection [102] mainly requires four different images to construct an overall tomographic image. The time required to get these individual images is relatively beyond the in vivo decorrelation time of less than 1 ms and as a result could make the parallel scheme susceptible to speckle decorrelation. Due to this, the speckle contrast method relatively

out-performs the parallel detection method.

Li and Wang [102] have previously outlined methods for signal acquisition and analysis and in a recent work by Hua et. al [112], a reflection mode laser feedback AOT system has been developed for angiography inside a highly scattering medium. To enhance imaging contrast, micro-bubbles were used. Imaging contrast was improved from 0.78 to 3.73 at resolution of 0.75 mm and a penetration depth of 5.5 cm in a tissue-mimicking medium. In addition to this development, Yuan et al. [113] have made a single-shot on-axis UOT with better speckle contrast. They report a speckle correlation time as low as 0.48 ms which could be clinically relevant.

With regards to signal improvement, Doktofsky et al. [114] used super-resolution optical fluctuations imaging (SOFI), initially used for microscopic imaging of blinking fluorophores to conduct AOT. This is not limited by the acoustic resolution constraint of transducers in conventional AOT. They demonstrated that super-resolved acousto-optical images could be acquired by statistical analysis of the temporal fluctuations of ultrasound tagged light. In their experiment, only one image was taken within the speckle decorrelation time frame and indicated that methods such as wavefront shaping to tighten the light intensity within an acoustic focus may not be necessary especially when considering cost and time effective advantages.

Similarly, optical diffraction-limited imaging has been conducted using AOT experiments [115]. This was done by extracting diffraction-limited image information from 'memory-effect'speckle-correlations in ultrasound tagged light fields. The aim of the work was to overcome the resolution limits of traditional acousto-optic imaging (AOI) and enable high-resolution, non-invasive optical imaging through scattering media. This was achieved by combining acousto-optic imaging with ptychography, a computational imaging technique. The goal was to extract diffraction-limited imaging information from speckle correlations within ultrasound-modulated scattered light fields. The approach provided imaging beyond the limits imposed by the ultrasound focus size, providing a resolution up to 40 times better than conventional AOI. This work has implications for applications such as deep-tissue optical microscopy [115]. To add to this attempt, Ruan et al.[116] imaged fluorescent targets with an improved resolution of ≤ 75 µm as compared to a resolution

of 1.3 mm with direct optical imaging within a scattering medium with decorrelation time of 17 ms. This makes it possible to image fluorescence contrast in highly scattering media at acoustic resolutions.

Barjean et al. were able to resolve images along the ultrasound axis at a SNR of 22 in a Fourier transform acousto-optic imaging (FT-AOI) that used a smart array for signal detection. This smart array was a complementary metal–oxide–semiconductor (CMOS). The integration time of the detection system was 70 µs and with an etendue suitable for in vivo applications [117, 118].

5.3 How multiple acoustic foci have been used in AOT

This section mentions some of the ways ultrasound frequencies have been applied in AOT. It also highlights how more than one ultrasound focus has also been used in AOT signal acquisition.

The study by [119] highlights the role of focused ultrasound in modulating and localizing scattering light, which directly affects the modulation efficiency and spatial resolution of AOT signals. The modulation depth, which refers to the variation of the scattered light intensity due to ultrasound, is a critical metric in determining the imaging sensitivity. Through experiments, the study assess the performance of ultrasound at various centre frequencies (1 MHz, 2.25 MHz, 5 MHz, and 10 MHz) and pulse energies.

The experimental setup involves shining a He-Ne laser through a scattering medium, such as intralipid solutions, while different ultrasound frequencies are applied. The scattered light is collected and analysed to determine how ultrasound parameters affect the modulation depth and signal-to-noise ratio (SNR). The results show that lower ultrasound frequencies produce a higher modulation efficiency and better SNR compared to higher frequencies. This finding is attributed to the fact that lower frequencies induce larger acoustic pressure variations, which more effectively modulate the scattering light.

The study also reveals that increasing the pulse energy of the ultrasound leads to a linear increase in modulation efficiency, further improving the sensitivity of AOT. However, variations in the repetition frequency of ultrasound pulses have little effect on the modulated scattering light, indicating that the modulation depth is primarily influenced by the frequency and energy of the ultrasound rather than its pulse repetition rate[60, 119].

Furthermore, apart from the knowledge of the frequency relationship with AOT signal Yang et al. [120] used two ultrasound transducers to create a beating effect in their time-reversed ultrasonically encoded optical setup. They introduce a technique that utilizes two intersecting ultrasonic beams emitted from separate transducers operating at slightly different frequencies. This method encodes diffuse light at the beat frequency within the intersection volume, allowing for improved spatial resolution when the light is time-reversed. By employing this dual ultrasonic modulation, the authors achieved an acoustic axial resolution of approximately 1.1 mm in turbid media, demonstrating a marked enhancement in focusing capabilities compared to previous methods that relied on longer ultrasound bursts.

Fiolka et al. [121] investigated the use of ultrasound transducer frequencies to enhance fluorescence imaging in scattering media. The research explored a method to accelerate the imaging process by using multiple focused ultrasound pulses with distinct carrier frequencies to simultaneously measure different wavefronts. These ultrasound pulses serve as "virtual guide stars" to localize the wavefronts in the scattering medium, and by operating at different frequencies, the signals from the individual foci can be separated and processed in parallel.

In the experimental setup, two ultrasound pulses with slightly different carrier frequencies (50 005 016 Hz and 50 005 018 Hz) were launched into the sample. By adjusting the timing and synchronization of the pulses, the spatial separation between them was minimized, ensuring that both foci were within the transducer's Rayleigh range. This allowed the system to capture two distinct wavefronts simultaneously, doubling the wavefront measurement speed and reducing the mechanical scanning required by half. By measuring the sound-modulated light from both acoustic foci in parallel using Fourier analysis, the researchers demonstrated that

the signal-to-noise ratio (SNR) remained unchanged, even with the introduction of a second focus.

The study showed that by employing multiple ultrasound foci at different frequencies, the imaging process becomes significantly faster, without compromising the quality of the measurements. The parallelization of wavefront detection using distinct carrier frequencies enhances the efficiency of light modulation, making it a promising approach for faster, deeper tissue imaging in biological systems.

Another study that uses more than one acoustic focus in AOT was demonstrated by Chandran et al. [122]. In that experiment, the tissue phantom was insonified by a dual-beam, confocal ultrasound transducer oscillating at slightly different frequencies, creating a beat frequency. The light modulation caused by this interaction was measured, and from the resulting variation in modulation depth, the natural frequencies of the insonified region were deduced.

The study demonstrated that the natural frequency, associated with the dominant vibration mode of the region, allows for the estimation of Young's modulus. This method was validated using three different phantoms with varying elastic properties, confirming that AOT can be used to recover quantitative information about tissue stiffness. The experimental and theoretical results showed close agreement, with the measured resonance frequencies corresponding well to the computed values.

5.4 Plane-Wave Ultrasound in AOT

Conventionally, focused US pulses have been employed to maximize image resolution by concentrating acoustic energy in a small focal region. However, this approach suffers from significant limitations, particularly in clinical applications where rapid image acquisition and wide-field imaging are essential. Focused pulses generate unwanted residual acoustic pressure fields that affect image quality, and their small insonified volume necessitates a large number of US pulses for effective signal averaging, leading to slow imaging speeds. In contrast, plane wave US pulses offer significant advantages in overcoming these limitations. By insonifying a larger region, plane waves reduce the influence of residual pressure fields

and allow for faster image acquisition by requiring fewer pulses, all while maintaining or enhancing signal-to-noise ratio (SNR) and contrast.

Laudereau et. al [123] aimed to address the limitations of traditional acousto-optic imaging (AOI), particularly the slow imaging rates and the high number of ultrasound (US) pulses required when using focused US pulses. By introducing plane wave US pulses, the study sought to significantly reduce the number of pulses needed for image acquisition, while preserving a high signal-to-noise ratio (SNR) and image contrast.

The study demonstrated that the use of plane waves resulted in a substantial reduction in the required number of pulses by a factor of up to 50, thereby increasing imaging speed and enabling real-time applications. Compared to focused pulses, plane waves insonify a larger volume, tagging more photons and delivering greater energy to the sample. This led to an enhanced contrast-to-noise ratio (CNR), improved signal strength, and a reduced mechanical index (MI), thereby lowering the risk of cavitation-induced tissue damage. Although the use of plane waves introduced some image distortion, particularly a reduction in lateral resolution due to the limited angular range of the ultrasound probes, this distortion was mitigated through tomographic reconstruction techniques. Furthermore, the study demonstrated that using two perpendicular probes could enhance image quality by compensating for lateral distortions.

Nowak and Steenbergen [124] explored a method of enhancing acousto-optic imaging (AOI) using non-steered plane ultrasound wave pulses in a reflection-mode geometry with speckle contrast detection (SCD). The study aimed to mitigate the effects of residual acoustic pressure fields that exist outside the desired imaging region but can still impact the quality of acousto-optic images. A key parameter in their analysis was the *confinity coefficient*, which describes the degree to which the acoustic pressure field is confined within the intended imaging volume. This coefficient was calculated as a function of depth for the ultrasound pulses investigated.

In the experiment shown in Figure 5.12, the system setup remained fixed, but the ultrasound transducer array was electronically controlled via apodization (activating 128 or 64 elements at specific imaging depths) to generate either a

focused spot or a non-focused plane wavefront. This allowed the researchers to compare the performance of plane waves with traditional focused pulses, demonstrating that plane waves could improve imaging performance by reducing the influence of residual pressure fields while still enabling clear reconstructions of light fluence rate maps.

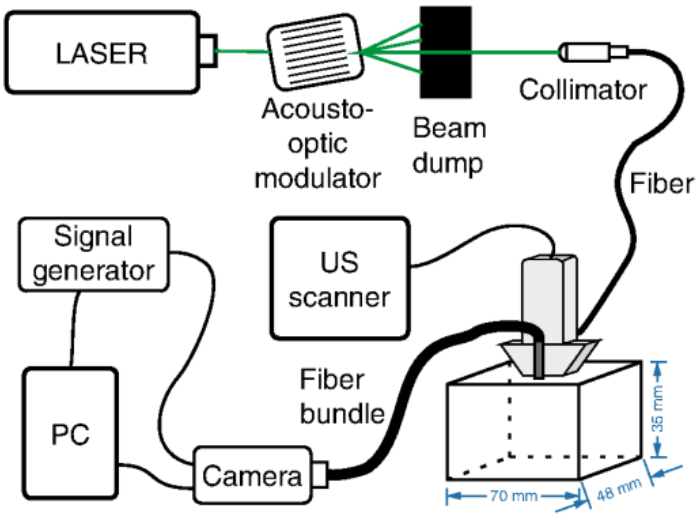


Figure 5.12: an acousto-optic imaging (AOI) set-up. The Laser source is pulse modulated acousto-optic modulator to emit 1 µs light pulses. The light sample was illuminated using a multimode fiber, and then detected with a fibre bundle creating a detectable intereference patterns on the CCD camera [124].

In conclusion, this chapter has gone through the technique of acousto-optical tomography, detailing the theoretical concepts and the technological progress of AOT as an imaging modality. The exploration has emphasized the usefulness of ultrasound engineering to refine the resolution and depth of optical imaging. The development of various ultrasound processes were delved into.

PART 2

Diffuse reflectance spectroscopy for colorectal cancer surgical guidance

6

6.1 Background of colorectal cancer . . 75
6.2 Material and Methods 77
6.2.1 DRS systems 78
6.2.2 Data collection and analysis 79
6.3 Results of the publications associated with this work . . . 80
6.4 DRS in the AOT framework 84

From this section, the part 2 of thesis proceeds to works I have been directly involved in the data acquisition. This chapter gives an in-depth description of the DRS in colorectal cancer study. It considers the wavelength ranges and their sensitivities to detecting tumor and healthy mucosa by using sophisticated machine learning methods. This is necessary in the provision of surgical guidance for clinicians. The papers (Paper I, Paper II, Paper III and Paper IV) associated with this study are placed in the appendix.

This chapter highlights my specific contributions to the work on DRS. In these publications, I contributed to the design and implementation of the meticulous data collection methodologies that were essential for capturing the reflectance spectra from different tissue samples including colorectal cancer tumor tissues. In addition to this, I helped in developing specialized MATLAB software algorithms critical for spectral pre-processing in the analyses of the data. Finally, I was active in the manuscript preparation ensuring clarity and technical correctness as well as coherence in our scientific findings. I would like to highlight here that I did not directly contribute to the machine learning development and the statistical processing involved.

6.1 Background of colorectal cancer

Colorectal cancer (CRC) is a significant health concern, with various genetic and environmental factors contributing to its development. For example in 2018, CRC diagnosis contributed to 10.2% of all cancer cases and 9.2% of cancer related mortalities. These numbers are respectively expected to grow from 63.4% to 71.5% by 2040 [128–130]. Work done by [131] highlighted the importance of molecular screening for hereditary non-polyposis colorectal cancer, which lacks distinctive clinical features but is characterized by a germline mutation of DNA mismatch-repair genes. Their study found that at least 2 % of patients with colorectal cancer in Finland had this hereditary form of the disease, emphasizing

the need for screening in individuals with specific criteria such as a family history of colorectal or endometrial cancer. The authors of [132] conducted the National Polyp Study to investigate the impact of colonoscopic polypectomy on reducing the incidence of colorectal cancer. Their findings supported the practice of removing adenomatous polyps to prevent colorectal cancer, as colonoscopic polypectomy resulted in a lower than expected incidence of the disease. This study provided evidence that colorectal adenomas progress to adenocarcinomas, further supporting the importance of polyp removal in preventing colorectal cancer. In [133], the work explored the clinical implications of tumor microsatellite instability in young patients with colorectal cancer. They found that high-frequency microsatellite instability was associated with a significant survival advantage and reduced likelihood of metastases, independent of standard prognostic factors. This highlights the potential for microsatellite instability to serve as a predictive factor for favourable outcomes in colorectal cancer patients. Furthermore, [134] and [135] delved into the role of *Fusobacterium nucleatum* in colorectal cancer. Specifically, [134] demonstrated the persistence of *F. nucleatum* and its associated microbiome in colorectal cancer tissues, with potential implications for antimicrobial interventions as a treatment approach while [135] found that *F. nucleatum* promoted chemo-resistance in colorectal cancer by modulating autophagy pathways, suggesting a potential target for improving patient outcomes.

The relative prevalence of colorectal cancer and its disturbing projected growth has called for different effective ways of diagnosis and treatments. Chief among these methods is colonoscopy which could be quite invasive. However, colonoscopy has been guided by DRS. Some studies in this area have reported achieving sensitivity and specificity rates as high as 100%, although these results were based on a limited number of samples and spectra[136–143]. Additional optical spectroscopic techniques used for detecting colorectal cancer during colonoscopy include Fluorescence Spectroscopy (FS), Time-Resolved Fluorescence Spectroscopy (TR-FS), Raman Spectroscopy (RS), and Fourier-Transform Infrared Spectroscopy (FTIR)[144–159]. Many studies using fluorescence spectroscopy have reported high sensitivity and specificity rates for diagnosis. Nevertheless, a significant number of these studies require the utilisation of contrast agents or ultraviolet illumination, which restricts the length

of optical guidance because of the potential hazards linked to extended ultraviolet exposure and the gradual build-up of contrast agents in cancerous lesions. Although there are difficulties, label-free FS, TR-FS, RS, and FTIR spectroscopy have been investigated in a small number of samples to determine their diagnostic capabilities. The results have shown that these techniques can achieve tissue classification performances with sensitivity and specificity of up to 100% [144–159].

In this work, we have made use of DRS emphasizing the response of cancer composition to various spectral ranges from 350 nm to 1919 nm and devising multivariate and machine learning means to identify tumors and healthy mucosa. We have also studied the influence of probe size on depth probing via the source-detector separations.

6.2 Material and Methods

This section shows how the experimental specimen were acquired as well as the description of the DRS system. The process of data acquisition is also described.

The study data was collected from tissue samples excised from 47 patients having colorectal surgery at the Mercy University Hospital in Cork, Ireland. These patients were part of the research study, and their demographics were recorded for analysis, while paying attention to their anonymity. The demographics are shown in Table 6.1.

Informed consent was obtained from all participants, and the study was done heeding the guidelines and regulations of the Clinical Research Ethics Committee of the University College Cork. During the surgical resection, about 15 sites of ex vivo mucosal tissues and 15 sites of tumor tissues were considered for data acquisition on each colorectal specimen. The tissue heterogeneity was ensured by collecting spectral readings from a typical area of 100 cm^2. After the specimens were removed in about 15 to 20 min of blood occlusion, they were moved to a measurement bench where they were cleaned and prepared for diffuse reflectance spectroscopy (DRS) measurements. Actual data acquisition started 40 minutes after experienced surgeons have identified the mucosa and tumor regions on the specimens. Tissue moisture was maintained

Table 6.1: Patient Demographics and Tumor Characteristics.

Characteristic	Value
Number of patients	47
Gender	
Male	32
Female	15
Age (years)	
Median	69
Minimum	40
Maximum	89
Interquartile range	13.5
Cancer types	
Adenocarcinoma	46
Carcinoma	1
Tumor stage	
pT1	5
pT2	7
pT3	26
pT4	9

using a damp cloth to preserve physiological conditions during data collection. Once the DRS data acquisition was completed, each specimen was returned to the Pathology Department for further processing and analysis. This process ensured that the tissue samples used in the study were collected systematically, with attention to detail in maintaining tissue integrity and ensuring accurate correlation between the DRS measurements and the tissue types being analysed for colorectal cancer detection.

6.2.1 DRS systems

The diffuse reflectance spectroscopy (DRS) configuration utilized in the study consisted of a broadband light source (HL-2000-HP, Ocean Optics, Edinburgh, United Kingdom) emitting light in the range of 350 nm to 2400 nm. This light source was fed into a fibre bundle in a source-detector arrangement. Two low-OH silica fiber optic probes were used. The first was a 630 µm SDD quadrifurcated probe (*one for ligth delivery and two were used for collecting reflected light*) and the second was a 2500 µm SDD trifurcated probe. The DRS system used two spectrometers, with one operating in the visible or short wavelength NIR range (350–1140 nm) and the other covering the long wavelength NIR range (1090–1920 nm).

The image in Figure 6.1 shows this arrangement.

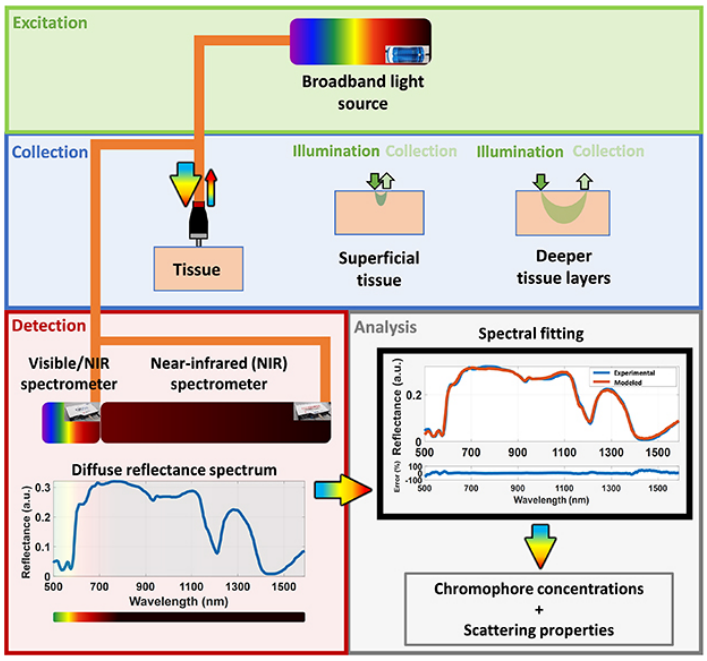


Figure 6.1: Experimental set up for Diffuse reflectance spectroscopy. Copied from [160].

6.2.2 Data collection and analysis

The excised specimen was placed on a grided sheet to provide coordinates of the tumor and healthy mucosa sites as shown in Figure 6.2.

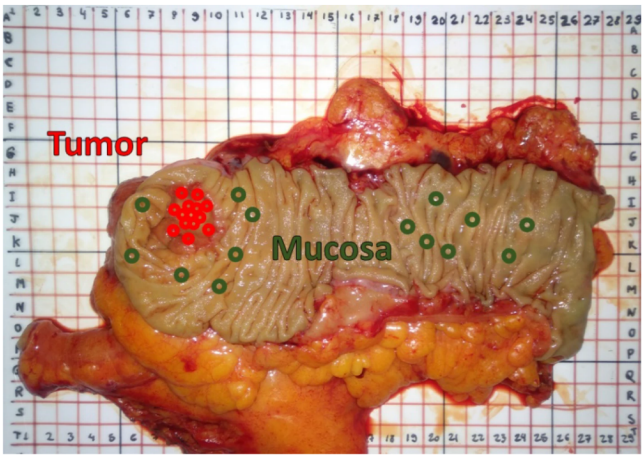


Figure 6.2: Resected colon showing tumor and healthy mucosa. The scale of the grid is in centimeters. Copied from [41].

These coordinates were used to identify the spectra in the data analysis process. Before and after the spectral data collection on the specimen, the background (*without light*) and reference measurements were made. The reference measurements were taken from a reflectance standard (FWS-99-01c,

Avian Technologies LLC, New London, USA) . This was conducted using a specialised holder that maintained a constant distance of probe and reflectance standard separation of 2 mm for the small probe and 6 mm between the large probe. For the spectral data collection on the tissue, the probes were shielded with polyvinyl chloride (PVC) film to prevent potential contamination. During the collection of tissue data, measurements were conducted by placing the probe at a 90° angle from the surface of the tissue. A combined total of 1363 spectra were obtained from the small SDD probe with a diameter of 630 µm (small probe), and 1526 spectra were obtained from the large SDD probe with a diameter of 2500 µm (large probe). In the data processing, the individual spectral data collected from the specimen by the respective spectrometers were joined together to form a continuous spectral data. The merging process involved having an interpolation of the overlapping region between the two spectrometers. The interpolated data were then used to calculate a weighted sum according to the equation:

$$R(\lambda) = \sum_{i=0}^{100} \frac{((100 - i) \times \text{Visible reflectance} + i \times \text{NIR reflectance})}{100}. \tag{6.1}$$

6.3 Results of the publications associated with this work

In this work, I contributed immensely to the data acquisition and the software for spectral processing. Our study used machine learning algorithms like support vector machines (SVMs), classification and regression tree (CART) and partial least square (PLS) regression analysis.

In the realm of colorectal cancer detection and surgical guidance, diffuse reflectance spectroscopy (DRS) has shown great promise, as extensively explored in associated publications of the thesis. Each of these studies contributes uniquely to the understanding and application of DRS in clinical settings, offering valuable insights into the technology's diagnostic precision and utility.

The study in Paper IV [41] emphasizes the practical application of DRS in real-time during surgical procedures, highlighting its ability to improve the accuracy of tumor margin assessments, which is critical for the complete removal of cancerous tissues. This capability significantly enhances the surgical outcomes by reducing the likelihood of cancer recurrence. This was achieved by using the experimental reflectance spectra to acquire absorption and scattering properties through parameters such as THb (Total Haemoglobin) which is the total haemoglobin concentration in the tissue, R_{vessel}, which is a parameter related to tissue size and density, F_{lipid} and F_{bile} which are respective concentrations of lipid content and bile content in the tissue. Other parameters included the reduced scattering amplitude, α' , b_{Mie} which is the Mie scattering power, F_{Ray} which is the Rayleigh scattering contribution as well as the oxygen saturation ($StO2$) and water concentration (F_{water}). The Figure 6.3 (a) and (b) show the boxplots for the different biomarkers for both small probe and large probe respectively. The outliers (red points) occur at more than 1.5 $\times$ the interquartile range (which shows the spread of the middle 50% of data). In the boxplots, three different tissues are identified. These are the fat, tumor and the colorectal wall (CW) tissues. Because the data used is not normally distributed, the median of the boxplots for various biomarkers becomes a determining parameter for tissue identification. In the case of both probes, clear distinctions of different tissues could be seen using biomarkers such as the reduced scattering amplitude (α'), oxygen saturation ($StO2$), the Mie scattering power (b_{Mie}), and the Rayleigh scattering (F_{Ray}).

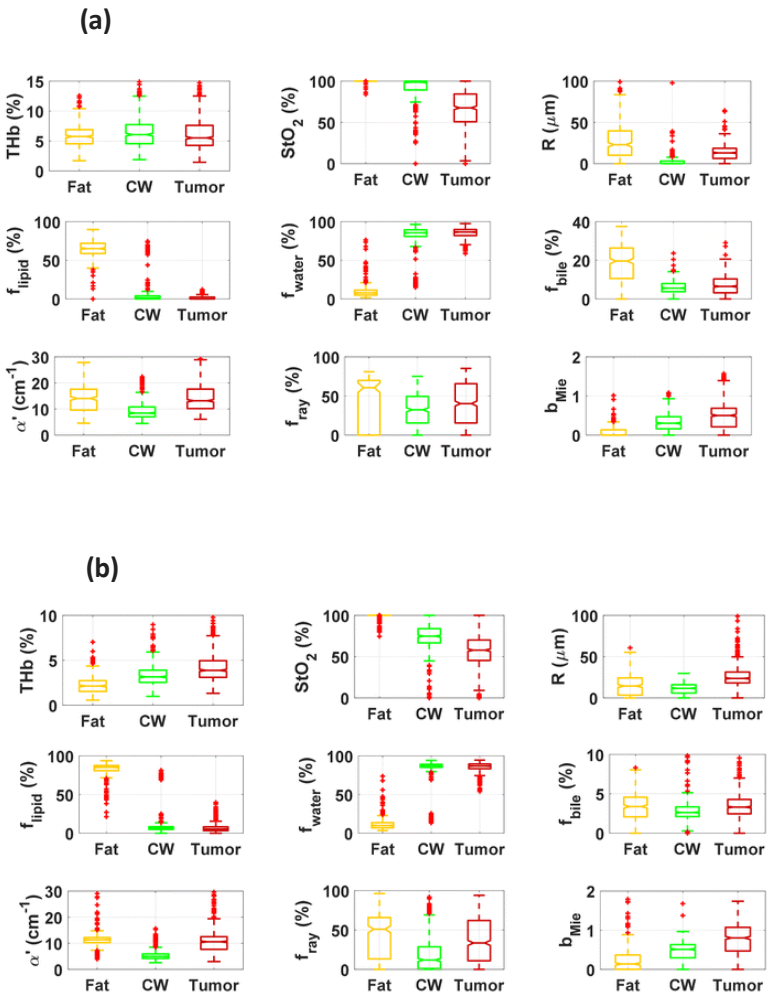


Figure 6.3: Boxplots showing tissue classification for small probe in (a) and large probe in (b). Copied from [41]. The outliers (red points) appear at more than (1.5 × the interquartile range) in both (a) and (b). The changes in median are seen in biomarkers such as α', $StO2$, b_{Mie} and F_{Ray}.

In Paper I [161], the focus shifts to optimizing the spectroscopic process by identifying the most effective wavelengths for detecting malignant tissues. This paper details how different wavelengths interact with tissue components and how these interactions can be harnessed to enhance the specificity and sensitivity of cancer detection, thereby fine-tuning the DRS technique for better diagnostic accuracy. These analyses covered both probes using various SMV models. For both probes, the quadratic SVM is recommended as can be seen in Table 6.2 and Table 6.3 with an appreciable sensitivity and specificity. Using the quadratic SVM model, various wavelengths were analyzed as shown in Table 6.4.

Various wavelength ranges were then studied using this quadratic SVM classifier. The performance metrics for near-infrared wavelengths surpass those achieved by analysing only the visible wavelength range. Furthermore, the performance increases as the near-infrared range being evaluated becomes broader and longer. The evaluation of wavelengths

ranging from 1000 nm to 1919 nm demonstrated comparable tissue classification performance to the entire range of wavelengths examined in this study (from 350 nm to 1919 nm).

Type of SVM	**Sensitivity (%)**	**Specificity (%)**	**Accuracy (%)**	**AUC**
Linear	95.2 ± 1.9	91.8 ± 1.1	93.6 ± 1.5	0.970 ± 0.007
Quadratic	93.5 ± 2.4	94.0 ± 1.7	93.8 ± 2.0	0.971 ± 0.014
Cubic	93.8 ± 0.5	93.3 ± 1.9	93.6 ± 1.2	0.988 ± 0.011
Fine Gaussian	86.4 ± 2.3	90.1 ± 1.3	88.2 ± 2.1	0.960 ± 0.007
Medium Gaussian	90.7 ± 3.3	88.0 ± 1.7	89.4 ± 1.0	0.965 ± 0.005
Coarse Gaussian	80.8 ± 3.7	79.9 ± 2.5	80.4 ± 3.1	0.878 ± 0.023

Table 6.2: Comparison of the classification performance of SVM classifiers for the dataset of the small SDD probe (n = 1363) containing reflectance values from 350 to 1919 nm.

Type of SVM	**Sensitivity (%)**	**Specificity (%)**	**Accuracy (%)**	**AUC**
Linear	93.1 ± 0.2	91.9 ± 0.6	92.5 ± 0.4	0.963 ± 0.004
Quadratic	96.1 ± 1.8	95.7 ± 0.6	95.9 ± 1.2	0.987 ± 0.005
Cubic	94.9 ± 0.7	95.5 ± 0.4	95.2 ± 0.5	0.983 ± 0.004
Fine Gaussian	82.4 ± 1.9	95.1 ± 1.3	88.4 ± 1.6	0.970 ± 0.005
Medium Gaussian	94.7 ± 0.8	89.6 ± 0.6	92.3 ± 0.7	0.975 ± 0.005
Coarse Gaussian	90.5 ± 1.5	85.1 ± 0.8	87.9 ± 1.2	0.935 ± 0.005

Table 6.3: Comparison of the classification performance of SVM classifiers for the dataset of the large SDD probe (n=1526) containing reflectance values from 350 to 1919 nm.

Analyzed Wavelengths	Sensitivity (%)	Specificity (%)	Accuracy (%)	AUC
From 350 to 760 nm	84.7 ± 2.4	87.0 ± 2.3	85.8 ± 2.4	0.922 ± 0.014
From 350 to 860 nm	87.4 ± 2.1	87.3 ± 2.7	87.4 ± 2.4	0.933 ± 0.009
From 400 to 440 nm and from 540 to 580 nm	84.2 ± 2.9	86.3 ± 2.2	85.2 ± 2.6	0.917 ± 0.012
From 400 to 1000 nm	90.5 ± 1.2	92.0 ± 0.5	91.2 ± 0.9	0.963 ± 0.004
From 405 to 665 nm	85.6 ± 1.4	90.0 ± 0.7	87.7 ± 1.1	0.930 ± 0.010
From 405 to 750 nm	86.8 ± 0.5	89.0 ± 0.3	87.8 ± 0.4	0.927 ± 0.005
From 470 to 700 nm	82.3 ± 2.2	86.0 ± 0.8	84.1 ± 1.6	0.900 ± 0.008
From 415 to 425 nm, from 495 to 505 nm, from 525 to 545 nm, and wavelengths 465 nm and 625 nm	74.5 ± 0.4	83.0 ± 0.8	78.5 ± 0.6	0.863 ± 0.005
405.235 nm, 406.42 nm, 408.794 nm, 414.736 nm, 422.48 nm, 468.76 nm, 559.489 nm, 577.506 nm, 594.342 nm, 957.948 nm, and 1000.31 nm	78.2 ± 0.7	86.0 ± 0.5	81.9 ± 0.6	0.903 ± 0.005
From 900 to 1900 nm	86.9 ± 3.5	88.0 ± 3.7	87.4 ± 3.6	0.921 ± 0.020
From 1000 to 1919 nm	92.1 ± 1.2	92.3 ± 1.4	92.2 ± 1.3	0.950 ± 0.011
From 350 to 1919 nm	93.5 ± 2.4	94.0 ± 1.7	93.8 ± 2.0	0.971 ± 0.014

Table 6.4: Performance metrics of each wavelength range analysed using the quadratic SVM classifier on the dataset of the small SDD probe.

The Paper III [162] delves into the biochemical interactions that underpin the DRS signals. By understanding the sources of biochemical variance in tissues, this study aids in refining the interpretation of DRS data, enhancing the ability to distinguish between different tissue types based on their molecular signatures.

Finally, Paper II [160] explores the microstructural differences in tissues that DRS can detect. This study not only adds depth to the understanding of how DRS differentiates between healthy and cancerous tissues but also contributes to the development of more precise models for predicting tissue pathology based on DRS data.

Collectively, these studies demonstrate the robust potential of DRS in improving the detection and surgical treatment of

colorectal cancer. By integrating detailed spectral analysis with clinical procedures, DRS facilitates more informed surgical decisions, potentially leading to better patient outcomes and a lower risk of recurrence. The ongoing advancements documented in these papers underscore the growing importance of DRS in medical diagnostics and the potential for future innovations that could further revolutionize the field of oncology.

6.4 DRS in the AOT framework

In the light of this thesis, diffuse reflectance and for that matter acousto-optics, seek to be of great potential advantage over purely light-based imaging or spectroscopy. Also, by using an acoustic focus as the secondary source of light, source to detector distances will require a new look theoretically.

The source to detector distances used in this work was primarily limited to the probes used. A hybrid technique utilising both DRS and AOT could serve the purpose of being able to access the biomolecular composition of tumors as well as quantifying tumor stiffness using the acoustic influence. A hybrid method could leverage the deep penetration capabilities of AOT and the surface-level analysis strength of DRS to study tissues at multiple depths and larger tissue volumes. This could lead to better understanding of diseases that affect deeper tissues which are typically hard to analyse with DRS alone. In order words, using the acoustic focus as a guide star, the area of interest could be precisely controlled. This kind of arrangement will call for reflection mode AOT and create a push towards the building of clinical probes. In fact, the requirement for spectral hole burning methods for extracting the ultrasound modulated light cannot be underestimated. This is particularly of interest considering that there is optimum sensitivity, specificity and accuracy of DRS spectra within the wavelength range of 1000 to 1919 nm which will work well for some real earth crystals too.

Acousto-optics with digital heterodyne holography

7

7.1 Theory 86
7.1.1 2-Phase 87
7.1.2 4-Phase 87
7.2 Method 88
7.3 Results 92
7.3.1 Simulation 92
7.3.2 Experiment 93
7.4 Discussion 96
7.5 Conclusion 97

This chapter underlines the principles of digital holography which is the method used in this thesis for the detection of ultrasound-tagged light. It will also encompass the concepts off-axis digital holography with a 4-phase shifting method. Finally, the chapter will provide a methodology for the construction of the holographic set-up.

Digital holography [163] is an enhancement of the conventional holography which requires photochemical procedures. In digital holography, this photochemical processes are replaced by the introduction of CCD cameras which captures the holographic interference created by the superposition of sample and reference beams. Unlike traditional photography which records only the intensity information of the sample under study, the invention of holography by Dennis Garbor in 1948 presented a means of getting the phase information of the sample as well as the amplitude [164, 165].

To add to that, holography in itself has progressed through several stages, beginning with the basic inline method, in which the reference and sample beams use the same optical path. While simple and efficient, inline holography frequently suffers from twin-image distortion and zero-order diffraction interference, which can obscure important details in image reconstruction. Recognising these challenges, Leith and Upatnieks [166, 167] created off-axis holography, which introduces an angle between the sample and the reference beams. This configuration alters the frequency of the interference pattern, spatially separating the real and twin images, as well as the zero-order component in the Fourier domain. Such separation greatly simplifies the reconstruction process, resulting in clearer, more accurate images without the overlapping effects which is common in inline setups.

Furthermore, one can also use phase-shifting methods in off-axis digital holography to eliminate twin images as well. This phase shifting is an advanced technique that enhances the precision and quality of holographic images by manipulating the phase of the reference beam during the recording process. However, this is not applicable to PRC based detection. The phase shifting method involves capturing multiple

holograms, each with a systematically varied phase of the reference wave, which allows for the elimination of twin images and zero-order diffraction spots.

7.1 Theory

With reference to the intensity recorded on the camera, we will have the components:

$$\text{Reference Field: } E_R(t) = \epsilon_R e^{i\omega_R t} \tag{7.1}$$

$$\text{Tagged Field: } E_T(t) = \epsilon_T e^{i\omega_T t} \tag{7.2}$$

$$\text{Untagged Field: } E_U(t) = \epsilon_U e^{i\omega_U t} \tag{7.3}$$

Given the frequency definitions for tagged and untagged signal as:

$$\omega_T = \omega_L + \omega_{US} \tag{7.4}$$

$$\omega_U = \omega_L \tag{7.5}$$

With these fields, the intensity $I(t)$ can be calculated:

$$\begin{aligned} I(t) = (&\epsilon_R e^{i\omega_R t} + \epsilon_T e^{i\omega_T t} + \epsilon_U e^{i\omega_U t}) \times \\ &(\epsilon_R^* e^{-i\omega_R t} + \epsilon_T^* e^{-i\omega_T t} + \epsilon_U^* e^{-i\omega_U t}) \end{aligned} \tag{7.6}$$

Expanding and substituting the frequency differences:

$$\begin{aligned} I(t) = I_R + I_T + I_U \\ &+ \epsilon_R \epsilon_T^* e^{i((\omega_R - \omega_T)t)} + \epsilon_R^* \epsilon_T e^{-i((\omega_R - \omega_T)t)} \\ &+ \epsilon_R \epsilon_U^* e^{i((\omega_R - \omega_U)t)} + \epsilon_R^* \epsilon_U e^{-i((\omega_R - \omega_U)t)} \\ &+ \epsilon_T \epsilon_U^* e^{i(\omega_{US} t)} + \epsilon_T^* \epsilon_U e^{-i(\omega_{US} t)} \end{aligned} \tag{7.7}$$

Now considering that the intensity on the camera (I_c) is a

sum of I(t) over time, we can write that:

$$I_c(M) = \int_{t_M}^{t_M+\Delta T} I(t)dt, \tag{7.8}$$

where M is the instantaneous number order of the image acquired, t_M is the associated time and ΔT is the exposure time. The average of the last two terms of Eqn. 7.7 are oscillatory and evens out because the exposure time ΔT is long compared to the period of the ultrasound. Therefore, we can select the real signal (tagged signal) where $\omega_R = \omega_T$ in:

$$I_c(M) = \underbrace{I_R + I_T + I_U}_{\text{zero order term}} + \underbrace{\epsilon_R \epsilon_T^*}_{\text{twin signal}} + \underbrace{\epsilon_R^* \epsilon_T}_{\text{real signal}} \tag{7.9}$$

7.1.1 2-Phase

For the 2-phase shifting holography, a phase shift of π is placed on the reference beam between the first image and the second image using this condition:

$$e^{i(\omega_R+\pi)t} = -e^{i\omega_R t}$$

we therefore get:

$$I_0 = I_R + I_T + I_U + \epsilon_R \epsilon_T^* + \epsilon_R^* \epsilon_T$$
$$I_\pi = I_R + I_T + I_U - \epsilon_R \epsilon_T^* - \epsilon_R^* \epsilon_T,$$

where I_0 is the intensity without a shift on the reference beam and I_π is there reference beam with a π phase shift. Subtracting these intensities accounts for the elimination of the zero order term and calculate the complex hologram as:

$$H_c = I_0 - I_\pi = 2(\epsilon_R \epsilon_T^* + \epsilon_R^* \epsilon_T) \tag{7.10}$$

7.1.2 4-Phase

Now if we conside 4-phase shifting holography, intensities are calculated at four different phases of the reference beam

as:

$$
\begin{aligned}
I_0 &= I_R + I_T + I_U + \epsilon_R \epsilon_T^* + \epsilon_R^* \epsilon_T \\
I_{\pi/2} &= I_R + I_T + I_U + i\epsilon_R \epsilon_T^* - i\epsilon_R^* \epsilon_T \\
I_\pi &= I_R + I_T + I_U - \epsilon_R \epsilon_T^* - \epsilon_R^* \epsilon_T \\
I_{3\pi/2} &= I_R + I_T + I_U - i\epsilon_R \epsilon_T^* + i\epsilon_R^* \epsilon_T
\end{aligned}
$$

The complex hologram H_c in 4 phase holography is computed by combining the differences in recorded intensities at four phase shifts as:

$$
\begin{aligned}
Re &= I_0 - I_\pi \\
Im &= I_{\pi/2} - I_{3\pi/2} \\
H_c &= Re + i \cdot Im \\
&= [I_0 - I_\pi] + i \left[I_{\pi/2} - I_{3\pi/2} \right]
\end{aligned}
$$

Therefore,

$$
H_c = 4\epsilon_R^* \epsilon_T \tag{7.11}
$$

This equation eliminates both the zero order and twin signal components. Experimentally, we achieve the phase shifting by ensuring the reference field is:

$$
E_R = \epsilon_R e^{i(\omega_T + \frac{\omega_c}{4})t} \tag{7.12}
$$

where $\omega_c = 2\pi f_c$, with f_c being the camera frame-rate of 50 Hz, giving the time between images as 20 ms. With regards to Eqn. 7.8, t_M =0,$\frac{1}{f_c}$,$\frac{2}{f_c}$,$\frac{3}{f_c}$.

7.2 Method

The digital holography set-ups are as shown in Figure 7.1 (a) and (b) respectively for series and parallel arrangements of acousto optic modulators (AOMs). The light source was split into sample and reference beams. The interference conditions of both beams could be controlled using the AOMs. In the series arrangement of Figure 7.1 (a), it ensures that much light goes through the sample, however the parallel arrangement in Figure 7.1 (b) allows for a better control of each beam because one can use the acousto optic modulators to turn both beams on and off.

To acquire ultrasound-tagged light with the phase shifting method, the field of interest to be recorded on the camera would have a reference beam with frequency, $\omega_R = \omega_L \pm (\omega_{AOM\ 1} - \omega_{AOM\ 2}) + \frac{\omega_C}{M}$. Here, ω_C is the camera frame-rate and M, defines the number of frames to be acquired, ω_L is the light frequency and $\omega_{AOM\ 1}$ and $\omega_{AOM\ 2}$ are the tuned frequencies of the respective acousto optic modulators. The introduction of the term $\frac{\omega_C}{M}$ is an experimental trick for the phase shifting of the reference beam which requires that four images would be acquired at 0, $\frac{\pi}{2}$,π,$\frac{3\pi}{2}$. This is to introduce an additional slow frequency shift on the reference that corresponds to the camera frame-rate.

With reference to Figure 7.1 (a) for example, one can detect pure heterodyne signal when $\omega_{AOM\ 1} = \omega_{AOM\ 2}$ and the ultrasound transducer is turned off. The untagged-light signal could then be acquired by turning on the transducer. To detect the ultrasound-tagged light, requires that: $|\omega_{AOM\ 1} - \omega_{AOM\ 2}| = \omega_{US}$ while the transducer is turned on. This configuration holds for Figure 7.1 where the positive first order of AOM 1 is fed into the AOM 2 and the negative first order of AOM 2 gets expanded and directed unto the camera. With regards to the arrangements in Figure 7.1 (b), the condition needed is: $\omega_R = \omega_L + \omega_{AOM\ 2} + \frac{\omega_C}{M}$ and the sample beam will require that the overall frequency shifts on the sample be $\omega_{Sample} = \omega_L + \omega_{AOM\ 1} + \omega_{US}$. These manipulations of the frequencies is essential when one wants to eliminate the twin signal as well. Experimentally, the lens and the aperture are needed to perform spatial filtering in order to remove the twin signal. The aperture image is formed at the focal plane of lens unto the camera where not all the interference terms cancel out because of noise. With reference to 7.11, a back propagation from the camera plane to the aperture plane is performed using an inverse Fourier transform to get the total tagged light intensity where all interference terms are separated. In this case, the field in the aperture plane $H_A = \mathcal{F}^{-1}(H_C)$.

In the configurations of the instruments, a computer was used to control a BNC pulse generator (Model 525 Pulse/Delay Generator). Two ports of this generator were used to send trigger pulses to function generators that controlled the ultrasound and the acousto-optic modulators that controlled the laser light (Sacher Lasertechnik Group, 785 nm). The laser has a linewidth of less than 300 kHz and supplied an output

light power of 200 mW into the holographic setup where the setup was tuned to deliver 80 mW of power onto the scattering samples used. A third port of the pulse generator was used to trigger the camera (IDS Imaging uEye-Edmund Optics). The camera has a full well charge of 13.5 ke^- and a dynamic range of 60 dB with a pixel pitch is 5.5×5.5 µm. All experiments were conducted below the full well charge of the camera. The ultrasound was generated using the function generator (AIM TTI-TGF4242) whose output was fed to the input of an ultrasound amplifier (RF Power Amplifier: Electronics and Innovation A075). This amplifier generated an output that controlled the ultrasound transducer (5 MHz, Olympus V307). For the generation of the light, the function generator (AIM TTI-TGF4162) was used to modulate the output of another function generator (RIGOL-DG4102), which controlled the RF drivers of the acousto optic modulators (AOM, AA optoelectronics), AOM 1 and AOM 2 via the generator outputs of channel 1 and channel 2, respectively. The RF drivers were powered by a 12 Volts power supply. The block diagram in Figure 7.2 illustrates these connections.

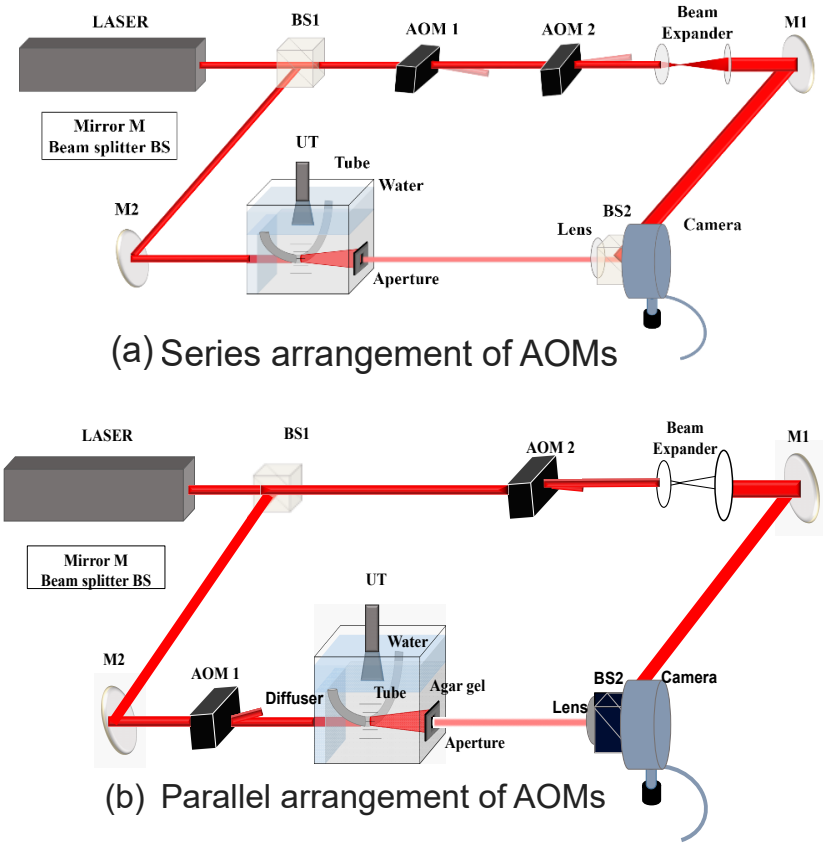


Figure 7.1: Digital heterodyne holography for the selection of ultrasound shifted light. A coherent laser source is split into an reference beam and a sample beam by a beam splitter (BS 1). From mirror (M2), the sample beam goes through a diffuser that is attached to a container holding the block of agar fitted with a tube containing blood mimicking fluid. The tube is placed in the focus of the Ultrasound transducer (UT). Water is used to couple the ultrasound wave propagation. An aperture is placed close to the sample holder the emerging light is focused on a lens (Bi-convex, focal length=75 mm) placed 5 cm away together with a beam splitter (BS2) and a camera. The sample beam is modulated by AOM 1 at 80 MHz at its -1 order was directed unto the sample. The reference beam was created with the -1 order of AOM 2 and modulated at 8 500 012 500 MHz before being expanded by a beam expander (Plano-concave lens, $f = -30$ mm). This was then reflected on mirror M1 unto the camera through beam splitter BS2.

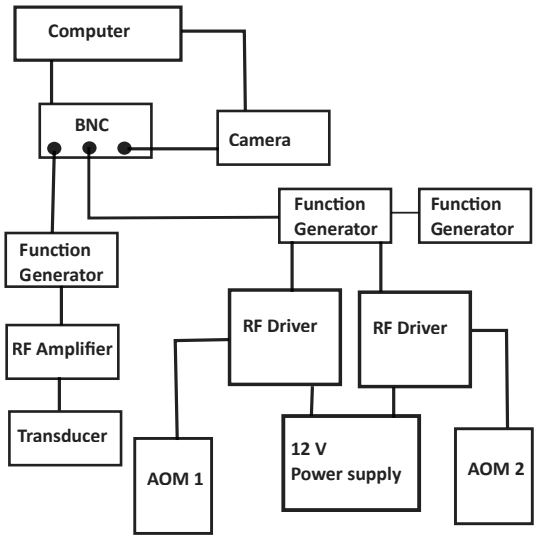


Figure 7.2: Electronic component connections.

7.3 Results

This result section has been split into two: the simulation and experimental parts. The simulation distinguishes between 2-phase and 4-phase digital holography results. The experimental part shows the results using the 4-phase shifting holographic method which was used in the data acquisition for the thesis.

7.3.1 Simulation

This section presents simulated differences between 2-phase and 4-phase shifting holographic methods. The intensity of light within the aperture is shown together with the twin image as in Figure 7.3 for 2-phase holography, where DX and DY are the number of pixels of the camera along the horizontal and vertical axes respectively. Similarly, the 4-phase detection simulation is shown in Figure 7.4. By accounting for the decorrelation effect, the twin image reappears as shown in Figure 7.5. The simulation parameters were based on the work by Gross [168].

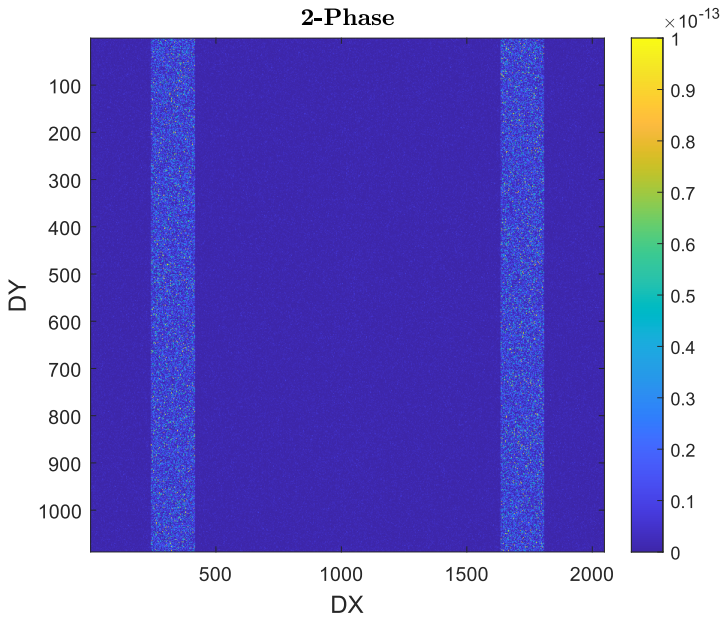


Figure 7.3: Signal detection within the aperture using 2-phase holography where both the real and twin signals appear.

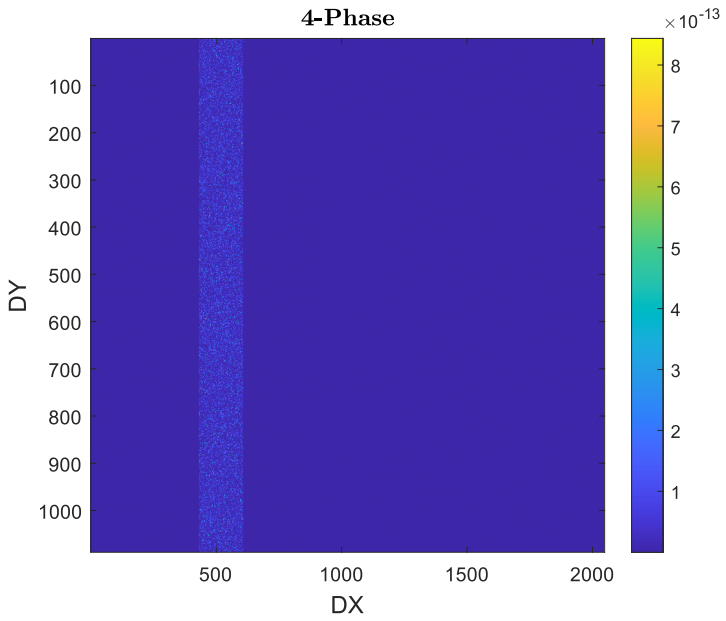


Figure 7.4: In the case of 4-phase detection, only the signal of interest can be extracted.

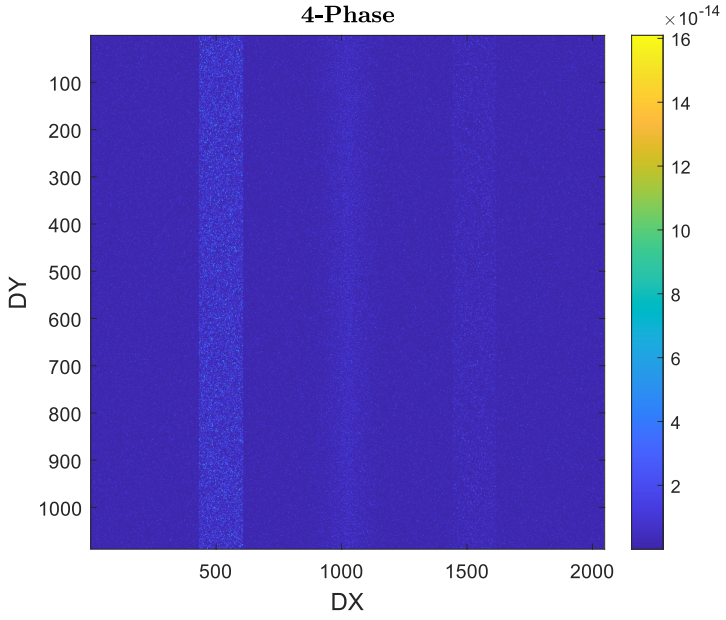


Figure 7.5: 4-phase holographic detection with a decorrelation effect representing the appearance of the twin signal.

7.3.2 Experiment

This section shows the experimental results from 4-phase digital holography using the optical setup built. The hologram of the aperture is shown in Figure 7.6. The signal of interest P, could be achieved by summing over the intensity values of the aperture and subtracting and normalizing by the background intensity: $P = \frac{P_s - P_n}{P_n}$, where P_s is the ultrasound-tagged light intensity within the aperture, and

P_n is the background intensity, calculated by taking a region outside the aperture regions. The plot of the sum of all the pixel values along DX is shown in Figure 7.7. This method has been used to acquire the heterodyne, untagged and tagged signals as shown in Figure 7.8. The sum of untagged and tagged light intensity should be equal to the heterodyne signal in a perfect situation where there is no drift in laser intensity.

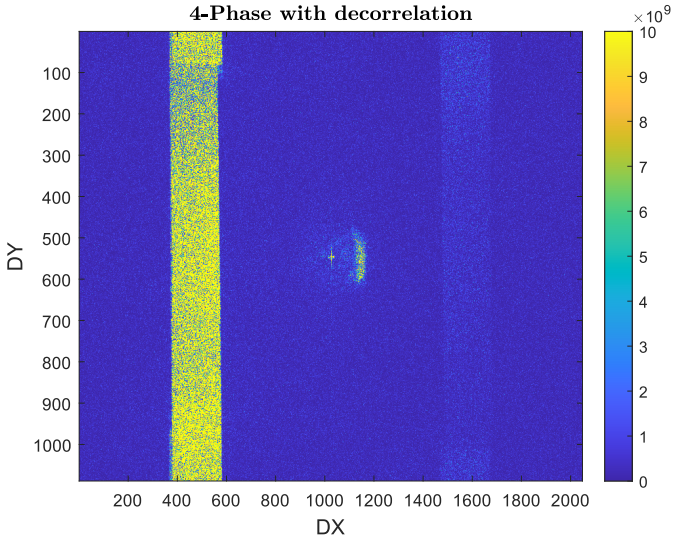


Figure 7.6: Image of the aperture and its conjugate. This shows the signal intensity from 390 to 600 on the camera dimension along the horizontal pixels, DX. The zero order term is located about 1000 while the twin signal is located from 1500 to 1610.

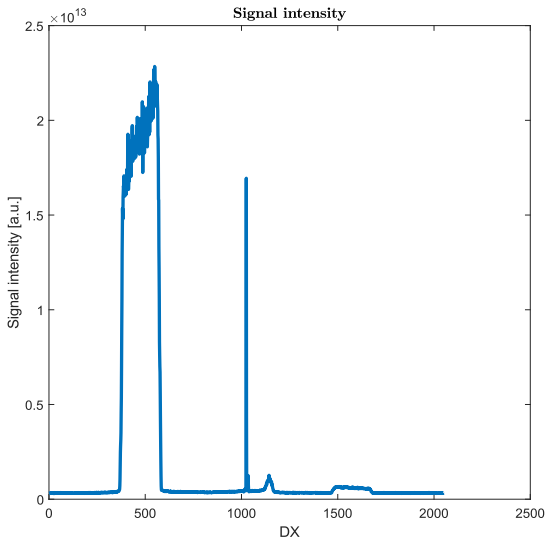


Figure 7.7: This is a plot of the total pixel intensity values spatially across the pixels of the camera.

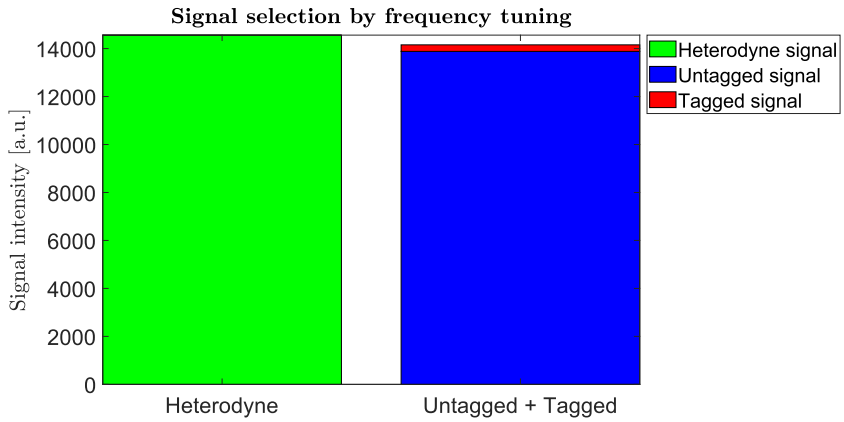


Figure 7.8: This show the types of signal to be acquired without the ultrasound waves and without frequency modulation of the light (heterodyne in green). When the the ultrasound is on, the untagged (blue) signal can be acquired and when the AOMs are tuned and with the ultrasound on, the tagged signal (red) could be acquired.

7.4 Discussion

The experiments in this thesis calculated the signals by subtracting the background intensity from the signal intensity and then dividing the value by the background intensity. The modulation depth is then calculated by the ratio of the tagged light signal to the heterodyne signal. The methods shown in Figure 7.1 (a) and Figure 7.1 (b) can enhance the tagged signal intensity by using the reference beam as a gain to increase the signal while being conscious of the saturation level of the camera pixels. It should be noted also that this interferometric setup is sensitive to vibrations.

The 2-phase and 4-phase holography are both extensions of the basic principles of holography, where an interference pattern between a reference beam and a sample beam is recorded. The off-axis effect could be achieved by setting a small angle between both reference and sample beams. In the setups used in this thesis, this was also possible by shifting the aperture off the principal propagation axis of the sample beam. The angle (θ_{max}) requirement is such that $\theta_{max} < \frac{\lambda}{2\Delta}$, where λ is the wavelength of light and Δ is the pixel pitch of the camera. For 2-phase, we have intensities of π shift difference and experimentally, for a 50 Hz camera frequency, each image could be acquired at 25 Hz. In 4-phase holography, these images are captured at 12.5 Hz each.

The primary advantage of employing 2-phase holography is its simplicity and speed, which are needed in applications that do not need to reconstruct the full field. By recording at two phases, typically 0 and π, and subtracting these two recorded intensities, 2-phase holography effectively enhances the visibility of the real image. The intensities of the real and twin signals are same in magnitude as it is evident in Figure 7.3. AOT is only interested in the total intensity of the ultrasound-tagged light and in that case, 2-phases digital holography would be adequate where noise effect is not a problem.

The 4-phase holography, on the other hand, takes this technique further by recording at four phase shifts: 0, $\pi/2$, π, and $3\pi/2$. By using four phases, the technique synthesizes both the real and imaginary components of the wavefront, allowing for a full complex field reconstruction. This complex reconstruction is imperative in precision applications

such as quantitative phase microscopy where phase errors can lead to significant inaccuracies in measured values. For example, under the same conditions, the introduction of a decorrelation effect results in the appearance of the twin image which intends reduces the maximum signal intensity. However, it should be noted that these two signal bands are conserved. The advantage of 4-phase digital holography is that, it is more sensitive because it uses 4 images so the "noise" is averaged a lot more than in a 2-phase situation.

The computational aspect of 4-phase holography, particularly the Fourier transform algorithms used to process the holograms, plays a critical role. The Fourier transform of the resulting intensity patterns, when processed, isolates the frequency terms corresponding to the virtual (or twin) and real images. These component separations could also be done experimentally by turning the mirror reflecting the reference beam on the beam splitter or by shifting the aperture. The mathematical basis for this is deeply rooted in the principles of wave optics and Fourier optics.

7.5 Conclusion

In summary, this section has looked at the processes of 2-phase and 4-phase holographies. It provided a complete stepwise process of constructing and configuring the electronic components in an acousto-optic based digital holographic detection.

The implementation of these holographic techniques requires careful consideration of the experimental setup, including the stability and coherence of the laser source. Misalignments or instabilities in any of these components can lead to phase errors, which degrade the quality of the reconstructed image. By changing the frequency conditions we could us digital holography to acquire heterodyne, untagged and tagged signals. In this part of the thesis, I have demonstrated the successfully implementation of a holographic detection of ultrasound-tagged light. This forms the basis for the experiments done in Chapter 8 and Chapter 9.

Viscosity contrast in blood mimicking fluids

8

This chapter studies the ability of distinguishing liquids of various glycerol concentrations or viscosities. In the changes of viscosity of coagulating blood, the optical properties also change. This chapter uses the concept of acousto optics to pick the opto-mechanical changes in these fluids with respect to the modulation depth and tagged light intensities. The chapter lays out the motivation for the study as well as the progress and the state of the art in blood coagulation measurements. The experimental procedures are provided for the tagged light signal acquisition. Although, the experiment does not explicitly make use of blood, it presents a foundation for blood based studies that could benefit from the acousto-optic techniques.

8.1 Motivation 99
8.2 The process of blood coagulation 100
8.3 Coagulation measurement tools . . 101
8.4 Material and method 103
8.4.1 Samples 103
8.4.2 Data acquisition . 104
8.4.3 Depth Scanning . 104
8.5 Results 105
8.6 Discussion 107
8.7 Conclusion 110

8.1 Motivation

Detecting changes in blood viscoelasticity *in situ* is a significant challenge in blood rheometry. This is especially critical when considering the assessment of haemodynamic and rheological properties of blood in large organs and during surgery where either procoagulant or coagulation inhibiting drugs are administered [169]. Utilizing viscoelasticity as a means of tissue characterization emerges as an essential strategy in diagnosing a range of biological abnormalities. The normal flow of blood through vessels depends on blood pressure, vascular resistance as well as a natural balance between thrombogenic and haemorrhagic agents at the vessel walls. This balance prevents changes in the state of blood during the circulatory process [170]. When the flow conditions are broken upon an injury to the endothelium lining of the blood vessels, two diagnosable situations namely; hypo-coagulation and hyper-coagulation could occur (if there is a mismatch between the coagulation activating and inhibiting agents) [171]. These medical conditions could either be inherited genetically or acquired through diseases and changes in environmental factors [172, 173]. In addition, both conditions could have fatal outcomes in patients in extreme cases or as have been reported recently about some COVID-19 vaccines

[174]. In hypo-coagulation, there is platelet deficiency such that, the coagulation pathways are not activated in due time because there is no initiation of platelet plug. Conversely, in hyper-coagulation, early initiation of the primary haemostasis results in the quick formation of the platelet plug thereby starting the coagulation cascade earlier than necessary.

The concept of acousto optic effect has been explored for flow studies in blood mimicking fluids [175]. In this chapter, we propose that ultrasound tagged light intensity measurement could be a time efficient approach in quantifying changes in viscoelasticity and optical scattering. This could be used in the classification of blood coagulopathies *in situ* and in deep tissue environments. The approach uses a more sophisticated digital heterodyne holography detection scheme with a 4-phase acquisition technique [58, 168]. The experiment measured tagged light intensity of blood-mimicking fluids (aqueous glycerol) at varying viscosities while maintaining the optical properties [176]. Before delving deep into the techniques employed in this chapter, the process of coagulation and the trends used in coagulation monitoring would be discussed in the next sections.

8.2 The process of blood coagulation

Until the coagulation process is initiated, the platelets, endothelial cells and the blood clot proteins co-exist independently to perform their respective duties. Upon a significant rupture or injury at the vessels, procoagulants and coagulation inhibitors become unbalanced. When this occurs, conditions leading to primary haemostasis are established and the haemostatic reaction is triggered. The platelets then undergo morphological changes and become activated. Upon activation, von Willebrand's factor is released and the platelets adhere to each other and with the collagen network in the subendothelium layer of the blood vessel [170, 177]. This initial phenomenon produces thrombin which converts fibrinogen to the fibrin clot, thereby forming the plug. A secondary haemostasis then creates fibrin strands to ensure the maturation and stability of the plug [178]. Complete healing of the injury or the end of the coagulation process later occurs when there is a breakdown of the fibrin network in the fibrinolysis process. In this chapter, it is hypothesized that these changes

in the material property of the coagulating blood could be studied using acousto-optics. The experiment in this work uses blood mimicking fluid to study the response of viscosity changes to ultrasound-tagged light.

8.3 Coagulation measurement tools

Most established modalities for measuring blood rheological properties require an invasive drawing of significant blood volumes to be worked on in a dedicated laboratory. This *ex vivo* solution could be time consuming. Various techniques have been explored to address some of these challenges. Notably, laser speckle rheology (LSR) [179, 180] presents a compelling optical option for time efficient rheological studies, while ultrasound-based methods also present associated advantages applicable to deep tissue studies. Vibroacoustography [181, 182], shear wave dispersion ultrasound vibrometry [183], shear wave spectroscopy [184], and viscoelastic creep imaging [74] stand among the array of ultrasound methods employed for studying viscoelastic behaviour of blood. A more recent approach for *in vivo* sensing of blood viscosity was based on frequency-resolved Photoacoustic measurements [185]. Several non-invasive methods have been proposed to estimate blood viscosity, including ultrasound Doppler, magnetic resonance, and optical coherence methods. However, these techniques are beset by limitations such as resolution, penetration depth, sensitivity, and practical constraints associated with patients with metallic implants.

Determination of hypo-coagulable states is direct since platelet function and count could be evaluated to find the onset of primary haemostasis. On the other hand, evaluating hypercoagulability depends on considerations such as understanding the intrinsic, extrinsic and common pathways in the coagulation process in order to interpret test results. For example, activated clotting time (ACT) and prothrombin time (PT) use extrinsic and common pathways to characterize hypocoagulability whereas partial thromboplastin time (PTT) provides same information through the intrinsic and common pathways during the second haemostasis [171]. These methods provide information on the time at which clot formation is initiated in the blood plasma when there is

calcium and tissue thromoplastin [186]. The use of PT/PTT to characterize hyper-coagulability has been deemed not reliable enough [187–189]. Some established tests are based on the fibrinolysis at the end of the clot formation rather than real time dynamics of the coagulation system [171]. As a result, various techniques have been developed to monitor the entire coagulation process. Some of these methods include thromboelastogram (TEG) and rotational thromboelastometry (ROTEM) that utilize the viscoelastic property of blood in the process [190]. A common metric used in the study of blood coagulation is the coagulation index (CI) as used in TEG. This depends on the reaction time (R), maximal amplitude (MA), clot formation time (K) and the angle tangential to the TEG curve. Another known metric is the international normalize ratio (INR) which depends on the PT, mean normal PT (MNPT) and the international sensitivity index (ISI).

Other techniques that have changed the methods of coagulation monitoring include the use of microfluidics, fluorescent microscopy, electrochemical sensing and micro/nano electromechanical systems (MEMS/NEMS) [191, 192]. For example, the integration of microfluidic technology into the field of coagulation diagnostics indicates a significant advancement. These devices employ extremely small amounts of blood to simulate vascular conditions, enabling the evaluation of clotting beneath flow conditions that closely resemble the physiological environment. This capability not only enhances the accuracy of coagulation assessments but also facilitates rapid testing at the point of care, essential in emergency and remote settings[193]. Furthermore, the advent of emerging technologies in biosensors and wearable devices is paving the way for significant advancements in the field of coagulation monitoring. The primary objective of these innovations is to offer uninterrupted and instantaneous monitoring of coagulation parameters in point of care devices as well. In these times, the role of machine learning and artificial intelligence cannot be underestimated in the sophistication of the coagulation monitoring methods [194].

In the remaining section, the thesis proceeds to the experimental protocols used in accessing the glycerol concentration and optical differences of blood mimicking fluids in a tube buried in an agar block phantom in order to simulate deep tissue sensing.

8.4 Material and method

The experimental sample was made of a 3 cm thick agar block with its natural scattering. This block was fitted with a 5 mm diameter-tube burried 3 cm deep from the surface of the agar phantom. This was to simulate a blood vessel deep within a tissue. In the experiment, the tube was positioned within the focus (about 5 cm) of a 5 MHz ultrasound transducer. The transducer supplied a 14 cycle ultrasound burst such that the burst length was 6 mm. To access the acousto-optic signal within the inner diameter of the tube, short signal bursts of US wave of the order of the diameter of the tube is required. Ultrasound-tagged light intensities were measured using the methods described in Chapter 7.

8.4.1 Samples

The experiment was conducted using the experimental procedure described in Chapter 7. The agar phantom was prepared with 740 g of water, and 9.47 g of agar boiled to 92 °C before allowing it to cool at room temperature within the sample holder fitted with a tube. The blood mimicking fluids were prepared using glycerol-water mixtures resulting in samples with viscosities ranging from 2 cP to 7 cP [195, 196]. For samples that required reduced optical scattering of 5 cm^{-1}, 7 cm^{-1} and 10 cm^{-1} , a TiO_2 solution for the required scattering properties was prepared using the guide that 50 mg of TiO_2 in 100 mL of water yields μ_s' of 5 cm^{-1}. While the TiO_2 solution was being stirred on a magnetic plate, equal volume of it was pipetted into the aqueous glycerol samples and sonicated for 20 min before measurement commenced.

To measure difference in μ_s' of the fluids with viscosities of 2 cP and 7 cP , we utilized a time domain diffuse optical spectroscopy (TD-DOS) setup [197, 198]. During the measurement of the optical properties of the fluid samples, the sample was gradually stirred with a magnetic stirrer in order to ensure the uniform distribution of the TiO_2 particles.

8.4.2 Data acquisition

The location of the tube in the path of both the transducer and the laser was identified by identifying the position of the empty tube with respect to the pixel arrays on the camera. To confirm the location of the tube, indian ink was gently pippetted into the tube to check that the light is absorbed. A volume of 1 mL of each sample was fed into the tube and measurements taken one after the other. The tube was washed and dried in between measurements from different samples. Clear samples (aqueous glycerol) of varying dynamic viscosities were measured in order to observe the trend of the change in modulation depth. The order of measurement was randomized such that, data acquisition was not sequential from 2 cP to 7 cP in order to factor out influence of laser drift on the interpretation of the results. This protocol was followed when measuring the samples with optical scattering.

8.4.3 Depth Scanning

For the depth scanning of the embedded tube within a scattering agar block ($\mu_s' = 3\,\mathrm{cm}^{-1}$), a 5 MHz ultrasound transducer (Olympus V307) was used. Figure 8.1 shows the how the delay (dt_{US}) of the ultrasound was tuned to match the illumination by the light on the tube while the camera is on. The delay was changed accordingly for the axial ultrasound scan while the light was switched on for $t_L = 4\,\mu\mathrm{s}$.

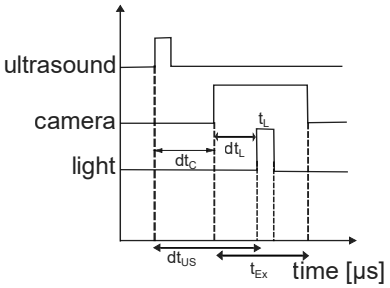


Figure 8.1: The delay (dt_{US}) of the ultrasound signal was used to scan in an around the embedded tube. The camera was opened at $dt_L = 10\,\mu\mathrm{s}$ by adjusting dt_C before the acousto-optic interaction. The exposure time of the camera was $t_{Ex} = 30\,\mu\mathrm{s}$ and the light stayed on for $t_L = 4\,\mu\mathrm{s}$.

The data acquisition was performed at a depth scanned from 3.45 cm to 8.55 cm of the principal axis of the transducer. An axial acquisition of 11 data locations at an interval of 5.1 mm were collected and holographic signal processing was done without cropping of the tube area since the sample scattered the light uniformly in the agar block phantom. This corresponded to a scanning range from 3.45 cm to 8.55 cm from the ultrasound transducer as shown in Figure 8.5. This is to demonstrate the depth probing of the agar block to locate the tube and its content.

8.5 Results

The optical scattering measurements for samples with viscosities of 2 cP (22% glycerol) and 7 cP (48% glycerol) are obtained using the time domain diffuse optical spectroscopy (TD-DOS) setup. For the sample with a viscosity of 2 cP, the reduced scattering coefficient, μ_s', was approximately 4.4 cm^{-1}, while for the 7 cP sample, it was about 5.6 cm^{-1}.

Figure 8.2 presents the holographic reconstruction of the embedded tube within the agar block. In part (a), the image reveals the reconstructed tube when it was empty, captured using 4-phase digital holography. In contrast, part (b) shows the reconstruction when the tube was filled with pure india ink. The difference in contrast between the empty and filled tube, particularly in the red-annotated region, is highlighted in part (c) of the figure (between the red lines).

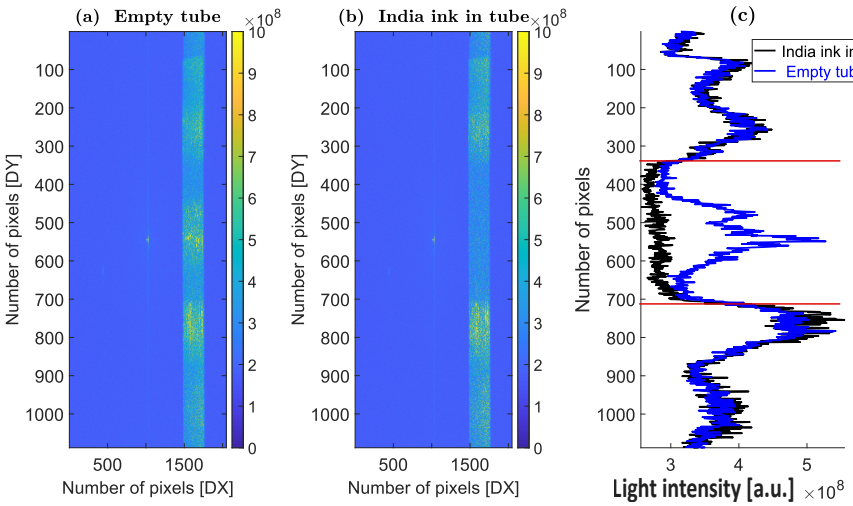


Figure 8.2: Locating the tube embedded in an agar block. The position of the tube is over the array of camera pixels. The pixel values from 320 to 710 on the DY axis show the position of the tube on the camera after holographic processing. Image **(a)** shows an empty tube while image **(b)** shows a the tube filled with Indian ink. Image **(c)** shows the contrast between the empty tube and the filled tube.

The analysis provided in Figure 8.3, shows significant variation in the measurement of modulation depth against viscosity of clear (non scattering) aqueous glycerol. This can indicate that the refractive index contribution to the change and the acoustic absorption in the acousto-optic signal is dominant as compared to scattering effects. This is evident in the negative trend of the relationship between the modulation depth and increase viscosity and refractive index. Comparatively, Figure 8.4 shows the modulation depth versus viscosity or glycerol concentration for multiple scattering fluid having different scattering coefficients and depicts how the modulation depth is directly related to optical scattering, viscosity and refractive index.

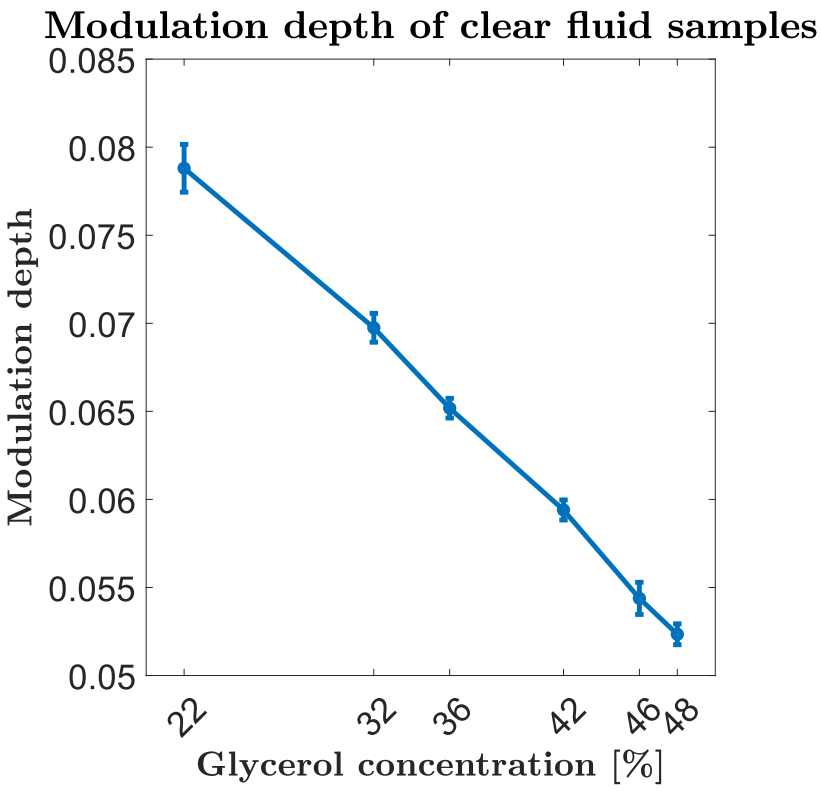


Figure 8.3: The modulation depth of non scattering aqueous glycerol of varying concentrations showing a negative dependence.

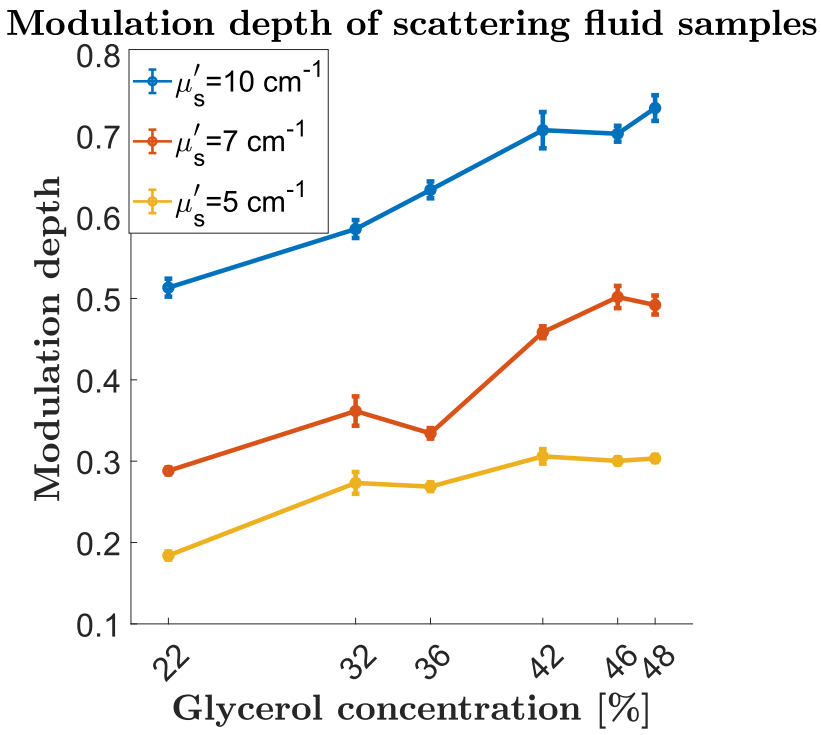


Figure 8.4: A study of the modulation depth dependence on optical scattering and glycerol concentration.

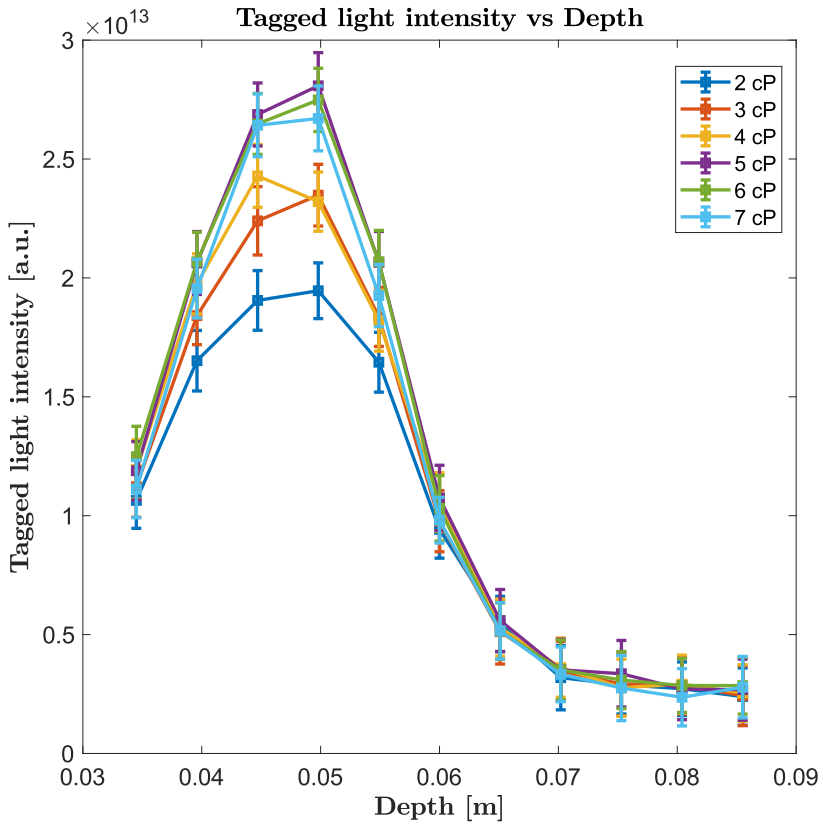


Figure 8.5: An axial acquisition of 11 data locations at an interval of 5.1 mm were collected. This corresponded to a scanning range from 3.45 cm to 8.55 cm from the ultrasound transducer. The plot shows the mean and the associated standard error.

8.6 Discussion

The modulation depth as it is discussed in acousto-optic imaging is the ratio of the tagged light intensity to the heterodyne light intensity. The mechanisms of light-ultrasound interactions have been studied extensively [54, 199–201]. The overall intensity achieved by the light-ultrasound interaction could be influenced by some primary mechanisms like refractive index change, movement of scatterers and their subsequent effects [202].

The sample with more glycerol is more viscous and denser with higher refractive index. In addition to this, its higher viscosity implies that it has higher acoustic absorption. As a result, by increasing viscosity of the clear aqueous glycerol, the acousto-optical signal decreases as shown in Figure 8.3. The data processing was such that 200 intensity values corresponding to the averaged image (of 200 images) as shown in Figure 8.2 Image **(a)** and Image **(b)** were used to create 200 data points from which mean and standard deviations were calculated. The image region in the tube

region as well as the region above and below the tube region of Figure 8.2 were averaged individually within from pixel number 1149 till the end of the camera pixel on DX (2048). This range is meant to include the signal band region of DX. After this, 1-D plots of these ranges across all cropped regions were linearly fitted to locate the background level of the camera in order to calculate the area under curve of the signal (signal band) in all these cropped regions. All these individually averaged regions were subtracted from each intensity value yielding the 200 data points. The errors associated with the measurement of the modulation depth were calculated with the error propagation formula:

$$\sigma_{MD} = MD \times \sqrt{\left(\frac{\sigma_{\text{tagged}}}{\mu_{\text{tagged}}}\right)^2 + \left(\frac{\sigma_{\text{hetero}}}{\mu_{\text{hetero}}}\right)^2} \tag{8.1}$$

where:

- σ_{MD} is the standard error of the modulation depth,
- MD is the mean modulation depth,
- σ_{tagged} is the standard deviation of the tagged signal,
- μ_{tagged} is the mean of the tagged signal,
- σ_{hetero} is the standard deviation of the heterodyne signal,
- μ_{hetero} is the mean of the heterodyne signal.

Finally, axial scanning results for the agar block, aimed at identifying the tube's content, are shown in Figure 8.5. This figure illustrates the tagged light intensity for samples with viscosities ranging from 2 cP to 7 cP, providing insight into the depth-resolved measurements of the sample. The tagged light intensity was recorded for the scattering fluid samples. In this situation, the agar block was made such that it had a μ_s' of $3\,\text{cm}^{-1}$. The fluid samples of varying viscosities and μ_s' of $1\,\text{cm}^{-1}$ were pipetted into the tube and the optomechanical changes in the samples were measured.

From Figure 8.3, the modulation depth decreases with increasing glycerol concentration but upon adding TiO_2 to the clear samples (aqueous glycerol), the optical scattering resulted in a trend reversal of the relationship between modulation depth and glycerol concentration as shown in Figure 8.4. The addition of scatterers to the clear samples also introduces changes in refractive index, changes in optical scattering and particle displacement which is also directly related to the modulation depth [54, 201]. This is shown in

Figure 8.4 for samples with μ_s' of 5 cm^{-1}, 7 cm^{-1} and 10 cm^{-1}. The modulation depth increases with increase in optical scattering.

The increase of about 26 % in μ_s' from 2 cP to 7 cP could be a contributory factor to the change in modulation depth. The modulation depth increase observed could also be attributed to the associated differences in optical scattering rather that solely due to viscosity of the fluids. The holographic method used is also sensitive to the rate of speckle decorrelation as a result of the mean-squared displacement (MSD) of TiO_2 scatterers within these fluids of varying viscosities. The concept of extracting viscoelastic behaviour of fluids from the MSD has been studied through the generalized Stokes–Einstein relation (GSER). This application has also been utilized in laser speckle rheology [203]. In the experiment, it was observed that as the viscosity increases, both the ultrasound controlled and Brownian motions of the scatterers will be restricted in displacement because of the increase in resistive forces. This restriction is expected to cause an increase in signal in samples that have same optical properties but different viscosities.

This study does not account for flow conditions of the blood mimicking fluids in the tube. Various studies have looked at this phenomenon emphasising on the effect of cerebral blood flow (CBF) on acousto optic light intensity [175, 204, 205]. This established a direct relationship between cerebral flow index (CFI) and flow velocity. Blood is a non-Newtonian fluid and its viscosity depends on the shear rate of flow. For example, at body temperature, blood viscosity could lie between 3.5 cP and 5.5 cP [206] but several factor could alter these values. These factors could be changes in red blood cells and temperature among others [207, 208]. Because of the flow conditions, viscosity of 60 cP could be recorded at a shear rate of 0.1 s^{-1} or 6 cP at a shear rate of 200 s^{-1}[206]. Here in this study, the focus was to change viscosity and determine its effect on the acousto-optic signal but the optical variation of the scattering samples with viscosities of 2 cP and 7 cP was significant and could be responsible for the differences in signals.

8.7 Conclusion

The study used a 4-phase holographic detection of ultrasound-tagged light to study the influence of glycerol concentration and optical scattering changes in relation to the ultrasound-tagged light intensity and modulation depth as it relates to acousto-optical tomography. The results show direct dependence of the signal on opto-mechanical property of scattering samples and an inverse relationship with glycerol concentration of clear aqueous glycerol. The experiment could be well suited for a reflection-mode detection set-up. The aqueous glycerol could be a simplified situation of blood mimicking fluid which does not mimick directly the dynamics of actual blood. As a result, further studies that directly uses blood could throw much light on these results. Alternatively, by using the methods of PEGylation, it could be possible to creates samples of same optical properties but varying viscosities. This could be possible through the uniform suspension of optical scatterers in the aqueous glycerol, thereby preventing aggregation of the scatterers.

Measurement of decorrelation time under flow conditions

9

9.1 Introduction 111
9.2 Materials and methods 112
9.3 Results 112
9.4 Discussion and conclusion 114

9.1 Introduction

The study of fluid dynamics within the realm of life sciences and biology is of significant importance, particularly when examining substances with dynamic internal structures such as blood. These fluids present unique challenges due to their complex scattering properties and the rapid motion of scatterers, such as cells and proteins, which significantly influence light-based measurements. Techniques such as laser Doppler broadening and laser speckle analysis have been extensively utilized to measure the decorrelation times of different blood substances and biological samples, providing essential insights into the physiological conditions affecting blood flow and tissue decorrelation [49, 209].

Light-based approaches offer non-invasive tools for real-time monitoring and diagnostics. For instance, laser Doppler broadening exploits the Doppler effect of light scattered by moving particles within the fluid to assess flow velocity and turbulence. Similarly, laser speckle analysis utilizes the random interference pattern generated when coherent light, like that from a laser, scatters off the microscopic structures within blood. The temporal and spatial variations in these speckle patterns, known as decorrelation can be indicative of microvascular dynamics [209].

Furthermore, heterodyne detection techniques have been employed to study the frequency spectrum of scattered light, where the broadening of the heterodyne signal is directly related to speckle decorrelation such that the intensity of the signal reduces with increasing frequency as shown in Figure 9.1. The broadening of the heterodyne signal in this case is dependent on the frequency of the incident light (f_i), the frequency of the scattered light (f_s) as well as the velocity (v) of scattered particles under flow, light wavelength (λ) and the angle of incidence (φ). This is given by the formula [210]:

$$f_i - f_s = \Delta f = \frac{2v \sin \varphi}{\lambda} \tag{9.1}$$

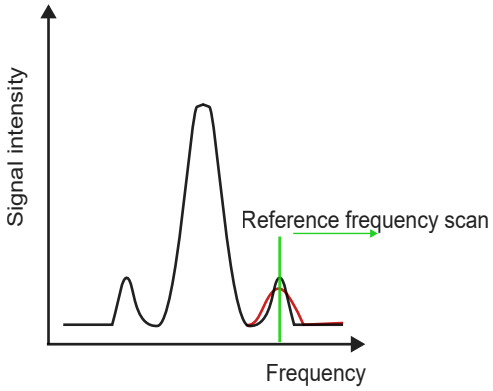


Figure 9.1: Frequency scanning for the flow rate and its effects on decorrelation. The frequency scan broadens the bandwidth of the frequency which is the red band.

The decorrelation time could be estimated using the interception of the half-width at half-maximum (HWHM) with the frequency scan profile of the signal band. The decorrelation time, $dt = \frac{1}{\Delta f}$, where Δf is the frequency value of the interception.

In this study, the aim was to link flow rate of scattering liquid (milk) with speckle decorrelation using 4-phase digital holography integrated with acousto-optic modulation. This advanced approach allows us to use AOT to evaluate flow rate in biological media. By combining acousto-optic signals with the capabilities of digital holography, we can achieve measurements of the frequency spectrum that characterises the fluid motion, offering knowledge into the measurement of decorrelation times [211].

9.2 Materials and methods

This section makes use of the method discussed in Chapter 7. In this chapter, the application of digital holography is used to find the decorrelation times of flowing milk through a tube. The experiment made use of a 1 m long tube in 3 cm thick clear agar phantom as in Figure 7.1 and the siphon principle was applied to vary the rate of flow of milk through the tube. The undiluted milk had a reduced optical scattering was about 18 cm^{-1}. This was measured with a time of flight (TOF) system demonstrated in Chapter 8. The milk was then diluted to obtain reduced optical scattering of 6 cm^{-1} for the flow experiment.

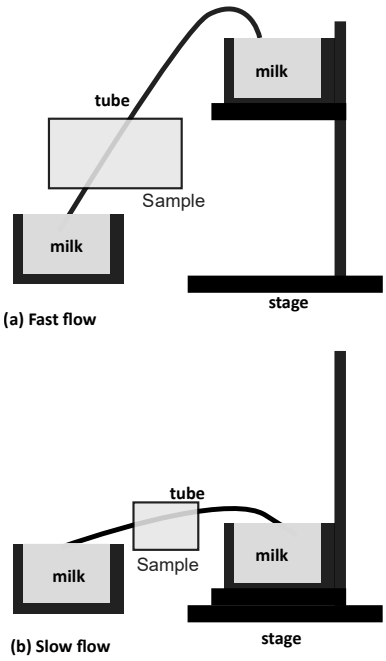


Figure 9.2: Using the siphoning principle to ensure different flow conditions: (a) fast flow condition (3 $m\,s^{-1}$), (b) slow flow condition (1.7 $m\,s^{-1}$).

The data collected were for a state of no flow of the milk, fast flow (3 $m\,s^{-1}$) of the milk and slow flow (1.7 $m\,s^{-1}$) of the milk as shown in Figure 9.2 (a) and (b) respectively. The signal collected was the ultrasound-tagged light intensity with using the frequency shift of the reference beam from 0 kHz to 700 kHz.

9.3 Results

The holographic representation of the signal within the aperture is shown in Figure 9.3 which is the mean image

of 200 images. The black annotated area within the image represents the tube region in the agar. Only the last 900 points along the DX axis and the 300 to 500 range along DY were used in the signal processing. This data is represented in Figure 9.4 where it shows the mean of the signal intensity with an exponential fit. The intensity values in Figure 9.5 was then calculated by subtracting the area under the exponential curve within the tube region from each acquired intensity value in order to calculate the mean intensity and the standard error within the tube. This is repeated for the measurement of all the different frequencies and the different flows. Figure 9.5 also shows the frequency scanned from 0 kHz to 700 kHz for a condition of no flow of milk, slow flow and fast flow of the milk.

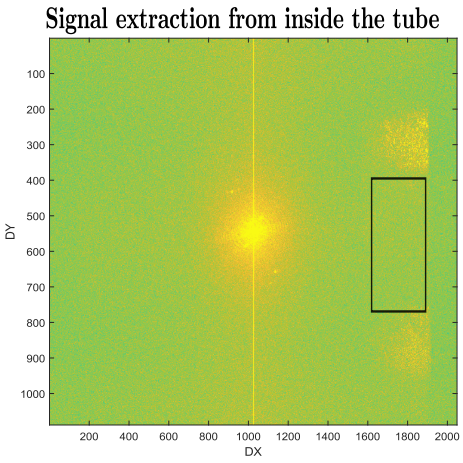


Figure 9.3: Holographic signal of flowing milk (fluid). The black box represent the location of the tube embedded in the clear agar block. The signals above and below this box is out of the tube region. This is the mean of 200 images.

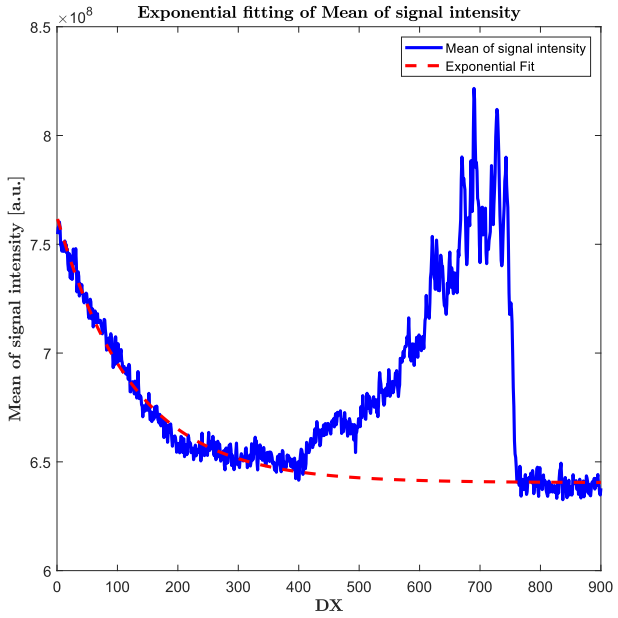


Figure 9.4: Fitting of the sum of the pixel values in the tube region to find the background signal of the camera.

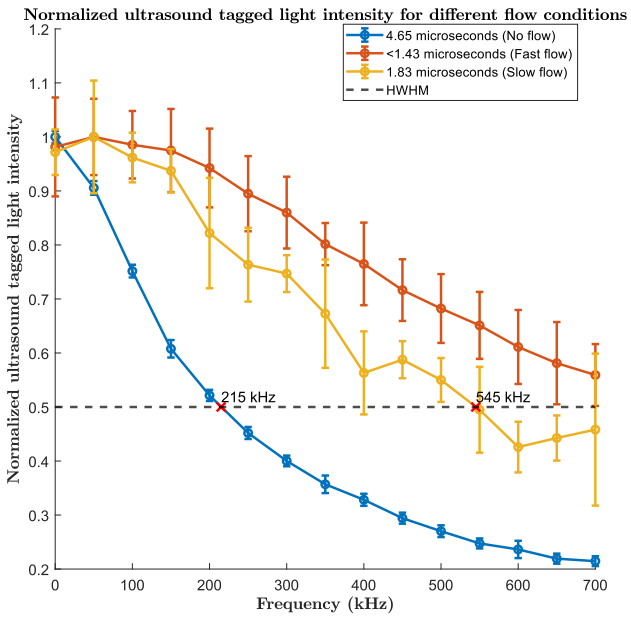


Figure 9.5: Frequency scanned normalized ultrasound tagged signal for different flow conditions. The blue curve signifies the no flow condition which shows little broadening of the signal as compared to the slow flow and fast flow. For the decorrelation time calculated from half-with at half maximum (HWHM) of the tagged signal, then the time for no flow is 4.65 µs, it is 1.83 µs at 1.7 m s^{-1} and at 3 m s^{-1}, it is less than 1.43 µs.

9.4 Discussion and conclusion

The relationship between speckle decorrelation and the probing frequency of the reference beam is determined using the flow rate of milk. The ultrasound-tagged light intensity was collected over a range of frequency scanned. This result is shown in Figure 9.5 of how the decorrelation time calculated from the half width at half maximum (HWHM) as the inverse of the intercepted frequencies $\left(dt = \frac{1}{\Delta f}\right)$. These intercepted frequencies were (215 kHz, 545 kHz and over 700 kHz). The corresponding flow speeds respectively associated with these frequencies were 0 m s^{-1} (No flow), 1.7 m s^{-1} (Slow flow) and over 3 m s^{-1} (Fast flow). Here, these frequencies correspond to decorrelation times of 4.65 µs, 1.83 µs and less than 1.43 µs respectively based on the respective speeds. This trend is consistent with theoretical predictions and previous empirical studies, where faster-moving scatterers within a tissue sample led to a quicker decorrelation of the speckle patterns [211]. The results are indicative of the enhanced mixing and interactions among the scatterers, predominantly the fat globules and proteins within milk that occur at higher flow velocities as in the case of this investigation.

The application of acousto-optic modulation in conjunction with digital holography has been used to study the flow speed of fluids. By integrating these technologies, we can obtain a

more detailed and comprehensive analysis of fluid dynamics, beyond what is achievable with traditional laser Doppler or speckle methods alone. This integration not only enhances measurement accuracy but also provides a broader range of diagnostic capabilities, from assessing fluid viscosity to detecting anomalies in flow patterns. An associated study has used laser speckle imaging to achieve these measurement however, they are suitable for ex vivo and tissue surface applications [212] .

This study has successfully extended the application of acousto-optical techniques combined with digital holography to measure the decorrelation times of milk under varying flow conditions. The findings confirm that this integrated approach can effectively characterize the dynamic properties of fluids, offering a powerful tool for real-time and non-invasive analysis. The ability to measure decorrelation times with high precision opens new avenues for acousto-optics in biological tissues.

The implications of these findings are broad, ranging from enhancing the understanding of complex fluid behaviours in biomedical contexts to improving industrial processes in food production. Future studies should aim to refine these techniques further, exploring their applicability across different types of complex fluids and under variable environmental conditions. Additionally, scaling this technology for industrial applications could revolutionize process monitoring and quality assurance in various sectors, showcasing the potential of integrating advanced optical techniques in practical, real-world settings.

Discussion and conclusion of the thesis

10

This thesis has explored two essential techniques to obtain diagnostic information based on tissue optical properties. These techniques are diffuse reflectance spectroscopy (DRS) and acousto-optic interactions in biological tissues using digital holographic methods. Each chapter of this work has contributed to the understanding and application of these technologies and how useful they can be in medical imaging, diagnostics, and therapeutic strategies. Now, in this chapter, the following discussion dwells on works done in CRC and how DRS fits in the perspective of tumor detection. The chapter further discusses acousto optic techniques and new trends in relation to the results of this thesis. Finally, a conclusion of the thesis is drawn.

10.1 Diffuse Reflectance Spectroscopy for Colorectal Cancer 117
10.2 Acousto-Optics and Digital Holography in decorrelation and Flow Monitoring 120
10.3 Conclusion 122

10.1 Diffuse Reflectance Spectroscopy for Colorectal Cancer

As it stands now (in 2024), surgery is the most efficient method of treating a person suffering from colorectal cancer. The overall survival rate after 5 year of diagnosis and treatment has a success rate of over 80 % to 90 % in stage I and II colon cancer. This declines to 68 % to 72 % in the case of stage III and 11 % to 14 % in stage IV metastatic colorectal cancer [213]. This indicates that early detection of CRC is of ultimate importance. Also, during surgery, it is of essence to be mindful of tumor margins in order to spare healthy tissue as well. Typically, surgery could then be followed by chemotherapy to ensure efficient eradication of cancerous cells [214]. The state-of-the- art is pushing towards robotic or minimally invasive surgical interventions, as well as precision in tumor identification in cancer staging and treatment [215]. This target could be achieved through current computing powers, artificial intelligence and deep machine learning algorithms. Other diagnostic mechanisms include the use of liquid biopsy, physical review, colonoscopy and in general, different treatment methods are tailored to different patients.

Furthermore, the early detection of of CRC could be precipitated by monitoring of predictive biomarkers such as molecular biomarkers which has to do with the gene alterations [214, 216]. The monitoring could also be feasible through liquid biopsies of circulating biomarkers like the circulating tumor Deoxyribonucleic Acid (ctDNA) or tumor cells [217, 218]. In addition to that, the epigenetic biomarkers could be monitored through blood, tissue samples and stool of patients.

In line with the above assertion, the studies conducted in Paper II and Paper III take a complementary approach to the study of CRC detection using biomolecular composition like β-carotene, bile, bilirubin, ceroid, collagen, de-oxyhaemoglobin (Hb), oxyhaemoglobin (HbO2), methaemoglobin (MetHb), water, lipid, and melanin. This study makes use of two different sizes of probes to distinguish tumor and healthy tissues. This was achieved by the use of binary decision tree and for both probes, the parameters of interest were lipid, amplitude of reduced scattering coefficient, and Mie scattering power. In addition to that, tissue identification using Hb and HbO2 data could be determined with wavelength ranges from 350 to 590 nm or 600 to 1230 nm for superficial tissue (short-SDD probe), and 380 to 400 nm, 420 to 610 nm, and 650 to 950 nm for deeper tissue layers (long-SDD probe). The wavelength sensitivity of DRS in this classification is demonstrated in Paper I. It was noticed that probing superficial tissue (with short-SDD probe) yielded (93.5 ± 2.4)% sensitivity, (94.0 ± 1.7)% specificity, and 0.971 ± 0.014 AUROC, while sampling deeper tissue layers (with long-SDD probe) yielded (96.1 ± 1.8)% sensitivity, (95.7 ± 0.6)% specificity, and 0.987 ± 0.005 AUROC. These results are comparable to that achieved by colonoscopy and CT colonography [219]. Some recent works on spectroscopic studies of CRC has also utilised Raman spectroscopy. These studies have targeted domains like Liquid biopsy, endoscopy for in vivo applications and micro-spectroscopic studies for tissue biopsies [219]. The work done in the use of laser induced fluorescence and Raman spectra for CRC diagnosis yielded a diagnostic accuracy of 88 % and 83 % [220–222].

There have been related studies that considered the NIR region for colorectal cancer detection [223, 224]. The study in this thesis takes an additional approach to this by exploring the inclusion of the visible spectral range in the enhancement

of the sensitivity and specificity. The results in this study is an interpretation acquired from over 2889 spectra which goes beyond the sample sizes compared in some of the past studies [219]. The new trend of spectroscopic work has to do with the use of indocyanine green (ICG), machine learning capabilities and fluorescence guided surgery [224]. This study in particular [224] focuses on the use of intraoperative near-infrared (NIR) functional imaging, specifically utilizing indocyanine green (ICG) perfusion characterization, to enhance the detection and discrimination of rectal cancer during surgical procedures. Using AI decision-making tools and models, the study correlates ICG retention with factors like permeability and angiogenesis, which are critical in cancer diagnostics. The methods presented achieved approximately 90 % accuracy in distinguishing significant rectal polyps and small cancers from normal tissue. This was accomplished by extracting ICG curve features that reflect the wash-in and wash-out phases of ICG from intraoperative imaging. The wash-in phase refers to the time it takes for ICG to enter the tissue and bind to plasma proteins, while the wash-out phase describes how quickly the dye is cleared from the tissue. With regards to this thesis, such degree of detection accuracy has been attained without the use of external agents like ICG thereby avoiding extra unwanted outcomes such as allergies to ICG, report of transient visual disturbance by patients as well as potential overdose.

This thesis established the foundation for understanding diffuse reflectance spectroscopy (DRS) using the Kubelka-Munk model in Chapter 3. It then shifted to the practical application of DRS in colorectal cancer surgeries. By analysing over 2889 spectral data from 47 patients, the study demonstrated the efficacy of DRS in distinguishing between healthy and malignant tissues. The results showed the real-time potential of DRS to enhance surgical precision, minimizing the removal of healthy tissue and improving patient outcomes. The spectral data, spanning visible to near-infrared wavelengths, provided insights into the optical properties of tissues and identified biomarkers linked to tumor development. In Chapter 6, machine learning algorithms were used to extract and analyse DRS-based information, significantly improving the diagnostic accuracy of DRS by identifying subtle differences between healthy and malignant tissues. The study also explored the use of small and large probes, as shown in Figure 6.3 (a) and (b), revealing trends with dif-

ferences in spread and median values, likely due to varying probing depths. These boxplots are essential for understanding the distinct optical properties of tissue types, which could enhance the accuracy of tissue classification during surgery, aiding in precise tumor removal while conserving healthy tissue with the help of artificial intelligence.

10.2 Acousto-Optics and Digital Holography in decorrelation and Flow Monitoring

In this work, acousto-optics and digital holography were employed to investigate viscosity changes in scattering media, and the relationship between flow speed and acousto-optic signals detected with 4-phase digital holography. These techniques hold potential for diagnosing medical conditions related to blood flow and viscosity changes, such as in cardiovascular diseases, coagulation disorders, and circulatory problems. By combining acousto-optic principles with digital holography, a framework for non-invasive, real-time monitoring of biological processes in deep tissues is established.

During coagulation, blood transitions from a liquid to a gel-like solid. This process can potentially be monitored using acousto-optics. Hence, AOT could be a valuable tool for non invasively diagnosing conditions like thrombosis or disseminated intravascular coagulation (DIC), where abnormal clot formation presents life-threatening risks [191, 225]. AOT offers a non-invasive alternative to traditional techniques like thromboelastography (TEG), which rely on blood samples of significant volumes. Real-time monitoring of blood coagulation using holography can provide timely insights during surgeries, trauma care, or anticoagulant therapy, potentially improving patient well-being.

The acousto-optic method used here modulates light with ultrasound to enable localized, viscosity change sensing in specific regions. This is particularly valuable in diagnosing diseases where blood viscosity plays an important role, such as hyper-viscosity syndrome, diabetes, and atherosclerosis [226, 227]. Elevated blood viscosity increases resistance to flow, impairing tissue perfusion and raising the risk of clot formation. In conditions like hypertension and heart failure,

real-time blood viscosity monitoring offers early warning signs and could guide therapeutic interventions. Traditional methods for measuring blood viscosity, such as rotational viscometers, are ex vivo and invasive. By contrast, the techniques demonstrated in this work lay the groundwork for quasi in vivo, non-invasive monitoring, potentially offering continuous insights into blood viscosity dynamics. Although the significant difference observed between samples could be due to optical variations than solely viscosity changes, it is recommended that future attempt to improve this could make use of PEGylation techniques to ensure there is no optical variations due to aggregation of scattering particles between samples of different viscosities. By doing this, the influence of viscosity on the acousto-optical signals could be isolated.

An essential component of this research is the relationship between flow speed and acousto-optic signals, as detected by 4-phase digital holography. Using milk as a model fluid, the study offers insights into the correlation between flow speed and acousto-optic responses, as shown in Figure 9.5. The result underpins the rate of decorrelation to the frequency broadening of the holographically detected signals. Understanding this relationship could offer interesting insights into developing new techniques for diagnosing condition associated with abnormal blood flow, such as arterial stenosis or vascular occlusion [228, 229]. By analysing flow speed, one can infer the presence of blockages or abnormalities in blood vessels, potentially predicting events like stroke or myocardial infarction. Digital holography thus provides a non-invasive tool for real-time haemodynamic assessment.

The applications of flow speed monitoring extend to a range of medical contexts. For instance, in cerebral blood flow monitoring, real-time assessments of flow speed and viscosity can aid in treating conditions such as traumatic brain injury or cerebral aneurysms, where blood flow abnormalities critically impact patient's health. Traditional techniques like ultrasound imaging and fluorescence-based methods are often used to monitor clotting in vivo. The methods demonstrated in this work could complement these approaches, particularly for monitoring flow dynamics in larger vessels, such as the carotid artery, where reduced flow speed might indicate stenosis or other vascular issues.

Wearable devices for measuring blood viscosity and flow are

gaining popularity due to advancements in sensor technology and the growing emphasis on personal health monitoring. These devices use miniaturized sensors and microfluidic systems to provide non-invasive or minimally invasive assessments, allowing users to monitor blood viscosity in real time. The integration of wearable technology with mobile health applications enhances user engagement, facilitating data visualization, alerts, and easy sharing with healthcare providers. As research improves the accuracy and reliability of these technologies, the market for wearable health devices is expanding, reflecting a shift toward proactive health management and personalized care solutions. The work presented in this thesis could complement and validate state-of-the-art wearable sensor technologies by offering foundational insights into flow and viscosity dynamics.

The integration of acousto-optics and digital holography thereby offers a novel and non-invasive approach for assessing blood viscosity, flow dynamics, and viscoelastic transitions. These techniques represent significant advances in diagnostic methodologies, especially for early detection and management of cardiovascular diseases, coagulopathies, and circulatory disorders. Real-time monitoring of blood-like properties, as demonstrated in this study, has the potential to revolutionize patient care by enabling continuous, in vivo measurements essential for timely medical interventions. Although this research did not explicitly use blood (opting for aqueous glycerol and milk as model fluids), it lays the groundwork for future studies to incorporate non-Newtonian fluids like blood, where shear rate effects play a significant role.

10.3 Conclusion

The thesis presents two distinct yet complementary techniques: Diffuse Reflectance Spectroscopy (DRS) and Acousto-Optic (AO) methods. When these methods are integrated, the combined advantage could overcome critical challenges in medical diagnostics, particularly for deep tissue imaging. DRS, with its high sensitivity to tissue composition, excels at providing molecular-level information non-invasively. This makes it particularly effective for distinguishing between

different tissue types based on their unique optical properties. However, due to the limitations of light scattering within tissues, DRS struggles to deliver accurate diagnostic information from deeper tissue layers.

In contrast, acousto-optic techniques, which rely on ultrasound, allow for greater depth penetration due to the reduced scattering of acoustic waves in biological media. Pure acoustic methods are adept at providing structural and mechanical information about tissues, such as stiffness and elasticity, but they lack the molecular sensitivity that AOT and DRS offer. The advantage of DRS compared to AOT is the speed at which data is acquired however, the disadvantage of DRS compared to AOT is the poor penetration depth. The two techniques thus complement each other: where DRS falls short in depth, acousto-optics (AO) can extend the reach of diagnostic capabilities, and where AO lacks speed, DRS can fill the gap.

The potential merger of these two approaches could lead to major advancements in non-invasive medical imaging and diagnostics. By combining the molecular diagnostic strengths of DRS with the depth and resolution advantages of AO, it would be possible to achieve detailed, and comprehensive imaging of biological tissues especially with an AO detection method like spectral hole burning (with possible breakthrough in crystal technologies). For instance, in applications such as cancer detection or surgical guidance, this combination could offer better insights into both the structural and molecular characteristics of tissues at greater depths within considerable time range, providing clinicians with a deeper understanding of diseases.

While this thesis does not integrate the two techniques directly, it lays the groundwork for future studies that could explore the merging of DRS and AO. When brought together, these methods could revolutionize the way deep tissue diagnostics are performed, overcoming the limitations of each technique when used in isolation and enhancing the accuracy, depth, and quality of medical imaging.

11 Personal reflections

Light is so ubiquitous that imagining its endless potential could take an eternity. This thesis contributes to the many ways in which light has been beneficial to humanity. Conducting fundamental experiments in hospital environments highlighted the practical potential of DRS, especially when considering that, ultimately, a patient's life could be improved. This instilled in me a deep sense of contributing meaningfully to life. On another front, the study of acousto-optic (AO) interactions fosters hope for better imaging modalities in the future. Becoming familiar with the AO lab and constructing experimental setups has been therapeutic in itself. I look forward to the continuation of this study, particularly the development of diffuse reflectance imaging enhanced by ultrasound engineering to probe tissue in depth and provide direct spectroscopic information.

Undertaking this study has not only expanded my understanding of the usefulness of light and mechanical waves in biological media, but it has also been a challenge that cultivated important life skills. These include the ability to stay focused and determined during turbulent times, and to maintain emotional balance throughout.

In the early stages of my PhD especially up to my second year, I was learning how to adapt. I promptly completed all my mandatory coursework. Over the period of my studies, I worked as a teaching assistant for two years, during which I interacted with many students. It reminded me of my undergraduate years. In secondary school in Ghana, I studied Geography, Economics, and Mathematics, but my passion always lay in the Sciences. Although I was not placed in a Science-based school, I was determined to study Physics and Chemistry independently after secondary school, drawing inspiration from the everyday practical work I observed around me. Fortunately, when I applied to the University of Cape Coast (UCC) in Ghana, the only requirement for admission to study Engineering Physics was a strong mathematical background. I was admitted, graduated, and immediately became a teaching assistant, where I enthusiastically supported many students. This personal journey enabled me

to deeply connect with my students at University College Cork (UCC). I took special interest in preparing tutorials and experimental demonstrations for them.

I vividly remember my first experience in an optical lab during my PhD, where we had to build everything from the ground up. The challenge of acquiring new equipment without being fully certain it would meet our needs was daunting. I received invaluable support from Baptiste Jayet, who created a clear path for me. I often say that without him, I would have been like someone who can't swim being dropped in the middle of the ocean. One of the emotional challenges was dealing with expensive equipment that needed frequent troubleshooting, all while staying mindful of academic deadlines. These experiences were part of the broader PhD journey, which has equipped me to face real-life challenges in the professional world.

Embarking on a PhD is a formidable challenge under normal circumstances, but mine was further complicated by the COVID-19 pandemic. The two research domains I worked in required rigorous experimentation, meticulous data analysis, and consistent collaboration with peers and advisors: tasks that became significantly more difficult during the global health crisis. For example, hospital access was restricted, leading to the abrupt cancellation of several DRS experimental plans. Despite these challenges, I received steadfast support from my team and supervisor, Professor Stefan Andersson-Engels, which ensured that work progressed effectively. This experience taught me the value of working in an environment of support, togetherness, and harmony. Thanks to this unique atmosphere, I was able to successfully build an ultrasound-tagged light detection setup and conduct multiple experiments, while also contributing to the writing of published articles on DRS.

The early days of the pandemic were marked by profound uncertainty. The psychological impact, coupled with the isolation of remote work, tested my resilience and determination. To maintain momentum, I had to develop new routines and strategies. Creating a disciplined daily schedule helped mitigate the blurring lines between work and personal life. One of the most important lessons from this period was the value of adaptability and psychological resilience. The pandemic forced me to overcome a wide range of emotional

and logistical challenges. Staying connected with the academic community through virtual conferences and webinars provided intellectual stimulation and kept me abreast of the latest developments in my field. Engaging with the broader scientific community online fostered a sense of solidarity and shared purpose.

In conclusion, my PhD journey during the COVID-19 pandemic demonstrated the power of determination and adaptability. The challenges I encountered required innovation and perseverance, ultimately enriching both my research and personal growth. This experience has prepared me to navigate future scientific endeavors with purpose and unwavering commitment—whether in academia or in practical, industrial environments.

Bibliography

Here are the references in citation order.

[1] Alexander Bengtsson et al. 'Characterization and modeling of acousto-optic signal strengths in highly scattering media'. In: *Biomed. Opt. Express* 10.11 (Nov. 2019), pp. 5565–5584. DOI: 10.1364/BOE.10.005565 (cited on page 2).

[2] Daniel Elson et al. 'Ultrasound-mediated optical tomography: A review of current methods'. In: *Interface focus* 1 (Aug. 2011), pp. 632–648. DOI: 10.1098/rsfs.2011.0021 (cited on pages 2, 3).

[3] V. Ntziachristos and B. Chance. 'Breast imaging technology: Probing physiology and molecular function using optical imaging - applications to breast cancer'. In: *Breast Cancer Res* 3.1 (2000), pp. 41–46. DOI: 10.1186/bcr269 (cited on page 2).

[4] A. P. Mosk et al. 'Controlling waves in space and time for imaging and focusing in complex media'. In: *Nature Photon* 6.5 (2012), pp. 283–292 (cited on page 3).

[5] V. Ntziachristos. 'Going deeper than microscopy: the optical imaging frontier in biology'. In: *Nature Methods* 7.8 (2010), pp. 603–614. DOI: 10.1038/nmeth.1483 (cited on page 3).

[6] J. Fujimoto. 'Optical coherence tomography for ultrahigh resolution in vivo imaging'. In: *Nat Biotechnol* 21.11 (2003), pp. 1361–1367 (cited on page 3).

[7] D. Huang et al. 'Optical coherence tomography'. In: *Science* 254.5035 (1991), pp. 1178–1181. DOI: 10.1126/science.1957169 (cited on page 3).

[8] C. Kim, C. Favazza, and L. V. Wang. 'In Vivo Photoacoustic Tomography of Chemicals: High-Resolution Functional and Molecular Optical Imaging at New Depths'. In: *Chemical Reviews* 110.5 (2010), pp. 2756–2782. DOI: 10.1021/cr900266s (cited on page 3).

[9] F. Helmchen and W. Denk. 'Deep tissue two-photon microscopy'. In: *Nat Methods* 2.12 (2005), pp. 932–940 (cited on page 3).

[10] L. Fu et al. 'Nonlinear optical endoscopy based on a double-clad photonic crystal fiber and a MEMS mirror'. In: *Opt. Express* 14.3 (Feb. 2006), pp. 1027–1032. DOI: 10.1364/OE.14.001027 (cited on page 3).

[11] T. Čižmár. 'Exploiting multimode waveguides for in vivo imaging'. In: *SPIE Newsroom accessed on 03.10.2022* (2015) (cited on page 3).

[12] C. A. DiMarzio and T. W Murray. 'Medical imaging techniques combining light and ultrasound.' In: *Subsurface Sens. Technol. Appl* 4.1 (2003), pp. 289–309 (cited on page 3).

[13] L. V. Wang. 'Ultrasound-mediated biophotonic imaging: a review of acousto-optical tomography and photo-acoustic tomography'. In: *Disease Markers* 19.2-3 (2003-2004), pp. 123–138 (cited on page 3).

[14] Y. E. Chung and K. W. Kim. 'Contrast-enhanced ultrasonography: advance and current status in abdominal imaging'. In: *Ultrasonography* 34.1 (2015), pp. 3–18 (cited on page 4).

[15] G. P. Luke, D. Yeager, and S. Y. Emelianov. 'Biomedical Applications of Photoacoustic Imaging with Exogenous Contrast Agents'. In: *Ann Biomed Eng* 40.1 (2012), pp. 422–437 (cited on page 4).

[16] Jorge Ripoll Lorenzo. *Principles of Diffuse Light Propagation: Light Propagation in Tissues with Applications in Biology and Medicine Hardcover*. World Scientific Publishing Company; 1st edition, 2012 (cited on pages 9, 13, 15, 17).

[17] Igor Mokhun et al. 'Experimental analysis of the Poynting vector characteristics'. In: *Appl. Opt.* 51.10 (Apr. 2012), pp. C158–C162. DOI: 10.1364/AO.51.00C158 (cited on page 10).

[18] Max Born, Emil Wolf, and A. B. Bhatia. *Principles of Optics: Electromagnetic Theory of Propagation, Interference and Diffraction of Light*. Cambridge University Press, 1999 (cited on page 11).

[19] Fabrizio Martelli et al. *Light Propagation through Biological Tissue and Other Diffusive Media: Theory, Solutions, and Software*. 2009 (cited on pages 17–19).

[20] Lin Wang et al. 'Harnessing the Power of Hybrid Light Propagation Model for Three-Dimensional Optical Imaging in Cancer Detection'. In: *Frontiers in Oncology* 11 (2021). DOI: 10.3389/fonc.2021.750764 (cited on page 17).

[21] Akira Ishimaru. *Wave Propagation and Scattering in Random Media*. Academic Press, New York, 1978 (cited on page 17).

[22] J.L. Sandell and T.C. Zhu. 'A review of in-vivo optical properties of human tissues and its impact on PDT'. In: *J Biophotonics* 4.11–12 (2011), pp. 773–787. DOI: 10.1002/jbio.201100062 (cited on page 18).

[23] J. Lee et al. 'Design and Implementation of Embedded-Based Vein Image Processing System with Enhanced Denoising Capabilities'. In: *Sensors (Basel)* 22.21 (2022), p. 8559. DOI: 10.3390/s22218559 (cited on page 23).

[24] D. J. Parekh, W. Lin, and S. D. Herrell. 'Optical spectroscopy characteristics can differentiate benign and malignant renal tissues: a potentially useful modality'. In: *Journal of Urology* 174.5 (2005), pp. 1754–1758. DOI: 10.1097/01.ju.0000177484.33596.c9 (cited on page 29).

[25] Y. Ti, P. Chen, and W. Lin. 'In vivo characterization of myocardial infarction using fluorescence and diffuse reflectance spectroscopy'. In: *Journal of Biomedical Optics* 15.3 (2010), p. 037009. DOI: 10.1117/1.3442505 (cited on page 29).

[26] Lin W.C. et al. 'Diffuse reflectance spectroscopy for in vivo pediatric brain tumor detection'. In: *Journal of Biomedical Optics* 15.6 (2010), p. 061709. DOI: 10.1117/1.3505012 (cited on page 29).

[27] Lin W.C. and Song Yinchen. 'Interoperative guidance system for tumor surgery'. US 20170164837 A1. U.S. Patent and Trademark Office. June 2017 (cited on page 29).

[28] Bing Yu et al. 'Diffuse reflectance spectroscopy with a self-calibrating fiber optic probe'. In: *Opt. Lett.* 33.16 (Aug. 2008), pp. 1783–1785. DOI: 10.1364/OL.33.001783 (cited on page 29).

[29] Yu B., Fu H.L., and Ramanujam N. 'Instrument independent diffuse reflectance spectroscopy'. In: *J Biomed Opt* 16.1 (2011), p. 011010. DOI: 10.1117/1.3524303 (cited on page 29).

[30] Yu Bing, Ramanujan N., and Lo J. Y. 'Diffuse reflectance spectroscopy device for quantifying tissue absorption and scattering'. US 20110105865 A1. U.S. Patent and Trademark Office. May 2011 (cited on page 29).

[31] Ramanujam N. and Liu Q. 'Scaling Method For Fast Monte Carlo Simulation Of Diffuse Reflectance Spectra From Multi-Layered Turbid Media And Methods And Systems For Using Same To Determine Optical Properties Of Multi-Layered Turbid Medium From Measured Diffuse Reflectance'. US 20080270091 A1. U.S. Patent and Trademark Office. Oct. 2008 (cited on page 30).

[32] Ramanujam N. and Palmer G. M. 'Method For Extraction Of Optical Properties From Diffuse Reflectance Spectra'. US 7570988 B2. U.S. Patent and Trademark Office. Aug. 2009 (cited on page 30).

[33] Zoya I. Volynskaya et al. 'Diagnosing breast cancer using diffuse reflectance spectroscopy and intrinsic fluorescence spectroscopy'. In: *Journal of Biomedical Optics* 13.2 (2008), p. 024012. DOI: 10.1117/1.2909672 (cited on page 30).

[34] Messerschmidt R. G. and Sting D. W. 'Diffuse Reflectance Spectroscopy System And Method'. US 4859064 A. U.S. Patent and Trademark Office. Aug. 1989 (cited on page 30).

[35] Messerschmidt R. G. and Robinson M. R. 'Diffuse Reflectance Monitoring Apparatus'. US 6230034 B1. U.S. Patent and Trademark Office. May 2001 (cited on page 30).

[36] F. Stelzle et al. 'Optical nerve detection by diffuse reflectance spectroscopy for feedback controlled oral and maxillofacial laser surgery'. In: *Journal of Translational Medicine* 9.1 (2011), pp. 70–82. DOI: 10.1186/1479-5876-9-20 (cited on page 30).

[37] Florian Stelzle et al. 'In Vivo Optical Tissue Differentiation by Diffuse Reflectance Spectroscopy: Preliminary Results for Tissue-Specific Laser Surgery'. In: *Surgical Innovation* 19.4 (2012). PMID: 22344924, pp. 385–393. DOI: 10.1177/1553350611429692 (cited on page 30).

[38] Salmon Landi et al. 'Use and misuse of the Kubelka-Munk function to obtain the band gap energy from diffuse reflectance measurements'. In: *Solid State Communications* 341 (2022), p. 114573. DOI: https://doi.org/10.1016/j.ssc.2021.114573 (cited on pages 31, 32).

[39] R. Alcaraz de la Osa et al. 'The extended Kubelka–Munk theory and its application to spectroscopy'. In: *ChemTexts* 6.2 (2020), p. 14862. DOI: /10.1007/s40828-019-0097-0 (cited on page 31).

[40] R.W. Frei. *Diffuse Reflectance Spectroscopy Environmental Problem Solving*. CRC Press, 2019 (cited on pages 32, 34).

[41] Marcelo Saito Nogueira et al. 'Diffuse reflectance spectroscopy for colorectal cancer surgical guidance: towards real-time tissue characterization and new biomarkers'. In: *Analyst* 149.1 (2024), pp. 88–99 (cited on pages 33, 34, 79, 81, 82).

[42] Liang Lim et al. 'Probe pressure effects on human skin diffuse reflectance and fluorescence spectroscopy measurements'. In: *Journal of Biomedical Optics* 16.1 (2011), p. 011012. DOI: 10.1117/1.3525288 (cited on page 35).

[43] Ricky Hennessy et al. 'Effect of probe geometry and optical properties on the sampling depth for diffuse reflectance spectroscopy'. In: *Journal of Biomedical Optics* 19.10 (2014), p. 107002. DOI: 10.1117/1.JBO.19.10.107002 (cited on page 35).

[44] Haim Azhari. *Basics of Biomedical Ultrasound for Engineers*. John Wiley & Sons, Inc., 2010 (cited on pages 38, 41–43).

[45] Kinsler L.E. and Frey P. *Fundamentals of Acoustics*. John Wiley & Sons, New York, 1962 (cited on page 41).

[46] L. Brillouin. 'Diffusion de la lumidre et des rayons X par un corps transparent homogdne'. In: *Ann. Phys. (Paris)* 17 (1922), pp. 8–122 (cited on page 45).

[47] R. Lucas and P. Biquard. 'Propriétés optiques des milieux solides et liquides soumis aux vibration glastiques ultra sonores'. In: *J. Phys. Rad.* 3 (1932), pp. 464–477 (cited on page 45).

[48] P. Debye and F. W. Sears. 'On the scattering of light by supersonic waves'. In: *Proc. Nut. Acad. Sci. (US.)* 18 (1932), pp. 464–477 (cited on page 45).

[49] Aner Lev and Bruno Sfez. 'In vivo demonstration of the ultrasound-modulated light technique'. In: *J. Opt. Soc. Am. A* 20.12 (Dec. 2003), pp. 2347–2354. DOI: 10.1364/JOSAA.20.002347 (cited on pages 45, 111).

[50] W. Leutz and G. Maret. 'Ultrasonic modulation of multiply scattered light'. In: *Physica B: Condensed Matter* 204.1 (1995), pp. 14–19. DOI: https://doi.org/10.1016/0921-4526(94)00238-Q (cited on pages 46, 49, 50, 52, 64).

[51] L.V. Wang. 'Mechanisms of ultrasonic modulation of multiply scattered coherent light: a Monte Carlo model'. In: *Opt. Lett.* 26.15 (Aug. 2001), pp. 1191–1193. DOI: 10.1364/OL.26.001191 (cited on pages 46, 52, 53).

[52] L. V. Wang. 'Mechanisms of Ultrasonic Modulation of Multiply Scattered Coherent Light: An Analytic Model'. In: *Phys. Rev. Lett.* 87 (4 July 2001), p. 043903 (cited on pages 46, 52, 53).

[53] Max Born and Emil Wolf. *Principles of optics: electromagnetic theory of propagation, interference and diffraction of light*. Elsevier, 2013 (cited on page 46).

[54] Yujia Huang et al. 'Investigating ultrasound–light interaction in scattering media'. In: *Journal of Biomedical Optics* 25.2 (2020), p. 025002. DOI: 10.1117/1.JBO.25.2.025002 (cited on pages 47, 107, 108).

[55] Ajoy Kumar Ghatak and K. Thyagarajan. *Optical Electronics*. Cambridge University Press, 1989, pp. 519–545 (cited on pages 47–49).

[56] Adam Kinos. *Frequency shifting of light via multiple ultrasound waves in scattering media*. 2024. URL: https://arxiv.org/abs/2409.04182 (cited on pages 47, 48).

[57] G. D. Mahan et al. 'Ultrasonic tagging of light: theory'. In: *Proc Natl Acad Sci USA* 24.95 (1998), pp. 14015–14019. DOI: https://www.pnas.org/doi/abs/10.1073/pnas.95.24.14015 (cited on page 49).

[58] M. Gross et al. 'Detection of the tagged or untagged photons in acousto-optic imaging of thick highly scattering media by photorefractive adaptive holography'. In: *Eur Phys J E Soft Matter* 2.28 (2009), pp. 173–182. DOI: https://pubmed.ncbi.nlm.nih.gov/19104857/ (cited on pages 49, 100).

[59] David A Weitz and David J Pine. 'Diffusing-wave spectroscopy'. In: *Dynamic Light Scattering* (Jan. 1993), pp. 652–720. DOI: 10.1093/oso/9780198539421.003.0016 (cited on page 51).

[60] J. Gunther and S. Andersson-Engels. 'Review of current methods of acousto-optical tomography for biomedical applications'. In: *Front. Optoelectron* 10 (2017), pp. 211–238 (cited on pages 54, 63, 70).

[61] C. W. Jarrett, C. F. Caskey, and J.C. Gore. 'Detection of a Novel Mechanism of Acousto-Optic Modulation of Incoherent Light'. In: *PLoS ONE* 9.8 (2014) (cited on page 55).

[62] N. T. Huynh et al. ' Ultrasound modulated imaging of luminescence generated within a scattering medium'. In: *J Biomed Opt.* 18.2 (2013) (cited on page 55).

[63] Junaid Ahmad et al. 'Ultrasound-mediation of self-illuminating reporters improves imaging resolution in optically scattering media'. In: *Biomed. Opt. Express* 9.4 (Apr. 2018), pp. 1664–1679. DOI: 10.1364/BOE.9.001664 (cited on page 55).

[64] H.W. Schytz, S. Guo, and L.T. et al. Jensen. 'A New Technology for Detecting Cerebral Blood Flow: A Comparative Study of Ultrasound Tagged NIRS and 133Xe-SPECT'. In: *Neurocrit Care* 17 (2012), pp. 139–145. DOI: 10.1007/s12028-012-9720-2 (cited on page 55).

[65] L. Zhu et al. 'Noninvasive blood glucose measurement by ultrasound-modulated optical technique'. In: *Chin. Opt. Lett.* 11.2 (Feb. 2013), p. 021701 (cited on page 55).

[66] Steffen Resink, Erwin Hondebrink, and Wiendelt Steenbergen. 'Solving the speckle decorrelation challenge in acousto-optic sensing using tandem nanosecond pulses within the ultrasound period'. In: *Opt. Lett.* 39.22 (Nov. 2014), pp. 6486–6489. DOI: 10.1364/OL.39.006486 (cited on page 56).

[67] S. Sakadžić and L. V. Wang. 'High-resolution ultrasound-modulated optical tomography in biological tissues'. In: *Opt. Lett.* 29.23 (Dec. 2004), pp. 2770–2772. DOI: 10.1364/OL.29.002770 (cited on page 56).

[68] M. Lesaffre et al. 'In situ monitoring of the photorefractive response time in a self-adaptive wavefront holography setup developed for acousto-optic imaging'. In: *Opt. Express* 15.3 (Feb. 2007), pp. 1030–1042. DOI: 10.1364/OE.15.001030 (cited on page 56).

[69] A. Cand, J-P. Monchalin, and X. Jia. 'Detection of inplane and out of plane ultrasonic displacements by a two channel confocal Fabry-Perot interferometer'. In: *Applied Physics Letters* 64 (1994), pp. 414–416 (cited on page 56).

[70] G. Rousseau, A. Blouin, and J-P. Monchalin. 'Ultrasound-modulated optical imaging using a high-power pulsed laser and a double-pass confocal Fabry–Perot interferometer'. In: *Opt. Lett.* 34.21 (Nov. 2009), pp. 3445–3447. DOI: 10.1364/OL.34.003445 (cited on page 56).

[71] G. Rousseau, A. Blouin, and J-P. Monchalin. 'Ultrasound-modulated optical imaging using a powerful long pulse laser'. In: *Opt. Express* 16.17 (Aug. 2008), pp. 12577–12590. DOI: 10.1364/OE.16.012577 (cited on page 56).

[72] Youzhi Li et al. 'Detection of ultrasound-modulated diffuse photons using spectral-hole burning'. In: *Opt. Express* 16.19 (Sept. 2008), pp. 14862–14874. DOI: 10.1364/OE.16.014862 (cited on pages 57, 58).

[73] Mattias Nilsson et al. 'Hole-burning techniques for isolation and study of individual hyperfine transitions in inhomogeneously broadened solids demonstrated in Pr^{3+}: Y_2SiO_5'. In: *Phys. Rev. B* 70 (21 Dec. 2004), p. 214116. DOI: 10.1103/PhysRevB.70.214116 (cited on page 57).

[74] Caroline Venet et al. 'Ultrasound-modulated optical tomography in scattering media: flux filtering based on persistent spectral hole burning in the optical diagnosis window'. In: *Opt. Lett.* 43.16 (Aug. 2018), pp. 3993–3996. DOI: 10.1364/OL.43.003993 (cited on pages 57, 59, 101).

[75] Quang Minh Thai et al. 'In vivo ultrasound modulated optical tomography with a persistent spectral hole burning filter'. In: *Biomed. Opt. Express* 13.12 (Dec. 2022), pp. 6484–6496. DOI: 10.1364/BOE.475449 (cited on page 57).

[76] Jacqueline E. Gunther et al. 'Deep tissue imaging with acousto-optical tomography and spectral hole burning with slow light effect: a theoretical study'. In: *Journal of Biomedical Optics* 23.7 (2018), p. 071209. DOI: 10.1117/1.JBO.23.7.071209 (cited on page 57).

[77] R. Purchase and S. Völker. 'Spectral hole burning: examples from photosynthesis'. In: *Photosynth Res* 101 (2009), pp. 245–266. DOI: 10.1007/s11120-009-9484-5 (cited on page 57).

[78] Flurin Könz et al. 'Temperature and concentration dependence of optical dephasing, spectral-hole lifetime, and anisotropic absorption in Eu^{3+}: Y_2SiO_5'. In: *Phys. Rev. B* 68 (8 Aug. 2003), p. 085109. DOI: 10.1103/PhysRevB.68.085109 (cited on page 57).

[79] Li Y. et al. 'Pulsed ultrasound-modulated optical tomography using spectral-hole burning as a narrowband spectral filter'. In: *Appl Phys Lett.* 93.1 (July 2008), p. 11111. DOI: doi:10.1063/1.2952489 (cited on page 58).

[80] A. Bengtsson et al. 'Characterization and modeling of acousto-optic signal strengths in highly scattering media'. In: *Biomedical Optics Express* 10 (11 2019), p. 5565. DOI: 10.1364/boe.10.005565 (cited on page 59).

[81] X. Xu, H. Liu, and L. Wang. 'Time-reversed ultrasonically encoded optical focusing into scattering media'. In: *Nature Photon* 5 (2011), pp. 154–157 (cited on pages 59–61).

[82] Lai P. et al. 'Reflection-mode time-reversed ultrasonically encoded optical focusing into turbid media'. In: *J Biomed Opt.* 16.8 (2011) (cited on page 60).

[83] Suzuki Y. et al. 'Energy enhancement in time-reversed ultrasonically encoded optical focusing using a photorefractive polymer'. In: *J Biomed Opt.* 17.8 (2012) (cited on page 60).

[84] B. Jayet, J.-P. Huignard, and F. Ramaz. 'Optical phase conjugation in Nd:YVO4 for acousto-optic detection in scattering media'. In: *Opt. Lett.* 38.8 (Apr. 2013), pp. 1256–1258. DOI: 10.1364/OL.38.001256 (cited on page 60).

[85] Juze Zhang et al. 'Snapshot time-reversed ultrasonically encoded optical focusing guided by time-reversed photoacoustic wave'. In: *Photoacoustics* 26 (2022), p. 100352. DOI: https://doi.org/10.1016/j.pacs.2022.100352 (cited on page 60).

[86] Ori Katz et al. 'Controlling light in complex media beyond the acoustic diffraction-limit using the acousto-optic transmission matrix'. In: *Nature Communications* 10 (2017) (cited on page 60).

[87] T.W. Murray et al. 'Detection of ultrasound-modulated photons in diffuse media using the photorefractive effect'. In: *Opt. Lett.* 29.21 (Nov. 2004), pp. 2509–2511. DOI: 10.1364/OL.29.002509 (cited on pages 61–63).

[88] F. Ramaz et al. 'Photorefractive detection of tagged photons in ultrasound modulated optical tomography of thick biological tissues'. In: *Opt. Express* 12.22 (Nov. 2004), pp. 5469–5474. DOI: 10.1364/OPEX.12.005469 (cited on pages 61, 63, 64).

[89] M. Gross et al. 'Theoretical description of the photorefractive detection of the ultrasound modulated photons in scattering media'. In: *Opt. Express* 13.18 (Sept. 2005), pp. 7097–7112. DOI: 10.1364/OPEX.13.007097 (cited on page 61).

[90] Yariv A. 1989 (cited on page 61).

[91] M. Gross. 'Speckle decorrelation in ultrasound-modulated optical tomography made by heterodyne holography'. In: *arXiv preprint* (2016) (cited on page 62).

[92] M. Gross et al. 'Theoretical description of the photorefractive detection of the ultrasound modulated photons in scattering media'. In: *Optics Express* 13.18 (2005), pp. 7097–7112 (cited on page 62).

[93] Salma Farahi et al. 'Time resolved three-dimensional acousto-optic imaging of thick scattering media'. In: *Opt. Lett.* 37.13 (July 2012), pp. 2754–2756. DOI: 10.1364/OL.37.002754 (cited on page 62).

[94] J. P. Huignard and A. Marrakchi. 'Two-wave mixing and energy transfer in Bi12SiO20 crystals: application to image amplification and vibration analysis'. In: *Opt. Lett.* 6.12 (Dec. 1981), pp. 622–624. DOI: 10.1364/OL.6.000622 (cited on page 62).

[95] Mojca Jazbinšek et al. 'Wavelength dependence of visible and near-infrared photorefraction and phase conjugation in Sn2P2S6'. In: *J. Opt. Soc. Am. B* 22.11 (Nov. 2005), pp. 2459–2467. DOI: 10.1364/JOSAB.22.002459 (cited on page 63).

[96] Tobias Bach et al. 'Tailoring of infrared photorefractive properties of Sn2P2S6 crystals by Te and Sb doping'. In: *J. Opt. Soc. Am. B* 24.7 (July 2007), pp. 1535–1541. DOI: 10.1364/JOSAB.24.001535 (cited on page 63).

[97] Salma Farahi et al. 'Photorefractive acousto-optic imaging in thick scattering media at 790 nm with a Sn2P2S6:Te crystal'. In: *Opt. Lett.* 35.11 (June 2010), pp. 1798–1800. DOI: 10.1364/OL.35.001798 (cited on page 63).

[98] Yuta Suzuki et al. 'High-sensitivity ultrasound-modulated optical tomography with a photorefractive polymer'. In: *Opt. Lett.* 38.6 (Mar. 2013), pp. 899–901. DOI: 10.1364/OL.38.000899 (cited on page 63).

[99] Puxiang Lai et al. 'Exploring ultrasound-modulated optical tomography at clinically useful depths using the photorefractive effect'. In: *Photons Plus Ultrasound: Imaging and Sensing 2013*. Ed. by Alexander A. Oraevsky and Lihong V. Wang. Vol. 8581. International Society for Optics and Photonics. SPIE, 2013, p. 85812X. DOI: 10.1117/12.2003270 (cited on page 63).

[100] F. A. Marks, H. W. Tomlinson, and G. W. Brooksby. 'Comprehensive approach to breast cancer detection using light: photon localization by ultrasound modulation and tissue characterization by spectral discrimination'. In: *Photon Migration and Imaging in Random Media and Tissues*. Ed. by Britton Chance and Robert R. Alfano. Vol. 1888. International Society for Optics and Photonics. SPIE, 1993, pp. 500–510. DOI: 10.1117/12.154670 (cited on pages 64, 67).

[101] S. Lévêque et al. 'Ultrasonic tagging of photon paths in scattering media: parallel speckle modulation processing'. In: *Opt. Lett.* 24.3 (Feb. 1999), pp. 181–183. DOI: 10.1364/OL.24.000181 (cited on page 64).

[102] Jun Li, Geng Ku, and Lihong V. Wang. 'Ultrasound-modulated optical tomography of biological tissue by use of contrast of laser speckles'. In: *Appl. Opt.* 41.28 (Oct. 2002), pp. 6030–6035. DOI: 10.1364/AO.41.006030 (cited on pages 64, 65, 67, 68).

[103] Bengtsson A et al. 'Comparison of contrast-to-noise ratios of different detection methods in ultrasound optical tomography.' In: *Biomed Opt Express* 13.9 (2022), pp. 4834–4850. DOI: 10.1364/BOE.457075 (cited on pages 65, 66).

[104] Yan Liu et al. 'Imaging through highly scattering human skulls with ultrasound-modulated optical tomography'. In: *Opt. Lett.* 45.11 (June 2020), pp. 2973–2976. DOI: 10.1364/OL.390920 (cited on page 65).

[105] F. Le Clerc, L. Collot, and M. Gross. 'Numerical heterodyne holography with two-dimensional photodetector arrays'. In: *Opt. Lett.* 25.10 (May 2000), pp. 716–718. DOI: 10.1364/OL.25.000716 (cited on page 66).

[106] L. Wang, S. L. Jacques, and X. Zhao. 'Continuous-wave ultrasonic modulation of scattered laser light to image objects in turbid media'. In: *Opt. Lett.* 20.6 (Mar. 1995), pp. 629–631. DOI: 10.1364/OL.20.000629 (cited on page 67).

[107] L.V. Wang and G. Ku. 'Frequency-swept ultrasound-modulated optical tomography of scattering media'. In: *Opt. Lett.* 23.12 (June 1998), pp. 975–977. DOI: 10.1364/OL.23.000975 (cited on page 67).

[108] M. Lesaffre et al. 'Acousto-optical coherence tomography using random phase jumps on ultrasound and light'. In: *Opt. Express* 17.20 (Sept. 2009), pp. 18211–18218. DOI: 10.1364/OE.17.018211 (cited on page 67).

[109] Gang Yao, Shuliang Jiao, and Lihong V. Wang. 'Frequency-swept ultrasound-modulated optical tomography in biological tissue by use of parallel detection'. In: *Opt. Lett.* 25.10 (May 2000), pp. 734–736. DOI: 10.1364/OL.25.000734 (cited on page 67).

[110] Gang Yao and Lihong V. Wang. 'Theoretical and experimental studies of ultrasound-modulated optical tomography in biological tissue'. In: *Appl. Opt.* 39.4 (Feb. 2000), pp. 659–664. DOI: 10.1364/AO.39.000659 (cited on page 67).

[111] Jun Li and Lihong V. Wang. 'Methods for parallel-detection-based ultrasound-modulated optical tomography'. In: *Appl. Opt.* 41.10 (Apr. 2002), pp. 2079–2084. DOI: 10.1364/AO.41.002079 (cited on page 67).

[112] Ziyu Hua et al. 'Contrast-enhanced ultrasound-modulated laser feedback imaging with microbubbles'. In: *Optics and Lasers in Engineering* 157 (2022), p. 107134. DOI: https://doi.org/10.1016/j.optlaseng.2022.107134 (cited on page 68).

[113] Dean Yuan et al. 'Single-shot ultrasound-modulated optical tomography with enhanced speckle contrast'. In: *Opt. Lett.* 46.13 (July 2021), pp. 3095–3098. DOI: 10.1364/OL.425535 (cited on page 68).

[114] Daniel Doktofsky, Moriya Rosenfeld, and Ori Katz. 'Acousto optic imaging beyond the acoustic diffraction limit using speckle decorrelation'. In: *Commun Phys.* 3.5 (2020) (cited on page 68).

[115] Moriya Rosenfeld et al. *Acousto-optic Ptychography*. 2021. URL: https://opg.optica.org/optica/fulltext.cfm?uri=optica-8-6-936&id=452112 (cited on page 68).

[116] Haowen Ruan et al. 'Fluorescence imaging through dynamic scattering media with speckle-encoded ultrasound-modulated light correlation'. In: *Nat. Photonics* 14 (2020), pp. 511–516 (cited on page 68).

[117] K. Barjean et al. 'Fourier transform acousto-optic imaging with a custom-designed CMOS smart-pixels array'. In: *Optics Letters* 40.5 (2015), pp. 705–708 (cited on page 69).

[118] Kinia Barjean, François Ramaz, and Jean-Michel Tualle. 'Theoretical study of Fourier-transform acousto-optic imaging'. In: *J. Opt. Soc. Am. A* 33.5 (May 2016), pp. 854–862. DOI: 10.1364/JOSAA.33.000854 (cited on page 69).

[119] Lili Zhu et al. 'Experimental study of ultrasound-modulated scattering light using different frequencies ultrasound probes'. In: *Chin. Opt. Lett.* 12.7 (July 2014), p. 071701 (cited on pages 69, 70).

[120] Qiang Yang et al. 'Time-reversed ultrasonically encoded optical focusing using two ultrasonic transducers for improved ultrasonic axial resolution'. In: *Journal of Biomedical Optics* 18.11 (2013), p. 110502. DOI: 10.1117/1.JBO.18.11.110502 (cited on page 70).

[121] Reto Fiolka, Ke Si, and Meng Cui. 'Parallel wavefront measurements in ultrasound pulse guided digital phase conjugation'. In: *Opt. Express* 20.22 (Oct. 2012), pp. 24827–24834. DOI: 10.1364/OE.20.024827 (cited on page 70).

[122] R. Sriram Chandran et al. 'Ultrasound modulated optical tomography: Young's modulus of the insonified region from measurement of natural frequency of vibration'. In: *Opt. Express* 19.23 (Nov. 2011), pp. 22837–22850. DOI: 10.1364/OE.19.022837 (cited on page 71).

[123] Jean-Baptiste Laudereau et al. 'Ultrafast acousto-optic imaging with ultrasonic plane waves'. In: *Opt. Express* 24.4 (Feb. 2016), pp. 3774–3789. DOI: 10.1364/OE.24.003774 (cited on page 72).

[124] Nowak L.J. and W. Steenbergen. 'Reflection-mode acousto-optic imaging using plane wave ultrasound pulses'. In: *Journal of Biomedical Optics* 26.9 (2021), p. 096001. DOI: 10.1117/1.JBO.26.9.096001 (cited on pages 72, 73).

[125] T. R. Nelson et al. 'Ultrasound biosafety considerations for the practicing sonographer and sonologist'. In: *Journal of Ultrasound in Medicine* 28.2 (2009), pp. 139–150 (cited on pages 223, 224).

[126] C. Kollmann et al. 'Ultraschall emissionen: thermische (ti) und mechanische (mi) indizes. Ultraschall in Der Medizin'. In: *European Journal of Ultrasound* 34.5 (2013), pp. 422–434 (cited on page 224).

[127] S. Mallidi, G. P. Luke, and S. Emelianov. 'Photoacoustic imaging in cancer detection, diagnosis, and treatment guidance.' In: *Trends in Biotechnology* 29.5 (2011), pp. 213–221 (cited on page 225).

[128] Freddie Bray et al. 'Global cancer statistics 2018: GLOBOCAN estimates of incidence and mortality worldwide for 36 cancers in 185 countries'. In: *CA: a cancer journal for clinicians* 68.6 (2018), pp. 394–424 (cited on page 75).

[129] Jacques Ferlay et al. 'Global cancer observatory: cancer today'. In: *Lyon, France: international agency for research on cancer* 3.20 (2018), p. 2019 (cited on page 75).

[130] International Agency for Research on Cancer et al. *Estimated number of incident cases from 2018 to 2040, all cancers, both sexes, all ages*. 2020 (cited on page 75).

[131] L A Aaltonen et al. 'Incidence of Hereditary Nonpolyposis Colorectal Cancer and The Feasibility of Molecular Screening for The Disease'. In: *THE NEW ENGLAND JOURNAL OF MEDICINE* volume number (1998). Impact Factor: 9, page numbers (cited on page 75).

[132] S J Winawer et al. 'Prevention of Colorectal Cancer By Colonoscopic Polypectomy. The National Polyp Study Workgroup'. In: *THE NEW ENGLAND JOURNAL OF MEDICINE* volume number (1993). Impact Factor: 9, page numbers (cited on page 76).

[133] R Gryfe et al. 'Tumor Microsatellite Instability and Clinical Outcome in Young Patients with Colorectal Cancer'. In: *THE NEW ENGLAND JOURNAL OF MEDICINE* volume number (2000). Impact Factor: 8, page numbers (cited on page 76).

[134] Susan Bullman et al. 'Analysis of Fusobacterium Persistence and Antibiotic Response in Colorectal Cancer'. In: *SCIENCE (NEW YORK, N.Y.)* volume number (2017). Impact Factor: 8, page numbers (cited on page 76).

[135] TaChung Yu et al. 'Fusobacterium Nucleatum Promotes Chemoresistance To Colorectal Cancer By Modulating Autophagy'. In: *CELL* volume number (2017). Impact Factor: 8, page numbers (cited on page 76).

[136] E. J. M. Baltussen et al. 'Comparing in vivo and ex vivo fiberoptic diffuse reflectance spectroscopy in colorectal cancer'. In: *Translational Biophotonics* 1.1-2 (2019), e201900008 (cited on page 76).

[137] E. J. M. Baltussen et al. 'Optimizing algorithm development for tissue classification in colorectal cancer based on diffuse reflectance spectra'. In: *Biomedical Optics Express* 10.12 (2019), pp. 6096–6113 (cited on page 76).

[138] G. C. Langhout et al. 'Differentiation of healthy and malignant tissue in colon cancer patients using optical spectroscopy: A tool for image-guided surgery'. In: *Lasers in Surgery and Medicine* 47.7 (2015), pp. 559–565 (cited on page 76).

[139] G. C. Langhout et al. 'Colorectal cancer identified using optical spectroscopy'. In: *Annals of Oncology* 25 (2014), p. 206 (cited on page 76).

[140] E. J. M. Baltussen et al. 'Diffuse reflectance spectroscopy as a tool for real-time tissue assessment during colorectal cancer surgery'. In: *Journal of Biomedical Optics* 22.10 (2017), p. 106014 (cited on page 76).

[141] E. J. M. Baltussen et al. 'Hyperspectral imaging for tissue classification, a way toward smart laparoscopic colorectal surgery'. In: *Journal of Biomedical Optics* 24.1 (2019), p. 16002 (cited on page 76).

[142] E. J. M. Baltussen et al. 'Using diffuse reflectance spectroscopy to distinguish tumor tissue from fibrosis in rectal cancer patients as a guide to surgery'. In: *Lasers in Surgery and Medicine* 52 (2019), p. 604 (cited on page 76).

[143] E. J. M. Baltussen et al. 'Tissue diagnosis during colorectal cancer surgery using optical sensing: An in vivo study'. In: *Journal of Translational Medicine* 17.1 (2019), pp. 1–10 (cited on page 76).

[144] R. Prosst and J. Gahlen. 'Fluorescence diagnosis of colorectal neoplasms: a review of clinical applications'. In: *International Journal of Colorectal Disease* 17.1 (2002), pp. 1–10 (cited on pages 76, 77).

[145] R. M. Cothren et al. 'Detection of dysplasia at colonoscopy using laser-induced fluorescence: A blinded study'. In: *Gastrointestinal Endoscopy* 44.2 (1996), pp. 168–176 (cited on pages 76, 77).

[146] M. K. Saini, M. Juneja, and A. Mittal. 'Colorectal Cancer Detection from Colonoscopy Videos: A Comprehensive Survey of Computer-Aided Diagnosis Techniques'. In: *Molecular Imaging* (2018) (cited on pages 76, 77).

[147] A. Molckovsky et al. 'Diagnostic potential of near-infrared Raman spectroscopy in the colon: Differentiating adenomatous from hyperplastic polyps'. In: *Gastrointestinal Endoscopy* 57.3 (2003), pp. 396–402 (cited on pages 76, 77).

[148] E. Widjaja, W. Zheng, and Z. Huang. 'Classification of colonic tissues using near-infrared Raman spectroscopy and support vector machines'. In: *International Journal of Oncology* 32.3 (2008), pp. 653–662 (cited on pages 76, 77).

[149] S. Li et al. 'Identification and characterization of colorectal cancer using Raman spectroscopy and feature selection techniques'. In: *Optical Express* 22.21 (2014), pp. 25895–25908 (cited on pages 76, 77).

[150] A. Salman et al. 'Insights on colorectal cancer relapse by infrared microscopy from anastomosis tissues: Further analysis'. In: *Vibrational Spectroscopy* 83 (2016), pp. 17–25 (cited on pages 76, 77).

[151] P. S. Andersson et al. 'Fluorescence endoscopy instrumentation for improved tissue characterization'. In: *Medical Physics* 14.4 (1987), pp. 633–636 (cited on pages 76, 77).

[152] B. Mayinger et al. 'Endoscopic light-induced autofluorescence spectroscopy for the diagnosis of colorectal cancer and adenoma'. In: *Journal of Photochemistry and Photobiology B: Biology* 70.1 (2003), pp. 13–20 (cited on pages 76, 77).

[153] X. Shao, W. Zheng, and Z. Huang. 'In vivo diagnosis of colonic precancer and cancer using near-infrared autofluorescence spectroscopy and biochemical modeling'. In: *Journal of Biomedical Optics* 16.6 () (cited on pages 76, 77).

[154] C.-Y. Wang, J.-K. Lin, and H. K. Chiang. 'Autofluorescence spectroscopy to identify normal and cancerous colorectal tissues'. In: *Proc. 20th Annual International Conference of the IEEE Engineering in Medicine and Biology Society*. Vol. 20. Biomedical Engineering Towards the Year 2000 and Beyond. 1998, pp. 967–969 (cited on pages 76, 77).

[155] L. C. Kwek et al. 'High-sensitivity and specificity of laser-induced autofluorescence spectra for detection of colorectal cancer with an artificial neural network'. In: *Applied Optics* 44.19 (2005), pp. 4004–4008 (cited on pages 76, 77).

[156] S. Coda et al. 'Fluorescence lifetime spectroscopy of tissue autofluorescence in normal and diseased colon measured ex vivo using a fiber-optic probe'. In: *Biomedical Optics Express* 5.2 (2014), pp. 515–538 (cited on pages 76, 77).

[157] G. Tang et al. 'Detection of human colonic adenoma by laser-induced autofluorescence integrated with diffuse reflectance spectroscopy'. In: *Biomedical Photonics and Optoelectronic Imaging* 4224 (2000), pp. 174–178 (cited on pages 76, 77).

[158] M. B. Wallace and R. Kiesslich. 'Advances in endoscopic imaging of colorectal neoplasia'. In: *Gastroenterology* 138.6 (2010), pp. 2140–2150 (cited on pages 76, 77).

[159] H. Aihara, H. Tajiri, and T. Suzuki. 'Application of autofluorescence endoscopy for colorectal cancer screening: Rationale and an update'. In: *Gastroenterology Research and Practice* 2012 (2012), p. 1. DOI: 10.1155/2012/971383 (cited on pages 76, 77).

[160] M. S. Nogueira et al. 'Tissue biomolecular and microstructure profiles in optical colorectal cancer delineation'. In: *Journal of Physics D: Applied Physics* 54.45 (2021), p. 454002. DOI: doi.org/10.1088/1361-6463/ac1137 (cited on pages 79, 83).

[161] Marcelo Saito Nogueira et al. 'Evaluation of wavelength ranges and tissue depth probed by diffuse reflectance spectroscopy for colorectal cancer detection'. In: *Scientific Reports* 11.1 (2021), p. 798. DOI: doi.org/10.1038/s41598-020-79517-2 (cited on page 82).

[162] Marcelo Saito Nogueira et al. 'Insights into Biochemical Sources and Diffuse Reflectance Spectral Features for Colorectal Cancer Detection and Localization'. In: *Cancers* 14.22 (2022). DOI: 10.3390/cancers14225715 (cited on page 83).

[163] M. Gross, P. Goy, and M. Al-Koussa. 'Shot-noise detection of ultrasound-tagged photons in ultrasound-modulated optical imaging'. In: *Opt. Lett.* 28.24 (Dec. 2003), pp. 2482–2484. DOI: 10.1364/OL.28.002482 (cited on page 85).

[164] Dennis Gabor. 'A New Microscopic Principle'. In: *Nature* 161 (1948), pp. 777–778. DOI: 10.1038/161777a0 (cited on page 85).

[165] Dennis Gabor. 'Microscopy by reconstructed wave-fronts'. In: *Proceedings of the Royal Society of London. Series A. Mathematical and Physical Sciences* 1051.197 (1949), pp. 454–487. DOI: 10.1098/rspa.1949.0075 (cited on page 85).

[166] Emmett N. Leith and Juris Upatnieks. 'Wavefront Reconstruction with Continuous-Tone Objects*'. In: *J. Opt. Soc. Am.* 53.12 (Dec. 1963), pp. 1377–1381. DOI: 10.1364/JOSA.53.001377 (cited on page 85).

[167] Tatiana Latychevskaia et al. 'Off-axis and inline electron holography: Experimental comparison'. In: *Ultramicroscopy* 110.5 (2010). Hannes Lichte 65th Birthday, pp. 472–482. DOI: https://doi.org/10.1016/j.ultramic.2009.12.007 (cited on page 85).

[168] M. Gross. 'Selection of the tagged photons by off axis heterodyne holography in ultrasound-modulated optical tomography'. In: *Appl. Opt.* 56.7 (Mar. 2017), pp. 1846–1854. DOI: 10.1364/AO.56.001846 (cited on pages 92, 100).

[169] O.K. Baskurt. 'In vivo correlates of altered blood rheology'. In: *Biorheology* (2008), pp. 629–638 (cited on page 99).

[170] S. Palta, R. Saroa, and A. Palta. 'Overview of the coagulation system'. In: *Indian J Anaesth* 58 (2014), pp. 515–523 (cited on pages 99, 100).

[171] S. M. Donahue and C. M. Otto. 'Thromboelastography: a tool for measuringhypercoagulability, hypocoagulability, andfibrinolysis'. In: *Journal of Veterinary Emergency and Critical Care* 15 (2005), pp. 9–16 (cited on pages 99, 101, 102).

[172] F. R. Rosendaal. 'Venous Thrombosis, a multicausal disease'. In: *Lancet* 353 (1999), pp. 1167–1173 (cited on page 99).

[173] M. Crous-Bou, L. B. Harrington, and C. Kabrhel. 'Environmental and Genetic Risk Factors Associated with Venous Thromboembolism'. In: *Semin Thromb Hemost* 42 (2016), pp. 808–820 (cited on page 99).

[174] S. Biswas et al. 'Blood clots in COVID-19 patients: Simplifying the curious mystery'. In: *Med Hypotheses* 146 (2021), p. 110371 (cited on page 100).

[175] N Racheli et al. 'Non-invasive blood flow measurements using ultrasound modulated diffused light'. In: *Photons Plus Ultrasound: Imaging and Sensing 2012*. Vol. 8223. SPIE. 2012, pp. 438–445 (cited on pages 100, 109).

[176] Yue Zhao et al. 'In vivo blood viscosity characterization based on frequency-resolved photoacoustic measurement'. In: *Applied Physics Letters* 113.14 (Oct. 2018), p. 143703. DOI: 10.1063/1.5039538 (cited on page 100).

[177] J. Whalen and K. J. Tuman. 'Monitoring hemostasis'. In: *Int Anesthesiol Clin* 34 (1996), pp. 195–213 (cited on page 100).

[178] J. W. Heemskerk, E. M. Bevers, and T. Lindhout. 'Platelet activation and blood coagulation'. In: *Thromb Haemost* 88 (2002), pp. 186–193 (cited on page 100).

[179] M. M. Tripathi et al. 'Assessing blood coagulation status with laser speckle rheology'. In: *Biomed Opt Express.* 5 (2014), pp. 817–831 (cited on page 101).

[180] M. M. Tripathi et al. 'Assessing blood coagulation status with laser speckle rheology'. In: *Biomed Opt Express* 5.3 (2014 Feb 24), pp. 817–831. DOI: https://doi:10.1364/BOE.5.000817 (cited on page 101).

[181] Mostafa Fatemi and James F Greenleaf. 'Ultrasound-stimulated vibro-acoustic spectrography'. In: *Science* 280.5360 (1998), pp. 82–85 (cited on page 101).

[182] Mostafa Fatemi and James F. Greenleaf. 'Vibro-acoustography: An imaging modality based on ultrasound-stimulated acoustic emission'. In: *Proceedings of the National Academy of Sciences* 96.12 (1999), pp. 6603–6608. DOI: 10.1073/pnas.96.12.6603 (cited on page 101).

[183] Shigao Chen, Mostafa Fatemi, and James F. Greenleaf. 'Quantifying elasticity and viscosity from measurement of shear wave speed dispersion'. In: *The Journal of the Acoustical Society of America* 115 (2004), p. 2781. DOI: doi.org/10.1121/1.1739480 (cited on page 101).

[184] Thomas Deffieux et al. 'Shear wave spectroscopy for in vivo quantification of human soft tissues visco-elasticity'. In: *IEEE transactions on medical imaging* 28.3 (2008), pp. 313–322 (cited on page 101).

[185] Yue Zhao et al. 'In vivo blood viscosity characterization based on frequency-resolved photoacoustic measurement'. In: *Applied Physics Letters* 113.14 (2018) (cited on page 101).

[186] M. Louka et al. 'Development of an Optical Method for the Evaluation of Whole Blood Coagulation'. In: *Biosensors (Basel)* 11 (2021), p. 113 (cited on page 102).

[187] R. A. Green and J. S. Thomas. *Hemostatic disorders: coagulopathies and thrombosis, In: Ettinger SJ, Feldman EC. eds.* Philadelphia: WB Saunders: Textbook of Veterinary Internal Medicine, 4th edn, 1995 (cited on page 102).

[188] K. G. Palmer, L. G. King, and T. J. Van Winkle. 'Clinical manifestations and associated disease syndromes in dogs with cranial vena cava thrombosis: 17 cases (1989-1996)'. In: *J Am Vet Med Assoc* 213 (1998), pp. 220–224 (cited on page 102).

[189] C. M. Otto et al. 'Evidence of hypercoagulability in dogs with parvoviral enteritis'. In: *J Am Vet Med Assoc* 217 (2000), pp. 1500–1504 (cited on page 102).

[190] M. T. Ganter and C. K. Hofer. 'Coagulation monitoring: current techniques and clinical use of viscoelastic point-of-care coagulation devices'. In: *Anest. Analg.* 106 (2008), pp. 1366–1375 (cited on page 102).

[191] M. M. Aria, A. Erten, and O. Yalcin. 'Technology Advancements in Blood Coagulation Measurements for Point-of-Care Diagnostic Testing'. In: *Frontiers in Bioengineering and Biotechnology* 7 (2019), p. 395 (cited on pages 102, 120).

[192] A. Voleisis et al. 'Ultrasonic method for monitoring the clotting process during whole blood coagulation'. In: *Ultrasonics* 78 (2014), pp. 146–151 (cited on page 102).

[193] Qinan Ban et al. 'A point-of-care microfluidic channel-based device for rapid and direct detection of fibrinogen in whole blood'. In: *Lab on a Chip* 22.14 (2022), pp. 2714–2725 (cited on page 102).

[194] Emmanuel J. Favaloro and Davide Negrini. 'Machine learning and coagulation testing: the next big thing in hemostasis investigations?' In: *Clinical Chemistry and Laboratory Medicine (CCLM)* 59.7 (2021), pp. 1177–1179. DOI: doi:10.1515/cclm-2021-0216 (cited on page 102).

[195] A. Volk and C.J. Kähler. 'Density model for aqueous glycerol solutions'. In: *Exp Fluids* 59.75 (2018). DOI: https://doi.org/10.1007/s00348-018-2527-y (cited on page 103).

[196] M. Jeschonneck et al. 'Abnormal microcirculation and temperature in skin above tender points in patients with fibromyalgia'. In: *Rheumatology* 39.8 (2000), pp. 917–921. DOI: https://doi.org/10.1093/rheumatology/39.8.917 (cited on page 103).

[197] Sanathana Konugolu Venkata Sekar et al. 'Broadband (600–1350 nm) Time-Resolved Diffuse Optical Spectrometer for Clinical Use'. In: *IEEE Journal of Selected Topics in Quantum Electronics* 22.3 (2016), pp. 406–414. DOI: 10.1109/JSTQE.2015.2506613 (cited on page 103).

[198] Sanathana Konugolu Venkata Sekar et al. 'Broadband Time Domain Diffuse Optical Reflectance Spectroscopy: A Review of Systems, Methods, and Applications'. In: *Applied Sciences* 9.24 (2019). DOI: 10.3390/app9245465 (cited on page 103).

[199] Gang Yao and Lihong V. Wang. 'Ultrasound-modulated optical tomography in biological tissue: theoretical and experimental studies'. In: *Biomedical Optical Spectroscopy and Diagnostics*. Optica Publishing Group, 2000, SuF2. DOI: 10.1364/BOSD.2000.SuF2 (cited on page 107).

[200] Jovan M. Elazar and Oleg Steshenko. 'Doppler effect's contribution to ultrasonic modulation of multiply scattered coherent light: Monte Carlo modeling'. In: *Opt. Lett.* 33.2 (Jan. 2008), pp. 131–133. DOI: 10.1364/OL.33.000131 (cited on page 107).

[201] Cuncheng Weng and Youwu He. 'Dependences of ultrasonic modulation of coherent light on optical frequency shift and phase modulation'. In: *Physica Scripta* 96.2 (2020), p. 025505. DOI: 10.1088/1402-4896/abcce4 (cited on pages 107, 108).

[202] L. V. Wang. 'Ultrasonic modulation of scattered light in turbid media and a potential novel tomography in biomedicine'. In: *Photochem Photobiol.* 67.1 (1998), pp. 41–49 (cited on page 107).

[203] Z. Hajjarian and S.K. Nadkarni. 'Tutorial on laser speckle rheology: technology, applications, and opportunities'. In: *J Biomed Opt* 5 (2020 May 25), pp. 1–19. DOI: doi:10.1117/1.JBO.25.5.050801 (cited on page 109).

[204] Marlon Schwarz et al. 'Acousto-Optic Cerebral Blood Flow Monitoring During Induction of Anesthesia in Humans'. In: *Neurocritical Care* 24 (2016), pp. 436–441 (cited on page 109).

[205] A. Tsalach et al. 'Ultrasound modulated light blood flow measurement using intensity autocorrelation function: a Monte-Carlo simulation'. In: *Biomedical optics*. 2014 (cited on page 109).

[206] E. Nader et al. 'Blood Rheology: Key Parameters, Impact on Blood Flow, Role in Sickle Cell Disease and Effects of Exercise'. In: *Front Physiol.* 5.3 (2019 Oct 17), pp. 817–831. DOI: doi:10.3389/fphys.2019.01329 (cited on page 109).

[207] GR Cokelet and HJ Meiselman. 'Handbook of hemorheology and hemodynamics'. In: *Macro-and micro-rheological properties of blood. IOS Pres s Washington DC* (2007), pp. 45–71 (cited on page 109).

[208] Oguz K Baskurt and Herbert J Meiselman. 'Blood rheology and hemodynamics'. In: *Seminars in thrombosis and hemostasis*. Vol. 29. 05. 2003, pp. 435–450 (cited on page 109).

[209] J. David Briers. 'Laser Doppler, speckle and related techniques for blood perfusion mapping and imaging'. In: *Physiological Measurement* 22.4 (1996), R35 (cited on page 111).

[210] Zuzana Kovacsova, Gemma Bale, and Ilias Tachtsidis. 'Medical Utility of NIR Monitoring'. In: *Encyclopedia of Biomedical Engineering*. Ed. by Roger Narayan. Oxford: Elsevier, 2019, pp. 415–431. DOI: https://doi.org/10.1016/B978-0-12-801238-3.64141-7 (cited on page 111).

[211] Michel Gross et al. 'Heterodyne detection of multiply scattered monochromatic light with a multipixel detector'. In: *Optics Letters* 30.11 (2005), pp. 1357–1359 (cited on pages 112, 114).

[212] H. Jeon et al. 'Laser speckle decorrelation time-based platelet function testing in microfluidic system'. In: *Scientific Reports* 9.1 (2019), p. 16514 (cited on page 115).

[213] Hyuna Sung et al. 'Global cancer statistics 2020: GLOBOCAN estimates of incidence and mortality worldwide for 36 cancers in 185 countries'. In: *CA: a cancer journal for clinicians* 71.3 (2021), pp. 209–249 (cited on page 117).

[214] Ha Thi Nguyen and Hong-Quan Duong. 'The molecular characteristics of colorectal cancer: Implications for diagnosis and therapy'. In: *Oncology letters* 16.1 (2018), pp. 9–18 (cited on pages 117, 118).

[215] J. Vilsan et al. 'Open, laparoscopic, and robotic approaches to treat colorectal cancer: a comprehensive review of literature'. In: *Cureus* (2023). DOI: 10.7759/cureus.38956 (cited on page 117).

[216] Jiaxin Liu et al. 'Identification of CPT2 as a prognostic biomarker by integrating the metabolism-associated gene signature in colorectal cancer'. In: *BMC cancer* 22.1 (2022), p. 1038 (cited on page 118).

[217] Isabel Heidrich et al. 'Clinical applications of circulating tumor cells and circulating tumor DNA as a liquid biopsy marker in colorectal cancer'. In: *Cancers* 13.18 (2021), p. 4500 (cited on page 118).

[218] Ann Tivey et al. 'Circulating tumour DNA—looking beyond the blood'. In: *Nature reviews clinical oncology* 19.9 (2022), pp. 600–612 (cited on page 118).

[219] Hemanth Noothalapati, Keita Iwasaki, and Tatsuyuki Yamamoto. 'Non-invasive diagnosis of colorectal cancer by Raman spectroscopy: Recent developments in liquid biopsy and endoscopy approaches'. In: *Spectrochimica Acta Part A: Molecular and Biomolecular Spectroscopy* 258 (2021), p. 119818. DOI: https://doi.org/10.1016/j.saa.2021.119818 (cited on pages 118, 119).

[220] Xiaozhou Li et al. 'Detection and identification of Colon Cancer and Rectum Cancer Using Fluorescence and Raman Spectrum'. In: *2005 IEEE Engineering in Medicine and Biology 27th Annual Conference*. 2005, pp. 1453–1456. DOI: 10.1109/IEMBS.2005.1616705 (cited on page 118).

[221] Xiaozhou Li, Deli Wang, and Yue Wang. 'Discrimination of normal and colorectal cancer using Raman spectroscopy and fluorescence'. In: *European Conference on Biomedical Optics*. Optica Publishing Group. 2007, 6633_60 (cited on page 118).

[222] Xiaozhou Li, Tianyue Yang, and Siqi Li. 'Discrimination of serum Raman spectroscopy between normal and colorectal cancer using selected parameters and regression-discriminant analysis'. In: *Applied optics* 51.21 (2012), pp. 5038–5043 (cited on page 118).

[223] Hui Chen et al. 'Diagnosis of colorectal cancer by near-infrared optical fiber spectroscopy and random forest'. In: *Spectrochimica Acta Part A: Molecular and Biomolecular Spectroscopy* 135 (2015), pp. 185–191. DOI: https://doi.org/10.1016/j.saa.2014.07.005 (cited on page 118).

[224] P. A. Boland et al. 'Intraoperative near infrared functional imaging of rectal cancer using artificial intelligence methods - now and near future state of the art.' In: *European Journal of Nuclear Medicine and Molecular Imaging* 51.10 (2024), pp. 3135–3148 (cited on pages 118, 119).

[225] Alfred L. Copley. 'Bleeding time, other in vivo hemostasis tests and the arrest of hemorrhage'. In: *Thrombosis Research* 4.1 (1974), pp. 1–23. DOI: https://doi.org/10.1016/0049-3848(74)90200-X (cited on page 120).

[226] Hiroshi Kadowaki et al. 'Feasibility Verification of Blood Viscosity Measurement Using Doppler Ultrasound'. In: *ASME Journal of Medical Diagnostics* 4.2 (2022), p. 024501. DOI: 10.1115/1.4050793 (cited on page 120).

[227] Y. Luo et al. 'Miniature viscometer incorporating gan optical devices with an ultrawide measurement range'. In: *Light: Advanced Manufacturing* 4 (1 2023), p. 1. DOI: 10.37188/lam.2023.002 (cited on page 120).

[228] M. V. d. Arruda et al. 'Standardization for obtaining blood viscosity: a systematic review'. In: *European Journal of Haematology* 106 (5 2021), pp. 597–605. DOI: 10.1111/ejh.13594 (cited on page 121).

[229] J. Hathcock. 'Flow effects on coagulation and thrombosis'. In: *Arteriosclerosis, Thrombosis, and Vascular Biology* 26 (8 2006), pp. 1729–1737. DOI: 10.1161/01.atv.0000229658.76797.30 (cited on page 121).

Appendix

scientific reports

Check for updates

OPEN

Evaluation of wavelength ranges and tissue depth probed by diffuse reflectance spectroscopy for colorectal cancer detection

Marcelo Saito Nogueira[1,2]✉, Siddra Maryam[1,2], Michael Amissah[1,2], Huihui Lu[1], Noel Lynch[3], Shane Killeen[3], Micheal O'Riordain[3] & Stefan Andersson-Engels[1,2]

Colorectal cancer (CRC) is the third most common type of cancer worldwide and the second most deadly. Recent research efforts have focused on developing non-invasive techniques for CRC detection. In this study, we evaluated the diagnostic capabilities of diffuse reflectance spectroscopy (DRS) for CRC detection by building 6 classification models based on support vector machines (SVMs). Our dataset consists of 2889 diffuse reflectance spectra collected from freshly excised ex vivo tissues of 47 patients over wavelengths ranging from 350 and 1919 nm with source-detector distances of 630-µm and 2500-µm to probe different depths. Quadratic SVMs were used and performance was evaluated using twofold cross-validation on 10 iterations of randomized training and test sets. We achieved (93.5 ± 2.4)% sensitivity, (94.0 ± 1.7)% specificity AUC by probing the superficial colorectal tissue and (96.1 ± 1.8)% sensitivity, (95.7 ± 0.6)% specificity AUC by sampling deeper tissue layers. To the best of our knowledge, this is the first DRS study to investigate the potential of probing deeper tissue layers using larger SDD probes for CRC detection in the luminal wall. The data analysis showed that using a broader spectrum and longer near-infrared wavelengths can improve the diagnostic accuracy of CRC as well as probing deeper tissue layers.

Colorectal cancer (CRC) is third most common type of cancer worldwide and the second most deadly. CRC comprised 10.2% (1.85 million) of the diagnosed cancer cases and 9.2% (0.88 million) of the cancer related deaths in 2018. In the same year, CRC had the second highest 5-year prevalence (10.9% or 4.79 million of the cases)[1,2]. The number of incident cases is estimated to increase by 63.4% until 2040, whereas the number of deaths is estimated to increase by 71.5% in the same period[3]. The projected increased incidence of CRC and the improvement on patient prognosis generated by early CRC detection[4] has increased the interest in the development of novel techniques to detect precancerous lesions and lesions early in the polyp-carcinoma sequence[5].

Although current screening methods reduce the risk of CRC-associated mortality[6], their effectiveness varies due to issues related to suboptimal screening compliance, limitations of test performance and lack of accessibility[4]. With this in mind, initiatives have been taken to increase the range of diagnostic methods including blood and stool-based tests. The results of these tests show only the potential presence of the cancer and further investigation is required to locate potential tumors. Tumors can be visualized and identified by using minimally-invasive methods such as computed tomographic colonography, double contrast barium enema, and capsule endoscopy[4]. However, colonoscopy with biopsy remains the gold standard diagnostic test for evaluation of colonic disease.

Colonoscopy is predominantly a very safe procedure with a very low risk profile of serious complications but does pose significant inconveniences for patients from logistical perspective of bowel preparation, as the patients need to be accompanied home after sedation. Recent research efforts have focused on developing non-invasive techniques to identify cancerous lesions by comparing the techniques capable of generating tissue classification models closely matching the biopsy results. In particular, optical spectroscopy techniques can provide real-time and cost-effective tissue identification, which can provide more accurate and faster than conventional detection methods such as visualization, palpation, and histology[7–20]. One of these techniques is diffuse reflectance spectroscopy (DRS).

[1]Tyndall National Institute, Lee Maltings, Dyke Parade, Cork, Ireland. [2]Department of Physics, University College Cork, College Road, Cork, Ireland. [3]Department of Surgery, Mercy University Hospital, Cork, Ireland. ✉email: marcelosaitonogueira@gmail.com

Number of patients	47
Gender	
Male	32
Female	15
Age (years)	
Median	69
Minimum	40
Maximum	89
Interquartile range	13.5
Cancer types	
Adenocarcinoma	46
Carcinoma	1
Tumor stage	
pT1	5
pT2	7
pT3	26
pT4	9

Table 1. Patient demographics and tumor characteristics.

DRS is an optical method capable of tissue identification based on the biochemical composition, oxygenation and microstructure of the tissue. DRS technology is based on delivering light to the tissue and capturing the reflected light that travels inside it. The reflected light contains information about the light scattering (related to the tissue microstructure) and absorption (associated with its biomolecular content). The combination of scattering and absorption (optical properties) as well as the geometry of the light source and detector defines the probed depth into the tissue[21]. Since the optical properties vary with the wavelength of the light source, the wavelength range determines the number of biomolecules that can be investigated using DRS.

Previous studies used DRS to distinguish tumor tissue from healthy surrounding tissues in the oral cavity (head and neck cancer)[7], breast[8,13], lung[14], and liver[15,16]. Recent studies have also investigated the detection of colorectal cancer during surgery[9–12,17–20]. In terms of primary colorectal cancer, DRS and related optical spectroscopic techniques have mainly been used to guide colonoscopy by distinguishing the normal mucosa and malignant tissue inside the colon (luminal side). Several of these studies have demonstrated sensitivity and specificity as high as 100% in a limited number of samples and collected spectra[9–12,17–20]. Other optical spectroscopic techniques applied to CRC detection during colonoscopy include fluorescence spectroscopy (FS), time-resolved fluorescence spectroscopy (TR-FS), Raman spectroscopy (RS), Fourier-transform infrared spectroscopy (FTIR)[22–38]. Numerous fluorescence spectroscopy studies achieved both sensitivity and specificity close to 100% for diagnosis[22]. On the other hand, most of the studies performed require contrast agents and/or ultraviolet illumination. This requirement restricts the optical guidance time to the safe limits of ultraviolet exposure and the time contrast agents remain accumulated in the cancerous lesion. Although the diagnostic abilities of label-free FS, TR-FS, RS and FTIR spectroscopy have been investigated for a limited number of samples, the tissue classification performance has also demonstrated sensitivity and specificity up to 100%[23–28,31–38]. Challenges on the repeatability and reproducibility of the classification performance arise from increasing the data collection and analyzing the factors contributing to higher sensitivities and specificities. Factors for DRS include the measured wavelength range as well as the tissue depth investigated by using specific source-to-detector distances (SDD).

Most of the prior studies using DRS and related optical spectroscopic techniques probed only the superficial colorectal tissue by using fiber optic probes with small SDD or collecting hyperspectral images from wide-illuminated tissue areas[39–50]. In addition, previous optical spectroscopy studies have investigated relatively narrow visible and near-infrared wavelength ranges compared to the wavelength range exploited in this study (from 350 to 1919 nm).

In this study, we developed a multivariate analysis model for colorectal cancer detection in ex vivo specimens for future application in colonoscopy settings. We compared its classification performance with previous DRS, elastic scattering spectroscopy, near-infrared spectroscopy and hyperspectral imaging (HSI) studies of other research groups. This performance was evaluated for the broad wavelength range from 350 to 1919 nm as well as ranges used in other studies[39–50]. Furthermore, we investigate the usefulness of the probed tissue depth on cancer identification by using fiber optic probes with SDDs of 630 μm (small SDD for superficial tissue measurements) and 2500 μm (large SDD). Our DRS spectra dataset contained 2889 spectra of freshly excised ex vivo tissues of 47 patients. To the best of our knowledge, this is the first DRS study to investigate the potential of probing deeper tissue layers using larger SDD probes for CRC detection during colonoscopy.

Methodology

Clinical study protocol and research ethics. The study included 47 patients undergoing bowel resection for cancer of the colon or rectum at Mercy University Hospital (Cork, Ireland). Patient demographics are shown in Table 1. The study was performed under the approval of the Clinical Research Ethics Committee of

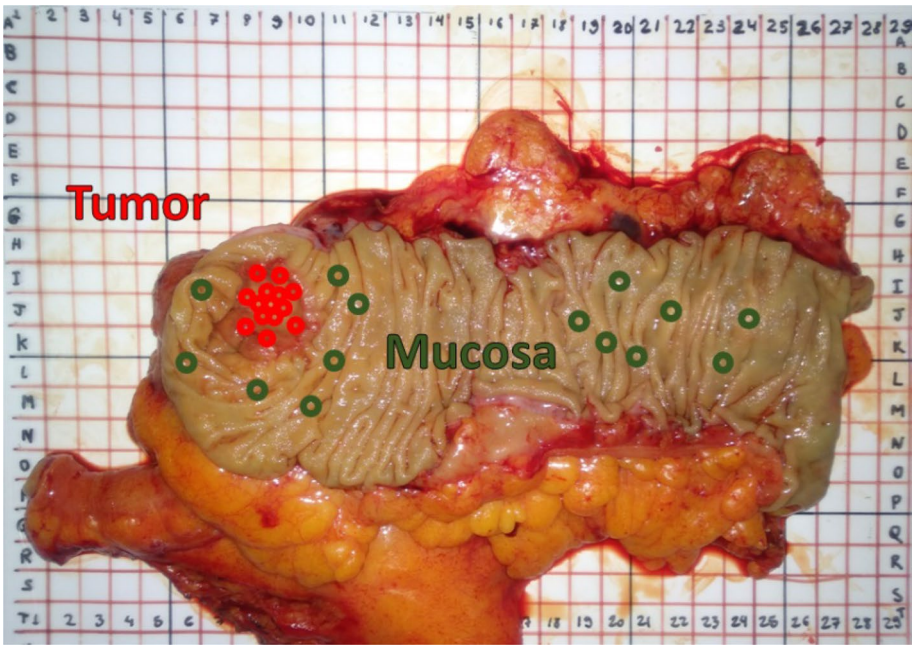


Figure 1. Mucosa and tumor measurement locations on the specimen. Measurements were distributed over a large area in order to obtain a robust dataset containing tissue heterogeneity information.

University College Cork. All methods were performed in accordance with the relevant guidelines/regulations. Informed consent was obtained from all participants of the study. The specimen was removed 15–25 min after the blood supply to the specimen had been cut off. Once the specimen was removed from the patients, its lumen was exposed and cleaned with slow running water in order to remove any remaining feces and blood in the surface of the specimen. Then, healthy and cancerous tissues were identified by experienced surgeons prior to the data collection. The time between the specimen removal and the start of the data collection was 40 min on average. The pH was not stabilized by saline solution. The data was collected from ex vivo mucosal/submucosal tissues and tumors of the specimen within an average time of 60 min after surgical resection. Test conditions were kept as uniform as possible throughout the data collection by keeping the tissue moisture with a wet wipe. Approximately 15 sites were measured for healthy tissues (mucosa/submucosa) and 15 for cancerous tissues over a typical area of 100 cm^2 (Fig. 1).

The location of every measurement was recorded on a photograph taken with a red–green–blue (RGB) camera. After the acquisition of all optical DRS data, the specimen was returned to the Pathology Department for processing and analysis according to standard protocols. The ground truth of every measurement was obtained by histopathology analysis.

Diffuse reflectance spectroscopy system and probes. Our DRS system comprised of a tungsten-halogen broadband light source (HL-2000-HP, Ocean Optics, Edinburgh, United Kingdom) with an emission spectrum ranging from 350 to 2400 nm, which delivers and captures light via optical fibers coupled to both light source and detectors (spectrometers). First, the excitation light is sent through the fiber optic probe. Next, the diffuse-reflected light is collected by optical fibers in the same probe. These fibers deliver the diffuse-reflected light to a visible-wavelength spectrometer (QE-Pro, Ocean Optics, Edinburgh, United Kingdom) and a near-infrared spectrometer (NIR-Quest, Ocean Optics, Edinburgh, United Kingdom). Finally, the light intensity detected by the spectrometers is pre-processed ("Data preprocessing and analysis" section) in order to obtain the tissue reflectance spectra. A schematic drawing of the DRS system is shown in Fig. 2.

In order to obtain the reflectance spectrum preferentially from the superficial tissue (tens of microns deep), we used a quadrifurcated 600-µm-core Low-OH-Silica fiber optic probe (BF46LS01 1-to-4 Fan-Out Bundle, Thorlabs, Munich, Germany) with 630 µm source-to-detector distance (SDD; fiber center-to-center distance represented in Fig. 2). One of the optical fibers was used for illumination, two other fibers were used for collection, and the remaining one was not used during the reflectance measurements. We also used a 2500 µm SDD probe containing one source fiber in the center and 10 collection fibers surrounding it (five for the visible-wavelength detection alternating with five for the near-infrared detection), as seen in Fig. 2. The configuration allows probing deeper tissue layers while achieving higher efficiency on the light collection.

The depth interrogated by each probe was estimated by using a spectral fitting algorithm to extract the optical properties from our DRS measurements. This algorithm was based on forward Monte Carlo simulations of steady-state light transport in multilayered tissues (MCML)[51]. In particular, we used optimized simulations accelerated by graphics processing unit (GPU) reported by Alerstam et al.[52] by considering tissue as a semi-infinite homogeneous medium with the optical properties (absorption coefficient μ_a and scattering coefficient

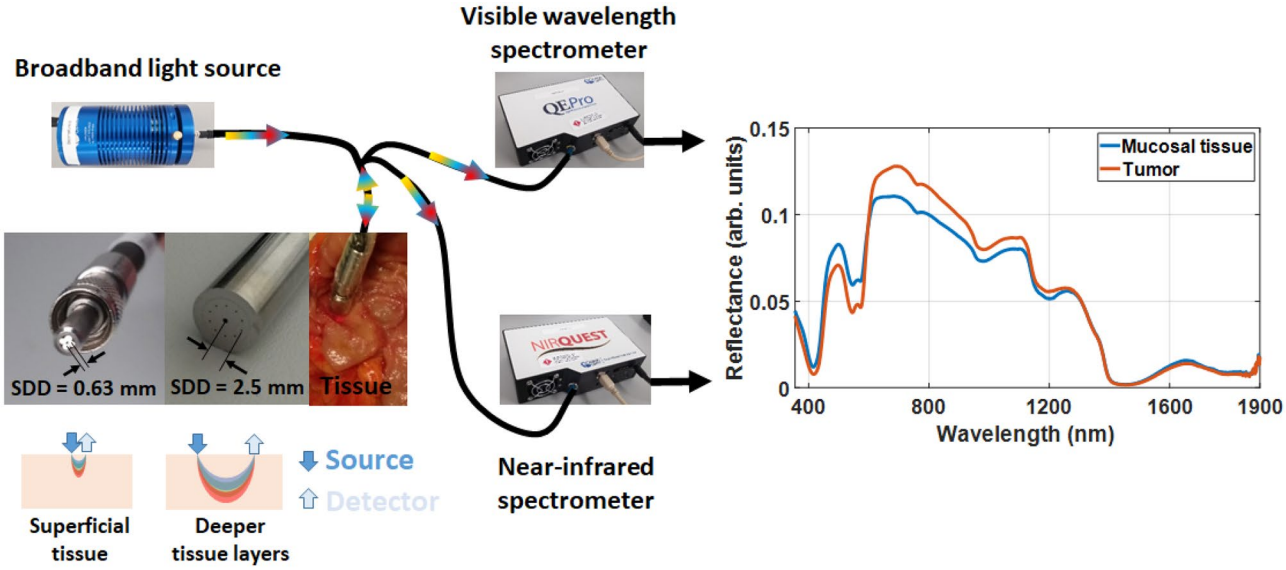


Figure 2. Schematic image of the DRS system. The reflected light can be collected in a wide range of wavelengths and thus, allow the investigation of a larger variety of chromophores in biological tissues.

μ_s) extracted by using a spectral fitting algorithm described in previous studies[12,14,15]. Fluence maps of 5 × 5 mm were generated with simulations using 10 million photon packets, refractive index of the outer medium (η_{out}) of 1, tissue refractive index (η_{rel}) of 1.4, anisotropy factor (g) of 0.9, and 50 µm of radial and depth resolution. Based on these fluence maps, the photon hitting density maps of 3.75 mm × 5 mm were computed by converting cylindric to cartesian coordinates and multiplying the fluence maps at the positions of the source and collection fibers. Then, the position of the maximum photon hitting density value at the mean position between the source and detector was taken as the average probed depth for each wavelength. Then, the minimum and maximum probed depth were reported in this study in order to show the independence of the datasets acquired with each probe and the importance of evaluating the classification performance at each tissue probed volume.

Optical data collection protocol. Prior to and after each run of clinical data collection, we collected the background and reference measurements. The reference measurements were taken on a specialized holder able to keep a fixed distance of 2 mm and 6 mm between the small SDD or large SDD probe and the reflectance standard (FWS-99-01c, Avian Technologies LLC, New London, USA), respectively. The fixed distance allows the comparison of the reflectance data across patients. Prior to each set of tissue measurements, the probes were covered with polyvinyl chloride (PVC) film to avoid possible contamination. The same probes were used for every clinical measurement throughout this study. During the tissue data collection, measurements were performed by positioning the probe 90 degrees from the tissue surface. A total of 1363 spectra were collected for the small SDD probe (630 µm SDD) and 1526 for the large SDD probe (2500 µm SDD).

Data preprocessing and analysis. The data preprocessing comprised of the background subtraction and subsequent division of the captured signal (tissue reflected intensity) by the reflected intensity of the reference (reflectance standard):

$$Reflectance(\lambda) = \frac{Tissue\ reflected\ intensity - Background\ intensity}{Reference\ reflected\ intensity - Background\ intensity}.$$

Once the reflectance spectra were obtained for both visible and near-infrared spectra, these spectra were merged based on the overlapping spectral region between the two spectrometers (from 1095 to 1130 nm). The merging was performed by first doing an interpolation of the overlapping region of the two spectrometers. The interpolated data were used for a weighted sum following:

$$Reflectance(\lambda) = \sum_{i=0}^{100} \frac{\left((100 - i) \times reflectance\ of\ \ VIS\ spectrometer + i \times reflectance\ of\ \ NIR\ spectrometer\right)}{100}$$

The result is a smooth reflectance curve where the reflectance measured by each spectrometer has more contribution in the wavelength regions where they are most sensitive. In order to prepare the reflectance data for classification, the data was centered and scaled/normalized between − 1 and + 1. This scaling ensures the contribution of data at each wavelength is similar for building the classification models used in this study.

Our data analysis consisted of building tissue classification models based on support vector machines (SVMs) and evaluating their accuracy. The training set for the classification was $\{\boldsymbol{x}_i^m, y_i\}_{i=1}^n$ with n samples (e.g. number of reflectance spectra) and with m features (e.g. number of wavelengths). The SVM classifier finds the best

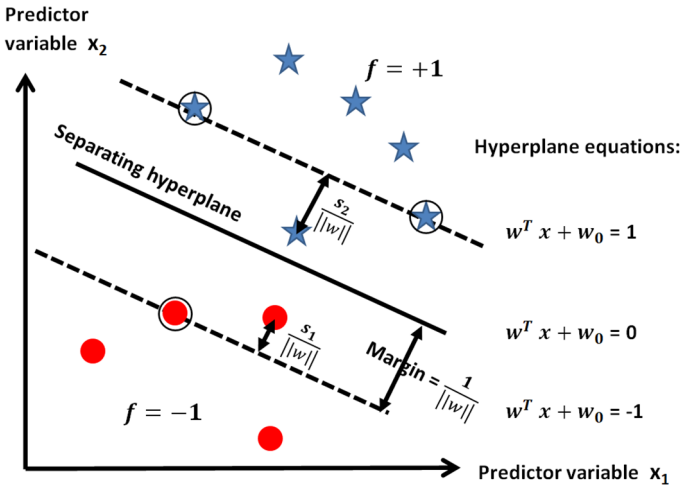


Figure 3. Graphical explanation of SVM hyperplane and accepted margins as defined by parameters involved on the hyperplane equations and slack variables s_i. The stiff condition of hard margins represented in this schematic is relaxed by slack variables, which act as local quantities that add flexibility to the margin.

hyperplane that separates two types of samples described by the class labels $y_i \in \{-1, +1\}$ (e.g. normal mucosa and tumor) based on a predictor variable $\boldsymbol{x}_i^m$ (e.g. reflectance values), where i = 1, 2, …, n. The hyperplane was calculated by:

$$\min_{w,w_0,s_i} \left(\frac{1}{2}||w^2|| + C_i \sum_i s_i \right) \text{subject to } y_i \left(\boldsymbol{w}^T \boldsymbol{x} + w_0 \right) \geq 1 - s_i \text{ and } s_i \geq 0,$$

where $\boldsymbol{w} \in \boldsymbol{R^p}$ and w_0 are parameters that define the hyperplane, C_i is the regularization parameter (or penalty strength) and s_i are the slack variables. s_i was used to measure the level of error accepted on the hyperplane margin, while C defines the penalty for misclassifications. The two parameters together determine the width of the accepted margin on the hyperplane (Fig. 3).

The classification is given by a sign function which determines the side of the hyperplane a given sample falls into:

$$f(\boldsymbol{x}) = sign\left(\sum_{i=1}^{n} y_i C_i K(\boldsymbol{x}, x_i) + w_0 \right)$$

where the $K(x_i, x_j)$ represents the Kernel function:

$$K(x_i, x_j) = y_i K(\boldsymbol{x}, x_i) = \emptyset_i \emptyset_j,$$

where $\emptyset$ is the transformed space for non-linear mapping.

The Kernel function for polynomial kernels is given by:

$$K(x_i, x_j) = (x_i x_j + 1)^p$$

where p is the order of the polynomial. The Kernel function for Gaussian kernels is defined by:

$$K(x_i, x_j) = \exp\left(-\frac{(x_i - x_j)^2}{2\sigma^2} \right).$$

Classification models based on SVMs were built by using the algorithms available in the classification learner app of MATLAB R2016a. All SVM classifiers used the penalty strength C (or Box constraint level in MATLAB) as 1. Linear, quadratic and cubic SVMs used MATLAB automatic heuristic procedure based on subsampling to select an appropriate Kernel scale factor. The software divides all elements of the predictor matrix (scaled reflectance values) by the Kernel scale factor and applies the kernel norm to compute the Gram matrix of the Kernel function. Fine, medium and coarse Gaussian SVMs used Kernel scale factors of 0.5, 2 and 8, respectively.

The models for the broadest wavelength range of this study (from 350 to 1919 nm) were built by several types of SVM algorithms using linear, quadratic, cubic, fine Gaussian, medium Gaussian and coarse Gaussian Kernel functions. In addition, quadratic SVMs were used to develop models on wavelength ranges covered by previous studies reported in the literature. The performance assessment of all generated classification models took into account their sensitivity, specificity, accuracy and area under the receiver operating characteristic curve (AUC). The performance parameters were obtained by using twofold cross-validation for 10 iterations with random

Type of SVM	Sensitivity (%)	Specificity (%)	Accuracy (%)	AUC
Linear	95.2 ± 1.9	91.8 ± 1.1	93.6 ± 1.5	0.970 ± 0.007
Quadratic	93.5 ± 2.4	94.0 ± 1.7	93.8 ± 2.0	0.971 ± 0.014
Cubic	93.8 ± 0.5	93.3 ± 1.9	93.6 ± 1.2	0.968 ± 0.011
Fine Gaussian	86.4 ± 2.3	90.1 ± 1.3	88.2 ± 2.1	0.960 ± 0.007
Medium Gaussian	90.7 ± 0.3	88.0 ± 1.7	89.4 ± 1.0	0.965 ± 0.005
Coarse Gaussian	80.8 ± 3.7	79.9 ± 2.5	80.4 ± 3.1	0.878 ± 0.023

Table 2. Comparison of the classification performance of SVM classifiers for the dataset of the small SDD probe (n = 1363) containing reflectance values from 350 to 1919 nm.

Type of SVM	Sensitivity (%)	Specificity (%)	Accuracy (%)	AUC
Linear	93.1 ± 0.2	91.9 ± 0.6	92.5 ± 0.4	0.963 ± 0.004
Quadratic	96.1 ± 1.8	95.7 ± 0.6	95.9 ± 1.2	0.987 ± 0.005
Cubic	94.9 ± 0.7	95.5 ± 0.4	95.2 ± 0.5	0.983 ± 0.004
Fine Gaussian	82.4 ± 1.9	95.1 ± 1.3	88.4 ± 1.6	0.970 ± 0.005
Medium Gaussian	94.7 ± 0.8	89.6 ± 0.6	92.3 ± 0.7	0.975 ± 0.005
Coarse Gaussian	90.5 ± 1.5	85.1 ± 0.8	87.9 ± 1.2	0.935 ± 0.005

Table 3. Comparison of the classification performance of SVM classifiers for the dataset of the large SDD probe (n = 1526) containing reflectance values from 350 to 1919 nm.

sampling. In order to do this, the dataset was first separated into training and tests sets of equal size. Next, the model was generated using the training set. Then, the model was applied to classify and validate the test set. Afterwards the test and training sets were switched and the same process repeated. At the end of this process, the output was the mean of each classification performance parameter. Then, the process is repeated 10 times. Then, the mean and standard deviation of the of the output of the 10 iterations were determined and reported in this study. The reproducibility of these parameters was assessed by the obtained standard deviations. Although fivefold cross-validation is the usual type of validation, this study used twofold cross-validation in order to show the patterns used for tissue differentiation in our dataset can be found by using 50% of the data as training set instead of 80%. Twofold cross-validation also allows the model to be tested in a larger dataset compared to fivefold cross-validation, which means that successful classification will occur only if the model is robust enough to describe half of the dataset by using half for training. In this case, successful classification means stronger potential of generalization of the model upon increase in sample size, especially compared to validation results using more than 50% of the dataset for training and less than 50% for testing.

Comparison with previous studies. The classification performance for colorectal cancer detection achieved in this study was compared to similar studies investigating DRS, elastic scattering, near-infrared spectroscopy (reflectance modality) and hyperspectral imaging[39–50]. This comparison involved listing the type of tissue evaluation (in vivo or ex vivo), number of patients, wavelength range, source-to-detector distance, types of tissue analyzed, number of analyzed spectra, tissue types used for classification, and diagnostic performance metrics (sensitivity, specificity, accuracy, and AUC). In order to consider comparable probed depths and biomolecules, the performance metrics of this study took into account the classification using similar SDD and wavelength ranges. The classifier used for all the comparisons was the quadratic SVM.

Results

Tissue classification. In order to choose which classifier would be used for comparison of the performance achieved with different wavelength ranges, we first evaluated classification models using SVMs and the entire wavelength range of the diffuse reflectance spectra. The performance of SVMs with linear, quadratic, cubic, fine Gaussian, medium Gaussian and coarse Gaussian Kernel functions on the dataset were assessed for the small SDD probe ($n_{normal\ tissue} = 728$ and $n_{tumor} = 635$) and the large SDD probe ($n_{normal\ tissue} = 804$ and $n_{tumor} = 722$). The probed depth for the small probe ranges from 300 to 1000 μm, whereas the one for the large probe ranges from 800 to 2000 μm (data not shown). Then, the tissue volume interrogated by each probe is different and can affect the classification performance parameters. Sensitivity, specificity, accuracy, and AUC are shown in Tables 2 and 3.

Table 2 shows that the classification performance (small SDD probe) for the polynomial (linear, quadratic and cubic) SVMs is higher than the Gaussian SVMs. The use of the linear SVM leads to higher sensitivity values, whereas quadratic and cubic SVMs can be used to obtain higher performance metrics in exchange for lower sensitivity. The increase in all performance metrics when comparing the coarse Gaussian SVMs with the fine

Analyzed wavelengths	Sensitivity (%)	Specificity (%)	Accuracy (%)	AUC
From 350 o 760 nm	84.7 ± 2.4	87.0 ± 2.3	85.8 ± 2.4	0.922 ± 0.014
From 350 to 800 nm	87.4 ± 2.1	87.3 ± 2.7	87.4 ± 2.4	0.933 ± 0.009
From 400 to 440 nm and from 540 to 580 nm	84.2 ± 2.9	86.3 ± 2.2	85.2 ± 2.6	0.917 ± 0.012
From 400 to 1000 nm	90.5 ± 1.2	92.0 ± 0.5	91.2 ± 0.9	0.963 ± 0.004
From 405 to 665 nm	85.6 ± 1.4	90.0 ± 0.7	87.7 ± 1.1	0.930 ± 0.010
From 405 to 750 nm	86.8 ± 0.5	89.0 ± 0.3	87.8 ± 0.4	0.927 ± 0.005
From 470 to 700 nm	82.3 ± 2.2	86.0 ± 0.8	84.1 ± 1.6	0.900 ± 0.008
From 415 to 425 nm, from 495 to 505 nm, from 525 to 545 nm, and wavelengths 465 nm and 625 nm	74.5 ± 0.4	83.0 ± 0.8	78.5 ± 0.6	0.863 ± 0.005
405.235 nm, 406.42 nm, 408.794 nm, 414.736 nm, 422.48 nm, 468.76 nm, 559.489 nm, 577.506 nm, 594.342 nm, 957.948 nm, and 1000.31 nm	78.2 ± 0.7	86.0 ± 0.5	81.9 ± 0.6	0.903 ± 0.005
From 900 to 1300 nm	86.9 ± 3.5	88.0 ± 3.7	87.4 ± 3.6	0.921 ± 0.020
From 1000 to 1919 nm	92.1 ± 1.2	92.3 ± 1.4	92.2 ± 1.3	0.950 ± 0.011
From 350 to 1919 nm	93.5 ± 2.4	94.0 ± 1.7	93.8 ± 2.0	0.971 ± 0.014

Table 4. Performance metrics of each wavelength range analyzed using the quadratic SVM classifier on the dataset of the small SDD probe.

and medium Gaussian SVMs suggests the optimum decision boundary is reasonably narrow. The narrower the boundary is, the higher the specificity and the lower the sensitivity achieved.

Table 3 indicates the classification performance for the large SDD probe has similar trends as that of the small SDD probe in terms of the comparison between polynomial and Gaussian SVMs. On the other hand, the decrease in the performance metrics when decreasing the Kernel scale factors (i.e. using finer Gaussian SVMs) is not as pronounced. In addition, the quadratic SVM model achieved the highest performance metrics. Since the quadratic SVM led to the highest performance for both probes, we used this SVM for comparing the performance metrics with other studies.

The comparison between the best performance metrics of the small and large SDD probes indicated an average gain of 2.6% sensitivity, 1.7% specificity, 2.1% accuracy and 0.16 AUC for tissue classification between 350 and 1919 nm. This suggests probing deeper tissue layers with this wavelength range may improve colorectal cancer detection during colonoscopy.

The performance metrics ((96.1 ± 1.8)% sensitivity, (95.7 ± 0.6)% specificity, (95.9 ± 1.2)% accuracy and 0.987 ± 0.005 AUC) for the large SDD probe are sufficiently high to show potential comparison with other techniques. Furthermore, these metrics are robust as they are based on twofold cross validation of a 1526 spectra dataset. The same robustness is shown for the dataset of the small SDD probe. The classification performance can be further improved by combining DRS with other optical techniques such as fluorescence spectroscopy (FS), time-resolved fluorescence spectroscopy, Raman spectroscopy, Fourier-transform infrared spectroscopy.

Usefulness of the extended wavelength range. Based on the classification performance on the wavelength ranges of previous studies[39–50], we analyzed the potential benefit of using the extended wavelength for colorectal cancer (CRC) detection. In order to be consistent with the findings of previous studies, this analysis consisted of the comparison of the sensitivity, specificity, accuracy and AUC using the small SDD probe (Table 4).

Table 4 shows the performance metrics for the wavelength ranges covering near-infrared wavelengths are higher than those achieved by analyzing only the visible wavelength range. Moreover, the broader and longer the near-infrared range evaluated, the higher the performance is achieved. The assessment of wavelengths from 1000 to 1919 nm showed similar tissue classification performance compared to the entire wavelength range analyzed in this study (between 350 and 1919 nm). This fact could not be observed by solely analyzing the diagnostic ability of previous studies, as comparison across studies was impossible due to insufficient overlap among investigated wavelength ranges.

Discussion

Relevant biochemical and structural differences for CRC detection. From a clinical perspective, biomolecular changes probed by optical techniques[53–79] can potentially obviate the need for multiple biopsies or polypectomies of normal mucosa as well as identify sessile serrated polyps, which may be difficult to recognize during colonoscopy at times[7–20]. The potential of optical spectroscopy for colorectal cancer (CRC) detection in ex vivo specimens or in vivo during colonoscopy has been evaluated for superficial tissues (small SDD probes) in several wavelength ranges[39–50]. To the best of our knowledge, this is the first study that uses DRS information from deeper tissue layers (2500 μm SDD) to detect cancerous tissues in the luminal wall of ex vivo specimens for colonoscopy applications. Even though light penetrates deeper for certain wavelengths, if small SDD probes are used, the collected light is predominantly reflected from the tissue surface (Fig. 4). Figure 4 shows that the probed depth in the near-infrared region where the maximum probed depth is achieved for both small and large probes. The probed depth of the small probe typically varies between 0.5 and 1 mm (> 0.8 mm for most wavelengths), while that of the large probe varies mostly between 0.5 and 1.9 mm (> 1.4 mm for most wavelengths; data not shown).

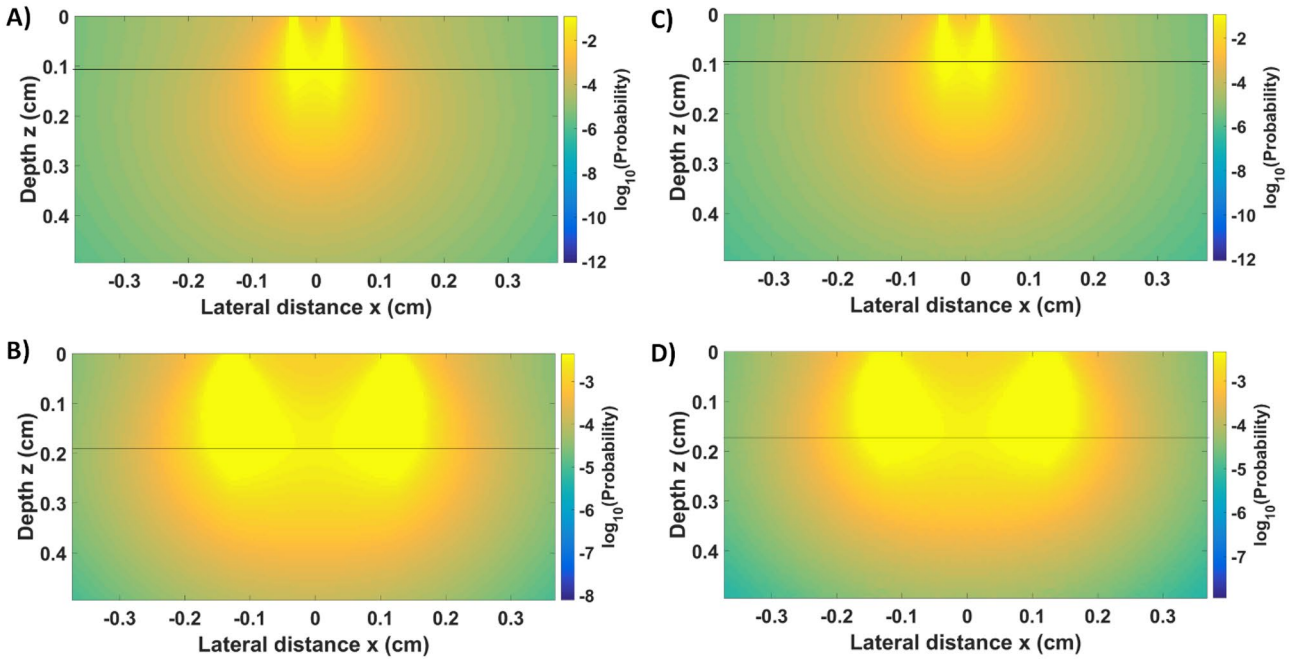


Figure 4. Photon hitting density (PHD) map generated from fluence maps of forward Monte Carlo simulations of light propagation in mucosa (**A**,**B**) tumor (**C**,**D**) tissues at 1150 nm. The black line shows the position of maximum in the middle of the PHD map, which indicates the probed depth at SDD for the (**A**) small probe (630-µm SDD) and (**B**) large probe (2500-µm SDD).

Previous studies used small SDD probes and visible/near-infrared wavelength ranges to investigate signals related to the biochemical composition (related to light absorption) and microstructure (associated to light scattering) of the tissue surface. This biochemical composition includes concentrations of oxyhemoglobin, deoxyhemoglobin, met-hemoglobin, bile, bilirubin, β-carotene, water, lipid, collagen, elastin, and other biomolecules. The tissue microstructure can be investigated due to refractive index mismatches caused by multicellular structures (such as vessels, fibers, etc.), cells size, number of organelles (e.g. mitochondria), composition of tissue layers, extracellular matrix, cell and organelle membranes, collagen fibers and fibrils, and other factors. Once factors such as tissue microstructure, biochemical composition and probed depth are better understood, novel designs of DRS and hyperspectral imaging systems can be proposed to improve the diagnostic accuracy for CRC.

In terms of colonoscopy applications, primary CRC needs to be differentiated from the surrounding normal mucosa (the inner lining of the colon). The intraluminal optical guidance may be affected by other tissue layers apart from the mucosa, especially when using large SDD probes. The colorectal wall is composed of layers of mucosa, submucosa, muscularis propria, and serosa ordered from the intraluminal to the extraluminal side[49]. Each tissue layer differs in their microstructure and biomolecular content which changes the scattering and absorption properties, respectively.

In normal mucosal tissues, the light that enters the colon from the luminal side is first absorbed by mucosal biomolecules (e.g. blood in mucosal capillaries) and scattered by collagen fibers and fibrils, epithelial cells, organelles, and cytoskeleton[80]. The diffuse-reflected light is composed of the scattering within the mucosal layer (Fig. 5) and the backscattered light at the boundary between mucosa and submucosa (refractive index mismatch). The diffuse-transmitted light enters the submucosal layer to be mostly absorbed by water and large submucosal vessels while scattered by the submucosal cellular and subcellular structures. Backscattering happens once more on the interface between the submucosa and muscle layers, which increases the percentage of diffuse-reflected light. In the muscle layer, large collagen bundles can scatter light forward. A small fraction of the light that was not absorbed by the muscle and serosa and backscattered within the muscle layer or in the interface with serosa is diffuse-reflected and may reach the light detector. The detected fraction of diffuse-reflected light of all tissue layers gives the DRS or elastic scattering spectroscopy signal. In tumor tissues, this fraction can be changed upon variation of optical properties resulting from biomolecular and structural associated to carcinogenesis[49].

Most of the precancerous changes on the healthy colorectal mucosa originate in the epithelial tissue[80]. As the cancer progresses, changes due to angiogenesis as well as size and density of collagen fibers can be observed. Angiogenesis generates alterations in blood oxygen saturation and increases the density, volume and disorganization of the blood microvasculature. Cancerous tissues tend to have a high metabolism and an increase in blood volume in the tumor periphery, which can prevent the oxygen and nutrient supply to the center of larger tumors. This lack of oxygen and nutrient supply leads to necrosis and subsequent loss of central microvasculature in late-stage cancers[49]. Most of the tumors probed in this study are of advanced stages which may exhibit more pronounced structural and biomolecular changes. However, these changes are expected to progress over tumor stages and thus, the identification of parameters for optimized early-stage tumor detection requires feasibility studies including tumors of diverse stages such as the present study. Parameters to be optimized include the

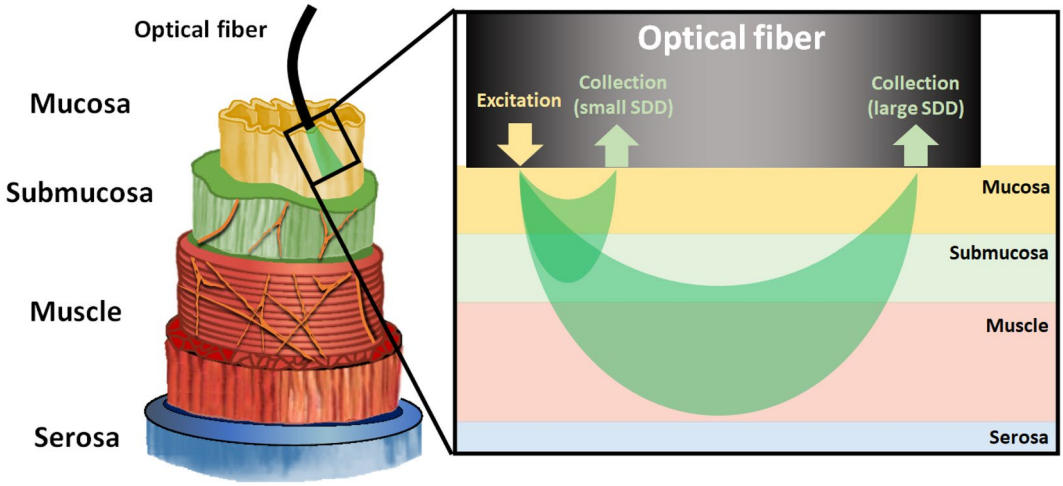


Figure 5. Tissue layers of the colon and rectum (left) and the light-tissue interaction volume interrogated by using the small SDD probe and the large SDD probe. The probed tissue depth increases with the SDD. Variations in the diffuse reflectance signal caused by carcinogenesis were evaluated based on the structural and biomolecular changes of the tissue layers investigated by each probe.

extended wavelength range and larger SDD explored in this study and discussed in more detail in "Wavelength selection and probed depth" section. In addition, DRS and optical spectroscopy are in the process of being introduced as a feasible tool for cancer detection in general, as already discussed in "Introduction" section. The use of DRS and hyperspectral imaging for CRC detection is discussed in the "Wavelength selection and probed depth", "Comparison with DRS-related optical spectroscopy studies" and "Comparison with hyperspectral imaging studies" sections. Limitations due to the dataset based on tumors visible by naked eye are discussed in the "Limitations and validity of this study" section.

In terms of changes to be probed with optical techniques for early-stage cancer detection, Backman and Roy[80] have shown that changes associated with carcinogenesis involve microvessel density in the mucosa (pericryptal network) and the superficial submucosa as well as structural changes on the mucosal crypts and stroma around 200–300 μm from the tissue surface (information from pictures of histology slides shown by the authors). Other suggested optically detectable alterations cited by the authors included nanostructural and microstructural changes in the chromatin structure, collagen fiber crosslinking and cytoskeleton.

Wavelength selection and probed depth. Previous DRS studies targeting cancer detection for colonoscopy guidance reported possible differentiation between luminal normal and premalignant or tumor tissue by using hemoglobin concentration and blood saturation information alone[39,40,81–83]. Similar considerations are made by studies evaluating hyperspectral imaging (HSI) for the same application[41,49,50]. Blood-related parameters are detected on the visible wavelength range, where the blood absorption is stronger (Fig. 6). Prior DRS and HSI studies focused on analysis using visible light, except by Chen et al.[45–47], Ehlen et al.[48] and Yuan et al.[42]. The typically targeted near-infrared wavelength region contains information about the water and lipid absorption. Longer wavelengths or shorter wavenumber also contain information about protein and carbohydrate content. The wavelength ranges used in prior studies are shown in Fig. 6.

In addition to the biochemical information of the wavelength ranges, the DRS signal contains tissue information on depths depending on the optical properties (absorption and scattering coefficients) and source-to-detector distance (SDD). Since the scattering coefficient is large on the visible wavelength range[53], most of the light in this range is diffuse-reflected close to the source of light. Then, using small SDD probes allows efficient collection of visible emitted light and large SDD probes will collect visible light from deeper layers. However, the tissue scattering coefficient is relatively low in the near-infrared wavelength range, which allows the small SDD probes to collect the diffuse-reflected light from the deeper tissue layers, whereas large SDD probes collect light from even deeper layers. Therefore, the DRS probed depth is mainly determined by the SDD of the fiber optic probe.

Although DRS and HSI collect similar tissue information, there are major differences with respect to the probed depth and reflectance standardization. DRS is taken from point measurements in contact with the tissue. In this case, adjusting the probe SDD will control the depth to be probed. Yet, hyperspectral images are taken from a certain tissue area and, thus, each tissue point has a different distance from the detector[85]. This means the tissue reflectance is not standardized, as the standardization process requires every tissue point to be at a fixed distance from both source and detector. Since HSI works by illuminating a tissue area right below the light source and detecting the reflected intensity from the same area, the detected light comes primarily from the tissue surface[85]. Similarly, to the smaller SDD probes for DRS, the wavelength range (and optical properties) will have a strong effect on the probed tissue depth.

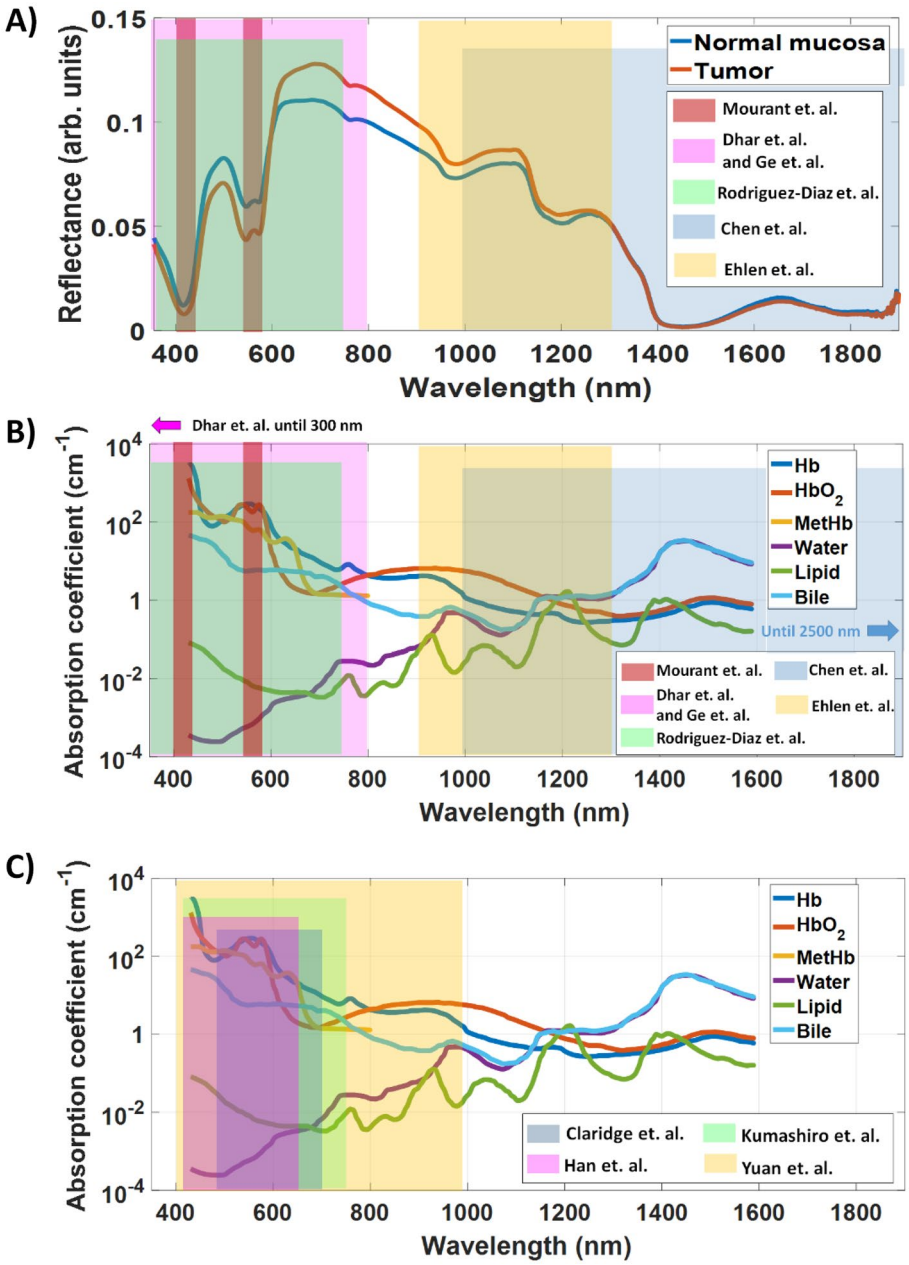


Figure 6. Wavelength ranges analyzed in previous DRS studies shown on the (**A**) mean spectra of normal mucosa and tumor (small SDD probe) collected in this study and (**B**) absorption spectra of endogenous tissue chromophores (biomolecules)[84]. (**C**) Absorption spectra of endogenous tissue chromophores showing the wavelength ranges investigated on previous hyperspectral imaging studies.

Comparison with DRS-related optical spectroscopy studies. By using quadratic SVMs, we analyzed the performance of classification models using the wavelength range of previous studies. Since prior studies used only small SDD probes, we used the dataset of the 630-μm-SDD probe to build the classification models. As already shown in Fig. 6, 4 of these studies focused their analysis on features of the visible wavelength range and near-infrared (NIR) range until 800 nm, whereas 4 studies analyzed the wavelengths higher than 900 nm. In general, studies probing wavelengths lower than 800 nm exhibit lower classification performance for tissue differentiation compared to studies in the NIR range above 900 nm (Table 5). Yet, it is important to note that most of the studies including visible wavelengths were conducted in vivo and with a larger sample size compared to the NIR studies above 900 nm.

The classification performance metrics achieved in this study is comparable to most of the previous studies (Table 5), especially those probing NIR wavelengths above 900 nm and those including visible wavelengths with similar sample size. Non-comparable classification performance metrics are observed in studies by Mourant et al.[39], who have investigated a substantially lower amount of spectra and patients, and Rodriguez-Diaz et al.[44],

Authors	Tissue evaluation	Patients	Wavelength range (analysis)	Source-to-detector distance (SDD)	Tissues considered for analysis	Number of spectra analyzed	Classification	Sensitivity (%)	Specificity (%)	Accuracy (%)	AUC
Mourant et al.[39]	In vivo	15	Analyzed range: 400–440 nm and 540–580 nm collected range: 300–750 nm)	300–400 µm	21 normal mucosa, 31 colitis, inflammatory bowel disease, Crohn's disease, 1 hyperplastic tissue, 6 adenomas and 1 adenocarcinoma	60 (1 spectrum per tissue site)	Non-cancer and cancer and tissues	100	98	–	–
Nogueira et al.[56]	Ex vivo	47	400–440 nm and 540–580 nm	630 µm	47 tumor and 47 normal tissues	1363 (728 normal mucosa and 635 cancer spectra)	Normal mucosa and cancer tissue	84.2 ± 2.9	86.3 ± 2.2	85.2 ± 2.6	0.917 ± 0.012
Dhar et al.[40]	In vivo	45	300–800 nm		138 colonic sites	483 (290 normal, 19 hyperplastic, 69 adenomatous polyps, 74 chronic colitis, and 31 colorectal cancer spectra)	Cancerous and normal tissue	80	86	–	–
							All pathological tissues and normal tissue	92	82	–	–
Ge et al.[43]	In vivo	153	350–800 nm	16 randomly placed fibers for tissue excitation and collection	107 non-neoplastic tissues (84 normal mucosa, 23 hyperplastic polyps) and 53 neoplastic tissues (44 adenomatous polyps, 9 adenocarcinomas)	244 (9 adenocarcinomas, 90 adenomatous polyps, 33 hyperplastic polyps, and 84 normal colon tissue spectra)	Neoplastic tissue from non-neoplastic tissue	79–91	74–91	–	–
							Adenomatous polyps from hyperplastic polyps	85–91	72–75	–	–
Nogueira et al.[56]	Ex vivo	47	350–800 nm	630 µm	47 tumor and 47 normal tissues	1363 (728 normal mucosa and 635 cancer spectra)	Normal mucosa and cancer tissue	87.4 ± 2.1	87.3 ± 2.7	87.4 ± 2.4	0.933 ± 0.009
Rodriguez-Diaz et al.[44]	In vivo	83	330–760 nm	250 µm	85 neoplastic tissue, 80 hyperplastic polyps and 53 polypoid colonic mucosa	218 spectra averaged from 1090 measurements (5 spectra per tissue)	Neoplastic and non-neoplastic tissues	91.5	92.2	91.9	-
Nogueira et al.[56]	Ex vivo	47	350–760 nm	630 µm	47 tumor and 47 normal tissues	1363 (728 normal mucosa and 635 cancer spectra)	Normal mucosa and cancer tissue	84.7 ± 2.4	87.0 ± 2.3	85.8 ± 2.4	0.922 ± 0.014
Chen et al.[45]	Ex vivo	20	1000–2500 nm (wavenumber interval from 4000 cm^{-1} to 10,000 cm^{-1})	Multiple (7.0 mm^2 of sampling area)	78 cancer and 108 normal tissues	78 tumor spectra and 108 normal tissue spectra	Normal and cancer tissues	92.3	100		–
Chen et al.[46]	Ex vivo	–	1000–2500 nm	Multiple (7.0 mm^2 of sampling area)	55 cancer and 55 normal tissue slices (stabilized in 4% formaldehyde)	110 (55 cancer and 55 normal tissue spectra)	Normal and cancer tissues	100	78.6	89.1	–
Chen et al.[47]	Ex vivo	–	1000–2500 nm	Multiple (7.0 mm^2 of sampling area)	58 paraffin tissue sections	58	Normal and cancer tissues	92.8	86.7	–	–
Nogueira et al.[56]	Ex vivo	47	1000–1919 nm	630 µm	47 tumor and 47 normal tissues	1363 (728 normal mucosa and 635 cancer spectra)	Normal mucosa and cancer tissue	92.1 ± 1.2	92.3 ± 1.4	92.2 ± 1.3	0.95 ± 0.011

Continued

Authors	Tissue evaluation	Patients	Wavelength range (analysis)	Source-to-detector distance (SDD)	Tissues considered for analysis	Number of spectra analyzed	Classification	Sensitivity (%)	Specificity (%)	Accuracy (%)	AUC
Ehlen et al.[48]	Ex vivo	10	Analyzed range: 900–1300 nm (collected range: 900–1720 nm)	400 µm + fiber cladding	10 tumor and 10 normal tissues	95 (50 tumor and 45 normal tissue spectra)	Normal mucosa and cancer tissue (DRS and FS)	98	93	96	–
							Normal mucosa and cancer tissue (only DRS)	93	68	82	
Nogueira et al.[56]	Ex vivo	47	900–1300 nm	630 µm	47 tumor and 47 normal tissues	1363 (728 normal mucosa and 635 cancer spectra)	Normal mucosa and cancer tissue	86.9 ± 3.5	88.0 ± 3.7	87.4 ± 3.6	0.921 ± 0.020

Table 5. Comparison of clinical data, instrument specifications and classification performance metrics across optical spectroscopy studies. The dataset of this study (represented by the Nogueira et al.[56] in the table) was evaluated in the wavelength ranges of previous studies and for comparison of classification results.

who have used 250 µm of fiber SDD and probed different types of tissue compared to the present study. In terms of purely NIR studies, the group of Chen et al.[45–47] showed the tissue discrimination achieved by using random forest, Adaboost and SVM classifiers. As expected, the closest classification performance compared to the present study was the SVM classifier. Still, Ehlen et al.[48] found 6.1% higher sensitivity, 20% lower specificity and 5.4% lower accuracy compared to the present study, which may be originated by using 400-µm fiber SDD and substantially smaller sample size (number of patients and spectra).

The accuracy achieved in our study tends to be higher (i.e. due to increased sensitivity and/or specificity) compared to the in vivo DRS studies (Table 5). It is unclear whether higher accuracy is obtained due to differences in the tissue evaluation procedure (in vivo or ex vivo), number of patients, region where the study was conducted, types of interrogated tissue or machine learning model used in each study. At all cases, our classification model contains the highest number of investigated spectra and therefore, the largest representation over heterogeneity caused by probe contact pressure effects, probe positioning and other factors contributing to DRS signal variation during contact measurements.

Comparison with hyperspectral imaging studies. In order to compare the performance metrics achieved by wavelength ranges of hyperspectral imaging (HSI) studies, we used quadratic SVM models build with the dataset of the 630-µm-SDD probe. The equivalent comparison comes from the information hyperspectral imaging gets from the superficial tissue, which is comparable to what is obtained by using the short SDD probe of our study. Most of the HSI studies have exploited the reflectance on the visible wavelength region and thus, based their tissue identification on blood absorption and relatively high superficial tissue scattering (Fig. 6, Table 6). Kumashiro et al.[50] extended the wavelength range up to 750 nm and Yuan et al.[42] extended the range further up to 1000 nm. Although the study of Yuan et al. investigated the water absorption signal at longer wavelengths, the study was limited by ex vivo samples of 4 patients.

Studies including data on wavelengths between 400–470 nm showed higher classification performance compared to the study of Claridge et al.[49], who used only wavelengths longer than 470 nm. This agrees with the results of our study and suggests that the blood content and oxygenation in superficial tissue layers highly contributes to the discrimination between mucosa and tumor tissues. In addition, even though Han et al.[41] investigated a substantially narrower wavelength range than Yuan et al.[42], they achieved higher classification performance in their in vivo study compared to an ex vivo study. This performance suggests that blood oxygenation changes in vivo, especially those probed between 405 and 665 nm, contribute significantly to the tissue differentiation. Still, further investigation is required to understand the origin of the contrast between normal and cancerous tissues by using HSI.

Previous HSI studies have investigated a significantly smaller patient population compared to DRS studies. However, the classification performance metrics obtained in this study as well as their changes due to wavelength ranges were comparable when considering similar specifications with respect to the probe depth investigated by either imaging from a distance or using lower SDD fiber probes. Compared to the performance metrics that could be achieved in this study by using the wavelength range between 405 and 665 nm, Han et al.[41] obtained significantly higher metrics on their in vivo study by using support vector machines. Conversely, the ex vivo tissue classification performed on a wider wavelength range (from 405 to 750 nm) by Kumashiro et al.[50] led to much lower performance metrics compared to our study.

Current hyperspectral imaging studies are limited by the number of patients, and lack of standardization on imaged angles, distance from the tissue and SDDs for each pixel. Therefore, comparison with performance metrics achieved by point spectroscopy (which standardizes measurement parameters and has proven to be robust among a large number of patients) still requires further investigation to address those limitations. On the other hand, HSI has the potential to cause a significant decrease in measurement times by acquiring data of multiple points at once. In order to keep the differentiation achieved by previous spectroscopic studies, HSI has to be used at optimum wavelengths for application-specific tissue identification.

Authors	Tissue evaluation	Patients	Wavelength range (analysis)	Normal and cancerous tissues considered for analysis	Number of images and spectra analyzed	Classification	Sensitivity (%)	Specificity (%)	Accuracy (%)	AUC
Claridge et al.[49]	Ex vivo	8	470–700 nm	7 adenocarcinomas, 2 adenomatous polyps, 1 adenoma, 1 tubulo-villous adenoma, 1 neoplastic polyp and 1 hyperplastic polyp and surrounding normal mucosa	–	Colorectal lesions and normal mucosa	85	78	–	–
Nogueira et al.[56]	Ex vivo	47	470–700 nm	47 tumor and 47 normal tissues	1363	Normal mucosa and cancer tissue	82.3 ± 2.2	86.0 ± 0.8	84.1 ± 1.6	0.900 ± 0.008
Kumashiro et al.[50]	Ex vivo	21	405–750 nm	40 tumor and 95 normal mucosa sites	135 (40 tumor and 95 normal mucosa images)	Normal mucosa and cancer tissue	72.5	82.1	–	–
						All pathological and normal tissues	75.0	55.8	–	–
Nogueira et al.[56]	Ex vivo	47	405–750 nm	47 tumor and 47 normal tissues	1363	Normal mucosa and cancer tissue	86.8 ± 0.5	89.0 ± 0.3	87.8 ± 0.4	0.927 ± 0.005
Han et al.[41]	In vivo	12	405–665 nm	21 colorectal tumors or adenomatous polyps and their surrounding normal mucosa	–	Normal mucosa and cancer tissue (all hyperspectral images)	96.9 ± 2.3	91.5 ± 4.1	94.5 ± 4.9	–
	In vivo	12	415–425 nm, 495–505 nm, 525–545 nm and the wavelengths 465 nm and 625 nm	21 colorectal tumors or adenomatous polyps and their surrounding normal mucosa	–	Normal mucosa and cancer tissue (selected wavelength bands)	94.7 ± 4.2	89.1 ± 3.2	92.9 ± 5.4	–
Nogueira et al.[56]	Ex vivo	47	405–665 nm	47 tumor and 47 normal tissues	1363	Normal mucosa and cancer tissue	85.6 ± 1.4	90.0 ± 0.7	87.7 ± 1.1	0.930 ± 0.010
Nogueira et al.[56]	Ex vivo	47	415–425 nm, 495–505 nm, 525–545 nm and the wavelengths 465 nm and 625 nm	47 tumor and 47 normal tissues	1363	Normal mucosa and cancer tissue	74.5 ± 0.4	83.0 ± 0.8	78.5 ± 0.6	0.863 ± 0.005
Yuan et al.[42]	Ex vivo	4	Analyzed: 405.235 nm, 406.42 nm, 408.794 nm, 414.736 nm, 422.48 nm, 468.76 nm, 559.489 nm, 577.506 nm, 594.342 nm, 957.948 nm, and 1,000.31 nm (collected: 400 nm and 1000 nm)	–	–	Cancerous and non-cancerous tissues	93.8	87.5	90.6	–
Nogueira et al.[56]	Ex vivo	47	400–1000 nm	47 tumor and 47 normal tissues	1363	Normal mucosa and cancer tissue	90.5 ± 1.2	92.0 ± 0.5	91.2 ± 0.9	0.963 ± 0.004
Nogueira et al.[56]	Ex vivo	47	405.235 nm, 406.42 nm, 408.794 nm, 414.736 nm, 422.48 nm, 468.76 nm, 559.489 nm, 577.506 nm, 594.342 nm, 957.948 nm, and 1,000.31 nm	47 tumor and 47 normal tissues	1363	Normal mucosa and cancer tissue	78.2 ± 0.7	86.0 ± 0.5	81.9 ± 0.6	0.903 ± 0.005

Table 6. Comparison of clinical data, instrument specifications and classification performance metrics across hyperspectral imaging studies and this study. The dataset of this study (represented by the Nogueira et al.[56] in the table) was evaluated in the wavelength ranges of previous studies and for comparison of classification results.

Limitations and validity of this study. Our paper has a number of limitations. First, this study does not include non-cancer pathology, which will be investigated in future research to incorporate data for improved tissue identification and possibly accurate sampling of areas to be biopsied. The measurements of this study have been performed in tumors of diverse stages with predominance of advanced stage tumors (Table 1). The tumor sites to be measured were identified by a combination of palpation and naked eye determination by experienced surgeons who demarcated the tumor region. However, this determination does not decrease the validity of our dataset and robust classification model, which is based on a larger dataset compared to previous studies (Tables 5, 6) and comprises variations on DRS spectra due to parameters discussed in this section. With this in mind, tissue alterations occurring in early-stage cancer (e.g. changes on the tissue microstructure due to cell proliferation) are expected to be the same as advanced cancer but with lower magnitude. Our feasibility study shows that these alterations are detectable and improved detection is achieved by larger SDD probes as well as extended wavelength ranges into the near-infrared.

Since the tissue blood oxygenation may change in ex vivo tissues during our measurements, we evaluated its changes over time in a pilot observation of the DRS signal in 3 patients and found no significant variations during the first 15 min of our data collection (measurements taken every 5 min and data not shown). Even though tissue oxygenation may be different between our research and prior in vivo studies due to collection of DRS measurements of ex vivo tissues, the trend observed in our data matches with that found in previous studies in general. Variations due to tissue blood oxygenation are expected to be similar to what was obtained by Baltussen et al.[9], who reported that blood content and StO_2 increased in the measured ex vivo within 1 h after resection in relation to in vivo tissues. Other factors changing ex vivo spectra include tissue dehydration, which was reduced as much as possible in this study by maintaining the tissue moisture with a wet wipe. However, it is important to remember that Baltussen et al.[9] used a 1290-µm SDD probe and investigated fat, tumor, and healthy colorectal wall tissues.

In terms of variations observed in every technique requiring contact measurements, probe contact pressure and sufficient optical contact may be challenging to accomplish during in vivo endoscopy. If we consider that the large SDD probe collects data from a larger tissue volume and pressure is applied more uniformly during measurements, a reduced sensitivity to optical contact and probe positioning is expected. In this case, higher repeatability of measurements with the large SDD may be associated with the higher classification performance with the large SDD probe. Yet, the larger probed volume means the probe contact pressure may lead to variations due to the thickness of tissue layers. The variations commented above were previously reported[62] and need to be further investigated in order to apply automated corrections to DRS spectra. Still, the measurements performed in this study incorporate variations due to probe contact pressure and temperature decrease in ex vivo tissues and a dataset substantially larger (1363 spectra for the small SDD probe and 1526 for the large SDD probe) than prior studies was generated in order to build a robust classification model.

Finally, other types of classification methods (e.g. deep neural networks) can be used to build classification models that can easily be run in the real-time. In fact, we tested other types of classification methods which resulted in sensitivities and specificities higher than 85% (data not shown). High performance metrics independent on the classification method used means our data clearly shows the discrimination between mucosa and cancer tissues. Therefore, we believe that future in vivo studies advancing research presented here should consider using larger SDD probes and extended wavelength ranges in the near-infrared for differentiation between mucosa and cancer tissues. As a factor for clinical translation, the incorporation of 2.5-mm-SDD probes is feasible, as the size of colonoscope channels range from 2.8 to 4.2 mm[86,87].

Conclusions

In this study, we evaluated the usefulness of the extended wavelength range for improving CRC detection using DRS and compared results achieved in this study with previous research. By using probing the superficial tissue, we obtained (93.5 ± 2.4)% sensitivity, (94.0 ± 1.7)% specificity and 0.971 ± 0.014 AUROC, whereas (96.1 ± 1.8)% sensitivity, (95.7 ± 0.6)% specificity and 0.987 ± 0.005 AUROC was achieved by sampling deeper tissue layers. To the best of our knowledge, this is the first DRS study to investigate the potential of probing deeper tissue layers using larger SDD probes for CRC detection in the luminal wall. Our study was conducted in ex vivo tissues, while it is straight forward to extend this methodology to an in vivo examination during endoscopy. Future studies employing diffuse reflectance spectroscopy, elastic scattering spectroscopy, near-infrared spectroscopy, hyperspectral imaging and spatial frequency domain imaging can exploit enhanced tumor detection due to the use of large SDD probes and the broadband wavelength range illustrated in this study. In a practical perspective, this study could potentially be used to develop a probe for CRC detection during colonoscopy. Real-time tissue classification is enabled by automated SVM model coupled with a DRS instrument capable of displaying the result of a single reading in about 2–3 s. By integrating this capability into a flexible fiberoptic probe which could be passed down a scope working channel, optical spectroscopy can obviate the need for multiple biopsies or polypectomies of normal mucosa as well as identify more subtle mucosal abnormalities such as sessile serrated polyps for example, which may be difficult to recognize during colonoscopy.

Received: 10 August 2020; Accepted: 4 December 2020
Published online: 12 January 2021

References

1. Bray, F. *et al.* Global cancer statistics 2018: GLOBOCAN estimates of incidence and mortality worldwide for 36 cancers in 185 countries. *CA Cancer J. Clin.* **68**(6), 394–424 (2018).
2. Ferlay, J. *et al. Global Cancer Observatory: Cancer Today* (International Agency for Research on Cancer, Lyon, 2018).
3. WHO. *Estimated Number of Incident Cases from 2018 to 2040, All Cancers, Both Sexes, All Ages* (WHO, Geneva, 2020).
4. Issa, I. A. & Noureddine, M. Colorectal cancer screening: An updated review of the available options. *World J. Gastroenterol.* **23**(28), 5086 (2017).
5. Vogelstein, B. *et al.* Genetic alterations during colorectal-tumor development. *N. Engl. J. Med.* **319**(9), 525–532 (1988).
6. Bond, J. H. Fecal occult blood test screening for colorectal cancer. *Gastrointest. Endosc. Clin.* **12**(1), 11–21 (2002).
7. De Koning, S. G. B. *et al.* Toward complete oral cavity cancer resection using a handheld diffuse reflectance spectroscopy probe. *J. Biomed. Opt.* **23**(12), 121611 (2018).
8. De Boer, L. L. *et al.* Fat/water ratios measured with diffuse reflectance spectroscopy to detect breast tumor boundaries. *Breast Cancer Res. Treat.* **152**(3), 509–518 (2015).
9. Baltussen, E. J. M. *et al.* Comparing in vivo and ex vivo fiberoptic diffuse reflectance spectroscopy in colorectal cancer. *Transl. Biophoton.* **1**(1–2), e201900008 (2019).
10. Baltussen, E. J. M., Sterenborg, H. J. C. M., Ruers, T. J. M. & Dashtbozorg, B. Optimizing algorithm development for tissue classification in colorectal cancer based on diffuse reflectance spectra. *Biomed. Opt. Express* **10**(12), 6096–6113 (2019).
11. Langhout, G. C. *et al.* Differentiation of healthy and malignant tissue in colon cancer patients using optical spectroscopy: A tool for image-guided surgery. *Lasers Surg. Med.* **47**(7), 559–565 (2015).
12. Langhout, G. C. *et al.* Colorectal cancer identified using optical spectroscopy. *Ann. Oncol.* **25**, 206 (2014).
13. Soares, J. S. *et al.* Diagnostic power of diffuse reflectance spectroscopy for targeted detection of breast lesions with microcalcifications. *Proc. Natl. Acad. Sci.* **110**(2), 471–476 (2013).
14. Spliethoff, J. W. *et al.* Improved identification of peripheral lung tumors by using diffuse reflectance and fluorescence spectroscopy. *Lung Cancer* **80**(2), 165–171 (2013).
15. Evers, D. J. *et al.* Optical sensing for tumor detection in the liver. *Eur. J. Surg. Oncol.* **39**(1), 68–75 (2013).
16. Tanis, E. *et al.* In vivo tumor identification of colorectal liver metastases with diffuse reflectance and fluorescence spectroscopy. *Lasers Surg. Med.* **48**(9), 820–827 (2016).
17. Baltussen, E. J. M. *et al.* Diffuse reflectance spectroscopy as a tool for real-time tissue assessment during colorectal cancer surgery. *J. Biomed. Opt.* **22**(10), 106014 (2017).
18. Baltussen, E. J. M. *et al.* Hyperspectral imaging for tissue classification, a way toward smart laparoscopic colorectal surgery. *J. Biomed. Opt.* **24**(1), 16002 (2019).
19. Baltussen, E. J. M. *et al.* Using diffuse reflectance spectroscopy to distinguish tumor tissue from fibrosis in rectal cancer patients as a guide to surgery. *Lasers Surg. Med.* **52**, 604 (2019).
20. Baltussen, E. J. M. *et al.* Tissue diagnosis during colorectal cancer surgery using optical sensing: An in vivo study. *J. Transl. Med.* **17**(1), 1–10 (2019).
21. Li, W., Liu, Y. & Qian, Z. Determination of detection depth of optical probe in pedicle screw measurement device. *Biomed. Eng. Online* **13**(1), 1–11 (2014).
22. Prosst, R. & Gahlen, J. Fluorescence diagnosis of colorectal neoplasms: a review of clinical applications. *Int. J. Colorectal Dis.* **17**(1), 1–10 (2002).
23. Cothren, R. M. *et al.* Detection of dysplasia at colonoscopy using laser-induced fluorescence: A blinded study. *Gastrointest. Endosc.* **44**(2), 168–176 (1996).
24. Saini, M. K., Juneja, M. & Mittal, A. *Colorectal Cancer Detection from Colonoscopy Videos: A Comprehensive Survey of Computer-Aided Diagnosis Techniques* (2018).
25. Molckovsky, A., Wong Kee Song, L. M., Shim, M. G., Marcon, N. E. & Wilson, B. C. Diagnostic potential of near-infrared Raman spectroscopy in the colon: Differentiating adenomatous from hyperplastic polyps. *Gastrointest. Endosc.* **57**(3), 396–402 (2003).
26. Widjaja, E., Zheng, W. & Huang, Z. Classification of colonic tissues using near-infrared Raman spectroscopy and support vector machines. *Int. J. Oncol.* **32**(3), 653–662 (2008).
27. Li, S. *et al.* Identification and characterization of colorectal cancer using Raman spectroscopy and feature selection techniques. *Opt. Express* **22**(21), 25895–25908 (2014).
28. Salman, A., Shufan, E., Sahu, R. K., Mordechai, S. & Sebbag, G. Insights on colorectal cancer relapse by infrared microscopy from anastomosis tissues: Further analysis. *Vib. Spectrosc.* **83**, 17–25 (2016).
29. Eker, C. *et al.* Clinical spectral characterisation of colonic mucosal lesions using autofluorescence and δ aminolevulinic acid sensitisation. *Gut* **44**(4), 511–518 (1999).
30. Andersson, P. S. *et al.* Fluorescence endoscopy instrumentation for improved tissue characterization. *Med. Phys.* **14**(4), 633–636 (1987).
31. Mayinger, B. *et al.* Endoscopic light-induced autofluorescence spectroscopy for the diagnosis of colorectal cancer and adenoma. *J. Photochem. Photobiol. B Biol.* **70**(1), 13–20 (2003).
32. Shao, X., Zheng, W. & Huang, Z. In vivo diagnosis of colonic precancer and cancer using near-infrared autofluorescence spectroscopy and biochemical modeling. *J. Biomed. Opt.* **16**(6), 67005 (2011).
33. Wang, C.-Y., Lin, J.-K. & Chiang, H. K. Autofluorescence spectroscopy to identify normal and cancerous colorectal tissues. In *Proc. 20th Annual International Conference of the IEEE Engineering in Medicine and Biology Society. Vol. 20 Biomedical Engineering Towards the Year 2000 and Beyond (Cat. No.98CH36286)* Vol. **2**, 967–969 (1998).
34. Kwek, L. C. *et al.* High-sensitivity and specificity of laser-induced autofluorescence spectra for detection of colorectal cancer with an artificial neural network. *Appl. Opt.* **44**(19), 4004–4008 (2005).
35. Coda, S. *et al.* Fluorescence lifetime spectroscopy of tissue autofluorescence in normal and diseased colon measured ex vivo using a fiber-optic probe. *Biomed. Opt. Express* **5**(2), 515–538 (2014).
36. Tang, G., Lu, H., Zhang, Y., Yan, S. & Chen, Z. Detection of human colonic adenoma by laser-induced autofluorescence integrated with diffuse reflectance spectroscopy. *Biomed. Photonics Optoelectron. Imaging* **4224**, 174–178 (2000).
37. Wallace, M. B. & Kiesslich, R. Advances in endoscopic imaging of colorectal neoplasia. *Gastroenterology* **138**(6), 2140–2150 (2010).
38. Aihara, H., Tajiri, H. & Suzuki, T. Application of autofluorescence endoscopy for colorectal cancer screening: Rationale and an update. *Gastroenterol. Res. Pract.* **2012**, 1 (2012).
39. Mourant, J. R. *et al.* Elastic scattering spectroscopy as a diagnostic tool for differentiating pathologies in the gastrointestinal tract: Preliminary testing. *J. Biomed. Opt.* **1**(2), 192–200 (1996).
40. Dhar, A. *et al.* Elastic scattering spectroscopy for the diagnosis of colonic lesions: Initial results of a novel optical biopsy technique. *Gastrointest. Endosc.* **63**(2), 257–261 (2006).
41. Han, Z. *et al.* In vivo use of hyperspectral imaging to develop a noncontact endoscopic diagnosis support system for malignant colorectal tumors. *J. Biomed. Opt.* **21**(1), 16001 (2016).

42. Yuan, X. *et al.* Hyperspectral imaging and SPA–LDA quantitative analysis for detection of colon cancer tissue. *J. Appl. Spectrosc.* **85**(2), 307–312 (2018).
43. Ge, Z., Schomacker, K. T. & Nishioka, N. S. Identification of colonic dysplasia and neoplasia by diffuse reflectance spectroscopy and pattern recognition techniques. *Appl. Spectrosc.* **52**(6), 833–839 (1998).
44. Rodriguez-Diaz, E. *et al.* Endoscopic histological assessment of colonic polyps by using elastic scattering spectroscopy. *Gastrointest. Endosc.* **81**(3), 539–547 (2015).
45. Chen, H. *et al.* "Diagnosis of colorectal cancer by near-infrared optical fiber spectroscopy and random forest. *Spectrochim. Acta A Mol. Biomol. Spectrosc.* **135**, 185–191 (2015).
46. Chen, H., Lin, Z., Mo, L. & Tan, C. Identification of colorectal cancer using near-infrared spectroscopy and adaboost with decision stump. *Anal. Lett.* **50**(16), 2608–2618 (2017).
47. Chen, H., Tan, C., Wu, H., Lin, Z. & Wu, T. Feasibility of rapid diagnosis of colorectal cancer by near-infrared spectroscopy and support vector machine. *Anal. Lett.* **47**(15), 2580–2593 (2014).
48. Ehlen, L. *et al.* Synergy of fluorescence and near-infrared spectroscopy in detection of colorectal cancer. *J. Surg. Res.* **242**, 349–356 (2019).
49. Claridge, E. & Hidović-Rowe, D. Model based inversion for deriving maps of histological parameters characteristic of cancer from ex-vivo multispectral images of the colon. *IEEE Trans. Med. Imaging* **33**(4), 822–835 (2013).
50. Kumashiro, R. *et al.* Integrated endoscopic system based on optical imaging and hyperspectral data analysis for colorectal cancer detection. *Anticancer Res.* **36**(8), 3925–3932 (2016).
51. Wang, L., Jacques, S. L. & Zheng, L. MCML—Monte Carlo modeling of light transport in multi-layered tissues. *Comput. Methods Progr. Biomed.* **47**(2), 131–146 (1995).
52. Alerstam, E. *et al.* Next-generation acceleration and code optimization for light transport in turbid media using GPUs. *Biomed. Opt. Express* **1**(2), 658–675 (2010).
53. Jacques, S. L. Optical properties of biological tissues: A review. *Phys. Med. Biol.* **58**(11), R37 (2013).
54. Richards-Kortum, R. & Sevick-Muraca, E. Quantitative optical spectroscopy for tissue diagnosis. *Annu. Rev. Phys. Chem.* **47**(1), 555–606 (1996).
55. de Paula Campos, C. *et al.* Fluorescence spectroscopy in the visible range for the assessment of UVB radiation effects in hairless mice skin. *Photodiagn. Photodyn. Ther.* **20**, 21–27 (2017).
56. Saito Nogueira, M., Cosci, A. & Kurachi, C. Assessment of oxidative stress and metabolic rates in liver grafts using time-resolved fluorescence spectroscopy. *Biophotonics Photonic Solut. Better Health Care* **6**, 144 (2018).
57. Kurachi, C., Pires, L., Nogueira, M. S. & Pratavieira, S. Lifetime fluorescence for the detection of skin lesions. *Biomed. Opt.* **2014**, BS4B.3 (2014).
58. da Silva, A. P., Saito Nogueira, M., Jo, J. A., Salvador Bagnato, V. & Mayumi Inada, N. Optical based diagnosis and treatment of onychomycosis. *Biomed. Opt.* **2016**, 37 (2016).
59. de Andrade, C. T. *et al*. Optical spectroscopy of radiotherapy and photodynamic therapy responses in normal rat skin shows vascular breakdown products. In *Proc. SPIE*, 969410 (2016).
60. Ono, B. A., Nogueira, M., Pires, L., Pratavieira, S. & Kurachi, C. Subcellular localization and photodynamic activity of Photodithazine (glucosamine salt of chlorin e6) in murine melanoma B16–F10: An in vitro and in vivo study. *Opt. Methods Tumor Treat. Detect. Mech. Tech. Photodyn. Ther.* **1047616**, 44 (2018).
61. Nicolodelli, G. *et al.* Fluorescence lifetime evaluation of whole soils from the Amazon rainforest. *Appl. Opt.* **56**(24), 6936–6941 (2017).
62. Saito Nogueira, M. *et al.* Diffuse reflectance spectroscopy for determination of optical properties and chromophore concentrations of mice internal organs in the range of 350 nm to 1860 nm. *Biophotonics Photonic Solut. Better Health Care* **6**, 125 (2018).
63. Carvalho, L. F. C. S., Nogueira, M. S., Neto, L. P. M., Bhattacharjee, T. T. & Martin, A. A. Raman spectral post-processing for oral tissue discrimination—A step for an automatized diagnostic system: Erratum. *Biomed. Opt. Express* **8**(11), 5218 (2017).
64. Carvalho, L. F. C. S., Nogueira, M. S., Neto, L. P. M., Bhattacharjee, T. T. & Martin, A. A. Raman spectral post-processing for oral tissue discrimination—A step for an automatized diagnostic system. *Biomed. Opt. Express* **8**(11), 5218–5227 (2017).
65. Saito Nogueira, M. *et al.* Portable fluorescence lifetime spectroscopy system for in-situ interrogation of biological tissues. *J. Biomed. Opt.* **22**(12), 1 (2017).
66. Nogueira, M. S. *Fluorescence Lifetime Spectroscopy for Diagnosis of Clinically Similar Skin Lesions* (Instituto de Física de São Carlos, Física Aplicada, 2016).
67. Felipe, L. & Nogueira, M. S. New insights of Raman spectroscopy for oral clinical applications. *Analyst* **143**, 6037–6048 (2018).
68. Leal, L. B. Vibration spectroscopy and body biofluids: Literature review for clinical applications. *Photodiagn. Photodyn. Ther.* **24**, 237–244 (2018).
69. Carvalho, L. F. C. S. *et al.* In vivo Raman spectroscopic characteristics of different sites of the oral mucosa in healthy volunteers. *Clin. Oral Investig.* **23**, 1–11 (2018).
70. Nogueira, M. S., Pratavieira, S. & Kurachi, C. Fluorescence lifetime spectroscopy for evaluation of photoaging process at sun exposed and non-exposed skin. Livro de Resumos. In *SIFSC - Integrated Graduation and Graduation Week of the São Carlos Institute of Physics* (2015).
71. Nogueira, M. S. *et al.* Portable fluorescence microendoscope system for smartphones and imaging processing software. Tech. Summ. In *SPIE Biophotonics South America* (2015).
72. Nogueira, M. S., Pratavieira, S. & Kurachi, C. Evaluation of photoaging at sun exposed and non-exposed skin using a fluorescence lifetime spectroscopy system. Livro de Resumos. In *SIFSC - Integrated Graduation and Graduation Week of the São Carlos Institute of Physics* (2015).
73. Saito Nogueira, M., Texeira Rosa, R. G., Pratavieira, S. S., de D'Almeida, C. P. C. D. P. & Kurachi, C. Assembly and characterization of a fluorescence lifetime spectroscopy system for skin lesions diagnostic. *Biophotonics S. Am.* **9531**, 95313 (2015).
74. Cosci, A. *et al.* Time-resolved fluorescence spectroscopy for clinical diagnosis of actinic cheilitis: erratum. *Biomed. Opt. Express* **7**(10), 4210–4219 (2016).
75. Cosci, A. *et al.* Time-resolved fluorescence spectroscopy for clinical diagnosis of actinic cheilitis. *Biomed. Opt. Express* **7**(10), 4210–4219 (2016).
76. Saito Nogueira, M. *et al.* Evaluation of actinic cheilitis using fluorescence lifetime spectroscopy. In *Proc. SPIE*, 97031U (2016).
77. Pires, L., Nogueira, M. S., Pratavieira, S., Moriyama, L. T. & Kurachi, C. Time-resolved fluorescence lifetime for cutaneous melanoma detection. *Biomed. Opt. Express* **5**(9), 3080 (2014).
78. Saito Nogueira, M. & Kurachi, C. Assessing the photoaging process at sun exposed and non-exposed skin using fluorescence lifetime spectroscopy. In *Proc. SPIE*, 97031W (2016).
79. Almeida, C. D. P. D., Campos, C., Nogueira, M. S. & Kurachi, C. Time-resolved and steady-state fluorescence spectroscopy for the assessment of skin photoaging process. *Biophotonics S. Am.* **9531**, 1–7 (2015).
80. Backman, V. & Roy, H. K. Advances in biophotonics detection of field carcinogenesis for colon cancer risk stratification. *J. Cancer* **4**(3), 251 (2013).
81. Roy, H. K. *et al.* Spectroscopic microvascular blood detection from the endoscopically normal colonic mucosa: biomarker for neoplasia risk. *Gastroenterology* **135**(4), 1069–1078 (2008).

82. Wang, H.-W. *et al.* Diffuse reflectance spectroscopy detects increased hemoglobin concentration and decreased oxygenation during colon carcinogenesis from normal to malignant tumors. *Opt. Express* **17**(4), 2805–2817 (2009).
83. Zonios, G. *et al.* Diffuse reflectance spectroscopy of human adenomatous colon polyps in vivo. *Appl. Opt.* **38**(31), 6628–6637 (1999).
84. Nachabé, R. *et al.* Effect of bile absorption coefficients on the estimation of liver tissue optical properties and related implications in discriminating healthy and tumorous samples. *Biomed. Opt. Express* **2**(3), 600–614 (2011).
85. Baltussen, E. J. M. *The Clinical Implementation of Optical Spectroscopy in Colorectal Cancer Surgery* (University of Twente, Enschede, 2020).
86. Varadarajulu, S. *et al.* GI endoscopes. *Gastrointest. Endosc.* **74**(1), 1–6 (2011).
87. Kay, M. & Wyllie, R. Colonoscopy, polypectomy, and related techniques. In *Pediatric Gastrointestinal and Liver Disease* (eds Wyllie, R. *et al.*) 650–667 (Elsevier, Amsterdam, 2011).

Acknowledgements

We acknowledge Eduardo Moriyama for the advice and logistics of the project associated with this manuscript, Shree Krishnamoorthy for the discussions on the same project, Haiyang Li for the design and assembly of the holder of the DRS system, Andrew McGuire for specimen retrieval of the second set of patients of this study and all the logistics related to it, Vivienne Curran, Aoife Foyle, Una McAuliffe, Evelyn Flanagan, Shauni Fitzgerald, and Edmund Manning for all the logistics of clinical procedures, research ethics documents, and search for patient information, Jacqueline Gunther for externally reviewing the manuscript and providing helpful comments.

Author contributions

M.S.N. Conceptualization, Methodology, Software, Validation, Formal analysis, Investigation, Resources, Data Curation, Writing—Original Draft, Writing—Review & Editing, Visualization, Supervision, Project administration, S.M. Investigation, Data Curation, Writing—Review & Editing, M.A. Investigation, Data Curation, Software, Writing—Review & Editing, H.L. Methodology, Investigation, Resources, Data Curation, Writing—Review & Editing, Supervision, N.L. Methodology, Investigation, Resources, Data Curation, Writing—Review & Editing, S.K. Investigation, Resources, Data Curation, M.O.R. Conceptualization, Methodology, Validation, Formal analysis, Investigation, Resources, Data Curation, Writing—Review & Editing, Supervision, Project administration, Funding Acquisition. S.A.E. Conceptualization, Methodology, Resources, Writing—Review & Editing, Supervision, Project administration, Funding Acquisition.

Funding

This study received financial support from Science Foundation Ireland (SFI): Grant ID SFI/15/RP/2828.

Competing interests

The authors declare no competing interests.

Additional information

Correspondence and requests for materials should be addressed to M.S.N.

Reprints and permissions information is available at www.nature.com/reprints.

Publisher's note Springer Nature remains neutral with regard to jurisdictional claims in published maps and institutional affiliations.

Open Access This article is licensed under a Creative Commons Attribution 4.0 International License, which permits use, sharing, adaptation, distribution and reproduction in any medium or format, as long as you give appropriate credit to the original author(s) and the source, provide a link to the Creative Commons licence, and indicate if changes were made. The images or other third party material in this article are included in the article's Creative Commons licence, unless indicated otherwise in a credit line to the material. If material is not included in the article's Creative Commons licence and your intended use is not permitted by statutory regulation or exceeds the permitted use, you will need to obtain permission directly from the copyright holder. To view a copy of this licence, visit http://creativecommons.org/licenses/by/4.0/.

© The Author(s) 2021

Journal of Physics D: Applied Physics

PAPER • OPEN ACCESS

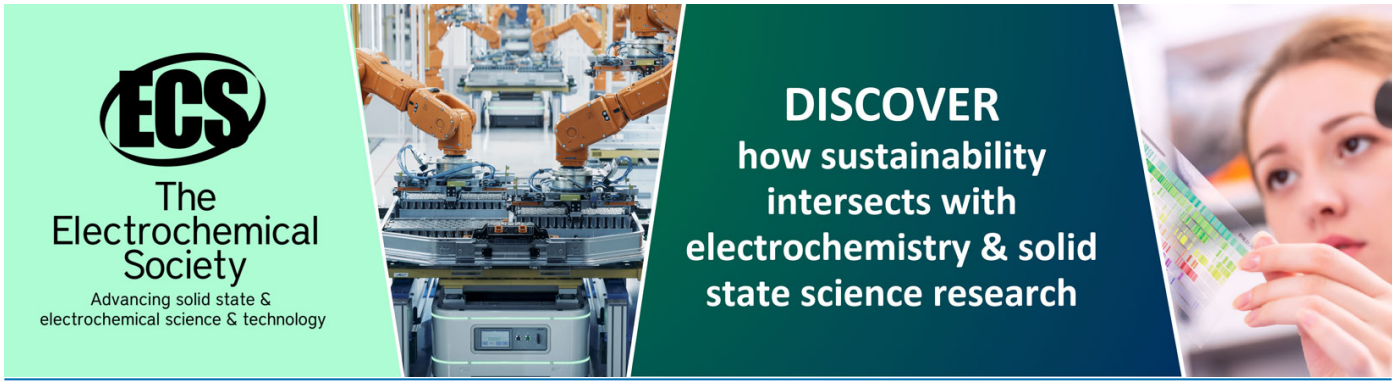
Tissue biomolecular and microstructure profiles in optical colorectal cancer delineation

To cite this article: Marcelo Saito Nogueira *et al* 2021 *J. Phys. D: Appl. Phys.* **54** 454002

View the article online for updates and enhancements.

You may also like

- Label-free monitoring of colorectal adenoma–carcinoma sequence based on multiphoton microscopy
J X Chen, H S Li, Z F Chen et al.
- Microphysiological systems to study colorectal cancer: state-of-the-art
Pedro Ramos, Mariana R Carvalho, Wei Chen et al.
- Deoxycholic acid-modified microporous SiO_2 nanofibers mimicking colorectal microenvironment to optimize radiotherapy-chemotherapy combined therapy
Lihuan Wang, Congzhao Zhao, Haoru Shan et al.



This content was downloaded from IP address 143.239.67.251 on 01/05/2024 at 12:26

OPEN ACCESS
IOP Publishing
Journal of Physics D: Applied Physics
J. Phys. D: Appl. Phys. **54** (2021) 454002 (18pp)
https://doi.org/10.1088/1361-6463/ac1137

Tissue biomolecular and microstructure profiles in optical colorectal cancer delineation

Marcelo Saito Nogueira[1,2,*], Michael Raju[1,2], Jacqueline Gunther[1], Siddra Maryam[1,2], Michael Amissah[1,2], Huihui Lu[1], Shane Killeen[3], Micheal O'Riordain[3] and Stefan Andersson-Engels[1,2]

[1] Tyndall National Institute, Lee Maltings, Dyke Parade, Cork, Ireland
[2] Department of Physics, University College Cork, College Road, Cork, Ireland
[3] Department of Surgery, Mercy University Hospital, Cork, Ireland

E-mail: marcelosaitonogueira@gmail.com

Received 28 February 2021, revised 8 June 2021
Accepted for publication 5 July 2021
Published 1 September 2021

Abstract

Colorectal cancer (CRC) is the 3rd most common and the 2nd most deadly type of cancer worldwide. Understanding the biochemical and microstructural aspects of carcinogenesis is a critical step towards developing new technologies for accurate CRC detection. To date, optical detection through analyzing tissue chromophore concentrations and scattering parameters has been mostly limited to chromophores in the visible region and analytical light diffusion models. In this study, tissue parameters were extracted by fitting diffuse reflectance spectra (DRS) within the range 350–1900 nm based on reflectance values from a look-up table built using Monte Carlo simulations of light propagation in tissues. This analysis was combined with machine learning models to estimate parameter thresholds leading to best differentiation between mucosa and tumor tissues based on almost 3000 DRS recorded from fresh *ex vivo* tissue samples from 47 subjects. DRS spectra were measured with a probe for superficial tissue and another for slightly deeper tissue layers. By using the classification and regression tree algorithm, the most important parameters for CRC detection were the total lipid content (f_{lipid}), the reduced scattering amplitude (α'), and the Mie scattering power (b_{Mie}). Successful classification with an area under the receiver operating characteristic curve higher than 90% was achieved. To the best of our knowledge, this is the first study to evaluate the potential tissue biomolecule concentrations and scattering properties in superficial and deeper tissue layers for CRC detection in the luminal wall. This may have important clinical applications for the rapid diagnosis of colorectal neoplasia.

* Author to whom any correspondence should be addressed.

Original content from this work may be used under the terms of the Creative Commons Attribution 4.0 licence. Any further distribution of this work must maintain attribution to the author(s) and the title of the work, journal citation and DOI.

Supplementary material for this article is available online

Keywords: diffuse reflectance spectroscopy, Monte Carlo, colorectal cancer, optical diagnostics, colonoscopy, near-infrared spectroscopy, biophotonics

(Some figures may appear in color only in the online journal)

1. Introduction

Colorectal cancer (CRC) is the 3rd most common type of cancer worldwide (11.3% of the diagnosed cancer cases in 2020) and 2nd most deadly (10.2% of the cancer related deaths in 2020) [1, 2]. There is an increasing emphasis on early detection of CRC and this is usually associated with a good outcome. With this in mind, screening and diagnostic tests (e.g. stool tests, flexible sigmoidoscopy and colonoscopy) have a positive impact in decreasing CRC death rates, especially by incorporating newer and more sophisticated endoscopic imaging modalities [3, 4]. Colonoscopy involves inserting an endoscope into the large bowel to visualize the colonic and rectal mucosa directly. The goal of colonoscopy is not only to detect cancer, but also to detect and remove benign neoplastic polyps with malignant potential, thus reducing the subsequent incidence of cancer. However, the sensitivity and specificity for the detection of premalignant polyps during conventional white-light colonoscopy are 82.9% and 80.0%, respectively [5], whereas, even small cancers can be overlooked particularly with flat lesions in the caecum and ascending colon [6–11].

Currently, the gold standard for the characterization of polyps is histopathology, but this is not available in real time. False classification of innocuous polyps as benign or malignant neoplasia at colonoscopy will lead to unnecessary polypectomy with associated risk to the patient [3, 12]. Furthermore, with increasing emphasis on local excision of early CRC, polypectomy may not remove a malignant polyp completely without accurate detection of field change, where neoplasia is not only localized to a small portion of colonic mucosa but may affect colorectal mucosa more diffusely [13–15]. Then, even apparently uninvolved, readily accessible mucosa which is part of the field will contain biomarkers of carcinogenesis [16]. Tissue biomarkers can be detected with optical spectroscopy. Optical spectroscopy has the potential to measure biomolecules at low concentration, of interest for metabolical (micromolar), immunological (nanomolar) and even genetical (picomolar) diagnostics—as opposed to structural changes (millimolar range) observed by current CRC screening and diagnostic methods [17]. By targeting tissue biochemical changes which occur before or simultaneously as structural alterations at cellular and tissue scales, the CRC detection can be performed in its early stages, and tumor delineation becomes more precise [16]. These changes can be probed by using optical methods such as diffuse reflectance spectroscopy (DRS).

DRS is a non-invasive technique of tissue identification based on delivering light to the targeted biological tissue, and detecting the diffuse reflected light which has propagated through the tissue. The detected light contains information about the tissue absorption and scattering properties. Scattering properties are associated to the tissue microstructure, especially extra- and intra-cellular inhomogeneity of particle sizes as well as refractive index mismatches of specific molecules (such as collagen fibers and fibrils), organelles (such as mitochondria), and cell membranes. Absorption properties consider in this work are associated with the tissue biomolecules including β-carotene, bile, bilirubin, ceroid, collagen, deoxyhemoglobin (Hb), oxyhemoglobin (HbO_2), methemoglobin (MetHb), water, lipid, and melanin. These properties are determined by the absorption bands defined by the electronic, vibrational and rotational energy levels of tissue biomolecules typically present at micromolar to nanomolar concentrations. These concentrations are typical for metabolic and immunologic markers of normal and cancer tissues [17].

Previous DRS studies for CRC detection and delineation have primarily adopted approaches based on either tissue classification by using machine learning methods directly on the measured diffuse reflectance (DR) spectra, or on extraction of the concentration of tissue absorbing biomolecules (or chromophores). The classification performance achieved with machine learning methods is heterogeneous among *ex vivo* and *in vivo* feasibility studies for CRC detection during colonoscopy [18–29]. The classification performance metrics for differentiation between neoplastic (benign or malignant) and non-neoplastic tissue has ranged from 79% to 100% sensitivity, 68% to 100% specificity, and 82% to 99% accuracy for DRS studies and from 72.5% to 96.9% sensitivity, 55.8% to 92% specificity, and 78.5% to 94.5% accuracy for hyperspectral imaging studies. In terms of determination of tissue chromophore concentrations, prior feasibility DRS studies for CRC detection during colonoscopy are scarce and limited to estimating HbO_2 and Hb concentrations, as the range of investigated wavelengths has been restricted to 350–800 nm. Hb and HbO_2 concentrations are used to calculate the tissue total hemoglobin concentration (THC) and blood oxygen saturation (StO_2). Zonios *et al* [30] obtained THC of 13.6 ± 8.8 mg dl^{-1} and StO_2 of 59% $\pm$ 8% for normal tissues, and THC of 72.0 ± 29.2 mg dl^{-1} and StO_2 of 63% $\pm$ 10% for adenomatous polyps by investigating DRS in the wavelength range between 350 and 700 nm in tissues of 13 patients. A similar study investigating wavelengths between 600 and 800 nm

was performed by Wang *et al* [31], who obtained StO_2 of 60.7% ± 7.7%, 51.3% ± 7.0%, and 26.4% ± 6.1% for normal tissues, premalignant adenomatous polyps and tumors of eight cancer patients, respectively. In terms of THC, the authors found 59.8 ± 19.0 μM for normal tissues and 153.8 ± 38.6 μM for cancerous tissues.

A range of studies evaluating the feasibility of CRC detection for colonoscopy guidance by using DRS [18, 19, 30–32] and hyperspectral imaging [20, 28, 29] focused on analyzing tissue responses in the visible or near-infrared (NIR) wavelength ranges. NIR studies were performed by Chen *et al* [24–26] and Ehlen *et al* [27], who built tissue classification models based on the NIR wavelength region containing information about the water and lipid absorption. To the best of our knowledge, most of the prior *ex vivo* and *in vivo* feasibility studies for CRC during colonoscopy using DRS and related optical spectroscopic techniques are limited in the investigated tissue probed depth, wavelength ranges, and types of light propagation models for estimation of tissue chromophores [18–31], and number of analyzed DRS spectra. First, these studies explored only superficial tissue layers by either using fiber optic probes with small source-to-detector distances (SDDs) or collecting hyperspectral images from wide-illuminated tissue areas. Second, DRS studies analyzed visible and NIR wavelength ranges either from specific ranges within 350–800 nm or 900–2500 nm. Third, studies determining tissue chromophore concentrations utilize analytical models based on the diffusion equation, which is known for not describing well the reflectance at small SDDs. Finally, the number of spectra collected in DRS studies ranges from 60 to 483 spectra in total (1–78 cancer spectra and 59–452 non-cancer spectra).

In this study, we quantified independent tissue biochemical and microstructural parameters with potential for clinical decision making in several applications including the differentiation between colorectal mucosa and tumors in the colorectal lumen. To do this, we combined model-based extraction of tissue chromophore concentrations and scattering properties with machine learning models for estimation of thresholds of chromophore concentrations and scattering properties leading to best differentiation between areas of normal mucosa and tumor tissues. To the best of our knowledge, we are the first to estimate those thresholds for CRC detection in the colorectal lumen. This estimation was performed by building binary-decision-tree models and evaluating the classification performance achieved with relevant parameters.

Finally, the quantification of tissue biochemical and microstructural parameters for the differentiation between mucosa and tumors complements our previous work [33], which evaluated the usefulness of the extended wavelength range and tissue probed depth as its primary aim. Hence, our previous study improved the diagnostic accuracy by using tissue classification based on support vector machines and by probing deeper tissue layers, whereas the present study focuses on determining thresholds of biomolecule concentrations and scattering properties as well as assessing their importance for CRC detection decision trees.

Table 1. Patient demographics, cancer types and tumor staging classification.

		Number of patients/ tumors
Total	—	47
Gender	Male	32
	Female	15
Age (years)	Range	40–89
	Mean (± standard deviation)	68 ± 11
Tumor types	Adenocarcinoma	46
	Carcinoma	1

2. Methodology

2.1. Clinical data collection

Our study included 47 patients undergoing bowel resection at the Mercy University Hospital, Cork, Ireland (patient demographics are shown in table 1). The study was approved by the Clinical Research Ethics Committee of the University College Cork. All methods were performed in accordance with the relevant guidelines/regulations. Informed consent was obtained from all participants of the study. Out of the 47 tumors investigated, five were in pT1 stage, seven were pT2, 26 were pT3 and nine were pT4. Twenty-eight patients had local lymph node metastases whereas 19 had not.

Data collection involved measuring about 15 sites of *ex vivo* mucosal tissues and 15 of tumor tissues on each colorectal specimen after surgical resection. Representation of the tissue heterogeneity was ensured by collecting spectral readings from a typical area of 100 cm^2. Devascularization periods (i.e. time between the restriction of blood supply to the specimen and its removal) typically varied between 1 and 2 h. Once the specimen was removed, it was transported to a measurement bench and opened to expose the colonic lumen for the DRS measurements. The specimen was gently rinsed with water and cleaned afterwards in order to remove the remaining stool and excess of blood. Next, the specimen was placed in a measurement grid showing the coordinates of the sites where DRS spectra was collected. Then, mucosa and tumor regions were identified by experienced surgeons so that DRS spectra could be correlate with the types of tissues measured. The average time between the specimen removal and the start of the data collection was 40 min. Data collection was performed within an average time of 1 h after surgical resection. The tissue moisture was kept by using a damp cloth in order to preserve physiological conditions as much as possible throughout the data collection. Upon finishing the DRS data acquisition, each specimen was returned to the Pathology Department for processing

and analysis according to standard protocols. Histopathology analysis was the ground truth of our DRS measurements.

2.2. DRS equipment

Our DRS system employed is illustrated in figure 1. A broadband light source (HL-2000-HP, Ocean Optics, Edinburgh, United Kingdom) with emission ranging from 350 nm to 2400 nm was employed. Low-OH silica fiber optic probes including a 630 μm SDD quadrifurcated probe (small probe or probe 1, BF46LS01 1-to-4 Fan-Out Bundle, Thorlabs, Munich, Germany) and a 2500 μm SDD trifurcated probe (large probe or probe 2, Fibertech Optica, Anjou, Canada) were used to deliver the light to and from the tissue sample. Two spectrometers detected the DRS signal, one in the visible/short wavelength NIR wavelength range between 350 and 1140 nm (QE-Pro, Ocean Optics, Edinburgh, United Kingdom) and one in the long wavelength NIR range between 1090 and 1920 nm (NIR-Quest, Ocean Optics, Edinburgh, United Kingdom). The overlapping wavelength region was used to merge the spectra into one broadband (350–1920 nm) spectrum, as described in the data preprocessing section (section 2.5). We used the 630 μm SDD probe (probe 1) to probe the superficial tissue at depths ranging from 0.3–1.1 mm (estimated from Monte Carlo (MC) simulations of light propagation into tissues, data not shown), whereas the 2500 μm SDD probe (probe 2) collected reflectance from depths ranging from 0.1 to 1.8 mm (data not shown). Probe 1 contained 600 μm core diameter fibers for both illumination and collection. Probe 2 had one central 600 μm core-diameter source fiber, and ten 200 μm core-diameter collection fibers surrounding it. At the spectrometer end of probe 2, each group of five collection fibers were positioned linearly to match the slit of the spectrometers to increase the detected signal.

The procedure to investigate the tissue depth probed is described in detail in [33]. Briefly the tissue depth investigated by using probes 1 and 2 was estimated through forward MC simulations of steady-state light transport in multi-layered tissues (MCML) [34] accelerated by graphics processing unit (GPU) [35, 36] using optical properties obtained from the analysis of the spectral fitting algorithm described in section 2.5. Light propagation through a semi-infinite homogeneous medium with refractive index of the outer medium (η_{out}) of 1, tissue refractive index (η_{rel}) of 1.4, anisotropy factor (g) of 0.9 was simulated. By using 10 million photon packets, we generated 5 $\times$ 5 mm light fluence maps with 10 μm of radial and depth resolution in order to compute the photon hitting density maps used to estimate the probed depth.

2.3. Optical measurement protocol

First, we collected the background and reference signals. Both these measurements were taken by placing each probe on a specialized holder designed to fix the distance between the fiber optic probes and our reflectance standard (FWS-99-01c, Avian Technologies LLC, New London, USA). Signal contamination due to backscattered light and ambient light was avoided be a closed environment with blackened walls of the holder. The background and reflectance measurements were taken with our broadband light source turned off and on, respectively. In order to avoid probe contamination, we covered our probes with polyvinyl chloride film and cleaned them with ethanol 70% after each set of measurements. All measurements of this study were performed with the same probes, which were positioned as close to 90° from the tissue surface as possible. Upon completion of the data collection, the data was safely stored for analysis. In this study, we collected a total of 1363 spectra for the small SDD probe (630 μm SDD) and 1526 for the large SDD probe (2500 μm SDD).

2.4. Data preprocessing

In order to obtain the tissue reflectance $R(\lambda)$, the intensity measurements (I^{Tissue}) of each spectrometer had their background subtracted ($I^{\text{Background}}$) and the resulting intensity was divided by the reference measurements $I^{\text{Reference}}$ (with background subtraction):

$$R(\lambda) = \frac{I^{\text{Tissue}}(\lambda) - I^{\text{Background}}(\lambda)}{I^{\text{Reference}}(\lambda) - I^{\text{Background}}(\lambda)}. \quad (1)$$

To merge the reflectance spectra and correct for any slight mismatch between the two spectrometers, we used the overlapping spectral range between 1090 and 1140 nm to perform an interpolation by using the weighted sum:

$$R(\lambda) = \sum_{i=0}^{100} \frac{((100-i) \times R_{\text{vis}} + i \times R_{\text{NIR}})}{100}. \quad (2)$$

The resulting reflectance spectra $R(\lambda)$ were used for the estimation of chromophore concentrations and scattering parameters.

2.5. Spectral fitting and extraction of biomolecule concentrations

A flowchart of the spectral fitting algorithm is shown in figure 2. Details of the steps of this algorithm can be found in the supplementary material (available online at stacks.iop.org/JPD/54/454002/mmedia). Briefly, the obtained reflectance spectra $R(\lambda)$ was used to extract the tissue absorption and scattering related parameters. The absorption-based parameters included are the concentrations of blood (total hemoglobin (THb) percentage and THC), lipid (f_{lipid}), water (f_{water}), bile (f_{bile}), met-hemoglobin (f_{metHb}), as well as oxygen saturation (StO_2), and average vessel diameter R. The scattering-based parameters, on the other hand, included the reduced scattering amplitude α', Mie scattering power b_{Mie}, and the percentage contribution of Rayleigh scattering f_{Ray}. The spectral fitting methodology is illustrated in figure 2 with a detailed description provided in the supplementary material. Briefly, the extraction was performed by using a spectral fitting based on the four types of inputs to the algorithm: the measured DR spectrum; the pure chromophore absorption spectra ($\mu_{\text{a,chromophore}}(\lambda)$); the Rayleigh and Mie scattering equations yielding the scattering coefficient as a function of wavelength; as well as a look-up table (LUT) of DR

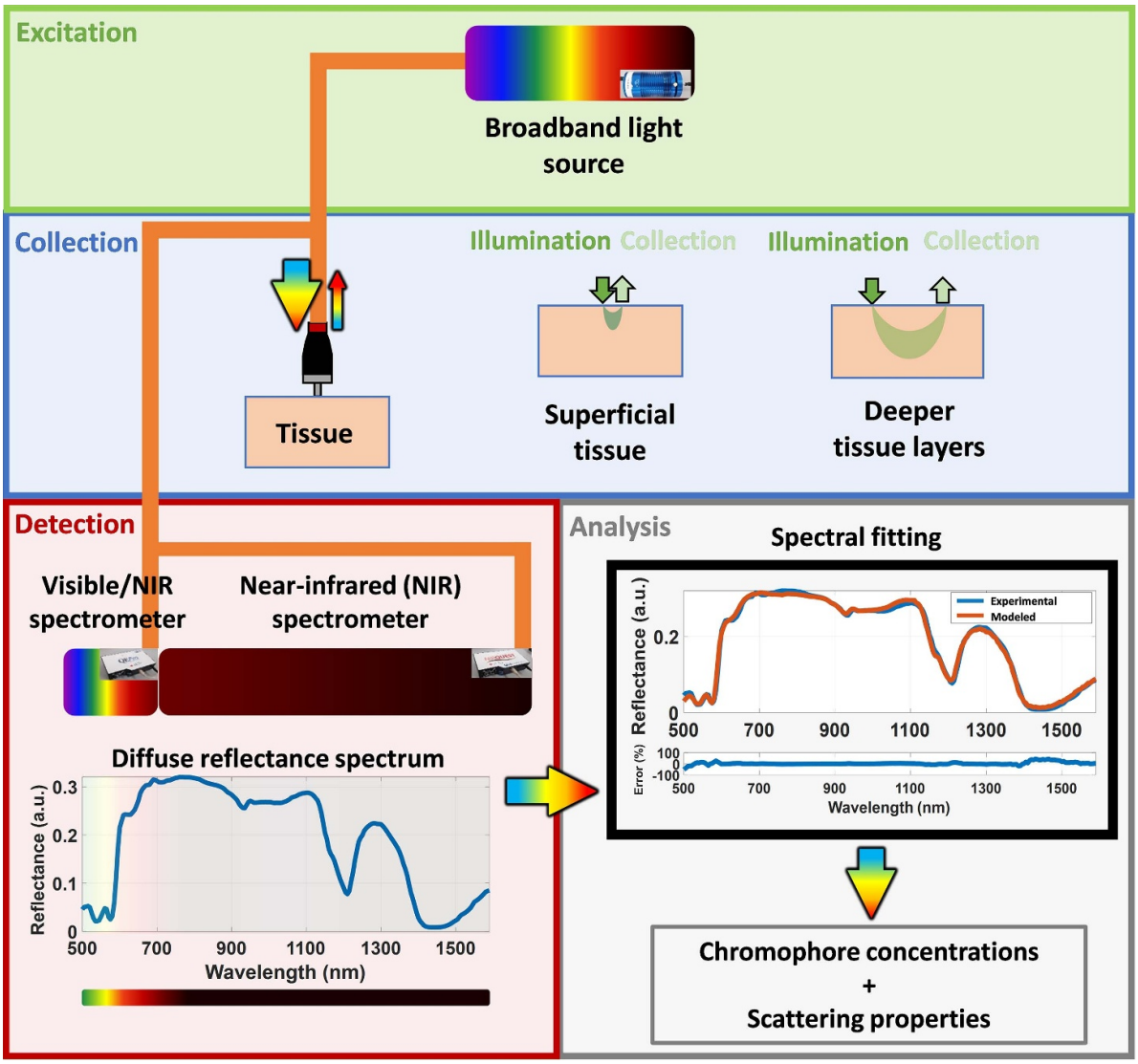


Figure 1. Schematic drawing of our DRS system and following analysis discussed in this paper. The reflected light can be collected in a wavelength range 350–1919 nm and allows the investigation of a larger variety of tissue chromophores compared to previous feasibility studies for CRC detection during colonoscopy.

($R(\mu_a,\mu_s)$) values describing the light propagation in tissue as a function of absorption coefficients (μ_a) between 0.01 and 300 cm^{-1}, and scattering coefficients (μ_s) between 0.1 and 1000 cm^{-1}. The LUT was generated by using a forward MC model of light propagation into tissues, which was accelerated by GPU [35, 36]. In this model, tissue optical properties including μ_a and μ_s were used as an input to simulate the light transport inside a homogeneous semi-infinite medium and calculate the reflectance at different positions of the medium (tissue) surface. MC simulations were performed with 10 million photon packets, refractive index of the outer medium (η_{out}) of 1, tissue refractive index (η_{rel}) of 1.4, anisotropy factor (g) 0.9. The results were stored with a radial and depth resolution of 10 μm. The contribution of photons launched in the excitation fiber was accounted through convolution of the incident photon beam [37]. The modeled reflectance was obtained by integrating the reflectance values in the area of the core diameter of the collection fibers (detector area) located at the specified SDD. This integration was performed for a wide range of optical properties involving values typically found in most biological tissues [38, 39]. The result is a MC LUT associating the modeled reflectance $R(\mu_a,\mu_s)$ with μ_a and μ_s values for the geometry of our fiber optic probe.

By using the MC LUT, chromophore absorption spectra and scattering equations, the modeled DRS spectrum was reconstructed. First, chromophore concentrations and scattering parameters are used to obtain the tissue absorption and scattering spectra. Next, for each wavelength of these spectra, combinations of absorption and scattering coefficients were associated to values of reflectance $R(\mu_a,\mu_s)$ in order to reconstruct the modeled DR spectrum $R_{modeled}(\lambda)$. $R_{modeled}(\lambda)$ was multiplied by a calibration factor and compared to the experimental spectrum $R_{experimental}(\lambda)$ in a fitting algorithm. The outputs of the algorithm are a fitted DR spectrum, the

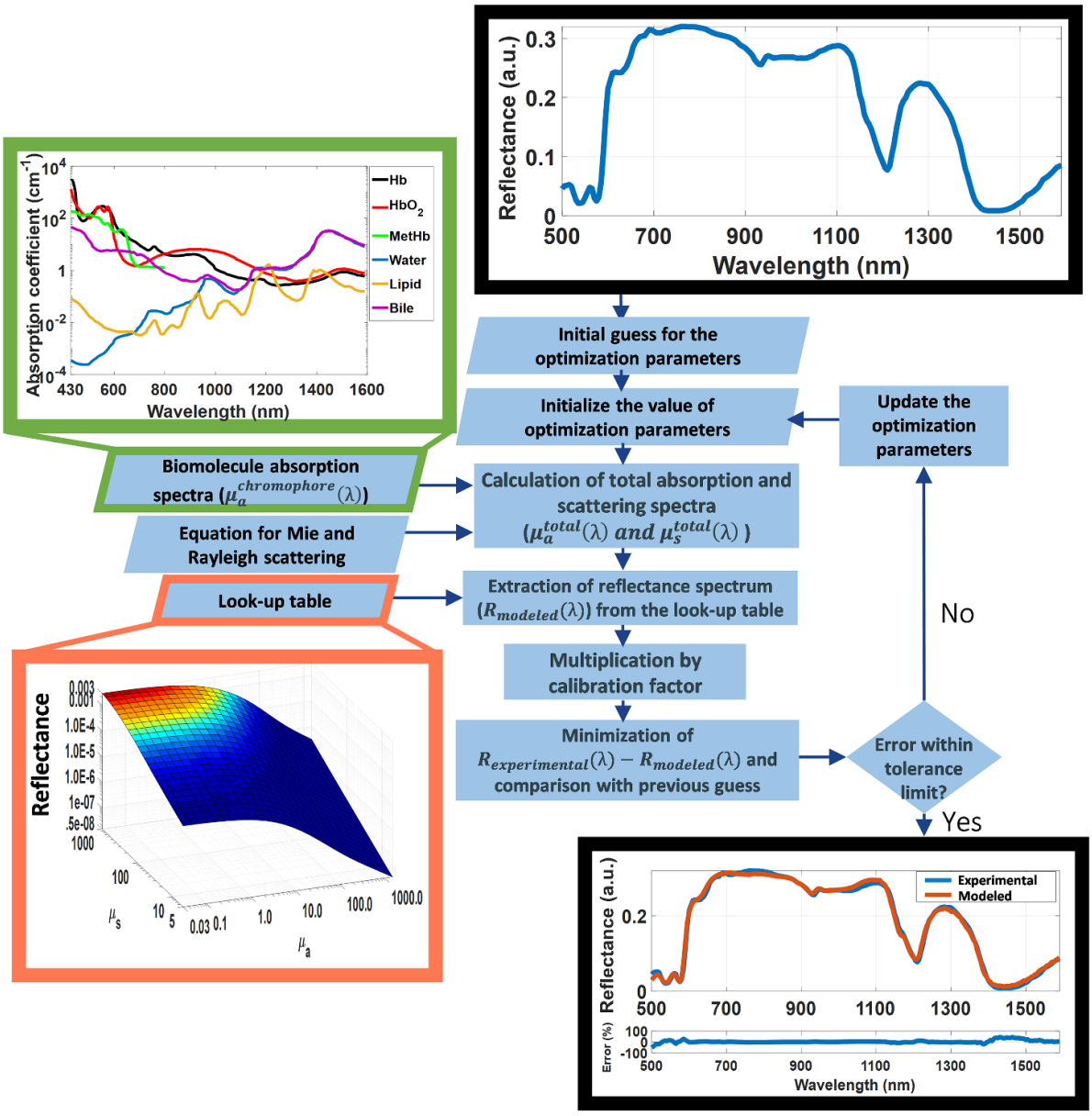


Figure 2. Flowchart of the steps of our spectral fitting algorithm.

values of the fitting parameters and a value for the fitting fidelity.

In the algorithm we implemented the same spectral fitting method as used by Nachabe *et al* [40, 41] (and is described in in more detail in the supplementary material). Validation studies of our fitting procedure were conducted in both phantoms and biological tissue samples and has been was presented elsewhere [42]. It is important to note that we refer to $f_{\text{blood}} = f_{\text{Hb}} + f_{\text{HbO}_2}$ as THb percentage in tissue, even though THb is a relative volume percentage of pure blood. We also emphasize that f_{bile} may contain traces of bilirubin found in blood at ranges between 5.8% and 40% in humans, especially considering that bilirubin blood serum levels can vary between 10 and 50 mg dl^{-1} [43] and hemoglobin blood levels vary between 121 and 172 mg dl^{-1} [39]. With that in mind, f_{bile} would represent the bile concentration added to a contribution of bilirubin varying between 5.8% and 40% of THb. The use of bilirubin absorption spectrum in our fitting is limited by the narrow wavelength range reported in the literature, which is not sufficient to fit a spectrum between 450 and 1590 nm.

2.6. Statistical tests

Significant statistical differences between spectral fitting parameters of normal mucosa and tumors were tested by using two-sample *t*-test and Wilcoxon rank sum test. To evaluate the adequate use of two-sample *t*-test, Anderson–Darling and Lilliefors normality tests were performed.

2.7. Classification using binary decision tree

The tissue chromophore concentrations and scattering properties obtained with our spectral fitting model were used for tissue classification in mucosa and tumor based on a binary decision tree algorithm. Our decision tree was built by using the classification and regression tree (CART) algorithm implemented with default fitctree MATLAB function. The method uses a recursive partitioning method to generate a classification tree from thresholds of the tissue parameters obtained by the spectral fitting described in section 2.5. These thresholds are selected from a training set of spectral data and applied to spectra on the test set for every iteration of cross-validation. This study used five-fold cross-validation, which consists of randomly dividing the dataset into five sets of training and test sets containing 80% and 20% of the spectra in our dataset, respectively. Each of these pairs is used to build a tissue classification model where the model is calibrated in the training set and validated on the test set. For each pair, the classification model was assessed by performance parameters involving the sensitivity, specificity, accuracy and area under the receiver operating characteristic curve (AUC) for identification tumor and mucosa tissues. The performance of the classification model was given by the mean of performance parameters among the five sets.

In order to ensure our tissue classification model was not overfitted, we reported the mean and standard deviation of the output of the 20 iterations of five-fold cross-validation with random sampling. In addition, we have used THb, R, f_{lipid}, f_{water}, f_{bile}, α', f_{Ray} and b_{Mie} as relevant parameters for tissue classification. StO_2, and f_{metHb} were not included in the model due to their variations in *ex vivo* settings, as it was not possible to control the blood oxygenation and conversion of Hb and HbO_2 into met-Hb once blood of the specimen was exposed to air.

3. Results

3.1. Tissue chromophore concentrations and scattering properties

Our spectral fitting analysis yielded relevant absorption and scattering parameters to be used for the tissue differentiation. Based on this analysis, we selected the tissue scattering-based microstructure parameters (reduced scattering amplitude α', Mie scattering power b_{Mie}, and the percentage contribution f_{Ray}), and concentrations of blood (THb), lipid (f_{lipid}), water (f_{water}), bile (f_{bile}), as well as oxygen saturation (StO_2) and average vessel diameter R as relevant parameters to be monitored and discussed (figures 3 and 4). All fitted variables are described in table 2. Values of f_{MetHb} were not considered relevant for our analysis as these values can vary due to exposure to oxidizing agents which convert Hb into metHb, even though f_{MetHb} needed to be included in our spectral fitting in order to eliminate the metHb influence on THb, THC and StO_2. Figure 3 shows a boxplot of the fitted parameters for all mucosa and tumor tissue spectra using probe 1. These plots suggest that the parameters which best discriminate mucosa and tumor tissues are THb, f_{lipid} and b_{Mie}.

Figure 4 suggests a similar behavior of chromophore concentrations and scattering properties differentiating mucosa and cancer tissues could be observed in both superficial tissue (figure 3 for probe 1) and deeper tissue layers (figure 4 for probe 2). The differentiation of parameters such as the scattering amplitude α', f_{lipid} and b_{Mie} increased by using probe 2. Yet, the trend observed for lower f_{Ray} in the tumor surface (figure 3) does not hold for deeper tissue layers in tumors.

Table 2 shows the mean and standard deviation of mucosal and cancerous biochemical and microstructural parameters extracted with our DR spectral fitting algorithm. In average, tumors had larger THb, THC, f_{water}, α', b_{Mie}, and smaller average vessel radius, f_{lipid} compared to normal mucosa. For probe 1, tumor tissues also exhibited lower f_{Ray}. Also, R, f_{lipid}, and b_{Mie} tend to be higher for probe 2 compared to probe 1 in both mucosa and tumor tissues, whereas all other parameters tend to be lower for probe 2. The standard deviation of THb, THC, f_{lipid}, f_{water} for probe 2 was lower to those of probe 1, even when considering the standard deviation relative to the mean values (coefficient of variation). The p-values of statistical tests leading to the representation of significant statistical differences in the boxplots can be found in table 3. Even though we show the result of statistical tests for t-test and Wilcoxon rank sum test, we emphasize that the distribution of spectral fitting parameters of normal mucosa and tumors are normal according to both Anderson–Darling and Lilliefors normality tests.

3.2. Tissue classification using decision trees

Classification trees were built with spectral fitting parameters of probes 1 and 2 in order to categorize tumors based on their particular ranges of chromophore concentrations and scattering properties. Figures 5(a) and (b) show the two separate branches of a decision tree with parameters leading to most of the differentiation between mucosa and tumor by using probe 1. These parameters are THb, R, f_{lipid}, f_{bile}, α', f_{Ray} and b_{Mie}. By using the five-fold cross-validation method described previously, we achieved 81.8% ± 1.1% sensitivity, 88.2% ± 1.4% specificity, 84.8% ± 0.6% accuracy, 0.900 ± 0.007 AUC. Also, it is important to note that parameters appearing close to the top of the decision tree are the most important for tissue classification. With this in mind, the parameters which appear on the top two layers of splits for probe 1 (figures 5(a) and (b)), i.e. f_{lipid}, α', f_{Ray} and b_{Mie}, are the directly or indirectly related to tissue scattering (section 4.3).

Similarly to probe 1, figures 6(a) and (b) show the two separate branches of a decision tree with parameters leading to most of the differentiation between mucosa and tumor by using probe 2. These parameters are THb, R, f_{lipid}, f_{bile}, α', and b_{Mie}. By using five-fold cross-validation, we achieved 87.1% ± 0.6% sensitivity, 89.7% ± 1.0% specificity, 88.3% ± 0.6% accuracy, 0.911 ± 0.006 AUC. Differently from probe 1, the parameters which appear on the top two layers of splits for probe 2 (THb, R, f_{lipid}, α', and b_{Mie}) include

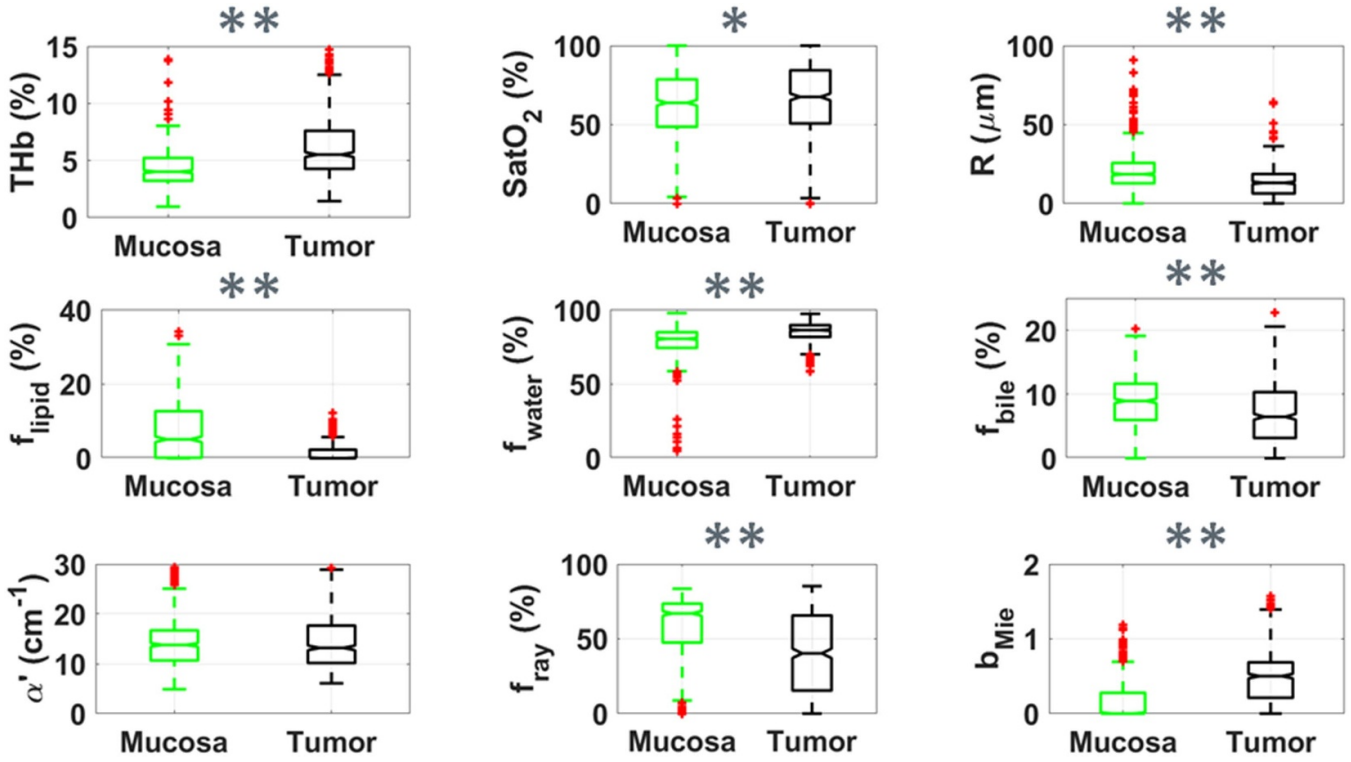


Figure 3. Boxplots of relevant parameters for differentiation between superficial tissue layers of mucosa (green, $n = 728$) and tumor (black, $n = 635$) by using probe 1. Red points represent outliers (points at more than 1.5 times the interquartile range away from the bottom or top of the box). Statistical difference for $p < 0.05$ is represented by * and that for $p < 0.001$ is represented by ** for the Wilcoxon rank sum test.

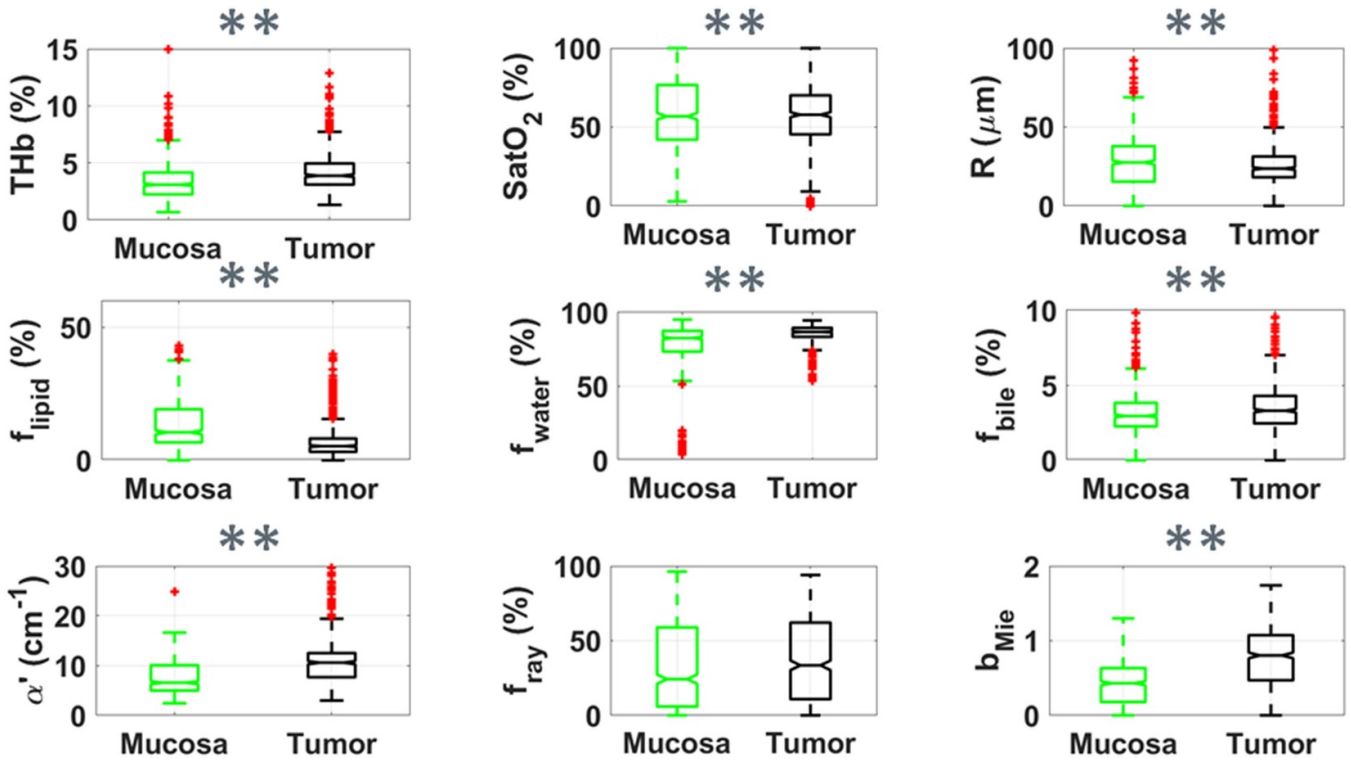


Figure 4. Boxplots of relevant parameters for differentiation between superficial tissue layers of mucosa (green, $n = 804$) and tumor (black, $n = 722$) by using probe 2. Red points represent outliers (points at more than 1.5 times the interquartile range away from the bottom or top of the box). Statistical difference for $p < 0.05$ is represented by * and that for $p < 0.001$ is represented by ** for the Wilcoxon rank sum test.

Table 2. Biochemical and microstructural parameters of mucosa and tumor tissues investigated with the small SDD probe (superficial tissue) and the large SDD probe (deeper tissue layers).

Biochemical/microstructural parameters	Abbreviation	Small SDD probe (probe 1)		Large SDD probe (probe 2)	
		Mucosa	Tumor	Mucosa	Tumor
Total hemoglobin percentage	THb (%)	5.0 ± 4.0	6.6 ± 3.9	3.5 ± 1.4	4.8 ± 1.9
Total hemoglobin molar concentration	THC (μM)	116 ± 92	154 ± 90	81 ± 33	111 ± 45
Oxygen saturation	StO_2 (%)	64 ± 21	66 ± 23	50 ± 17	56 ± 18
Average vessel radius (μm)	R (μm)	25 ± 36	14 ± 11	33 ± 15	24 ± 13
Lipid volume percent	f_{lipid} (%)	7.7 ± 8.6	1.4 ± 2.2	14.1 ± 8.9	4.8 ± 3.0
Water volume percent	f_{water} (%)	78.5 ± 10.2	84.9 ± 7.2	79.2 ± 9.0	86.7 ± 4.0
Bile volume percent	f_{bile} (%)	8.9 ± 4.5	7.0 ± 4.8	3.3 ± 1.3	3.7 ± 2.5
Met-hemoglobin volume percent	f_{MetHb} (%)	1.1 ± 0.6	1.1 ± 0.7	0.2 ± 0.2	0.3 ± 0.5
Amplitude of reduced scattering coefficient	α' (cm^{-1})	14.3 ± 5.5	15.9 ± 10.1	8.2 ± 3.7	12.0 ± 5.6
Mie scattering power	b_{Mie}	0.2 ± 0.2	0.5 ± 0.3	0.5 ± 0.3	0.9 ± 0.4
Rayleigh scattering fraction	f_{Ray} (%)	56 ± 24	40 ± 27	36 ± 28	36 ± 28

Table 3. *P*-values of *t*-test and Wilcoxon rank sum test for each biochemical and microstructural parameter of mucosa and tumor tissues investigated with the small probe (probe 1) and the large probe (probe 2). Statistical difference for $p < 0.05$ is represented by yellow background and that for $p < 0.001$ is represented by a green background.

Spectral fitting parameters	*p*-values of *t*-test		*p*-values of Wilcoxon rank sum test	
	Probe 1 (s)	Probe 2	Probe 1	Probe 2
THb (%) or THC (μM)	1×10^{-8}	1×10^{-45}	8×10^{-37}	1×10^{-45}
StO_2 (%)	0.140	1×10^{-12}	0.049	3×10^{-15}
R (μm)	1×10^{-15}	7×10^{-35}	3×10^{-31}	2×10^{-46}
f_{lipid} (%)	6×10^{-60}	5×10^{-126}	2×10^{-60}	6×10^{-133}
f_{water} (%)	6×10^{-60}	5×10^{-126}	1×10^{-60}	6×10^{-133}
f_{bile} (%)	1×10^{-9}	9×10^{-6}	4×10^{-13}	3×10^{-7}
f_{MetHb} (%)	0.142	1×10^{-11}	0.044	0.00006
α' (cm^{-1})	0.0006	1×10^{-48}	0.930	6×10^{-67}
b_{Mie}	1×10^{-83}	4×10^{-101}	1×10^{-88}	4×10^{-93}
f_{Ray} (%)	2×10^{-29}	0.858	1×10^{-26}	0.966

both absorption and scattering parameters. Still, f_{lipid}, α', and b_{Mie} appear as important parameters for both probes and may be explored in future studies for endoscopic CRC detection.

4. Discussion

4.1. Relevance of our work

The relevance of our work is highlighted by the limitations overcome with respect to prior research on CRC detection during colonoscopy using DRS. Compared to previous studies, we have collected a substantially larger (2889 DRS spectra) at the extended wavelength range between 350 and 1920 nm by using fiber optic probes with two SDDs in order to probe superficial and deeper tissue layers. By using a 630 μm SDD fiber optic probe, signals could be captured from superficial tissue at depths between 0.5 and 1 mm (>0.8 mm for most wavelengths), whereas a 2500 μm SDD probe was used to collect signals from deeper tissue layers with between 0.5 and 1.9 mm (>1.4 mm for most wavelengths) [33]. Our extraction of chromophore concentrations and scattering properties is not restricted by limitations of diffusion theory, as we use probabilistic MC models to build the LUT containing reflectance values to fit the DRS spectrum. Furthermore, our LUT covers a wider range of optical properties (scattering coefficient varying from 0.1 to 1000 cm^{-1} and absorption coefficient from 0.01 to 300 cm^{-1}) and a greater resolution (7200 reflectance values) compared to past studies, to the best of our knowledge.

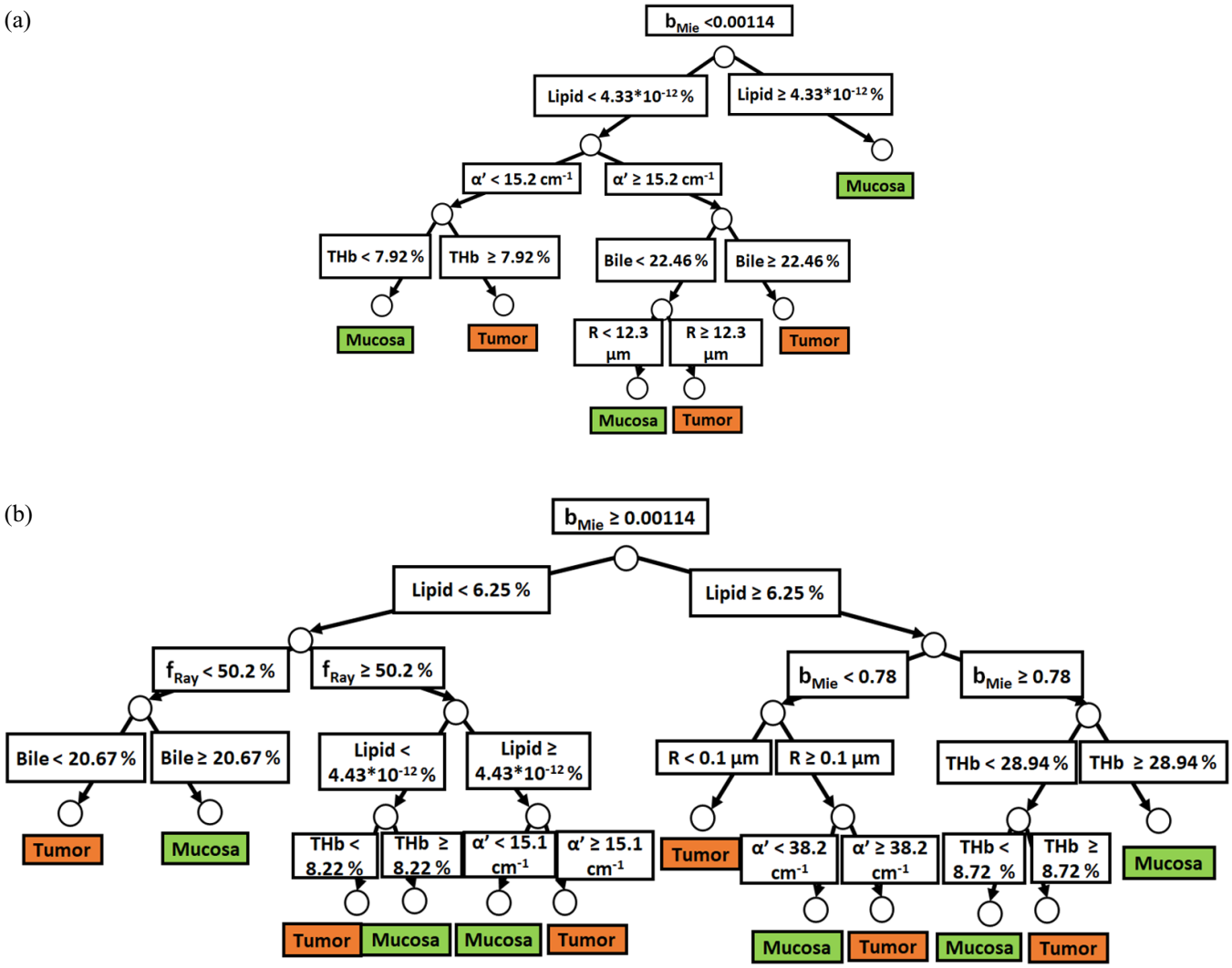


Figure 5. (a) Classification decision tree of the colorectal mucosa and tumor tissues based on parameter threshold values of probe 1 for $b_{\mathrm{Mie}} < 0.00114$. (b) Classification decision tree of the colorectal mucosa and tumor tissues based on parameter threshold values of probe 1 for $b_{\mathrm{Mie}} \geq 0.00114$.

4.2. Analysis of DRS measurements: multivariate analysis and spectral fitting model

In general, DRS measurements can be analyzed by using either machine learning methods [18–20, 22–29] for direct tissue differentiation or by spectral fitting models to obtain information on the tissue microstructure and biochemistry [18, 19, 30–32]. Machine learning is typically employed to build models for automated tissue discrimination without interpretation of the sources of this discrimination or to identify variables contributing most to the differentiation of two or more tissue types [18–29, 44–49]. Spectral fitting is used to extract chromophore concentrations and tissue optical properties such as the absorption and reduced scattering coefficients. The accuracy of spectral fitting models is dependent on the type of light transport model used as well the scattering and absorption properties of the medium where the light propagates [31, 40, 41, 50–56].

Analytical models provide a solution to the radiative transport equation often using the diffusion approximation (typically valid when the scattering coefficient $\mu'_{\mathrm{s,total}}$ is much higher than the absorption coefficient $\mu_{\mathrm{a,total}}$) [52, 57–67] or use a semi-empirical solution (often valid for media with particular sets of chromophores at specific geometries), while probabilistic models often use MC simulations to compute average parameters based on the photon packet paths and processes (e.g. absorption) inside the medium [31, 40, 41, 50–56]. Even though probabilistic models are more time-consuming, they provide the most accurate solution for the present case, as diffusion models are not accurate for short SDDs and for all tissue optical properties [31, 40, 41, 50–56, 68–82]. Among probabilistic models, we can exploit forward MC simulations to generate reflectance LUTs (i.e. a reflectance database as a function of μ_{a} and μ_{s}) for producing theoretical reflectance spectra based on wavelength-dependent of optical properties (referenced at scattering spectra and chromophore

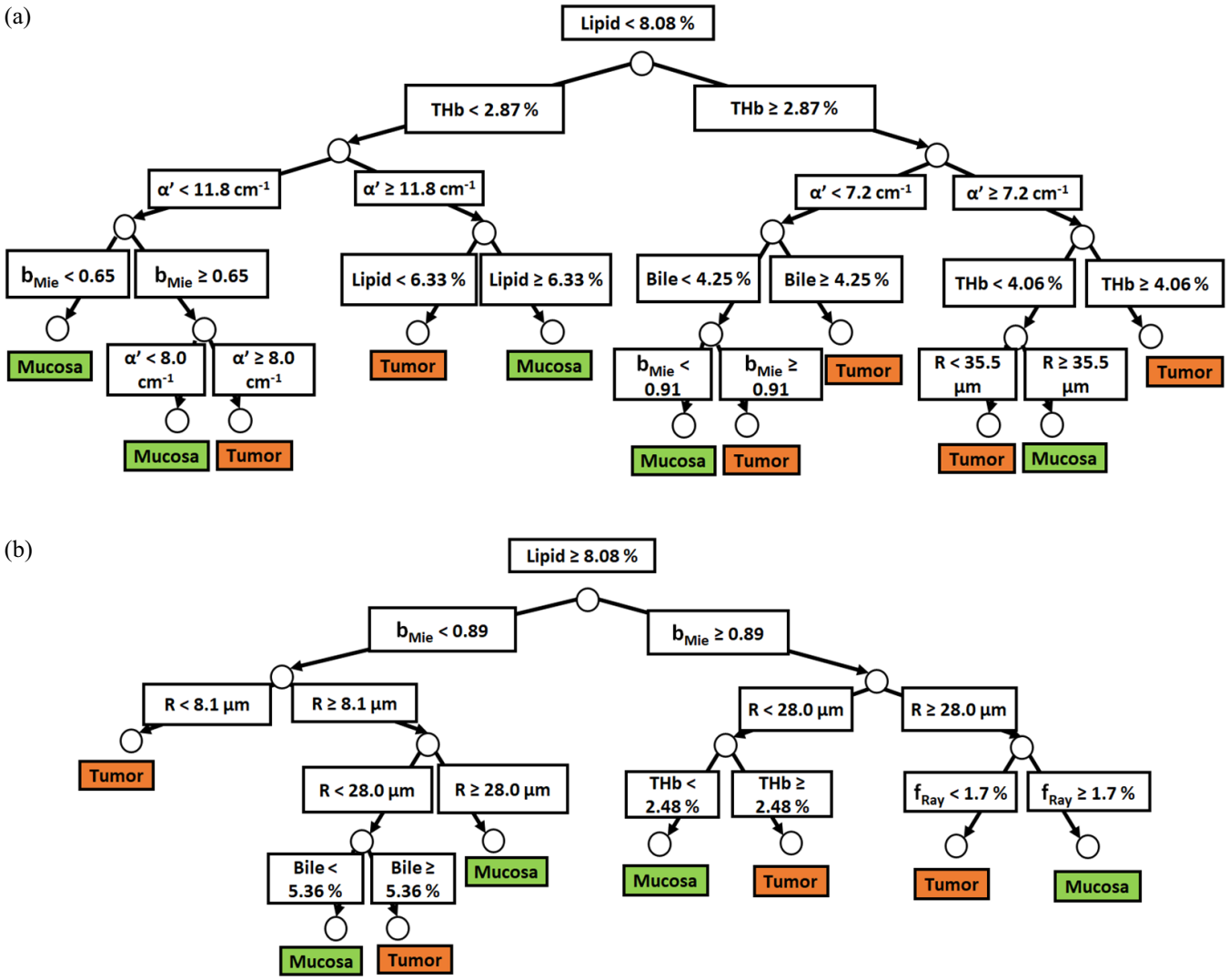


Figure 6. (a) Classification decision tree of the colorectal mucosa and tumor tissues based on parameter threshold values of probe 2 for $f_{\text{lipid}} < 8.08\%$. (b) Classification decision tree of the colorectal mucosa and tumor tissues based on parameter threshold values of probe 2 for $f_{\text{lipid}} \geq 8.08\%$.

absorption spectra equations described in the supplementary material).

Previous studies have used spectral fitting models based on diffusion theory [52, 57–67] and may not be accurate in estimating chromophore concentrations and scattering parameters from tissues with optical properties out of the range of validity of diffusion theory [31, 40, 41, 50–56, 68–82]. The spectral fitting model used in this study uses MC simulations for a variety of optical properties (μ_s ranging from 0.1 to 1000 cm^{-1} and μ_a ranging from 0.01 to 300 cm^{-1}). Therefore, our estimation of chromophore concentrations should be more accurate than prior studies. Furthermore, we combined our determined ranges of chromophore concentrations and scattering parameters which discriminate mucosa and tumor tissues with more than 90% AUC and 84% accuracy for probes investigating tissue depth up to 1 mm (small probe) and 1.9 mm (large probe).

We combine our spectral fitting model with machine learning in order to select the thresholds of chromophore concentrations and scattering parameters for highest differentiation between mucosa and CRC tissues. The selection of these thresholds can be performed directly by using the CART algorithm with no assumptions on the data distribution (i.e. reflectance values at each wavelength). Since the decision tree resulting from CART contains the most important parameters for tissue differentiation on the top (i.e. 1st nodes) of the tree, the importance of individual parameters can be checked by the order they appear on the tree. In addition, since parameters and their thresholds can be determined by tissue differentiation, it is possible to associate them with categories of mucosa and tumors occurring in cancer patients and, in particular, to identify cases where mucosa and tumors can be differentiated from each other. Thus, the results of our analysis offer not only a way to localize tumor tissues in normal mucosa, but a way of characterizing tissue microstructure and biochemistry that may influence clinical decision-making once parameter thresholds can be assessed in future *in vivo* studies involving sufficient number of patients. Finally, by understanding the cancer microstructure and biochemistry, it may be possible to

learn the origin of cancer and related diseases, as well as to identify cases leading to better patient prognosis.

4.3. Tissue optical scattering, HbO_2, Hb, water and lipid changes in mucosa and cancerous tissues

In this study, the most important parameters for discrimination between mucosa and tumor tissues for both probes were THb, *R*, f_{lipid}, f_{bile}, α', and b_{Mie} (figures 5(a), (b), 6(a) and (b)). Particularly for the small probe (probe 1), f_{Ray} was considered an important parameter for that discrimination based on reflectance of superficial tissue (figures 5(a) and (b)). As reported in previous studies, THb is expected to be higher in tumors due to the associated angiogenesis process to increase the local blood supply and support tumor growth. According to our results (tables 2 and 3 and figures 3 and 4), the investigated tumors had blood vessels with smaller average radius and slightly higher StO_2 in deeper tissue layers (probe 2) compared to mucosa, which may indicate that smaller vessels are created to increase the local oxygen supply in adenocarcinomas and carcinomas. Most previous studies investigated DRS for superficial tissue layers and reported higher THb and lower StO_2 in cancer tissues in relation to uninvolved mucosa [18, 19, 30–32]. By exploiting the wavelength range between 350 and 700 nm with a 550 μm SDD probe, Zonios *et al* [30] studied normal and cancerous tissues of 13 patients. The authors observed, respectively, THC of 13.6 $\pm$ 8.8 mg dl^{-1} and StO_2 of 59% $\pm$ 8% for normal tissues, whereas adenomatous polyps exhibited THC of 72.0 $\pm$ 29.2 mg dl^{-1} and StO_2 of 63% $\pm$ 10%. A higher THC and a slight increase of StO_2 for potentially malignant tissues (adenomatous polyps) agrees with our results of probe 1 (630 μm SDD probe). In addition, the mucosal THC of our study (THC 9.2 $\pm$ 9.5 mg dl^{-1}) was comparable to that of Zonios *et al*, while that of adenomatous polyps was about six-fold different from the THC values found in tumors of the present study (12.0 $\pm$ 8.7 mg dl^{-1}). The difference becomes even more apparent when comparing values to findings on probe 2, where lower THC and StO_2 were found (THC of 5.6 $\pm$ 2.4 mg dl^{-1} and StO_2 of 50% $\pm$ 17% for mucosa, and THC of 7.9 $\pm$ 3.5 mg dl^{-1} and StO_2 of 56% $\pm$ 18% for tumors, respectively). However, even lower values of THC have been found by Wang *et al* [31], who studied DRS of the tumors and surrounding normal tissues of 27 patients (17 with adenomatous polyps, eight with adenocarcinoma, and two with only normal tissues) in the visible wavelength range between 600 and 800 nm. By using probes with SDDs of 0.6, 1.5, 2.5, and 4 mm, Wang *et al* obtained mucosal THC of 59.8 $\pm$ 19.0 μM and tumor THC of 153.8 $\pm$ 38.6 μM. Even though the THC values are comparable to those of probe 2 of our study, their mucosal THC was lower while their tumor THC is higher on average (table 2). Wang *et al* found a much lower StO_2 for tumors (26.4% $\pm$ 6.1%) compared to normal tissue (60.7% $\pm$ 7.7%), which does not agree with our study. Finally, the THC values for probe 2 of our study are comparable to results obtained by Nandy *et al* [83], who performed spatial frequency domain imaging to *ex vivo* colorectal specimens of nine patients from which 15 (eight malignant and seven normal) regions were imaged. Images were taken by using 460, 530 and 630 nm wavelengths and two spatial frequencies (0 and 1 cm^{-1}). The authors found that THC varied between 46 and 80 μM in normal mucosa and between 57 and 118 μM in tumors.

In terms of scattering properties, tumors exhibit lower fraction of Rayleigh scattering (f_{Ray}), which may occur during cell division, when a relatively lower number of structures smaller than a wavelength exist in cells in order to create conditions for duplication of cellular structures. These structures include mitochondrion membranes (as mitochondria are under fragmentation for their equivalent distribution to daughter cells on cell division [84]) and cell membranes, replicating structures required for cell division. However, it is also important to remember that the number of mitochondria under fragmentation tends to increase during cell division in tumors. Since tumors contain cells in different stages of cell division, their tissue microstructure tends to be more heterogeneous compared to normal tissues. This heterogeneity can be observed in scattering parameters (figures 3 and 4), especially for superficial tissue (figure 3). The increase in the number of mitochondria and other organelles [85] agrees with the higher Mie scattering power (b_{Mie}) obtained in tumors, as it suggests that cancer tissues contain overall smaller-size particles and structures compared to normal tissues. Since Mie scattering is typically generated at organelle (e.g. mitochondria), nuclei, and cell scales [86], the presence of smaller structures (in average) generating Mie scattering agrees with the higher cell proliferation expected to be found in tumors [87–89].

Nandy *et al* [83] investigated scattering parameters by assuming an approximation of the total tissue scattering by a fitting to Mie scattering, which allows retrieving the scattering amplitude α' and the Mie scattering power b_{Mie} based on the three wavelengths investigated in their study instead of a broadband wavelength range as the present study. With this in mind, the authors reported that normal mucosa had α' between 11 and 19 cm^{-1}, b_{Mie} between 0.78 and 1.2, whereas tumor tissue had α' between 6 and 12 cm^{-1}, b_{Mie} between 0.2 and 0.8. While the values of α' and b_{Mie} are within the same range of those found for probe 2 in our study, their trend was exactly the opposite of our findings (lower α' and b_{Mie} for tumors compared to mucosa). Other studies have reported values of scattering coefficient at NIR wavelengths, which could be related to α', as the wavelength-dependent scattering coefficient has a much lower slope at NIR and longer wavelengths. Zeng *et al* [90] investigated eight cancer, one pre-malignant polyp, and five normal mucosa regions of nine patients by using a swept source-optical coherence tomography (SS-OCT) system. This system used 1310 nm as the center wavelength and had 110 nm for the full width half maximum bandwidth. In their study, cancerous specimens exhibited mean scattering coefficients (per image) ranging from 4.54 to 9.17 mm^{-1}, whereas those of normal tissues ranged from 2.50 to 8.21 mm^{-1}. The slightly higher scattering coefficients found in tumors agrees with the results of our study, as α' was higher for cancer tissues (table 2). On the other hand, higher scattering coefficient values disagree with results reported by Zhang *et al* [91], who used a spectral-domain OCT system with center wavelength at 850 nm and spectral bandwidth of 40 nm to study 16 cases

of malignant and normal colorectal tissues. The authors found that the scattering coefficient of 1.41 ± 0.18 mm^{-1} for malignant tissues (variation between 0.25 and 2.69 mm^{-1}) and 2.29 ± 0.32 mm^{-1} for normal tissues (values ranging from 1.09 to 5.41 mm^{-1}). Although scattering parameters have different trends among studies, it is important to consider that the wavelength range has a large influence on the probed depth and tissue layers investigated. Thus, microstructural parameters will differ, especially given the heterogeneity of tumor tissues. However, the range of α' and b_{Mie} obtained in this study (table 2 and figures 3 and 4) was still in a range, which is comparable to previous studies. Factors contributing to the difference between mucosa and cancer tissues were described by Backman and Roy [16] in terms of early increase in blood supply as well as nanostructural and microstructural changes such as alterations in the collagen fiber crosslinking, cytoskeleton, chromatin structure.

An indirectly related parameter with scattering is the lipid concentration, as lipid is present in structures which generate Rayleigh scattering such as membranes and lipid droplets [92]. Then, a lower f_{lipid} in tumors (tables 2 and 3 and figures 3 and 4) may mean less membranes and lipid droplets are present in the targeted cells/tissues, which leads to lower f_{Ray} (table 2). In both probes 1 and 2, the lipid content is lower in tumors (tables 2 and 3), which agrees with previous cancer studies [93, 94]. In a Raman spectroscopy study, Bergholt *et al* [93] found that colorectal tumors (adenomas and adenocarcinomas) had lower lipid concentration in relation to hyperplastic polyps and higher water content compared to normal tissues. A decrease in lipid concentration in cancer tissues is further confirmed with magnetic resonance spectroscopy in breast cancer [94]. Similar studies showed that tumors contain higher water-to-lipid ratio [95–99], which also agrees with the results of this study (table 2). Therefore, lipid and water content can be used individually or in combined parameters for cancer detection.

Finally, a combination of the parameters THb, R, f_{lipid}, f_{bile}, α', b_{Mie}, f_{Ray} was sufficient to provide classify normal mucosa and cancer tissues with $84.8\% \pm 0.6\%$ and $88.3\% \pm 0.6\%$ accuracy with probes 1 and 2, respectively (figures 5(a), (b), 6(a) and (b)). The parameter selection for classification of the decision trees (figures 5(a), (b), 6(a) and (b)) described nine subtypes of mucosa and tumors for probe 1 as well as ten subtypes of mucosa and tumors for probe 2. The number of tissue types shows that tissues interrogated with probe 2 tend to more heterogeneous compared to those interrogated with probe 1 (figures 5(a), (b), 6(a) and (b)). Even though the division into more tissue subtypes was expected from probing deeper tissue layers, it is important to note that the classification performed with probe 2 used less parameters (THb, R, f_{lipid}, f_{bile}, α', b_{Mie}) compared to probe 1 (THb, R, f_{lipid}, f_{bile}, α', b_{Mie}, f_{Ray}) and still obtained a higher tissue classification performance.

4.4. Considerations on biomolecular concentrations and probed depth for CRC detection

In our previous work [33], we showed that the probed depth for probe 1 ranges from 0.5 to 1 mm (0.8 to 0.9 mm for most wavelengths between 430 and 1590 nm), whereas that of probe 2 mostly between 0.5 and 1.9 mm (higher than 1.4 mm for most wavelengths between 430 and 1590 nm). Even though it is possible to quantify the probed depth, specifying which tissue layers are being probed in the colorectal wall still remains a challenge. A typical thickness of the total wall is about 2 mm, which may also be changed by a number of factors [100]. Individual thicknesses of the tissue layers may have a wide range of thicknesses. According to Castro-Poças *et al*, mucosa layers can vary from 0.3 to 1.2 mm, submucosa can vary between 0.2 and 1.8 mm and muscularis propria can vary from 0.3 to 2.4 mm [100]. This variance may contribute to the heterogeneity of the biochemical and microstructural parameters obtained in the present study (table 2). However, when comparing these parameters per probed depth, THb, THC, f_{lipid}, f_{water} extracted from DRS spectra of probe 2 exhibited a relatively lower coefficient of variation compared to those of probe 1. This result suggests that probing more tissue layers with probe 2 did not generate more inhomogeneity on absorption parameters such as THb, lipid and water concentrations. It is unclear how probing deeper tissue layers affects other parameters and it is expected that multilayered tissue structures influence the scattering parameters reported in this study.

In addition, our results indicate that deeper tissue layers of mucosa and tumor tend to have higher average vessel radius (R), lipid concentration (f_{lipid}), and Mie scattering power (b_{Mie}), whereas all other parameters tend to be lower for probe 2 (table 2 and figures 3 and 4). For tumors, a slightly higher R in deeper tissue layers may happen due to probing relatively less thin blood vessels (compared to the total number of vessels in the probed volume) created in the tumor surface during angiogenesis. A similar conclusion may be drawn from lower THb and THC (table 2 and figures 3 and 4), as most of the blood volume would be present on the superficial tissue layers. Since less blood vessels occur in deeper tumor layers, it would be expected a slower cell division, larger-sized cells, and less fragmented mitochondria. These three expected features lead to less refractive index mismatches, which agrees with our decreased scattering amplitude α'. Assuming Mie scattering is mostly generated by mitochondria [86], a lower number of mitochondria (larger size) would mean lower b_{Mie}, as per our results. Also, lower cell division rates mean less fragmented mitochondria, which generates less refractive index mismatches due to water-membranes transitions and thus leads to lower f_{Ray}. Finally, f_{water} was expected to be lower in the tissue surface due to dehydration caused during our *ex vivo* measurements. On the other hand, our procedure of keeping the tissue hydrated with a damp cloth from times to times during our measurements may have affected the water content extracted with our spectral fitting algorithm.

4.5. Validity and limitations of our study

Our study has several limitations due to variations caused in *ex vivo* tissues and contact measurements. First, the interrogated cancer tissues were from diverse stages with predominance of advance stage tumors (pT2 and above). The measured tumor sites were selected based on the palpation and naked eye determination by experienced surgeons who demarcated

the tumor region, although all these regions were confirmed subsequently with histology. It is important to note that this determination does not decrease the validity of our dataset and biochemical/microstructural analysis, as our dataset is larger compared to previous studies in the field (1363 spectra for probe 1 and 1526 for probe 2) and contains DRS spectra with variations due to parameters discussed in this section. With this in mind, early-stage cancer changes are expected to occur over the same tissue biomolecules and microstructure parameters but with lower magnitude in relation to advanced cancer.

Since our measurements were performed in *ex vivo* colorectal specimens, the blood oxygenation was not controlled during our data collection. However, we confirmed there was no significant variations on average Hb and HbO_2 in mucosa and tumor regions in a pilot *ex vivo* observation of the DRS signal in three patients. Our observation was limited by seven mucosa and seven tumor sites during the 1st 15 min of our measurements (data not shown). We are also aware that THb and StO_2 may increase and f_{water} may decrease in *ex vivo* tissues compared to *in vivo*, as described by Baltussen *et al* [101] in a previous study investigating different types of colorectal tissues (fat, tumor, and healthy colorectal wall). It is also important to note that, although the authors used the same optical technique (DRS) to draw those conclusions, their probe has a different SDD (1.29 mm center-to-center distance) compared to those of this study and their spectral fitting model uses diffusion theory approximation to estimate THb, StO_2 and f_{water}. In addition, the behavior of StO_2 is still not well understood, as previously reported studies disagree on their StO_2 trend on *ex vivo* tissues. While Baltussen *et al* reported an increased StO_2 in *ex vivo* tissues within 1 h after resection in relation to *in vivo* tissues, Salomatina *et al* [102] reported a decrease in StO_2 in mouse ear tissues 5–10 min after excision (*ex vivo*) of tissue and after 24 and 72 h of storage. Even though StO_2 varies, it was not considered as a relevant parameter in the classification of our decision tree. Also, we attempted to reduce tissue dehydration as much as possible by keeping the tissue moisture with a water wet wipe once every seven spectral measurements in average during the measurements. We attempted to not overhydrate tissues as they were wiped by not using an overly wet wipe. As illustrated by our results, only a small deviation on water content was found in tumor measurements, which can be mainly attributed to the tissue heterogeneity expected from cancer. Furthermore, if overhydration due to uncontrolled wiping (relatively 'random' event) had influenced our measurements, higher standard deviations in water concentration should have been associated with higher water-concentration measurements (i.e. tumor measurements), which is not what we observed.

We acknowledge that probe contact pressure and sufficient optical contact with interrogated tissues may be challenging to accomplish during *in vivo* endoscopy. With this in mind, a reduced sensitivity to optical contact and probe positioning is expected in our probe 2 due to its larger SDD, which may be related to higher measurement repeatability and less standard deviation present in some parameters of this probe. However, larger SDDs also means larger probed volume, which may cause more variations upon probe contact pressure if this pressure allows collecting the signal from heterogeneities of deeper tissue (e.g. interface between tissue layers). This type of variation was previously reported [103] and needs to be taken into account in order to correct DRS spectra. One should also note that the incorporation of large SDD probes is feasible in colonoscope channels, as long as the probe fits the diameter of the instrument channel (typically 2.8–4.2 mm [104, 105]).

Finally, not including non-cancer pathology in our study may change the classification performance of our CART model. With this in mind, future studies will include data on non-cancer pathology. On the other hand, the lack of non-cancer pathology does not affect our tissue biochemical/microstructural parameters. Therefore, comparison of these parameters with other studies is valid, especially considering our dataset includes a robust sampling of intra- and inter-patient variations (1363 + 1526 spectra of 47 patients) in both superficial and deeper tissue layers.

5. Conclusions

In this study, we assessed the most important microstructural and biochemical parameters for endoscopic CRC detection through broadband DRS as well as the thresholds of these parameters for differentiation between mucosa and tumors. These parameters were THb, R, f_{lipid}, f_{bile}, α', b_{Mie}, f_{Ray}, which were used to classify tissues based on decision trees for interrogating superficial (probe 1) and deeper (probe 2) tissue layers. When considering the most important parameters for CRC detection, emphasis can be given to f_{lipid}, α', and b_{Mie}, as these parameters appeared on the top of decision trees of botsh probes. Tissue classification with more than 90% AUC was achieved with both probes, with classification using probe 1 leading to 87.1% ± 0.6% sensitivity, 89.7% ± 1.0% specificity, 88.3% ± 0.6% accuracy, 0.915 ± 0.006 AUC, whereas that of probe 2 achieved 81.8% ± 1.1% sensitivity, 88.2% ± 1.4% specificity, 84.8% ± 0.6% accuracy, 0.900 ± 0.007 AUC. Therefore, the extracted parameters are relevant for cancer identification in the colorectal lumen. Furthermore, we solved the limitations of previous studies in terms of the quantification of independent tissue biochemical and microstructural parameters on superficial and deeper tissue layers without restrictions of diffusion theory and at an extended wavelength range for DRS.

To the best of our knowledge, this is the first study to evaluate the potential tissue biomolecule concentrations and scattering properties in superficial and deeper tissue layers for CRC detection in the luminal wall. Our study was conducted in *ex vivo* tissues and shows a proof-of-concept of probing tissue biochemistry and microstructure to be extended to *in vivo* interrogation during endoscopy. In a practical perspective, this study could potentially be used to develop a probe for CRC detection as well as indicate important tissue parameters for clinical decision-making during colonoscopy. The integration of this capability into a flexible fiberoptic probe which could be passed down a scope working channel could identify more subtle mucosal abnormalities such as sessile serrated polyps as well as obviate the need for multiple biopsies or

polypectomies of normal mucosa. In the long-term, identifying tissue microstructure and biochemistry related to CRC could help understanding its origin and natural history, as further tissue biochemical information can be extracted non-invasively and in real-time and possibly complement biochemical analysis that require time-consuming laboratory procedures. Our study provided a first-step on this type of analysis by recognizing categories of CRC and surrounding mucosa which can be found in cancer patients as well as the thresholds of tissue chromophores and scattering parameters characterizing each type of tissue. These parameters could potentially be combined with other analysis to help clinical decision-making and to improve patient prognosis.

Data availability statement

The data that support the findings of this study are available upon reasonable request from the authors.

Acknowledgments

We acknowledge Eduardo Moriyama for the advice and logistics of the project associated with this manuscript, Shree Krishnamoorthy for the discussions on the same project, Haiyang Li for the design and assembly of the holder of the DRS system, Noel Lynch and Andrew McGuire for specimen retrieval of patients of this study and all the logistics related to it, Vivienne Curran, Aoife Foyle, Una McAuliffe, Evelyn Flanagan, Shauni Fitzgerald, and Edmund Manning for all the logistics of clinical procedures, research ethics documents, and search for patient information. Shauni Fitzgerald and Edmund Manning were funded by the Mercy Foundation. This study received financial support from Science Foundation Ireland (SFI): Grant ID SFI/15/RP/2828.

Author contributions

M S N Conceptualization, Methodology, Software, Validation, Formal analysis, Investigation, Resources, Data Curation, Writing—Original Draft, Writing—Review and Editing, Visualization, Supervision, Project administration, M R Conceptualization, Methodology, Software, Validation, Formal analysis, J e.g. Conceptualization, Methodology, Software, Validation, S M Investigation, Data Curation, M. Investigation, Data Curation, Software, H L Methodology, Investigation, S K Investigation, Resources, Data Curation, M O R Conceptualization, Methodology, Validation, Investigation, Resources, Data Curation, Writing—Review and Editing, Supervision, Project administration, Funding Acquisition, S A E Conceptualization, Methodology, Resources, Software, Validation, Formal analysis, Investigation, Data Curation, Writing—Original Draft, Writing—Review and Editing, Visualization, Supervision, Project administration, Funding Acquisition.

Conflict of interest

The authors declare no conflicts of interest.

ORCID iDs

Marcelo Saito Nogueira https://orcid.org/0000-0002-5611-9620
Siddra Maryam https://orcid.org/0000-0003-2644-2088
Stefan Andersson-Engels https://orcid.org/0000-0001-5640-3122

References

[1] Bray F, Ferlay J, Soerjomataram I, Siegel R L, Torre L A and Jemal A 2018 Global cancer statistics 2018: GLOBOCAN estimates of incidence and mortality worldwide for 36 cancers in 185 countries *CA. Cancer J. Clin.* **68** 394–424
[2] Ferlay J, Ervik M, Lam F, Colombet M, Mery L, Piñeros M, Znaor A, Soerjomataram I and Bray F 2018 Global cancer observatory: cancer today *Lyon Fr. Int. Agency Res. Cancer* 1–6
[3] Wallace M B and Kiesslich R 2010 Advances in endoscopic imaging of colorectal neoplasia *Gastroenterology* **138** 2140–50
[4] Siegel R L, Fedewa S A, Anderson W F, Miller K D, Ma J, Rosenberg P S and Jemal A 2017 Colorectal cancer incidence patterns in the United States, 1974–2013 *JNCI J. Natl Cancer Inst.* **109** 8
[5] Su M-Y, Hsu C-M, Ho Y-P, Chen P-C, Lin C-J and Chiu C-T 2006 Comparative study of conventional colonoscopy, chromoendoscopy, and narrow-band imaging systems in differential diagnosis of neoplastic and nonneoplastic colonic polyps *Am. J. Gastroenterol.* **101** 2711–6
[6] Nicolás-Pérez D, Parra-Blanco A, Gimeno-Garc'ia A Z, Ortega-Sánchez J A, Carrillo-Palau M, Jiménez-Sosa A and Quintero-Carrion E 2013 Risk factors associated with colorectal flat adenoma detection *Eur. J. Gastroenterol. Hepatol.* **25** 302–8
[7] Dik V K, Moons L M G and Siersema P D 2014 Endoscopic innovations to increase the adenoma detection rate during colonoscopy *World J. Gastroenterol. WJG* **20** 2200
[8] Lee J, Park S W, Kim Y S, Lee K J, Sung H, Song P H, Yoon W J and Moon J S 2017 Risk factors of missed colorectal lesions after colonoscopy *Medicine* **96** 27
[9] Pickhardt P J, Nugent P A, Mysliwiec P A, Choi J R and Schindler W R 2004 Location of adenomas missed by optical colonoscopy *Ann. Intern. Med.* **141** 352–9
[10] Kaltenbach T, Friedland S and Soetikno R 2008 A randomised tandem colonoscopy trial of narrow band imaging versus white light examination to compare neoplasia miss rates *Gut* **57** 1406–12
[11] Sanduleanu S, Masclee A M and Meijer G A 2012 Interval cancers after colonoscopy—insights and recommendations *Nat. Rev. Gastroenterol. Hepatol.* **9** 550
[12] Rabeneck L, Paszat L F, Hilsden R J, Saskin R, Leddin D, Grunfeld E, Wai E, Goldwasser M, Sutradhar R and Stukel T A 2008 Bleeding and perforation after outpatient colonoscopy and their risk factors in usual clinical practice *Gastroenterology* **135** 1899–906
[13] Winawer S J *et al* 1997 Colorectal cancer screening: clinical guidelines and rationale *Gastroenterology* **112** 594–642
[14] Leedham S J, Graham T A, Oukrif D, McDonald S A C, Rodriguez–Justo M, Harrison R F, Shepherd N A, Novelli M R, Jankowski J A Z and Wright N A 2009 Clonality, founder mutations, and field cancerization in human

ulcerative colitis—associated neoplasia *Gastroenterology* **136** 542–50
[15] Aivado M, Gynes M, Gorelov V, Schmidt W U, Röher H D and Goretzki P E 2000 'Field cancerization'—an additional phenomenon in development of colon tumors? K-ras codon 12 mutations in normal colonic mucosa of patients with colorectal neoplasms *Chirurg* **71** 1230–4
[16] Backman V and Roy H K 2013 Advances in biophotonics detection of field carcinogenesis for colon cancer risk stratification *J. Cancer* **4** 251
[17] Pogue B W 2015 Optics in the molecular imaging race *Opt. Photonics News* **26** 24–31
[18] Mourant J R, Bigio I J, Boyer J D, Johnson T M, Lacey J, Bohorfoush A G and Mellow M H 1996 Elastic scattering spectroscopy as a diagnostic tool for differentiating pathologies in the gastrointestinal tract: preliminary testing *J. Biomed. Opt.* **1** 192–200
[19] Dhar A, Johnson K S, Novelli M R, Bown S G, Bigio I J, Lovat L B and Bloom S L 2006 Elastic scattering spectroscopy for the diagnosis of colonic lesions: initial results of a novel optical biopsy technique *Gastrointest. Endosc.* **63** 257–61
[20] Han Z, Zhang A, Wang X, Sun Z, Wang M D and Xie T 2016 *In vivo* use of hyperspectral imaging to develop a noncontact endoscopic diagnosis support system for malignant colorectal tumors *J. Biomed. Opt.* **21** 16001
[21] Yuan X, Zhang D, Wang C, Dai B, Zhao M and Li B 2018 Hyperspectral imaging and SPA–LDA quantitative analysis for detection of colon cancer tissue *J. Appl. Spectrosc.* **85** 307–12
[22] Ge Z, Schomacker K T and Nishioka N S 1998 Identification of colonic dysplasia and neoplasia by diffuse reflectance spectroscopy and pattern recognition techniques *Appl. Spectrosc.* **52** 833–9
[23] Rodriguez-Diaz E, Huang Q, Cerda S R, O'Brien M J, Bigio I J and Singh S K 2015 Endoscopic histological assessment of colonic polyps by using elastic scattering spectroscopy *Gastrointest. Endosc.* **81** 539–47
[24] Chen H, Lin Z, Wu H, Wang L, Wu T and Tan C 2015 Diagnosis of colorectal cancer by near-infrared optical fiber spectroscopy and random forest *Spectrochim. Acta* A **135** 185–91
[25] Chen H, Lin Z, Mo L and Tan C 2017 Identification of colorectal cancer using near-infrared spectroscopy and adaboost with decision stump *Anal. Lett.* **50** 2608–18
[26] Chen H, Tan C, Wu H, Lin Z and Wu T 2014 Feasibility of rapid diagnosis of colorectal cancer by near-infrared spectroscopy and support vector machine *Anal. Lett.* **47** 2580–93
[27] Ehlen L *et al* 2019 Synergy of fluorescence and near-infrared spectroscopy in detection of colorectal cancer *J. Surg. Res.* **242** 349–56
[28] Claridge E and Hidović-Rowe D 2013 Model based inversion for deriving maps of histological parameters characteristic of cancer from *ex vivo* multispectral images of the colon *IEEE Trans. Med. Imaging* **33** 822–35
[29] Kumashiro R, Konishi K, Chiba T, Akahoshi T, Nakamura S, Murata M, Tomikawa M, Matsumoto T, Maehara Y and Hashizume M 2016 Integrated endoscopic system based on optical imaging and hyperspectral data analysis for colorectal cancer detection *Anticancer Res.* **36** 3925–32
[30] Zonios G, Perelman L T, Backman V, Manoharan R, Fitzmaurice M, van Dam J and Feld M S 1999 Diffuse reflectance spectroscopy of human adenomatous colon polyps *in vivo Appl. Opt.* **38** 6628–37
[31] Wang H-W, Jiang J-K, Lin C-H, Lin J-K, Huang G-J and Yu J-S 2009 Diffuse reflectance spectroscopy detects increased hemoglobin concentration and decreased oxygenation during colon carcinogenesis from normal to malignant tumors *Opt. Express* **17** 2805–17
[32] Roy H K *et al* 2008 Spectroscopic microvascular blood detection from the endoscopically normal colonic mucosa: biomarker for neoplasia risk *Gastroenterology* **135** 1069–78
[33] Nogueira M S, Maryam S, Amissah M, Lu H, Lynch N, Killeen S, O'Riordain M and Andersson-Engels S 2021 Evaluation of wavelength ranges and tissue depth probed by diffuse reflectance spectroscopy for colorectal cancer detection *Sci. Rep.* **11** 1–17
[34] Wang L, Jacques S L and Zheng L 1995 MCML—Monte Carlo modeling of light transport in multi-layered tissues *Comput. Methods Programs Biomed.* **47** 131–46
[35] Alerstam E, Lo W C Y, Han T D, Rose J, Andersson-Engels S and Lilge L 2010 Next-generation acceleration and code optimization for light transport in turbid media using GPUs *Biomed. Opt. Express* **1** 658–75
[36] Alerstam E, Svensson T and Andersson-Engels S 2008 Parallel computing with graphics processing units for high-speed Monte Carlo simulation of photon migration *J. Biomed. Opt.* **13** 60504
[37] Wang L, Jacques S L and Zheng L 1997 CONV—convolution for responses to a finite diameter photon beam incident on multi-layered tissues *Comput. Methods Programs Biomed.* **54** 141–50
[38] Valery T 2000 *Tissue Optics: Light Scattering Methods and Instruments for Medical Diagnosis* (Bellingham, WA: SPIE Press)
[39] Jacques S L 2013 Optical properties of biological tissues: a review *Phys. Med. Biol.* **58** R37
[40] Nachabé R, Evers D J, Hendriks B H W, Lucassen G W, van der Voort M, Wesseling J and Ruers T J M 2011 Effect of bile absorption coefficients on the estimation of liver tissue optical properties and related implications in discriminating healthy and tumorous samples *Biomed. Opt. Express* **2** 600–14
[41] Nachabé R, Hendriks B H W, van der Voort M, Desjardins A E and Sterenborg H J C M 2010 Estimation of biological chromophores using diffuse optical spectroscopy: benefit of extending the UV–VIS wavelength range to include 1000–1600 nm *Biomed. Opt. Express* **1** 1432–42
[42] Nogueira M S, Lacerenza M, Sekar S K V, Buttafava M, Pifferi A, Tosi A, Contini D and Andersson-Engels S 2020 Broadband extraction of tissue optical properties using a portable hybrid time-resolved continuous wave instrumentation: characterization of *ex vivo* organs *Clin. Transl. Biophotonics* TM2B–3
[43] Cobbold J F L and Summerfield J A 2012 The liver in systemic disease *Handbook of Liver Disease* (Amsterdam: Elsevier) pp 297–307
[44] Keller M D, Majumder S K, Kelley M C, Meszoely I M, Boulos F I, Olivares G M and Mahadevan-Jansen A 2010 Autofluorescence and diffuse reflectance spectroscopy and spectral imaging for breast surgical margin analysis *Lasers Surg. Med. Off. J. Am. Soc. Laser Med. Surg.* **42** 15–23
[45] Laughney A M, Krishnaswamy V, Garcia-Allende P B, Conde O M, Wells W A, Paulsen K D and Pogue B W 2010 Automated classification of breast pathology using local measures of broadband reflectance *J. Biomed. Opt.* **15** 66019
[46] Wallace M B *et al* 2000 Endoscopic detection of dysplasia in patients with Barrett's esophagus using light-scattering spectroscopy *Gastroenterology* **119** 677–82
[47] Jayanthi J L, Nisha G U, Manju S, Philip E K, Jeemon P, Baiju K V, Beena V T and Subhash N 2011 Diffuse reflectance spectroscopy: diagnostic accuracy of a non-invasive screening technique for early detection of malignant changes in the oral cavity *BMJ Open* **1** 1

[48] Majumder S K, Keller M D, Boulos F I, Kelley M C and Mahadevan-Jansen A 2008 Comparison of autofluorescence, diffuse reflectance, and Raman spectroscopy for breast tissue discrimination *J. Biomed. Opt.* **13** 54009
[49] Wallace V P, Bamber J C, Crawford D C, Ott R J and Mortimer P S 2000 Classification of reflectance spectra from pigmented skin lesions, a comparison of multivariate discriminant analysis and artificial neural networks *Phys. Med. Biol.* **45** 2859
[50] Nilsson J H, Reistad N, Brange H, Öberg C-F and Sturesson C 2017 Diffuse reflectance spectroscopy for surface measurement of liver pathology *Eur. Surg. Res.* **58** 40–50
[51] Evers D J, Nachabe R, Hompes D, van Coevorden F, Lucassen G W, Hendriks B H W, van Velthuysen M-L, Wesseling J and Ruers T J M 2013 Optical sensing for tumor detection in the liver *Eur. J. Surg. Oncol.* **39** 68–75
[52] Wang L V and Jacques S L 2000 Source of error in calculation of optical diffuse reflectance from turbid media using diffusion theory *Comput. Methods Programs Biomed.* **61** 163–70
[53] Hennessy R J, Lim S L, Markey M K and Tunnell J W 2013 Monte Carlo lookup table-based inverse model for extracting optical properties from tissue-simulating phantoms using diffuse reflectance spectroscopy *J. Biomed. Opt.* **18** 37003
[54] Fredriksson I, Larsson M and Strömberg T 2012 Inverse Monte Carlo method in a multilayered tissue model for diffuse reflectance spectroscopy *J. Biomed. Opt.* **17** 47004
[55] Rajaram N, Nguyen T and Tunnell J W 2008 Lookup table—based inverse model for determining optical properties of turbid media *J. Biomed. Opt.* **13** 50501
[56] Zhong X, Wen X and Zhu D 2014 Lookup-table-based inverse model for human skin reflectance spectroscopy: two-layered Monte Carlo simulations and experiments *Opt. Express* **22** 1852–64
[57] Fantini S, Walker S A, Franceschini M A, Kaschke M, Schlag P M and Moesta K T 1998 Assessment of the size, position, and optical properties of breast tumors *in vivo* by noninvasive optical methods *Appl. Opt.* **37** 1982–9
[58] Martelli F, Contini D, Taddeucci A and Zaccanti G 1997 Photon migration through a turbid slab described by a model based on diffusion approximation. II. Comparison with Monte Carlo results *Appl. Opt.* **36** 4600–12
[59] Cuccia D J, Bevilacqua F P, Durkin A J, Ayers F R and Tromberg B J 2009 Quantitation and mapping of tissue optical properties using modulated imaging *J. Biomed. Opt.* **14** 24012
[60] Durduran T, Choe R, Culver J P, Zubkov L, Holboke M J, Giammarco J, Chance B and Yodh A G 2002 Bulk optical properties of healthy female breast tissue *Phys. Med. Biol.* **47** 2847
[61] Hielscher A H, Alcouffe R E and Barbour R L 1998 Comparison of finite-difference transport and diffusion calculations for photon migration in homogeneous and heterogeneous tissues *Phys. Med. Biol.* **43** 1285
[62] Ntziachristos V and Weissleder R 2001 Experimental three-dimensional fluorescence reconstruction of diffuse media by use of a normalized Born approximation *Opt. Lett.* **26** 893–5
[63] Jiang H 1998 Frequency-domain fluorescent diffusion tomography: a finite-element-based algorithm and simulations *Appl. Opt.* **37** 5337–43
[64] Pogue B W and Patterson M S 1994 Frequency-domain optical absorption spectroscopy of finite tissue volumes using diffusion theory *Phys. Med. Biol.* **39** 1157
[65] Fishkin J B, Coquoz O, Anderson E R, Brenner M and Tromberg B J 1997 Frequency-domain photon migration measurements of normal and malignant tissue optical properties in a human subject *Appl. Opt.* **36** 10–20
[66] Erickson T A, Mazhar A, Cuccia D J, Durkin A J and Tunnell J W 2010 Lookup-table method for imaging optical properties with structured illumination beyond the diffusion theory regime *J. Biomed. Opt.* **15** 36013
[67] Tromberg B J, Coquoz O, Fishkin J B, Pham T, Anderson E R, Butler J, Cahn M, Gross J D, Venugopalan V and Pham D 1997 Non-invasive measurements of breast tissue optical properties using frequency-domain photon migration *Phil. Trans. R. Soc.* B **352** 661–8
[68] Shi Z and Anderson C A 2010 Application of Monte Carlo simulation-based photon migration for enhanced understanding of near-infrared (NIR) diffuse reflectance. Part I: depth of penetration in pharmaceutical materials *J. Pharm. Sci.* **99** 2399–412
[69] Zhu C and Liu Q 2013 Review of Monte Carlo modeling of light transport in tissues *J. Biomed. Opt.* **18** 50902
[70] Sharma M, Hennessy R, Markey M K and Tunnell J W 2014 Verification of a two-layer inverse Monte Carlo absorption model using multiple source-detector separation diffuse reflectance spectroscopy *Biomed. Opt. Express* **5** 40–53
[71] Péry E, Blondel W C P M, Thomas C, Didelon J and Guillemin F 2006 Diffuse reflectance spectroscopy Monte–Carlo modeling: elongated arterial tissues optical properties *IFAC Proc. Vol* **39** 41–46
[72] Bevilacqua F and Depeursinge C 1999 Monte Carlo study of diffuse reflectance at source-detector separations close to one transport mean free path *J. Opt. Soc. Am. A* **16** 2935–45
[73] Yao G and Wang L V 1999 Monte Carlo simulation of an optical coherence tomography signal in homogeneous turbid media *Phys. Med. Biol.* **44** 2307
[74] Madsen S J, Wilson B C, Patterson M S, Park Y D, Jacques S L and Hefetz Y 1992 Experimental tests of a simple diffusion model for the estimation of scattering and absorption coefficients of turbid media from time-resolved diffuse reflectance measurements *Appl. Opt.* **31** 3509–17
[75] Doronin A and Meglinski I 2011 Online object oriented Monte Carlo computational tool for the needs of biomedical optics *Biomed. Opt. Express* **2** 2461–9
[76] Liu Q and Ramanujam N 2007 Scaling method for fast Monte Carlo simulation of diffuse reflectance spectra from multilayered turbid media *J. Opt. Soc. Am. A* **24** 1011–25
[77] Hiraoka M, Firbank M, Essenpreis M, Cope M, Arridge S R, van der Zee P and Delpy D T 1993 A Monte Carlo investigation of optical pathlength in inhomogeneous tissue and its application to near-infrared spectroscopy *Phys. Med. Biol.* **38** 1859
[78] Zonios G and Dimou A 2011 Modeling diffuse reflectance from homogeneous semi-infinite turbid media for biological tissue applications: a Monte Carlo study *Biomed. Opt. Express* **2** 3284–94
[79] Arimoto H, Egawa M and Yamada Y 2005 Depth profile of diffuse reflectance near-infrared spectroscopy for measurement of water content in skin *Ski. Res. Technol.* **11** 27–35
[80] Gardner C M, Jacques S L and Welch A J 1996 Light transport in tissue: accurate expressions for one-dimensional fluence rate and escape function based upon Monte Carlo simulation *Lasers Surg. Med.* **18** 129–38
[81] Wilson B C and Adam G 1983 A Monte Carlo model for the absorption and flux distributions of light in tissue *Med. Phys.* **10** 824–30
[82] Flock S T, Patterson M S, Wilson B C and Wyman D R 1989 Monte Carlo modeling of light propagation in highly scattering tissues. I. Model predictions and comparison

with diffusion theory *IEEE Trans. Biomed. Eng.* **36** 1162–8
[83] Nandy S, Chapman W, Rais R, Gonzalez I, Chatterjee D, Mutch M and Zhu Q 2018 Label-free quantitative optical assessment of human colon tissue using spatial frequency domain imaging *Tech. Coloproctol.* **22** 617–21
[84] Giacomello M, Pyakurel A, Glytsou C and Scorrano L 2020 The cell biology of mitochondrial membrane dynamics *Nat. Rev. Mol. Cell Biol.* **21** 204–24
[85] Wallace D C 2012 Mitochondria and cancer *Nat. Rev. Cancer* **12** 685–98
[86] Turzhitsky V, Qiu L, Itzkan I, Novikov A A, Kotelev M S, Getmanskiy M, Vinokurov V A, Muradov A V and Perelman L T 2014 Spectroscopy of scattered light for the characterization of micro and nanoscale objects in biology and medicine *Appl. Spectrosc.* **68** 133–54
[87] Cohen S M and Ellwein L B 1990 Cell proliferation in carcinogenesis *Science* **249** 1007–11
[88] Marangon Junior H, Leão P L R, Melo V V M, Caixeta Â B, Souza P E A, de Aguiar M C F and Horta M C R 2018 Cell proliferation is associated with intensity of tumor budding in oral squamous cell carcinoma *J. Oral Pathol. Med.* **47** 128–35
[89] Preston-Martin S, Pike M C, Ross R K, Jones P A and Henderson B E 1990 Increased cell division as a cause of human cancer *Cancer Res.* **50** 7415–21
[90] Zeng Y, Rao B, Chapman W C, Nandy S, Rais R, González I, Chatterjee D, Mutch M and Zhu Q 2019 The angular spectrum of the scattering coefficient map reveals subsurface colorectal cancer *Sci. Rep.* **9** 1–11
[91] Zhang Q Q, Wu X J, Tang T, Zhu S W, Yao Q, Gao B Z and Yuan X C 2012 Quantitative analysis of rectal cancer by spectral domain optical coherence tomography *Phys. Med. Biol.* **57** 5235
[92] Maier J S, Walker S A, Fantini S, Franceschini M A and Gratton E 1994 Possible correlation between blood glucose concentration and the reduced scattering coefficient of tissues in the near infrared *Opt. Lett.* **19** 2062–4
[93] Bergholt M S *et al* 2016 Simultaneous fingerprint and high-wavenumber fiber-optic Raman spectroscopy enhances real-time *in vivo* diagnosis of adenomatous polyps during colonoscopy *J. Biophotonics* **9** 333–42
[94] Thomas M A, Binesh N, Yue K and DeBruhl N 2001 Volume-localized two-dimensional correlated magnetic resonance spectroscopy of human breast cancer *J. Magn. Reson. Imaging* **14** 181–6
[95] Gilligam P, Flangan F L, Redmond O M, Walsh D, Carney D N and Ennis J T 1997 Proton magnetic resonance spectroscopy in MR mammographic evaluation of breast cancer *Proc. Int. Soc. Magn. Reson Med.* **5** 1378
[96] Jagannathan N R, Kumar M, Raghunathan P, Coshic O, Julka P K and Rath G K 1999 Assessment of the therapeutic response of human breast carcinoma using *in vivo* volume localized proton magnetic resonance spectroscopy *Curr. Sci.* **76** 777–82
[97] Sijens P E, Wijrdeman H K, Moerland M A, Bakker C J, Vermeulen J W and Luyten P R 1988 Human breast cancer *in vivo*: H-1 and P-31 MR spectroscopy at 1.5 T *Radiology* **169** 615–20
[98] Roebuck J R, Cecil K M, Schnall M D and Lenkinski R E 1998 Human breast lesions: characterization with proton MR spectroscopy *Radiology* **209** 269–75
[99] Jagannathan N R, Singh M, Govindaraju V, Raghunathan P, Coshic O, Julka P K and Rath G K 1998 Volume localized *in vivo* proton MR spectroscopy of breast carcinoma: variation of water–fat ratio in patients receiving chemotherapy *NMR Biomed.* **11** 414–22
[100] Castro-Poças F M, Dinis-Ribeiro M, Araújo T P and Pedroto I 2015 Echoendoscopic characterization of the human colon *Rev. Española Enfermedades Dig.* **107** 469–75
[101] Langhout G C *et al* 2018 Nerve detection using optical spectroscopy, an evaluation in four different models: in human and swine, *in vivo*, and post mortem *Lasers Surg. Med.* **50** 253–61
[102] Salomatina E and Yaroslavsky A N 2008 Evaluation of the *in vivo* and *ex vivo* optical properties in a mouse ear model *Phys. Med. Biol.* **53** 2797
[103] Saito Nogueira M, Raju M, Gunther J, Grygoryev K, Lu H, Komolibus K and Andersson-Engels S 2018 Diffuse reflectance spectroscopy for determination of optical properties and chromophore concentrations of mice internal organs in the range of 350 nm to 1860 nm *Biophotonics Photonic Solut. Better Heal. Care* VI **10685** 106853G
[104] Varadarajulu S *et al* 2011 GI endoscopes *Gastrointest. Endosc.* **74** 1–6
[105] Kay M and Wyllie R 2011 Colonoscopy, polypectomy, and related techniques *Pediatric Gastrointestinal and Liver Disease* (Amsterdam: Elsevier) pp 650–67

cancers

MDPI

Article

Insights into Biochemical Sources and Diffuse Reflectance Spectral Features for Colorectal Cancer Detection and Localization

Marcelo Saito Nogueira [1,2,*], Siddra Maryam [1,2], Michael Amissah [1,2], Andrew McGuire [3], Chloe Spillane [3], Shane Killeen [3], Stefan Andersson-Engels [1,2] and Micheal O'Riordain [3]

1 Tyndall National Institute, Lee Maltings, Dyke Parade, T12 R5CP Cork, Ireland
2 Department of Physics, University College Cork, College Road, T12 K8AF Cork, Ireland
3 Department of Surgery, Mercy University Hospital, T12 WE28 Cork, Ireland
* Correspondence: marcelo.nogueira@tyndall.ie or marcelosaitonogueira@gmail.com

Simple Summary: Colorectal cancer (CRC) is the third most common and second most deadly type of cancer worldwide. The early detection and accurate characterization of colorectal cancer are associated with improved outcomes. With increasing emphasis on early cancer detection and the use of minimally invasive microsurgical techniques, the development of accurate diagnostic technologies to identify tumors and define their boundaries in real time becomes of paramount importance. The current research identifies potential cancer biomarkers and associated light-based instrument specifications to manufacture next-generation medical devices for CRC detection. These specifications have been chosen so that miniaturized instruments can be integrated into colonoscopes. Cancer biomarkers are listed to enable the use of complementary biochemical methods to analyze biological tissues. The impact of using next-generation colonoscopes in reducing cancer deaths can be assessed once medical devices are manufactured.

Abstract: Colorectal cancer (CRC) is the third most common and second most deadly type of cancer worldwide. Early detection not only reduces mortality but also improves patient prognosis by allowing the use of minimally invasive techniques to remove cancer while avoiding major surgery. Expanding the use of microsurgical techniques requires accurate diagnosis and delineation of the tumor margins in order to allow complete excision of cancer. We have used diffuse reflectance spectroscopy (DRS) to identify the main optical CRC biomarkers and to optimize parameters for the integration of such technologies into medical devices. A total number of 2889 diffuse reflectance spectra were collected in *ex vivo* specimens from 47 patients. Short source-detector distance (SDD) and long-SDD fiber-optic probes were employed to measure tissue layers from 0.5 to 1 mm and from 0.5 to 1.9 mm deep, respectively. The most important biomolecules contributing to differentiating DRS between tissue types were oxy- and deoxy-hemoglobin (Hb and HbO_2), followed by water and lipid. Accurate tissue classification and potential DRS device miniaturization using Hb, HbO_2, lipid and water data were achieved particularly well within the wavelength ranges 350–590 nm and 600–1230 nm for the short-SDD probe, and 380–400 nm, 420–610 nm, and 650–950 nm for the long-SDD probe.

Keywords: diffuse reflectance spectroscopy; colorectal cancer; optical spectroscopy; optical diagnostics; colonoscopy; surgical guidance; metabolomics; biomedical optics; biophotonics; multivariate analysis; chemometrics

check for updates

Citation: Saito Nogueira, M.; Maryam, S.; Amissah, M.; McGuire, A.; Spillane, C.; Killeen, S.; Andersson-Engels, S.; O'Riordain, M. Insights into Biochemical Sources and Diffuse Reflectance Spectral Features for Colorectal Cancer Detection and Localization. *Cancers* **2022**, *14*, 5715. https://doi.org/10.3390/cancers14225715

Academic Editor: Fiona Lyng

Received: 9 October 2022
Accepted: 9 November 2022
Published: 21 November 2022

Publisher's Note: MDPI stays neutral with regard to jurisdictional claims in published maps and institutional affiliations.

Copyright: © 2022 by the authors. Licensee MDPI, Basel, Switzerland. This article is an open access article distributed under the terms and conditions of the Creative Commons Attribution (CC BY) license (https://creativecommons.org/licenses/by/4.0/).

1. Introduction

Colorectal cancer (CRC) is the third most common type of cancer worldwide, representing 11.3% (1.85 million) of diagnosed cancer cases and resulting in 10.2% (0.88 million) of cancer-related deaths in 2020 [1,2]. The large mortality caused by CRC can be attributed

to late-stage detection leading to poor patient prognosis. This, along with the significant morbidity and cost associated with standard surgery and associated adjuvant treatment modalities has led to the widespread adoption of screening methods to detect cancer at an early stage [3]. This is paralleled by a proliferation of minimally invasive methods such as Endoscopic Mucosal Resection (EMR), Endoscopic Submucosal Dissection (ESD), Transanal endoscopic microsurgery (TEM) and Transanal Minimally Invasive Surgery (TAMIS) to deal with these early lesions [4]. Currently, standard CRC screening tests such as the detection of blood in the stool have high false positive rates and accurate CRC detection is achieved by colonoscopy followed by relevant biopsies. However, screening and early diagnostic are limited by suboptimal compliance and lack of accessibility. With this in mind, global initiatives to develop early CRC detection methods have focused on CRC biomarkers and monitoring biochemical changes in tissues and biofluids. The high specificity of such biomarker detection methods is associated with their ability to detect low concentrations of specific molecules [5]. In tissue, structural changes are related to molecular concentrations in the millimolar range, whereas metabolic, immunologic and genetic features are associated with micromolar, nanomolar, and picomolar ranges, respectively [5]. Metabolic markers (e.g., enzymes, pO_2, pH, and minerals) and immunologic markers (e.g., growth factors, hormones and cytokines) can be directly expressed in tissue at sufficient levels for real-time and non-invasive detection by optical techniques. Therefore, *in vivo* optical detection of tissue metabolic biomarkers is attractive to identify and localize precisely the tumor area, for example at colonoscopy, with no requirements for sample preparation for analysis of tissue sections, biofluids, and other samples used for cancer screening purposes. However, optical techniques can only be integrated into medical devices (e.g., colonoscopes) if technology allows for miniaturization and cost-effectiveness. One of the main cost-effective and miniaturizable techniques capable of probing tissue endogenous biomolecules is diffuse reflectance spectroscopy (DRS), which includes elastic scattering spectroscopy and near-infrared (NIR) spectroscopy for point measurements and can be translated to imaging by using hyperspectral imaging techniques.

DRS is an optical technique capable of tissue identification based on its biochemical composition and microstructure [6–10]. DRS works by sending light to the interrogated biological tissue and detecting the diffusively reflected light (i.e., the light that emerges from the tissue surface after being scattered inside it). Since the detected light traveled inside the tissue, it contains information about the tissue's optical properties such as scattering and absorption [11–18]. Light scattering is dependent on the refractive index mismatches of tissue including sets of molecules (e.g., collagen fibers and fibrils), organelles (e.g., mitochondria), cell membranes, and inhomogeneity of the intracellular and extracellular environment [10,19–21]. Therefore, scattering is associated with the tissue microstructure. On the other hand, absorption is associated with the tissue biomolecular composition, as its absorption bands are dependent on the molecular energy levels (including electronic [10,22–45], vibrational [46–56] and rotational levels [57]). Tissue absorption is related to biological chromophores (or absorbing biomolecules), which were previously investigated in a number of clinical and preclinical studies [58]. These chromophores include β-carotene, bile, bilirubin, ceroid, collagen, deoxyhemoglobin (Hb), oxyhemoglobin (HbO_2), methemoglobin (MetHb), water, lipid, and melanin [58]. The chromophores probed with DRS are typically present in biomolecule concentrations from micromolar to nanomolar [5]. These concentrations describe metabolic and immunologic features of contrast between normal and cancer tissues [5].

Previous DRS studies have investigated the average concentration of specific tissue biomolecules (i.e., chromophores) based on spectral fitting models of diffuse reflectance, diffuse transmittance and fluorescence [24,26,32,58–67]. These concentrations were analyzed in clinical breast cancer studies about tumor vascularity [68], blood oxygenation [69], quantitative chemical information of oxy- and deoxyhemoglobin (HbO_2 and Hb, respectively), water, and lipids [70–72]. Bile, blood, water and lipid concentrations were also reported for clinical studies on liver cancer [61,73]. In addition, previous NIR spectroscopy studies

on brain, muscle, mammary, lung and prostate cancers of rats and mice reported altered vasculature, oxygen dynamics and HbO_2, Hb, water, lipid, protein and DNA content in tumor tissues [74–82]. In terms of CRC detection, DRS studies reported that hemoglobin concentration and blood oxygenation can be used to differentiate between normal and tumor tissues [83–87]. Indices of statistical differences in biomolecule concentrations have been reported for application in colorectal cancer surgery [88]. In addition, DRS was used together with machine learning methods for direct tissue classification. These studies include those distinguishing tumor tissue from healthy surrounding tissues in the oral cavity (head and neck cancer) [89], breast [90,91], lung [92], and liver [93,94]. Recent studies have investigated the detection of colorectal cancer during surgery [88,95–101]. In terms of primary colorectal cancer, DRS and related optical spectroscopic techniques have mainly been used to guide colonoscopy by distinguishing the normal mucosa and malignant tissue inside the colon (luminal side). However, DRS studies analyzing multiple chromophores in an extended NIR wavelength range into the short wavelength infrared (SWIR) region are rare. To the best of our knowledge, this is the first CRC study optimizing wavelength ranges of reflectance spectra based on the combination between statistical tests and machine learning methods. In addition, the extended wavelength range between 350 and 1920 nm has been probed and our analysis objectively determined the biomolecules most important for tissue classification based on their depth-dependent absorption and scattering. As a final novel point of our study, our objective analysis does not need any homogeneous-medium assumptions such as those required by reflectance spectral fitting models to work.

In this study, we analyzed the spectral regions of best diagnostic potential and the biochemical sources of the classification between normal mucosa and tumor tissues based on the DRS spectral machine-learning features associated with chromophore absorption. The importance of these sources for such classification was determined by (1) assessing the amplitude of partial least-squares components (PLSCs) at relevant wavelength ranges of tissue scattering and absorption, (2) comparing the shape of the PLSC loading curves and chromophore absorption spectra, and (3) evaluating the classification performance (sensitivity, specificity, accuracy and area under the receiver operating characteristic curve) for wavelength ranges of statistically significant difference at a significance level of $p = 0.001$ of *t*-test after ensuring normality by using Anderson-Darling and Lilliefors tests. Our study evaluated the tissue classification in both superficial and deeper layers by using probes with short and long source-to-detector distances (SDD) of 630 µm and 2500 µm, respectively. Biomolecules were probed in a wide wavelength range from 350 nm to 1920 nm, which allowed for the collection of tissue structural and biomolecular signals at different depths. Our DRS spectral dataset contained 2889 spectra of freshly excised *ex vivo* tissues of 47 patients, which was used for robust and reliable analysis of the tissue biochemistry.

2. Materials and Methods

2.1. Diffuse Reflectance Spectroscopy (DRS) Instrumentation

The DRS equipment used in this study, illustrated in Figure 1, consisted of a broadband light source (HL-2000-HP, Ocean Optics, Edinburgh, United Kingdom) with emission ranging from 350 nm to 2400 nm, a quadrifurcated fiber optic probe with source-to-detector distance (SDD) of 630 µm (BF46LS01 1-to-4 Fan-Out Bundle, Thorlabs, Munich, Germany), a trifurcated fiber optic probe with SDD of 2500 µm (Fibertech Optica, Anjou, Canada), a visible/near-infrared (NIR) wavelength spectrometer (QE-Pro, Ocean Optics, Edinburgh, UK) and a NIR/SWIR spectrometer (NIR-Quest, Ocean Optics, Edinburgh, UK). The fiber optic probes were made of low-OH silica in order to allow better transmission at the SWIR range. These probes were used for both illumination and collection of the reflected light to be detected by the spectrometers. The visible/NIR spectrometer collected light in the wavelength range between 350 nm and 1140 nm, while the NIR/SWIR spectrometer detects light from 1090 nm to 1920 nm. The overlapping region was used to merge the spectra into one broadband spectrum from 350 nm to 1920 nm. Once reflected light was detected by the

spectrometers, the intensity readings were preprocessed in order to obtain the tissue DRS spectra according to Section 2.5.

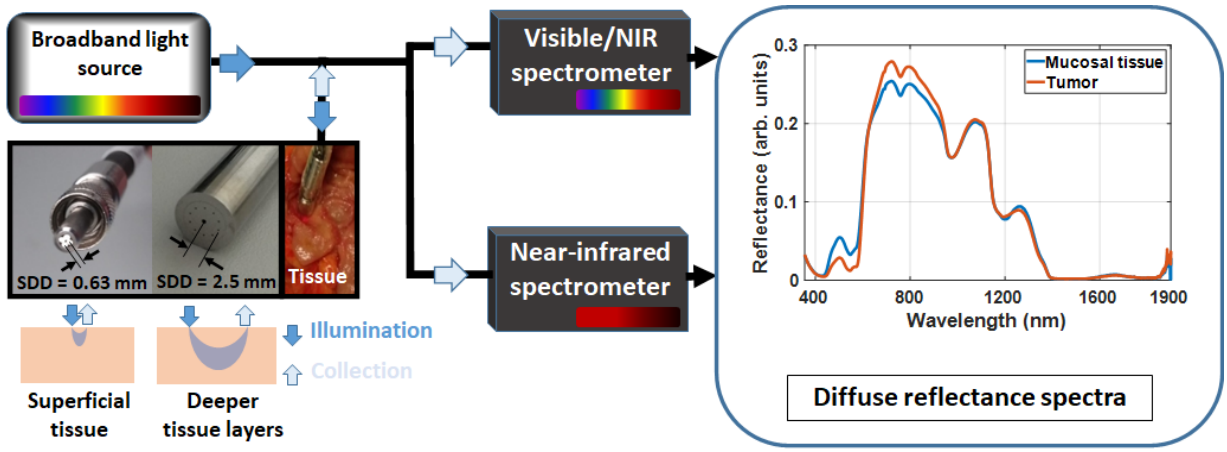


Figure 1. Schematic drawing of our DRS system. The obtained broadband reflectance contains information about a larger variety of tissue biomolecules compared to studies probing shorter wavelength ranges [61,86,87,102–111]. Broadband reflectance spectra were obtained by merging the visible and NIR spectra based on the overlapping spectral region between the two spectrometers (from 1090 nm to 1140 nm). The spectral merging procedure is described in detail in [11,12] and in Section 2.5. Briefly, in the overlapping spectral region, the two spectra are added with a smoothing weighting.

2.2. Probing Superficial or Deeper Tissue Layers

By using the 630 µm SDD probe (630 µm fiber center-to-center distance, Figure 1), our DRS system collected reflectance signals from 0.5 to 1 mm deep into tissue (between 450 and 1590 nm). In this case, the probe contained 600 µm core diameter fibers for both illumination and collection and will be referred to as a short-SDD probe throughout this article. In order to collect light from deeper tissue layers (between 0.5 and 1.9 mm deep between 450 and 1590 nm), we used a 2500 µm SDD probe (long-SDD probe) containing one source fiber in the center and 10 collection fibers surrounding it. Each 5 collection fibers were positioned linearly in the proximal end of the fiber to match the slit of the visible/NIR and NIR/SWIR spectrometers to optimize the light detection configuration. The source and collection fibers of the long-SDD probe had 600 µm and 200 µm core diameters, respectively.

In order to estimate the chromophores and depth interrogated by each probe, we used a spectral fitting algorithm to extract the optical properties from our DRS measurements. The fitting was based on a look-up table of Monte Carlo simulations of the light propagation into tissues and iteratively modifying chromophore concentrations and scattering properties. As a probe depth estimate for each wavelength, we used the depth of the maximum fluence value at the mean position between the source and detector. Then, the minimum and maximum probed depth were reported in this study with the purpose of illustrating the independence of the datasets acquired with each probe and its impact on the evaluation of the biochemical composition of superficial or deeper tissue layers.

2.3. Optical Data Collection

Our data collection started with the background and reference measurements. Reference measurements were taken by positioning each probe on a specialized holder able to keep a fixed distance between the fiber optic probes and our reflectance standard (FWS-99-01c, Avian Technologies LLC, New London, CT, USA). Since the holder was closed to avoid interference from ambient light, it was used to take both reference and background measurements. Probe contamination was avoided by covering our probes with transparent polyvinyl chloride (PVC) film during measurements. After each set of measurements, the

plastic film was removed and the probes were cleaned with ethanol 70%. The same probes were used for every clinical measurement throughout this study. Every measurement was performed by positioning the probe as close to a perpendicular angle to the tissue surface as possible. Measurements of both probes were performed at similar locations within millimeters of each other. Briefly, we positioned the sample on a board with a coordinate system, which allowed us to come back to a similar position for both probes. the experimental procedure is described in detail in [11,12]. After completing the data collection, the data were safely stored for subsequent analysis. In this study, we collected a total of 1363 spectra for the short SDD probe (630 µm SDD) and 1526 for the long SDD probe (2500 µm SDD). Each spectrum is an average of a triplicate measurement in the same tissue location.

2.4. Clinical Protocol and Research Ethics

Our study included 47 patients undergoing bowel resection at the Mercy University Hospital (Cork, Ireland). Patient demographics and tumor characteristics are shown in Table 1. The study was approved by the Clinical Research Ethics Committee of the University College Cork. Our procedure consisted of collecting around 15 measurements of *ex vivo* mucosal tissues and 15 tumor tissues on the specimen after surgical resection. Measurements were taken from a typical area of 100 cm^2. After a specimen was resected, the colonic lumen was exposed. The specimen was rinsed with water and cleaned afterward in order to remove the excess blood and any remaining feces from the mucosal surface. Then, the mucosa and tumor regions were identified by experienced surgeons. The time between the specimen removal and the start of the data collection was on average 40 min. All data collection was performed within an average time of 1 h after surgical resection. Physiological conditions were kept as much as possible throughout the data collection by keeping the tissue moist with a wet wipe. In order to correlate spectral readings with the tissues measured, the coordinate of every reading was registered by using a picture of the specimen over a grid. The boundary of each tissue type was determined by experienced surgeons. After the acquisition of all-optical DRS data, the specimen was returned to the Pathology Department for processing and analysis according to standard protocols. The ground truth of cancer tissue types was obtained by histopathology analysis.

Table 1. Patient demographics, cancer types and tumor staging classification.

Patient and Cancer Characteristics		Number of Patients/Tumors
Total		47
Gender	Male	32
	Female	15
Age (years)	Median	69
	Minimum	40
	Maximum	89
	Interquartile range	13.5
Cancer types	Adenocarcinoma	47
T (tumor) stage	pT1	5
	pT2	7
	pT3	26
	pT4	9
N (lymph node) stage	N0	19
	N1a	9
	N1b	12
	N1c	1
	N2	1
	N2a	4
	N2b	1

2.5. Data Preprocessing and Feature Selection

First, both visible and NIR tissue intensity spectra had their background subtracted and the resulting signal was divided by the reflected intensity of the reference (reflectance standard) according to the expression:

$$Reflectance(\lambda) = \frac{1}{Reference\ reflectivity} \times \frac{Tissue\ reflected\ intensity - Background\ intensity}{Reference\ reflected\ intensity - Background\ intensity} \quad (1)$$

Next, the broadband reflectance spectra were obtained by merging the visible and NIR spectra based on the overlapping spectral region between the two spectrometers (from 1090 nm to 1140 nm). The merging was performed by interpolating the overlapping region of the two spectrometers and performing the following weighted sum:

$$Reflectance(\lambda) = \sum_{i=0}^{100} \frac{((100 - i) \times reflectance\ of\ VIS\ spectrometer + i \times reflectance\ of\ NIR\ spectrometer)}{100} \quad (2)$$

The result is a smooth reflectance curve where the reflectance measured by each spectrometer has a higher contribution at their respective wavelength regions of higher sensitivity. As preparation for classification tests based on k-nearest neighbors (which may be prone to overfitting when using numerous variables in comparison to the sample size), feature extraction was performed by using partial-least squares (PLS).

PLS is a supervised method of orthogonal transformation used for linear dimension reduction in a given dataset. PLS is used to create a new set of linearly independent variables (partial least squares components or PLSCs) which maximize the covariance between the predictors (reflectance values for each wavelength) and responses (tissue types) [112]. As PLSCs are weighted sums of the original variables (or predictors), the combination of weights of the first PLSCs shows the wavelength regions which are responsible for most of the discrimination between two classes (tissue types). More details about the calculation of PLSCs and the importance of predictors for better tissue discrimination can be accessed from the publications of Brereton et al. [113] and Gromski et al. [114], respectively. We also emphasize that our PLSCs are the same as the principal components (PCs) of PLS.

In this study, the bias due to the incomparable scales of observations (reflectance values) at specific variables (reflectance at particular wavelengths) was avoided by scaling/normalizing observations between −1 and +1 for each wavelength. By compensating for the difference in scale on reflectance values, this scaling ensures the feature extraction equally takes into account the contributions of each wavelength on the new set of variables based on the PLS maximization of the discrimination between the two tissue types. This contribution is translated into the weights (loadings) of each wavelength on the variables selected to develop a tissue classification model. Finally, data preprocessing and analysis were performed using home-made MATLAB routines (MathWorks Inc., Natick, MA, USA).

2.6. Extraction of Spectral Features

The spectral features for differentiation between normal mucosa and cancer tissues were extracted by using the first four PLSCs, which were selected to avoid overfitting by stopping to include new PLSCs when accuracy increments were lower than approximately 2%. These features were interpreted based on the amplitude and spectral shape of PLSC loadings. The amplitude was used to determine the contribution of specific wavelength ranges to tissue classification, which were associated with the main absorbing ranges of typical tissue biomolecules (or chromophores). The spectral shape was associated with characteristics of the chromophore absorption spectra. More details of the interpretation of the spectral features are described in Section 4.2.

In order to provide information about which wavelength ranges were related to most of the tissue biomarkers associated with cancer detection, delineation and potential carcinogenesis, we evaluated the tissue classification performance parameters (sensitivity,

specificity, accuracy and area under the receiver operating characteristic curve; AUC) achieved by using wavelength ranges selected via statistically significant difference verified by a student *t*-test. First, normal distributions of DRS readings at each wavelength and tissue type were verified through Anderson-Darling and Lilliefors normality tests. Next, a student *t*-test was applied to the same distributions. Wavelength ranges leading to $p < 0.001$ were selected for building our tissue classification model. This model was built by applying PLS to the data on the relevant wavelength ranges and selecting the four highest-order PLSCs to be used with a weighted KNN classification algorithm. The weighted KNN algorithm used 10 neighbors and squared inverse distance between observations.

Based on the results of the KNN classification, its performance was evaluated by using two-fold cross-validation for 20 iterations. Each iteration consists of randomly dividing the dataset into training and test sets of equal size. The classification model was generated by using the training set and, then, applied for tissue classification on the test set. The process is repeated with the first test set used as the training set and vice versa. At the end of this process, the output was the mean of each classification performance parameter. The process is repeated 20 times. Then, the mean and standard deviation of the output of the 20 iterations were calculated. The reproducibility of these parameters was evaluated by the obtained standard deviations.

A flowchart summarizing the spectral analysis is shown in Figure 2.

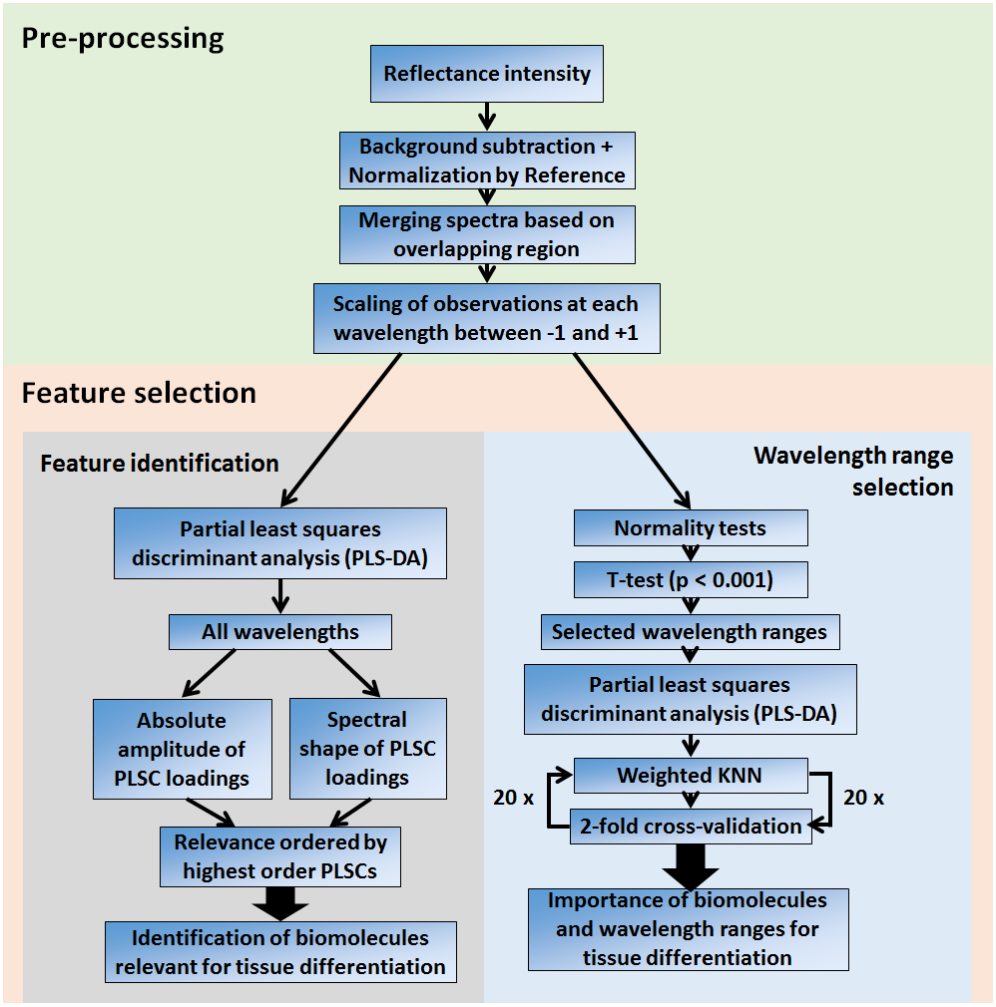


Figure 2. Flowchart of the steps of our spectral analysis.

3. Results

3.1. Tissue Classification Features Based on PLSC Amplitudes

Our first analysis for the selection of the features relevant to tissue classification was based on the PLSC loadings. The interpretation of the PLSC loadings is described in Section 4.2. Figure 3 illustrates that the PLSC1 loadings of the short-SDD probe exhibit the highest and second-highest absolute amplitudes in the range from 600 nm to 1350 nm and from 350 nm to 600 nm, respectively. A similar behavior is observed on the amplitudes of the PLSC1 of the long-SDD probe, whose first, second and third highest absolute amplitudes occur between 450 nm and 600 nm, between 650 nm and 1350 nm, and between 1350 nm and 1900 nm, respectively. These amplitudes suggest that most of the differentiation between mucosal and cancerous tissues may originate from the absorption and scattering processes below 1350 nm. Processes at the visible wavelength range 350–600 nm are predominantly related to blood absorption, and information regarding the near-infrared range 700–1350 nm could be associated with relatively lower absorption of oxyhemoglobin (HbO_2) and deoxyhemoglobin (Hb), lipid and water at slightly deeper tissue layers.

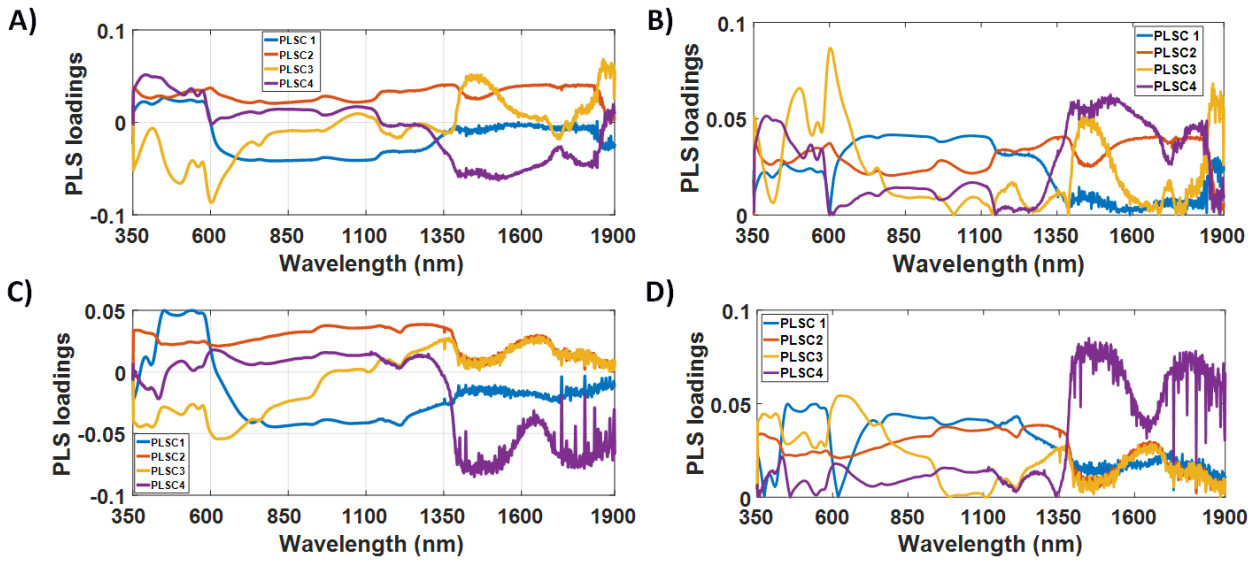


Figure 3. PLS components (PLSCs) for the classification between cancerous and mucosal/submucosal tissues. (**A**) Raw and (**B**) absolute values of PLSC loadings for the short-SDD probe and (**C**) Raw and (**D**) absolute values of PLSC loadings for the long-SDD probe.

On the PLSC2, PLSC3 and PLSC4 of the short-SDD probe, overall higher absolute amplitudes can be found for wavelengths below 700 nm and above 1350 nm, whereas the same components for the long-SDD probe have amplitude loadings more uniformly distributed over the full spectral window between 350 nm and 1900 nm. Particularly for PLSC4 of the long-SDD probe, the amplitude is higher for wavelengths above 1350 nm. While the high amplitudes below 700 nm for the short-SDD probe reinforce potentially relevant features of tumor detection at the UV-visible region (dominated by blood absorption), tissue classification using other wavelengths is unclear from only absolute PLS-loading amplitudes. With this in mind, we analyzed the shape of the PLSCs based on the wavelength regions and spectral shape of the chromophore absorption spectra, as shown in Section 3.3. On the other hand, this analysis is subjective and does not allow us to define specific wavelength ranges, as these would depend on subjective thresholds of the amplitude of PLSC loadings and the choice of how many PLSCs to be considered for thresholding. In addition, although PLSC1 is more important for tissue classification, the weight of each PLSC on the importance of wavelength ranges is unclear.

3.2. Wavelength Selection and Tissue Classification

Since analyzing the PLSC loadings may lead to subjective observations, we performed a more objective analysis by selecting wavelengths through statistically significant differences in the *t*-test ($p < 0.001$). In order to ensure that *t*-test could be applied to our dataset, Anderson-Darling and Lilliefors normality tests were applied to the data of each individual wavelength. Normal distributions were identified for all the wavelengths of both probes, except for those between 536 nm and 545 nm for the short-SDD probe. However, we confirmed statistically significant difference ($p < 0.001$) is obtained at those wavelengths upon application of the Wilcoxon rank-sum test (data not shown) and obtained no difference in tissue classification by including or excluding this wavelength range (Table 2).

Table 2. Tissue classification performance * of PLS-KNN for the short-SDD probe using wavelengths selected by *t*-test ($p < 0.001$). Blue fields represent the performance using visible/NIR light detection available in Si-detector-based spectrometers, orange fields cover the performance using NIR wavelengths detected by InGaAs-based spectrometers and green fields show the performance of both types of wavelength range combined. Means and standard deviations were taken from the outcomes of 20 iterations of 2-fold cross-validation.

Wavelengths	Sensitivity	Specificity	Accuracy	AUC
350–540 nm, 540–590 nm	(78.2 ± 0.9)%	(75.8 ± 1.6)%	(77.1 ± 1.0)%	(0.854 ± 0.007)
350–590 nm	(78.4 ± 1.1)%	(74.9 ± 1.4)%	(76.7 ± 0.8)%	(0.85 ± 0.005)
600–1230 nm	(79.8 ± 0.9)%	(84.4 ± 1.4)%	(81.9 ± 0.8)%	(0.894 ± 0.005)
350–590 nm, 600–1230 nm	(78.6 ± 0.7)%	(75.4 ± 1.0)%	(77.1 ± 0.7)%	(0.854 ± 0.006)
1530–1700 nm	(70.9 ± 1.1)%	(67.0 ± 1.6)%	(69.1 ± 1.0)%	(0.771 ± 0.009)
1730–1850 nm	(69.1 ± 1.0)%	(69.5 ± 1.3)%	(69.3 ± 0.9)%	(0.765 ± 0.007)
1530–1700 nm, 1730–1850 nm	(76.4 ± 0.9)%	(77.7 ± 1.1)%	(77.0 ± 0.7)%	(0.845 ± 0.006)
350–590 nm, 600–1230 nm, 1530–1700 nm, 1730–1850 nm	(85.5 ± 0.8)%	(84.0 ± 1.0)%	(84.8 ± 0.7)%	(0.919 ± 0.004)
350–1920 nm	(85.6 ± 0.9)%	(80.4 ± 1.1)%	(83.2 ± 0.8)%	(0.905 ± 0.005)

* Results corresponding to 2-fold cross-validation from 20 iterations of random sampling of training and test sets. Our validation provides a sufficiently robust estimation of classification performance metrics since the standard deviation of measurements within each individual patient is less than twice the standard deviation of all measurements of all patients. In addition, no clear trend among specific patients has been identified in our dataset of 47 patients. A typical measurement means and standard deviation for one patient can be found in Figure S1 of the Supplementary Material.

After confirmation of normality for most of the wavelengths, we applied a *t*-test for each wavelength. We used the wavelength ranges where a statistically significant difference ($p < 0.001$) was obtained (Figure 4) to select bands relevant for tissue classification.

By using the wavelength ranges of Figure 4 as well as combinations of those ranges for UV-visible or NIR, tissue PLS-KNN classification models were built and compared with the model using all the wavelengths. The classification performance of each model can be found in Tables 2 and 3.

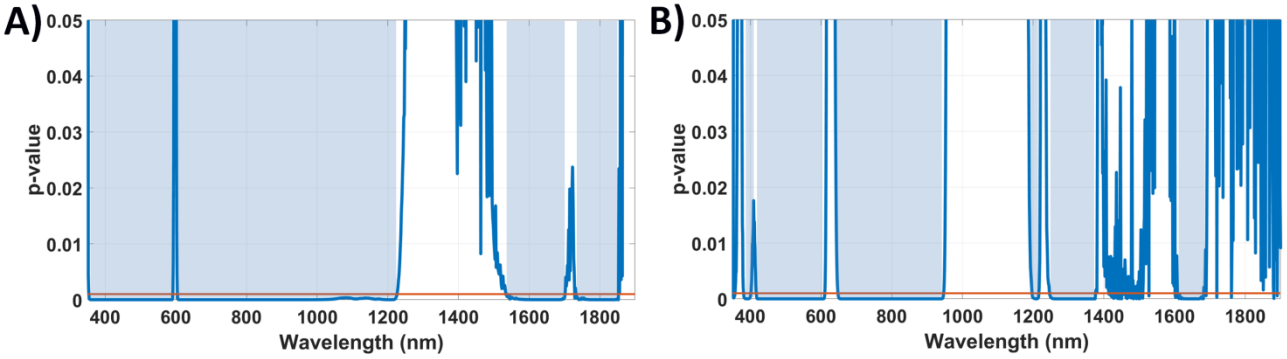


Figure 4. Selected spectral regions (blue) where statistically significant differences ($p < 0.001$) are found for (**A**) short-SDD probe and (**B**) long-SDD probe. The red line indicates the 0.001 cutoff for the p-value.

Table 3. Tissue classification performance * of PLS-KNN for the long-SDD probe using wavelengths selected by t-test ($p < 0.001$). Blue fields represent the performance using visible/NIR light detection available in Si-detector-based spectrometers, orange fields cover the performance using NIR wavelengths detected by InGaAs-based spectrometers and green fields show the performance of both types of wavelength range combined. Means and standard deviations were taken from the outcomes of 20 iterations of 2-fold cross-validation.

Wavelengths	Sensitivity	Specificity	Accuracy	AUC
380–400 nm	(86.0 ± 0.9)%	(85.0 ± 0.9)%	(85.6 ± 0.7)%	(0.925 ± 0.004)
420–610 nm	(85.6 ± 0.5)%	(87.2 ± 0.6)%	(86.3 ± 0.3)%	(0.93 ± 0.004)
650–950 nm	(89.6 ± 0.6)%	(89.7 ± 1.0)%	(89.7 ± 0.6)%	(0.96 ± 0.004)
380–400 nm, 420–610 nm, 650–950 nm	(87.0 ± 0.8)%	(85.5 ± 0.8)%	(86.3 ± 0.7)%	(0.931 ± 0.003)
1200–1220 nm	(67.8 ± 1.2)%	(63.3 ± 1.9)%	(65.7 ± 1.1)%	(0.707 ± 0.013)
1250–1380 nm	(77.1 ± 1.0)%	(80.7 ± 1.0)%	(78.8 ± 0.7)%	(0.87 ± 0.006)
1600–1690 nm	(62.4 ± 1.1)%	(58.3 ± 1.6)%	(60.4 ± 0.8)%	(0.654 ± 0.008)
1200–1220 nm, 1250–1380 nm, 1600–1690 nm	(77.6 ± 1.0)%	(84.7 ± 1.1)%	(81.0 ± 0.8)%	(0.883 ± 0.006)
380–400 nm, 420–610 nm, 650–950 nm, 1200–1220 nm, 1250–1380 nm, 1600–1690 nm	(89.1 ± 0.7)%	(90.2 ± 0.7)%	(89.6 ± 0.5)%	(0.957 ± 0.004)
350–1920 nm	(89.3 ± 0.6)%	(90.2 ± 0.7)%	(89.7 ± 0.5)%	(0.959 ± 0.003)

* Results corresponding to 2-fold cross-validation from 20 iterations of random sampling of training and test sets. Our validation provides a sufficiently robust estimation of classification performance metrics since the standard deviation of measurements within each individual patient is less than twice the standard deviation of all measurements of all patients. In addition, no clear trend among specific patients has been identified in our dataset of 47 patients. A typical measurement means and standard deviation for one patient can be found in Figure S1 of the Supplementary Material.

Table 2 indicates that the spectral regions 600–1230 nm and 350–590 nm are the first and second most important for tumor detection by using the short-SDD probe, as accuracy is higher for these wavelengths. When tissue classification is performed only with wavelengths of the first spectral region, the achieved sensitivity (79.8 ± 0.9)% and specificity (84.4 ± 1.4)% are comparable to that obtained by using all the selected wavelength regions combined. This result suggests that the difference between mucosa and tumors is generated from the combination of absorption of Hb, HbO_2, lipid and water as well as an optical

scattering of tissue layers slightly below the tissue surface. In particular, Hb and HbO_2 may play a significant role in classification across the superficial tissue layers, as the spectral regions leading to the highest discrimination cover all their absorption wavelengths.

In terms of the combination of wavelength ranges, the specificity achieved by combining the 350–590 nm and 600–1230 nm wavelength ranges was lower than using 600–1230 nm alone. This lower classification performance may be associated with higher absorption and scattering properties between 350 and 590 nm, which may lead to higher separation between the centers of the mucosa and tumor distributions recognized by PLS, while less contrast between the two distributions was achieved due to higher variation in reflectance values. On the other hand, higher classification performance over all parameters was obtained by combining the ranges 1530–1700 nm and 1730–1850 nm. Then, the information provided by Hb and HbO_2 in both wavelength ranges may be redundant, whereas signals associated with water and lipid absorption may be complementary. The information from all the selected wavelength ranges is also complementary, as their combination leads to higher classification performance compared to all ranges tested in this study, including a 3.6% higher specificity than that obtained by using all wavelengths (350–1920 nm).

Table 3 shows that wavelength ranges below 950 nm led to higher sensitivity than those above 1200 nm for the long-SDD probe. This indicates that Hb and HbO_2 are the chromophores that most contribute to accurate tumor detection in deeper tissue layers. Similarly to the short-SDD probe, the highest classification performance was achieved by using wavelengths on the optical window (in this case, 650–950 nm). Additionally, since the performance obtained for the long-SDD probe is higher than that obtained by using the short-SDD probe, signals of deep tissue layers may contain more relevant information for tissue discrimination, and probes could be designed in future studies to obtain information from relevant tissue depths. The importance of deeper tissue layer information is further reinforced by the higher classification performance achieved by using the ultraviolet (380–400 nm) and visible (420–610 nm) wavelengths alone compared to the best performance obtained by using the short-SDD probe.

Although the higher performance achieved by using the range 650–950 nm compared to shorter wavelengths may be attributed to the contribution of water and lipid absorption in the optical window, NIR wavelength ranges led to relatively low classification performance. In this case, the most informative NIR range was 1250–1380 nm, where features of higher variations in lipid and water absorption can be simultaneously observed (Figure 5).

Similar behavior was observed between the classification performance achieved by using the long-SDD probe and the short-SDD probe. By combining wavelength ranges containing ultraviolet and visible wavelengths, lower classification performance was obtained compared to the 650–950 nm range alone. In addition, the combination of NIR wavelength ranges improved tissue classification. Those results suggest that information from water and lipid absorption at deeper tissue layers probed by using long SDDs may be complementary and useful for cancer detection, while signals from Hb and HbO_2 absorption may not bring useful information for tissue classification. Finally, the combination of selected wavelength ranges led to the achievement of as good performance as using the entire wavelength range (350–1920 nm) investigated in this study.

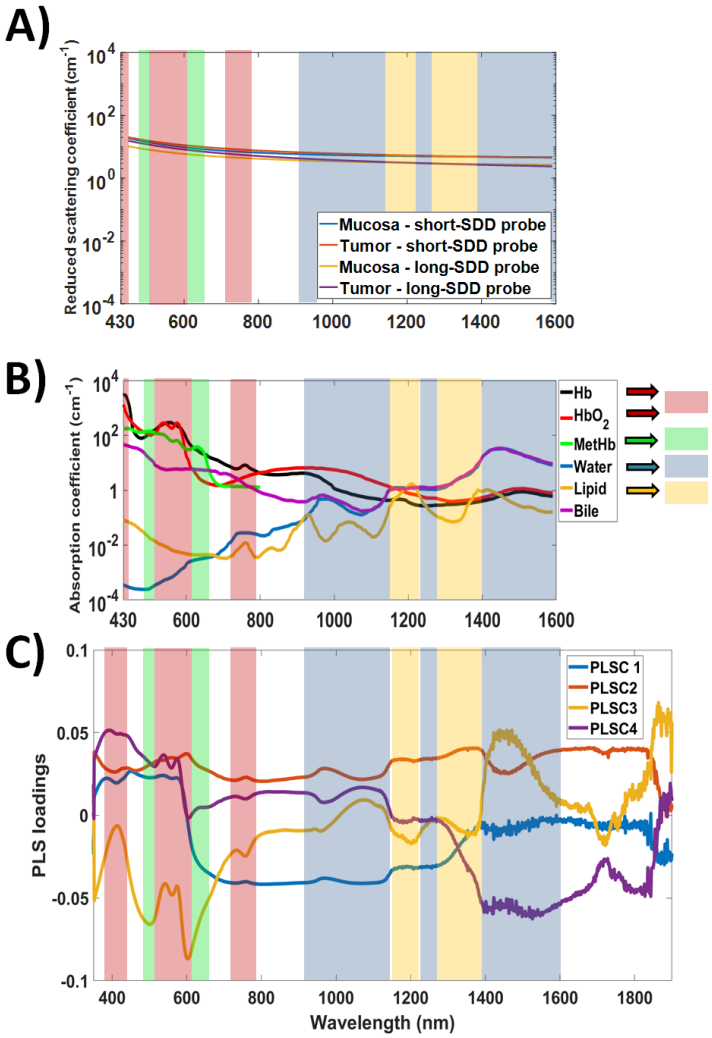


Figure 5. Wavelength regions with spectral features of mucosa and tumor scattering coefficients and each tissue chromophore shown at the (**A**) Reduced scattering spectra of mucosa and tumor tissues of both short-SDD and long-SDD probes, (**B**) chromophore absorption spectra and (**C**) PLSCs of the short-SDD probe.

3.3. Relationship between Tissue Classification Features and Tissue Biochemistry/Microstructure

Once the importance of wavelength bands and their combinations were assessed, we used the shape of the PLSC loadings to understand the biochemical and microstructural sources of tissue classification. This section covers the results of our analysis, whereas the interpretation of spectral features of tissue classification is discussed in Section 4.2. Our analysis comprised of the determination of contributions of tissue scattering and chromophore absorption based on the shape of the PLSC loadings at wavelength bands of highest absorption of tissue chromophores as well as the "flatness" of PLSC loadings (indicative of the predominant contribution of tissue scattering). The selection of wavelength bands for subsequent interpretation is illustrated in Figure 5.

Figure 5 shows the spectral ranges where particular features of specific chromophore absorption can be observed. As an example, the red region shows the features of oxyhemoglobin (HbO_2) and deoxyhemoglobin (Hb), including bands between 380 nm and 450 nm (peaks of HbO_2 at 414 nm, 542 nm and 576 nm [21], and peaks of Hb at 433 nm, 556 nm and 757 nm). In the case of the latter peak of Hb (at 757 nm), we assume the feature is from Hb instead of lipid (peak at 761 nm) due to the higher Hb absorption and potentially higher Hb concentration in biological tissues (resulting in overall higher tissue absorption due to Hb). In addition, the used bile spectrum (from Nachabe et al. [61]) includes the

water contained in the sample, as is obvious from the spectral range above 950 nm When the shape of the PLSC loadings is relatively flat and monotonic as a function of wavelength, we attributed scattering as the most important factor contributing to tissue classification using such PLSC. It is important to remember that, even though the chromophore spectra are not shown for wavelengths longer than 1600 nm in Figure 5, double absorption peaks between 1700 nm and 1800 nm are associated with lipid, whereas the increase in absorption close to 1900 nm is related to water [115,116]. By analyzing the spectral shape of the PLSCs, we obtained Table 4 below.

Table 4. Scattering and absorption features of the superficial tissue PLSCs.

		Scattering and Absorption Features						
		VIS Scat	**NIR Scat**	**Hb**	**HbO_2**	**MetHb**	**Water**	**Lipid**
PLS (Short-SDD probe)	**PLSC1**			X	X		X	
	PLSC2	X	X	X	X		X	
	PLSC3			X	X		X	X
	PLSC4			X	X		X	X
PLS (Long-SDD probe)	**PLSC1**			X	X		X	X
	PLSC2	X	X	X	X		X	X
	PLSC3			X	X		X	X
	PLSC4			X	X		X	X

Based on the loadings of PLCS1, Table 4 suggests that the features contributing to tissue classification between mucosa and tumor are mostly related to Hb, HbO_2 and water for the short-SDD probe and the Hb, HbO_2, water and lipid for the long-SDD probe. For both probes, absorption features from the same chromophores of PLSC1 appear in PLSC2, which also contain features of scattering in visible and near-infrared wavelength ranges. In addition, absorption features of Hb, HbO_2, water and lipid can be observed on the loadings of PLSC3 and PLSC4 of both probes. On the other hand, features of lipid absorption appear only at the loadings of PLSC3 and PLSC4 of the short-SDD probe, whereas characteristics of the same chromophore are exhibited in the loadings of PLSC1, PLSC2, PLSC3, and PLSC4 of the long-SDD probe.

4. Discussion

4.1. Impact of Depth-Resolved Determination of Wavelength Ranges and Biomarkers for Tissue Classification

Our study investigated the most important wavelength regions for discriminating colorectal mucosa and cancer tissues and how these regions can be related to the biomarkers contributing to this discrimination (discussed in Section 4.2). Furthermore, we provide information for two tissue probed depths, as these depths are dependent on the source-to-detector distance of our fiber optic probes (Section 4.2). Our optimization of wavelength ranges of reflectance spectra and evaluation of main biomarkers contributing to the classification of normal mucosa and tumor tissues is an extension of our previous work [11] showing the successful classification of these tissues by using support vector machines, as well as our study [12] estimating biomolecule concentrations by using a spectral fitting algorithm based on Monte Carlo simulations of light propagation in tissues (assuming homogeneous tissue models).

To the best of our knowledge, previous DRS studies did not perform an objective analysis of the importance of wavelength ranges for discrimination between mucosa and cancer tissues. These studies have been reviewed in our previous publication [11] and have only investigated specific wavelength ranges from 300 to 800 nm or from 900 to 2500 nm. No comparison between wavelength ranges objectively selected by statistical

methods has been performed by using DRS for CRC detection. With that in mind, our study provides the objective analysis of the importance of ultraviolet, visible and near-infrared wavelength ranges for classification between colorectal mucosa and tumor tissues, which is especially useful (1) to design new optical spectroscopy and imaging systems restricted to specific wavelength ranges (for cost-effectiveness, performance maintenance upon miniaturization and integration into medical devices, higher accuracy at specific wavelengths, and higher spatial resolution), (2) to determine the range of probed tissue depths where improved tissue classification can be achieved and where optical tissue biomarkers tend to significantly influence tissue classification, (3) to identify which tissue biomarkers are the most important for discrimination between mucosa and cancer tissues based on DRS signals.

Our study improves the subjectivity of analysis of amplitude and shape of PLSC loadings (Figure 3) by adding an objective analysis based on the selection wavelength ranges for tissue classification based on $p < 0.001$ (statistically significant difference) for the *t*-test and comparison of PLS-KNN classification performance metrics by using each combination of selected wavelength ranges. Higher classification performance at wavelength ranges of specific tissue chromophores (biomolecules) indicates the most important wavelength ranges and respective biomarkers to classify normal mucosa and cancer (Section 3.2). This classification performance adds to biomarker identification based on features of tissue scattering and chromophore absorption based on the amplitude (Section 3.1) and shape (Section 3.3) of PLSC loadings since statistical wavelength selection and subsequent classification cannot identify scattering contributions spread out all wavelengths. The scattering contribution to tissue classification is only observed by analysis of PLSC loading shapes as a function of wavelength.

In this study, the analysis of PLSC loadings suggests that tissue scattering is secondary but still important for tissue classification since only PLSC2 loadings resemble scattering coefficient curves as a function of wavelength (Section 3.3). However, it is worth noting that different combinations of optical properties (scattering and absorption coefficients) lead to probing a different depth in tissue. Probing different depths means that each wavelength of each DRS spectrum extracts biomarkers (chromophore concentrations and scattering properties) at a different tissue depth. Additionally, the higher source-detector distance increases the chances of collecting light which traveled longer and deeper into tissue. Therefore, short-SDD and long-SDD probes capture information on biomarkers at different depths, as these depths depend on both probe geometry and tissue optical properties. Based on Monte Carlo simulations of light propagation in tissues performed in our previous study [11], the probed depth of the short-SDD probe was mostly within 0.5–1 mm for wavelengths between 450 and 1590 nm, whereas that of the long-SDD probe varied between 0.5 and 1.9 mm for the same wavelength range. Statistical methods presented in this paper enable objective depth-resolved biomarker identification and selection of wavelength ranges. This depth-resolved analysis is not achievable by spectral fitting models assuming that tissue is homogeneous because tissue heterogeneity is neglected to keep the number of fitted parameters to a minimum. At the cost of a tissue homogeneity assumption, such spectral fitting models can retrieve average tissue scattering properties and chromophore concentrations. Although average concentrations are easy to interpret, they contain neither information about tissue depths nor wavelength ranges to best differentiate normal and cancerous tissues.

Previous studies have calculated sensitivity and specificity for tumor detection based on biomolecular concentrations obtained from assumptions of homogeneous media, especially using spectral fitting models of diffuse reflectance, transmittance and fluorescence [24,26,32,58–67]. In imaging and tomography applications, these concentrations are typically extracted from the absorption at a few wavelengths and used as diagnostic indexes in different applications [117], whereas point spectroscopy evaluates a larger number and often a wider range of wavelengths. However, the potential of point spectroscopy is not fully exploited if homogeneous media assumptions are made, as useful information can

potentially be extracted from such a larger number of wavelengths and depths probed. Our previous work [12] has shown that biomolecular concentrations are different depending on the probed depth by varying the probe SDD and by using a spectral fitting model for homogeneous tissue. In this study, the importance of measurements at each wavelength is considered separately. The probed depth of reflectance at each wavelength is different and incorporated into our analysis using statistical tests and machine learning methods. Analyzing DRS measurements of each wavelength separately means that information is extracted from tissue biochemistry and microstructure at multiple depths. Therefore, the importance of chromophores obtained in this study is based on more complete information compared with previous studies and exploits the full potential of DRS point spectroscopy measurements. By using our depth-resolved analysis, tissue biomarker information was interpreted by using PLSC loadings while the objective selection of optimized tissue classification parameters was determined by evaluating classification performance directly.

4.2. Spectral Features for Colorectal Cancer (CRC) Detection

The present study investigated the spectral regions and biomolecules associated with cancer development by identifying the most important spectral features for the differentiation between normal and cancerous tissues. This identification was performed by using partial least-squares (PLS). One of the advantages of using PLS methods is that they can provide insight into the variables most likely to be responsible for the differentiation between two groups via the interpretation of weights and loadings. With this in mind, PLS is typically used in exploratory studies focusing on which variables are best discriminators [113]. In molecular biology applications (e.g., metabolomics, proteomics, lipidomics, glycomics and others), these variables can be related to biomolecules via features of their generated physical processes present in the measured signal (e.g., the fluorescence emission of specific molecules in a tissue fluorescence measurement) [114]. In terms of optical techniques, this approach was used by Wang et. al., who found that NADH, collagen, and porphyrin were related to oral cancer detection by using fluorescence spectroscopy [118]. In this study, biomolecular contribution to the DRS signal is related to absorption features of tissue chromophores such as oxyhemoglobin (HbO_2) and deoxyhemoglobin (Hb), lipid and water, as well as scattering tissue features related to size and refractive index of the main scatterers. As a result, absorption and scattering features related to discrimination can be observed on the PLS loadings, since these loadings are based on the differentiation between mucosa and tumor tissues present on the DRS signal.

PLSC loadings can be interpreted based on their amplitude and spectral shape. Higher absolute amplitudes of PLSC loadings on spectral regions of absorption of specific molecules mean these molecules are associated with the PLSC(s). The same association is reinforced if the spectral shape of the PLSC loadings is similar to that of the biomolecular absorption spectra within the pertinent spectral regions. The first PLSCs are more relevant for tissue discrimination. Therefore, analyzing the absolute amplitudes and spectral shape of loadings of the first PLSCs allows us to determine which biomolecules are potentially more relevant for differentiating mucosal and cancerous tissues.

By analyzing parameters such as loadings of principal component analysis (PCA) or PLS, it is possible to determine which biomolecules are involved with the classification between groups of tissues. The loadings of PLS components are typically analyzed in metabolomics [114], where the focus is determining which variables (related to chemicals) are best discriminators for certain tissue groups (e.g., cancerous and healthy tissue) rather than understanding whether tissue classification is possible [113]. A similar rationale is used to analyze spectral features associated with other physical phenomena related to biomolecules. For optical techniques such as fluorescence spectroscopy, biomolecules include NADH, FAD, collagen, elastin, porphyrins and lipopigments [24,26,27,32,60,67,119–121], whereas Fourier-transform infrared (FTIR) spectroscopy and Raman spectroscopy probe chemicals such as amino acids, proteins, lipids, carbohydrates, nucleic acids, porphyrins, and water [47,49,122,123]. A more extensive list of altered biochemical composition

in CRC was reported by previous studies on lipidomics, proteomics, metabolomics, genomics, glycomics and other molecular biology sciences [124–133]. Out of all biomolecules in the extensive list of CRC tissue discriminators, our DRS study focuses on biomolecules with detectable absorption (chromophores) in the wavelength range between 350 and 1920 nm. These biomolecules include β-carotene, bile, bilirubin, ceroid, collagen, deoxyhemoglobin (Hb), oxyhemoglobin (HbO_2), methemoglobin (MetHb), water, lipid, and melanin.

Previous studies using PLS to investigate biomolecular features in optical measurements are scarce. By using fluorescence spectroscopy, Wang et al. [118] used PLS loadings to determine that the biomolecules involved with oral cancer detection were collagen, NADH and porphyrins. This determination was based on the peaks of the loadings as a function of wavelength, which occurred at 390 nm and 470 nm for the 320 nm excitation, and at 460 nm and 640 nm for the 360 nm excitation. Apart from the study of Wang et. al., our study used the amplitudes and shapes of PLSC loadings to identify CRC biomarkers and corresponding wavelength ranges based on the loadings of the four first PLSCs. These loadings suggest that only Hb, HbO_2, lipid, water and light scattering in tissue contribute to PLS features to be used for tissue classification (Section 3.3). In a qualitative analysis based on the amplitude of PLSC1 loadings, Hb and HbO_2 were the most important biomolecules for tissue classification since the highest and second highest absolute amplitudes (Figure 3) occurred between 350 and 1350 nm for both probes used (Section 3.1). Light scattering, lipid and water were of secondary importance, since only PLSC2 appears to contribute to scattering, and the wavelength range between 1350 and 1900 nm has the third highest absolute amplitude only for PLSC1 of the long-SDD probe (Section 3.1). It is important to note that all PLSCs used for tissue classification exhibit spectral features of water, and all PLSCs except PLSC1 and PLSC2 of the short-SDD probe have lipid features. The absence of PLSC1 and PLSC2 features for lipids suggests that no superficial lipid signal up to 1 mm deep contributes to CRC detection, as the maximum probed depth for the short-SDD probe is ~1 mm. Additionally, scattering may have contributed to PLSCs other than PLSC2 even though its contribution may not show any strong trend on the PLSC loadings (Figure 3). Finally, one reason the scattering properties may not be more relevant for tissue classification is due to the relatively short source-detector distance providing a low sensitivity to alterations in scattering properties between tissue types. This means there might be a scattering-related contrast between tissues that our instrument is not sensitive to because of our future endeavors of translating our findings to an endoscopic *in vivo* study requiring that the short-SDD probe and all supporting equipment fit within the endoscope. Non-endoscopic applications targeting the classification of normal mucosa and cancer tissues relying on longer SDD and/or quantities associated with tissue scattering may still be useful to find scattering differences between these tissues.

4.3. Considerations on Biomolecular Concentrations and Probed Depth for CRC Detection

Based on the current literature evidence that Hb, HbO_2, lipid and water concentrations differ in normal tissues and tumors, our results agree that these biomolecules can be used for tumor detection. In our study, the features of each biomolecule were illustrated in the shape of the PLSC loadings, while the molecular relevance for differentiation between colorectal mucosa and tumor could be determined with the amplitude of the loadings and higher classification performance of selected wavelength ranges. In general, there is an agreement between the wavelength ranges leading to higher classification performance and higher absolute amplitudes of the PLSC1 loadings. Since taking these ranges solely based on the loadings is subjective, we used a more objective analysis by selecting ranges of $p < 0.001$ in the *t*-test. This analysis suggested that Hb and HbO_2 information relevant to tumor detection can be collected from specific wavelength ranges within the UV-visible region and the optical window. A combination of these ranges may not lead to more accurate tissue classification. On the other hand, classification can be improved by probing water and lipid at several near-infrared (NIR) ranges which provide complementary information for

tissue discrimination. Our results regarding the importance of Hb, HbO_2, lipid, water and scattering for CRC detection agree with results based on our objective statistical analysis and add to the results of our previous work [11], which suggested that wavelengths in the optical window contribute to higher accuracies of CRC detection. When neglecting local blood oxygen saturation (StO_2) for reflectance spectral fitting under the homogeneous medium assumption, it is worth noting that lipid and scattering contributions to tissue classification become more important than contributions of total hemoglobin content [12]. However, when considering StO_2 and distribution of chromophores scattering properties over all probed tissue layers in DRS, near-infrared spectroscopy, elastic scattering spectroscopy and hyperspectral imaging, previous *in vivo* and *ex vivo* studies have shown that contributions of Hb and HbO_2 are comparable to those of lipid and water [11]. These contributions are evidenced by similar accuracies obtained when using wavelength ranges between 400 and 1000 nm (91.2 $\pm$ 0.9 accuracy) and between 1000 and 1920 nm (92.2 $\pm$ 1.3 accuracy) for the short-SDD probe [11].

In terms of wavelength ranges for differentiation between normal and cancer tissues, those in the optical window resulted in the highest classification performance for both short-SDD and long-SDD probes. This performance could have been achieved by considering the information on a number of biomolecules at variable depths and targeting wavelengths of higher light penetration. Our study suggests the latter is one of the main discriminatory factors, as probing deeper tissue layers with the long-SDD probe also led to higher performance compared with the short-SDD probe. Since more accurate tissue classification is achieved by using wavelengths at the optical window and using the long-SDD probe, the most relevant biomolecular changes associated with CRC detection, and potential carcinogenesis may occur at deeper tissue layers, which can be exploited by future studies.

Similar to the short-SDD probe, the highest classification performance was achieved by using wavelengths on the optical window (in this case, 650–950 nm). Additionally, since the performance obtained for the long-SDD probe is higher than that obtained by using the short-SDD probe, signals of deep tissue layers may contain more relevant information for tissue discrimination. This evidence can be further reinforced by the higher performance achieved by using the ultraviolet (380–400 nm) and visible (420–610 nm) wavelengths alone compared to the best performance obtained by using the short-SDD probe.

Our analysis of wavelength selection indicated that probing specific wavelength ranges for Hb, HbO_2, water and lipid absorption lead to similar classification accuracies as those achieved by using the wavelength range 350–1920 nm (Tables 2 and 3). These ranges may be used for future instrument design by keeping the geometrical configuration of the probe used in this study. In addition, extending the wavelength range towards longer NIR wavelengths may add information from other biomolecules as well as the contribution of the complementary data of water and lipid. With this in mind, future studies may investigate the complementarity of water and lipid information at wavelengths longer than 1920 nm and include features of other biomolecules absorbing at NIR and mid-infrared wavelengths (e.g., proteins, carbohydrates and nucleic acids).

4.4. Strength of the Cross-Validation of Our Model

In this study, we have used our PLS model to show the importance of objectively chosen wavelength ranges in tissue classification. Our tissue classification model was not used to assess the maximum classification performance to be obtained by testing several machine learning algorithms with our dataset. In fact, we have previously shown that higher classification performance can be obtained [11]. For correct interpretation of the influence of each wavelength range in the tissue classification, it is extremely important that our PLS model is general enough so that high classification performance parameters (sensitivity, specificity, accuracy and AUC) are not obtained due to overfitting by using large subsets of the dataset to build our classification model.

Although 5-fold cross-validation is frequently used for validation, this study used two-fold cross-validation in order to show a robust tissue classification in our dataset by using 50% of the data as a training set (two-fold) instead of 80% (5-fold). Two-fold cross-validation also allows the model to be tested in a larger dataset compared to 5-fold cross-validation, while the model is trained in a smaller subset of the total dataset. If the model is not general enough, training the model with smaller random subsets of the dataset while testing it in larger random subsets can lead to lower classification performance parameters. Therefore, robust classification through two-fold cross-validation means a stronger potential of generalization of the model upon an increase in sample size, especially compared to validation using more than 50% of the dataset for training and less than 50% for testing.

4.5. Limitations of Our Study

In order to evaluate oxygenation changes that could affect the results of the present study, we conducted a pilot observation of the DRS signal in 3 patients. We observed no significant variations in average Hb and HbO_2 of 7 mucosa sites and 7 tumor sites 15 min from the beginning of our measurements (data not shown). In this case, the DRS signal was monitored every 5 min during the collection time period. In terms of expected biochemical differences when translating our findings to *in vivo* studies, we expect a similar behavior showed by Baltussen et al. [88] in fat, tumor, and healthy colorectal wall tissues. The authors exhibited a statistically significant difference in blood concentration (%) and StO_2 (%) when measured *ex vivo* (within 1 h after resection) compared to in vivo. According to their study, both blood content and StO_2 increased, presumably due to an increase in blood volume in the capillaries after excision [134], exposure to air and decreased oxygen consumption by the cells in the specimen. Their study also suggests the water content decreases due to dehydration (vaporization and leakage) of the resected tissue, which was minimized in this study by keeping the tissue moist with wet wipes. However, it is important to remember that measurements by Baltussen et al. were taken by probing a different tissue depth compared to our study (probe with SDD 1.29 mm center-to–center distance) and the analyzed tissues are different from colorectal mucosa. Additionally, the behavior of StO_2 (%) is still not well understood, as results of Baltussen et al. disagrees with those of Salomatina et al. [135], who evaluated mouse ear tissues 5 to 10 min after excision (*ex vivo*) of tissue and after 24 and 72 h of storage.

Parts of our methodology are dependent on results achieved by using our dataset of almost 3000 measurements on 47 patients, which is assumed to be sufficiently robust for all analyses presented in this study. To ensure the wavelength selection was robust, the statistical test was based on all collected data. One should be aware that the wavelength selection was independent of the machine learning model. Therefore, classification performance metrics were affected by which wavelength ranges were selected, but not by the process to select wavelengths. It is worth noting that wavelengths were not used directly as descriptors/features of our machine learning (ML) models/classifiers. The four selected PLS components (PLSC) have been used as spectral features for tissue classification. A number of PLSCs have been selected as the minimum number of PLSCs before only increments of ~2% accuracy were gained upon inclusion of a new PLSC (data not shown). This threshold has been chosen to provide the best possible description of the data while avoiding overfitting. The four PLSCs were calculated on the entire dataset before two-fold cross-validation was performed for KNN models. Since PLSC loadings for tissue classification have been determined based on all the collected data (including the test set for the 20 iterations of two-fold cross-validation), it is important to note that the classification performance metrics were not calculated for optimized ML models in which spectral bands and PLSCs are selected at specific subsets of our dataset (discovery set) and subsequently training classifiers. Our classification performance metrics were used for the comparison of results obtained for each objectively/statistically selected wavelength range with the aim of placing wavelength ranges in the order of importance for tissue

classification, and subsequently, the main cancer biomarkers upon the association between these ranges and tissue chromophores and scattering properties were identified. For the estimation of classification performance metrics obtained with wider wavelength ranges, one should check our previous study [11].

Regarding the validation of our tissue classification model, the two-fold cross-validation with random sampling was performed spectrum-wise and not patient-wise. Hence, the data from different patients can be present in both training and test sets, but the same spectrum will only belong to either the training set or test set for each fold of cross-validation. However, this does not mean that the results of this study are invalid or that classification performance metrics have been overestimated. It is important to consider that the intra-patient is comparable to the inter-patient variation in our dataset (the standard deviation of measurements within each individual patient is less than twice the standard deviation of all measurements of all patients). A typical mean and standard deviation across all measured locations of one patient for both tumor and normal mucosa measured with both probes is given in Figure S1 in Supplementary Material. No clear trend has been identified in the data of specific patients, possibly due to the limited number of patients. If such a trend is identified in future studies, a patient-wise validation of our model would estimate the classification performance metrics of Tables 2 and 3 most likely as robustly. Since this trend has not been identified, a spectrum-wise validation of our tissue classification model could potentially be stronger because this validation includes the data of more patients compared with a patient-wise validation. This is especially important given that our study was limited to 47 patients.

Furthermore, the ultimate aim of our study is to classify normal mucosa and cancer tissues at each location within the same patient. Therefore, robust validation of our tissue classification model should consider both measurements of different patients as well as measurements from the same patient, but at different tissue locations, as we did in our study.

Our study focused on biochemical and DRS spectral differences between mucosa and cancer tissues, which, from a clinical perspective, would be especially useful for guidance on cancer margins and tumor delineation. Future studies exploring tumor detection will include data from tissues with non-cancer pathology. This would include a variety of non-neoplastic processes commonly seen in CRC patients including inflammatory bowel disease, radiation-induced fibrosis, and scarring following local excision of cancers.

From a research perspective, the results of our study can be used to design optimized optical instruments targeting the specific wavelength ranges and tissue probed depth, as well as to evaluate the feasibility of employing biochemical analysis methods targeting Hb, HbO_2, water and lipid for tissue classification. These methods include other optical sensors and/or combinations with existing instruments for CT, MRI, electrical measurements, mass spectrometry, and others. Simulations of light transport in tissues and DRS measurements may benefit from estimating accurate data of the chromophores most relevant for tissue classification. The same applies to the creation of 3D cell models (e.g., spheroids) mimicking mucosal and cancerous tissues in tissue engineering studies, where the right tissue types and thicknesses should accurately reproduce the tissue biochemistry.

5. Conclusions

In the present study, we evaluated the most important tissue biomarkers and wavelength ranges for CRC detection by using diffuse reflectance spectroscopy in the visible/near-infrared wavelength range from 350 nm to 1920 nm. In this range, the biomolecules most relevant for classification between normal and cancer tissues were Hb, HbO_2, lipid and water. Tissue classification using Hb and HbO_2 data can be achieved with wavelength ranges 350–590 nm or 600–1230 nm for superficial tissue (short-SDD probe), and 380–400 nm, 420–610 nm, and 650–950 nm for deeper tissue layers (long-SDD probe). Information collected in those wavelength ranges is redundant and the combination between them did not enhance the classification. On the other hand, water and lipid information are

complementary and may improve cancer detection and investigation of carcinogenesis upon extension of the wavelength range. Our results suggested that information from deeper tissue layers either accessed by probing the optical window or through the long-SDD probe can differentiate normal and cancer tissues more accurately. Wavelength ranges and probe geometrical configuration used in this study may be used for more specific future instrument design. From a practical perspective, these wavelength ranges and geometrical configurations will be used to develop an optical system for CRC detection during colonoscopy and intra-operatively. By optimizing the features for discrimination between normal and cancerous tissues, tissue identification is performed in real-time with a single reading of about 2–3 s. By means of the integration of real-time tissue identification into a flexible fiberoptic probe which could be passed down the working channel of an endoscope, optical spectroscopy may provide a powerful tool that can be used to detect cancer cells and direct management in real time. In addition, this spectroscopic technique can detect more subtle mucosal abnormalities such as sessile serrated polyps, which may be difficult to identify during colonoscopy. Once instruments with wavelength ranges and probe geometrical configuration found in this study have been miniaturized and integrated into colonoscopies, next-generation instruments can be manufactured and their impact in reducing CRC morbidity and morbidity can be assessed in future *in vivo* studies.

Supplementary Materials: The following supporting information can be downloaded at: https://www.mdpi.com/article/10.3390/cancers14225715/s1, Figure S1: Mean and standard deviation across broadband reflectance spectra of all measured locations of both tumor and normal mucosa measured with (A) the short-SDD and (B) the long-SDD probe for one patient.

Author Contributions: M.S.N. Conceptualization, Methodology, Software, Validation, Formal analysis, Investigation, Resources, Data Curation, Writing—Original Draft, Writing—Review and Editing, Visualization, Supervision, Software, Validation, Project administration, S.M. Investigation, Data curation, M.A. Investigation, Data Curation, A.M. Methodology, Investigation, Data Curation, Writing—Review and Editing, C.S. Methodology, Investigation, Data Curation, Writing—Review and Editing, S.K. Investigation, Resources, Data Curation, S.A.-E. Conceptualization, Methodology, Resources, Writing—Review and Editing, Supervision, Project administration, Funding Acquisition, M.O. Conceptualization, Methodology, Validation, Formal analysis, Investigation, Resources, Data Curation, Writing—Review and Editing, Supervision, Project administration, Funding Acquisition. All authors have read and agreed to the published version of the manuscript.

Funding: This study received financial support from Science Foundation Ireland (SFI): grant ID SFI/15/RP/2828. Shauni Fitzgerald and Edmund Manning were funded by the Mercy Foundation.

Institutional Review Board Statement: The study was conducted in accordance with the Declaration of Helsinki, and approved by the Clinical Research Ethics Committee of University College Cork (protocol approval numbers of ECM 4 (n) 07/03/18 and ECM 3 (hhh) 18/06/2019).

Informed Consent Statement: Informed consent was obtained from all subjects involved in the study. Written informed consent has been obtained from the patient(s) to publish this paper.

Data Availability Statement: The data presented in this study are available on request from the corresponding author.

Acknowledgments: The authors acknowledge Eduardo Moriyama for the advice and logistics of the project associated with this manuscript, Shree Krishnamoorthy for the discussions on the same project, Haiyang Li for the design and assembly of the holder of the DRS system, Noel Lynch for specimen retrieval of the first set of patients of this study and all the logistics related to it, Vivienne Curran, Aoife Foyle, Una McAuliffe, Evelyn Flanagan, Shauni Fitzgerald, and Edmund Manning for all the logistics of clinical procedures, research ethics documents, and search for patient information.

Conflicts of Interest: The authors declare no conflict of interest. The funders had no role in the design of the study; in the collection, analyses, or interpretation of data; in the writing of the manuscript, or in the decision to publish the results.

References

1. Bray, F.; Ferlay, J.; Soerjomataram, I.; Siegel, R.L.; Torre, L.A.; Jemal, A. Global cancer statistics 2018: GLOBOCAN estimates of incidence and mortality worldwide for 36 cancers in 185 countries. *CA Cancer J. Clin.* **2018**, *68*, 394–424. [CrossRef]
2. Ferlay, J.; Ervik, M.; Lam, F.; Colombet, M.; Mery, L.; Piñeros, M.; Znaor, A.; Soerjomataram, I.; Bray, F. *Global Cancer Observatory: Cancer Today*; International Agency for Research on Cancer: Lyon, France, 2018; Available online: https://gco.iarc.fr/ (accessed on 8 October 2022).
3. Shaukat, A.; Levin, T.R. Current and future colorectal cancer screening strategies. *Nat. Rev. Gastroenterol. Hepatol.* **2022**, *19*, 521–531. [CrossRef] [PubMed]
4. Ichkhanian, Y.; Zuchelli, T.; Watson, A.; Piraka, C. Evolving management of colorectal polyps. *Ther. Adv. Gastrointest. Endosc.* **2021**, *14*, 26317745211047010. [CrossRef] [PubMed]
5. Pogue, B.W. Optics in the molecular imaging race. *Opt. Photonics News* **2015**, *26*, 24–31. [CrossRef]
6. Nogueira, M.S.; Raju, M.; Gunther, J.; Maryam, S.; Amissah, M.; Lu, H.; Killeen, S.; O'Riordain, M.; Andersson-Engels, S. Accurate colorectal cancer detection and delineation by probing superficial and deeper tissue biochemistry and microstructure using diffuse reflectance spectroscopy. In Proceedings of the Molecular-Guided Surgery: Molecules, Devices, and Applications VIII, San Francisco, CA, USA, 22 January–28 February 2022; Volume 11943.
7. Nogueira, M.S.; Raju, M.; Komolibus, K.; Grygoryev, K.; Andersson-Engels, S. Assessment of tissue biochemical and optical scattering changes due to hypothermic organ preservation: A preliminary study in mouse organs. *J. Phys. D Appl. Phys.* **2021**, *54*, 37.
8. Nogueira, M.S.; Raju, M.; Gunther, J.; Maryam, S.; Amissah, M.; Killeen, S.; O'Riordain, M.; Andersson-Engels, S. Optical determination of superficial and deeper tissue biochemistry and microstructure for delineation and early detection of colorectal cancer. In Proceedings of the European Conference on Biomedical Optics, Munich, Germany, 20–24 June 2021; p. ETu3A-1.
9. Nogueira, M.S.; Maryam, S.; Amissah, M.; Lynch, N.; Killeen, S.; O'Riordain, M.; Andersson-Engels, S. Benefit of extending near-infrared wavelength range of diffuse reflectance spectroscopy for colorectal cancer detection using machine learning. In Proceedings of the European Conference on Biomedical Optics, Munich, Germany, 20–24 June 2021; p. EW4A-16.
10. Nogueira, M.S.; Raju, M.; Gunther, J.; Grygoryev, K.; Komolibus, K.; Lu, H.; Andersson-Engels, S. Diffuse reflectance spectroscopy for determination of optical properties and chromophore concentrations of mice internal organs in the range of 350 nm to 1860 nm. In Proceedings of the Biophotonics: Photonic Solutions for Better Health Care VI, Strasbourg, France, 22–26 April 2018; Volume 10685. [CrossRef]
11. Nogueira, M.S.; Maryam, S.; Amissah, M.; Lu, H.; Lynch, N.; Killeen, S.; O'Riordain, M.; Andersson-Engels, S. Evaluation of wavelength ranges and tissue depth probed by diffuse reflectance spectroscopy for colorectal cancer detection. *Sci. Rep.* **2021**, *11*, 798. [CrossRef]
12. Nogueira, M.S.; Raju, M.; Gunther, J.; Maryam, S.; Amissah, M.; Lu, H.; Killeen, S.; O'Riordain, M.; Andersson-Engels, S. Tissue biomolecular and microstructure profiles in optical colorectal cancer delineation. *J. Phys. D Appl. Phys.* **2021**, *54*, 454002. [CrossRef]
13. Mousavi, M.; Moriyama, L.T.T.; Grecco, C.; Nogueira, M.S.; Svanberg, K.; Kurachi, C.; Andersson-Engels, S. Photodynamic therapy dosimetry using multiexcitation multiemission wavelength: Toward real-time prediction of treatment outcome. *J. Biomed. Opt.* **2020**, *25*, 63812. [CrossRef]
14. Nogueira, M.S.; Maryam, S.; Amissah, M.; Lynch, N.; Killeen, S.; Lu, H.; O'Riordain, M.; Andersson-Engels, S. Improving colorectal cancer detection by extending the near-infrared wavelength range and tissue probed depth of diffuse reflectance spectroscopy: A support vector machine approach. In Proceedings of the Optical Biopsy XX: Toward Real-Time Spectroscopic Imaging and Diagnosis, San Francisco, CA, USA, 22 January–28 February 2022; Volume 11954.
15. Nogueira, M.S.; Amissah, M.; Maryam, S.; Lynch, N.; Killeen, S.; O'Riordain, M.; Andersson-Engels, S. Optimization of tissue classification for colorectal cancer detection using support vector machines and diffuse reflectance spectroscopy. In Proceedings of the European Conference on Biomedical Optics, Munich, Germany, 20–24 June 2021; p. EW4A-17.
16. Nogueira, M.S.; Jayet, B.; Matias, J.S.; Gunther, J.E.; Tyndall, C.; Andersson-Engels, S. Biophotonics web application for computer simulations in diffuse optics: Fostering multidisciplinary education and research. In Proceedings of the Optical Interactions with Tissue and Cells XXXIII; and Advanced Photonics in Urology, San Francisco, CA, USA, 22 January–28 February 2022; Volume 11958.
17. Saito Nogueira, M.; Gunther, J.E.; Jayet, B.; Souza Matias, J.; Tyndall, C.; Andersson-Engels, S. Biophotonics computer app: Fostering multidisciplinary distance self-paced learning with a user-friendly interface. In Proceedings of the OSA Technical Digest, San Francisco, CA, USA, 1–6 February 2021; pp. 1–2.
18. Nogueira, M.S.; Gunther, J.E.; Komolibus, K.; Andersson-Engels, S. User-friendly graphical user interface for simulating tissue optical properties and fluence rates: Improving students learning in tissue optics. In Proceedings of the Optical Interactions with Tissue and Cells XXXI, San Francisco, CA, USA, 1–6 February 2020; Volume 11238.
19. Mourant, J.R.; Freyer, J.P.; Hielscher, A.H.; Eick, A.A.; Shen, D.; Johnson, T.M. Mechanisms of light scattering from biological cells relevant to noninvasive optical-tissue diagnostics. *Appl. Opt.* **1998**, *37*, 3586–3593. [CrossRef]
20. Mourant, J.R.; Johnson, T.M.; Carpenter, S.; Guerra, A.; Aida, T.; Freyer, J.P. Polarized angular-dependent spectroscopy of epithelial cells and epithelial cell nuclei to determine the size scale of scattering structures. *J. Biomed. Opt.* **2002**, *7*, 378–387. [CrossRef]

21. Jacques, S.L. Optical properties of biological tissues: A review. *Phys. Med. Biol.* **2013**, *58*, R37. [CrossRef] [PubMed]
22. Nogueira, M.S. *Fluorescence Lifetime Spectroscopy for Diagnosis of Clinically Similar Skin Lesions*; Universidade de São Paulo: São Paulo, Brazil, 2016.
23. Nogueira, M.S.; Kurachi, C. Assessing the photoaging process at sun exposed and non-exposed skin using fluorescence lifetime spectroscopy. In Proceedings of the Optical Biopsy XIV: Toward Real-Time Spectroscopic Imaging and Diagnosis, San Francisco, CA, USA, 13–18 February 2016; Volume 9703.
24. Cosci, A.; Nogueira, M.S.; Pratavieira, S.; Takahama, A.; de Souza Azevedo, R.; Kurachi, C.; Kurachi, C. Time-resolved fluorescence spectroscopy for clinical diagnosis of actinic cheilitis: Erratum. *Biomed. Opt. Express* **2016**, *7*, 4210–4219. [CrossRef] [PubMed]
25. Lacerenza, M.; Pacheco, A.; Sekar, S.K.V.; Nogueira, M.S.; Buttafava, M.; Tosi, A.; Pifferi, A.; Contini, D.; Andersson-Engels, S. Functional monitoring of lung tissue using a hybrid hyperspectral Time-Resolved GASMAS system: A systematic study on ex vivo sample. In Proceedings of the Optical Tomography and Spectroscopy, Washington, DC, USA, 20–23 April 2020; p. SW1D-2.
26. Pires, L.; Nogueira, M.S.; Pratavieira, S.; Moriyama, L.T.; Kurachi, C. Time-resolved fluorescence lifetime for cutaneous melanoma detection. *Biomed. Opt. Express* **2014**, *5*, 3080. [CrossRef]
27. Kurachi, C.; Pires, L.; Nogueira, M.S.; Pratavieira, S. Lifetime fluorescence for the detection of skin lesions. In Proceedings of the Biomedical Optics 2014, Miami, FL, USA, 26–30 April 2014. [CrossRef]
28. Nogueira, M.S.; Cosci, A.; Pratavieira, S.; Takahama, A., Jr.; Azevedo, R.S.; Kurachi, C. Evaluation of actinic cheilitis using fluorescence lifetime spectroscopy. In Proceedings of the Optical Biopsy XIV: Toward Real-Time Spectroscopic Imaging and Diagnosis, San Francisco, CA, USA, 13–18 February 2016; Volume 9703.
29. Salvio, A.G.; Ramirez, D.P.; Inada, N.M.; Stringasci, M.D.; Nogueira, M.S.; Bagnato, V.S. Fractionated Illumination in a Single Visit Photodynamic Therapy for Basal Cell Carcinoma; Book of Abstracts. 2017. Available online: https://www.internationalphotodynamic.com/ (accessed on 8 October 2022).
30. Salvio, A.G.; Ramirez, D.P.; Nogueira, M.S.; Stringasci, M.D.; Oliveira, E.R.; Inada, N.M.; Bagnato, V.S. Evaluation of Pain and Treatment Effect during Large Area Photodynamic Therapy in 140 Patients with Widespread Actinic Keratosis of Upper Limbs; Book of Abstracts. 2017. Available online: https://www.internationalphotodynamic.com/ (accessed on 8 October 2022).
31. Nogueira, M.S.; Cosci, A.; Rosa, R.G.T.; Salvio, A.G.; Pratavieira, S.; Kurachi, C. Portable fluorescence lifetime spectroscopy system for in-situ interrogation of biological tissues. *J. Biomed. Opt.* **2017**, *22*, 121608.
32. de Paula Campos, C.; de Paula D'Almeida, C.; Nogueira, M.S.; Moriyama, L.T.; Pratavieira, S.; Kurachi, C. Fluorescence spectroscopy in the visible range for the assessment of UVB radiation effects in hairless mice skin. *Photodiagnosis Photodyn. Ther.* **2017**, *20*, 21–27. [CrossRef]
33. Nogueira, M.S.; Guimarães, F.E.G. Photophysical processes on biological tissues and photodynamic therapy using steady-state and time-resolved fluorescence techniques: Diagnosis applications, dosimetry and photodegradation kinetics. In *Livro de Resumos*; SIBiUSP-Integrated USP Libraries: São Paulo, Brazil, 2016.
34. Ono, B.A.; Nogueira, M.; Pires, L.; Pratavieira, S.; Kurachi, C. Subcellular localization and photodynamic activity of Photodithazine (glucosamine salt of chlorin e6) in murine melanoma B16-F10: An in vitro and in vivo study. In Proceedings of the Optical Methods for Tumor Treatment and Detection: Mechanisms and Techniques in Photodynamic Therapy XXVII, San Francisco, CA, USA, 27 January–1 February 2018; Volume 1047616, p. 44. [CrossRef]
35. Nogueira, M.S.; Bagnato, V.S.; Panhoca, V.H. Effectiveness of whitening treatments employing violet illumination alone or combined with bleaching agents. In Proceedings of the Lasers in Dentistry XXVIII, San Francisco, CA, USA, 22 January–28 February 2022; Volume 11942.
36. Panhóca, V.H.; Nogueira, M.S.; Bagnato, V.S. Treatment of facial nerve palsies with laser and endermotherapy: A report of two cases. *Laser Phys. Lett.* **2020**, *18*, 15601. [CrossRef]
37. Panhóca, V.H.; Nogueira, M.S.; Bagnato, V.S. Laser and vacuum therapy for treatment of facial nerve palsies. In Proceedings of the Imaging, Therapeutics, and Advanced Technology in Head and Neck Surgery and Otolaryngology 2022, San Francisco, CA, USA, 22 January–28 February 2022; Volume 11935, pp. 39–48.
38. Bomfin, L.S.; Kitakawa, D.; Nogueira, M.S.; de Silva, L.F. Low Level Laser Therapy as adjuvant treatment for lower lip lesion. In Proceedings of the Latin America Optics and Photonics Conference, Recife, Brazil, 7–11 August 2022; p. M2B-6.
39. Nogueira, M.S.; Lacerenza, M.; Sekar, S.K.V.; Buttafava, M.; Pifferi, A.; Tosi, A.; Contini, D.; Andersson-Engels, S. Broadband extraction of tissue optical properties using a portable hybrid time-resolved continuous wave instrumentation: Characterization of ex vivo organs. In Proceedings of the Clinical and Translational Biophotonics, Washington, DC, USA, 20–23 April 2020; p. TM2B-3.
40. Nogueira, M.S.; Bagnato, V.S.; Panhoca, V.H. Characterization of teeth fluorescence properties due to coffee pigmentation: Towards optimization of quantitative light-induced fluorescence for tooth color assessment. In Proceedings of the Optical Interactions with Tissue and Cells XXXI, San Francisco, CA, USA, 1–6 February 2020; Volume 11238.
41. Nogueira, M.S.; Pinto Junior, F.F.; Caface, R.A.; de Oliveira, K.T.; Guimarães, F.E.G. Optimization of curcumin formulations for fluorescence-based applications. In Proceedings of the Optical Interactions with Tissue and Cells XXXI, San Francisco, CA, USA, 1–6 February 2020; Volume 11238.
42. Nogueira, M.S.; Junior, F.F.P.; Caface, R.A.; de Oliveira, K.T.; Bagnato, V.S.; Guimarães, F.E.G. Characterization of photophysical properties of curcumin for theranostics of neurodegenerative diseases. In Proceedings of the Optical Interactions with Tissue and Cells XXX, San Francisco, CA, USA, 2–7 February 2019; Volume 10876.

43. Nogueira, M.S.; Komolibus, K.; Grygoryev, K.; Gunther, J.E.; Andersson-Engels, S. Fluorescence spectroscopy of mouse organs using ultraviolet excitation: Towards assessment of organ viability for transplantation. In Proceedings of the Optical Interactions with Tissue and Cells XXX, San Francisco, CA, USA, 2–7 February 2019; Volume 10876.
44. Nogueira, M.S.; Panhóca, V.H.; Bagnato, V.S. Fluorescence spectroscopy analysis of light-induced tooth whitening. In Proceedings of the Optical Interactions with Tissue and Cells XXX, San Francisco, CA, USA, 2–7 February 2019; Volume 10876.
45. De Andrade, C.T.; Nogueira, M.S.; Kanick, S.C.; Marra, K.; Gunn, J.; Andreozzi, J.; Samkoe, K.S.; Kurachi, C.; Pogue, B.W. Optical spectroscopy of radiotherapy and photodynamic therapy responses in normal rat skin shows vascular breakdown products. In Proceedings of the Optical Methods for Tumor Treatment and Detection: Mechanisms and Techniques in Photodynamic Therapy XXV, San Francisco, CA, USA, 13–18 February 2016; Volume 9694.
46. Saito Nogueira, M.; Ribeiro, V.; Pires, M.; Peralta, F.; Carvalho, L.F.D.C.E.S.D. Biochemical Profiles of In Vivo Oral Mucosa by Using a Portable Raman Spectroscopy System. *Optics* **2021**, *2*, 134–147. [CrossRef]
47. Carvalho, L.F.C.S.; Nogueira, M.S.; Bhattacharjee, T.; Neto, L.P.M.; Daun, L.; Mendes, T.O.; Rajasekaran, R.; Chagas, M.; Martin, A.A.; Soares, L.E.S. In vivo Raman spectroscopic characteristics of different sites of the oral mucosa in healthy volunteers. *Clin. Oral Investig.* **2019**, *23*, 3021–3031. [CrossRef]
48. Leal, L.B.; Nogueira, M.S.; Mageski, J.G.A.; Martini, T.P.; Barauna, V.G.; dos Santos, L.; Carvalho, L.F.D.C.E.S.D. Diagnosis of Systemic Diseases Using Infrared Spectroscopy: Detection of Iron Overload in Plasma—Preliminary Study. *Biol. Trace Element Res.* **2021**, *199*, 3737–3751. [CrossRef]
49. Carvalho, L.F.C.S.; Nogueira, M.S. New insights of Raman spectroscopy for oral clinical applications. *Analyst* **2018**, *143*, 6037–6048. [CrossRef]
50. Carvalho, L.F.C.S.; Nogueira, M.S.; Neto, L.P.M.; Bhattacharjee, T.T.; Martin, A.A. Raman spectral post-processing for oral tissue discrimination—A step for an automatized diagnostic system. *Biomed. Opt. Express* **2017**, *8*, 5218, Erratum in *Biomed. Opt. Express* **2018**, *9*, 649. [CrossRef] [PubMed]
51. Nogueira, M.S. Biophotonic telemedicine for disease diagnosis and monitoring during pandemics: Overcoming COVID-19 and shaping the future of healthcare. *Photodiagnosis Photodyn. Ther.* **2020**, *31*, 101836. [CrossRef] [PubMed]
52. Maryam, S.; Nogueira, M.S.; Krishnamoorthy, S.; Sekar, S.K.V.; Lu, H.; Gautam, R.; Burke, R.; Andersson-Engels, S.; Riordain, R.N.; Sheahan, P. Multi-configuration Raman spectrometer for early stage diagnosis of oral cancer. In Proceedings of the Biomedical Vibrational Spectroscopy 2022: Advances in Research and Industry, San Francisco, CA, USA, 22 January–28 February 2022; Volume 11957, pp. 20–26.
53. Nogueira, M.S.; Barreto, A.L.; Furukawa, M.; Rovai, E.S.; Bastos, A.; Bertoncello, G.; e Silva de Carvalho, L.F.d.C. FTIR spectroscopy as a point of care diagnostic tool for diabetes and periodontitis: A saliva analysis approach. *Photodiagn. Photodyn. Ther.* **2022**, *40*, 103036. [CrossRef] [PubMed]
54. Carnevalli, A.C.; Leal, L.; Scherma, A.; Morais, C.; Martin, F.; Bonnier, F.; Baker, M.; Byrne, H.J.; Chagas e Silva Carvalho, L.F.; Nogueira, M.S. Identification of diabetic patients via urine analysis by FTIR: Preliminary study (Conference Presentation). In Proceedings of the Photonic Diagnosis and Treatment of Infections and Inflammatory Diseases II, San Francisco, CA, USA, 2–7 February 2019; Volume 10863.
55. Ferreira, M.C.C.; Monteiro, G.R.; Peralta, F.; Castro, P.A.A.; Zezell, D.; Nogueira, M.S.; Carvalho, L.F.C.S. Assessment of bound water of saliva samples by using FT-IR spectroscopy. In Proceedings of the Latin America Optics and Photonics Conference, Recife, Brazil, 7–11 August 2022; p. M4B-1.
56. Nogueira, M.S.; Leal, L.B.; Marcarini, W.D.; Pimentel, R.L.; Muller, M.; Vassallo, P.F.; Campos, L.C.G.; Dos Santos, L.; Luiz, W.B.; Mill, J.G.; et al. Rapid diagnosis of COVID-19 using FT-IR ATR spectroscopy and machine learning. *Sci. Rep.* **2021**, *11*, 15409. [CrossRef]
57. Chow, K.K.; Short, M.; Lam, S.; McWilliams, A.; Zeng, H. A Raman cell based on hollow core photonic crystal fiber for human breath analysis. *Med. Phys.* **2014**, *41*, 92701. [CrossRef]
58. Bydlon, T.M.; Nachabé, R.; Ramanujam, N.; Sterenborg, H.J.C.M.; Hendriks, B.H.W. Chromophore based analyses of steady-state diffuse reflectance spectroscopy: Current status and perspectives for clinical adoption. *J. Biophotonics* **2015**, *8*, 9–24. [CrossRef]
59. Nachabé, R.; Hendriks, B.H.W.; van der Voort, M.; Desjardins, A.E.; Sterenborg, H.J.C.M. Estimation of biological chromophores using diffuse optical spectroscopy: Benefit of extending the UV-VIS wavelength range to include 1000 to 1600 nm. *Biomed. Opt. Express* **2010**, *1*, 1432–1442. [CrossRef]
60. Nogueira, M.S.; Brugnera, J.A.; Bagnato, V.S.; Panhóca, V.H. Evaluation of the whitening effectiveness of violet illumination alone or combined with hydrogen peroxide gel. *Photobiomodulation Photomed. Laser Surg.* **2021**, *39*, 395–402. [CrossRef]
61. Nachabé, R.; Evers, D.J.; Hendriks, B.H.W.; Lucassen, G.W.; van der Voort, M.; Wesseling, J.; Ruers, T.J.M. Effect of bile absorption coefficients on the estimation of liver tissue optical properties and related implications in discriminating healthy and tumorous samples. *Biomed. Opt. Express* **2011**, *2*, 600–614. [CrossRef]
62. Nogueira, M.S.; Matthews, R.; Killeen, S.; O'Riordain, M.; Andersson-Engels, S. Colorectal cancer detection based on the extraction of scattering properties and biochemical concentrations from fluorescence spectroscopy measurements. In Proceedings of the Clinical and Translational Biophotonics, Fort Lauderdale, FL, USA, 24–27 April 2022; 24–27 April 2022; p. TS2B-5. [CrossRef]
63. Swartling, J.; Pifferi, A.; Enejder, A.M.K.; Andersson-Engels, S. Accelerated Monte Carlo models to simulate fluorescence spectra from layered tissues. *JOSA A* **2003**, *20*, 714–727. [CrossRef]

64. Muller, M.; Hendriks, B.H.W. Recovering intrinsic fluorescence by Monte Carlo modeling. *J. Biomed. Opt.* **2013**, *18*, 27009. [CrossRef] [PubMed]
65. Chang, S.K.; Mar\'\in, N.; Follen, M.; Richards-Kortum, R.R. Model-based analysis of clinical fluorescence spectroscopy for in vivo detection of cervical intraepithelial dysplasia. *J. Biomed. Opt.* **2006**, *11*, 24008. [CrossRef] [PubMed]
66. Pfefer, T.J.; Wang, Q.; Drezek, R.A. Monte Carlo modeling of time-resolved fluorescence for depth-selective interrogation of layered tissue. *Comput. Methods Programs Biomed.* **2011**, *104*, 161–167. [CrossRef] [PubMed]
67. Marcu, L.; French, P.M.W.; Elson, D.S. *Fluorescence Lifetime Spectroscopy and Imaging: Principles and Applications in Biomedical Diagnostics*; CRC Press: Boca Raton, FL, USA, 2014.
68. Pogue, B.W.; Poplack, S.P.; McBride, T.O.; Wells, W.A.; Osterman, K.S.; Osterberg, U.L.; Paulsen, K.D. Quantitative hemoglobin tomography with diffuse near-infrared spectroscopy: Pilot results in the breast. *Radiology* **2001**, *218*, 261–266. [CrossRef] [PubMed]
69. Heffer, E.L.; Fantini, S. Quantitative oximetry of breast tumors: A near-infrared method that identifies two optimal wavelengths for each tumor. *Appl. Opt.* **2002**, *41*, 3827–3839. [CrossRef] [PubMed]
70. Cerussi, A.E.; Berger, A.J.; Bevilacqua, F.; Shah, N.; Jakubowski, D.; Butler, J.; Holcombe, R.F.; Tromberg, B.J. Sources of absorption and scattering contrast for near-infrared optical mammography. *Acad. Radiol.* **2001**, *8*, 211–218. [CrossRef]
71. Svensson, T.; Swartling, J.; Taroni, P.; Torricelli, A.; Lindblom, P.; Ingvar, C.; Andersson-Engels, S. Characterization of normal breast tissue heterogeneity using time-resolved near-infrared spectroscopy. *Phys. Med. Biol.* **2005**, *50*, 2559. [CrossRef]
72. Chance, B.; Nioka, S.; Zhang, J.; Conant, E.F.; Hwang, E.; Briest, S.; Orel, S.G.; Schnall, M.D.; Czerniecki, B.J. Breast cancer detection based on incremental biochemical and physiological properties of breast cancers: A six-year, two-site study1. *Acad. Radiol.* **2005**, *12*, 925–933. [CrossRef]
73. Nilsson, J.H.; Reistad, N.; Brange, H.; Öberg, C.-F.; Sturesson, C. Diffuse reflectance spectroscopy for surface measurement of liver pathology. *Eur. Surg. Res.* **2017**, *58*, 40–50. [CrossRef]
74. Conover, D.L.; Fenton, B.M.; Foster, T.H.; Hull, E.L. An evaluation of near infrared spectroscopy and cryospectrophotometry estimates of haemoglobin oxygen saturation in a rodent mammary tumour model. *Phys. Med. Biol.* **2000**, *45*, 2685. [CrossRef]
75. Steen, R.G.; Kitagishi, K.; Morgan, K. In vivo measurement of tumor blood oxygenation by near-infrared spectroscopy: Immediate effects of pentobarbital overdose or carmustine treatment. *J. Neurooncol.* **1994**, *22*, 209–220. [CrossRef]
76. Kragh, M.; Quistorff, B.; Horsman, M.R.; Kristjansen, P.E.G. Acute effects of vascular modifying agents in solid tumors assessed by noninvasive laser Doppler flowmetry and near infrared spectroscopy. *Neoplasia* **2002**, *4*, 263–267. [CrossRef] [PubMed]
77. Kragh, M.; Quistorff, B.; Lund, E.L.; Kristjansen, P.E.G. Quantitative estimates of vascularity in solid tumors by non-invasive near-infrared spectroscopy. *Neoplasia* **2001**, *3*, 324–330. [CrossRef] [PubMed]
78. Gu, Y.; Chen, W.R.; Xia, M.; Jeong, S.W.; Liu, H. Effect of Photothermal Therapy on Breast Tumor Vascular Contents: Noninvasive Monitoring by Near-infrared Spectroscopy. *Photochem. Photobiol.* **2007**, *81*, 1002–1009. [CrossRef]
79. Howe, F.A.; Connelly, J.P.; Robinson, S.P.; Springett, R.; Griffiths, J.R. The effects of tumour blood flow and oxygenation modifiers on subcutaneous tumours as determined by NIRS. In *Oxygen Transport to Tissue XXVI*; Springer: Boston, MA, USA, 2005; pp. 75–81.
80. Hirosawa, N.; Sakamoto, Y.; Katayama, H.; Tonooka, S.; Yano, K. In vivo investigation of progressive alterations in rat mammary gland tumors by near-infrared spectroscopy. *Anal. Biochem.* **2002**, *305*, 156–165. [CrossRef]
81. Xia, M.; Kodibagkar, V.; Liu, H.; Mason, R.P. Tumour oxygen dynamics measured simultaneously by near-infrared spectroscopy and 19F magnetic resonance imaging in rats. *Phys. Med. Biol.* **2005**, *51*, 45. [CrossRef]
82. Yu, G.; Durduran, T.; Zhou, C.; Wang, H.-W.; Putt, M.E.; Saunders, H.M.; Sehgal, C.M.; Glatstein, E.; Yodh, A.G.; Busch, T.M. Noninvasive monitoring of murine tumor blood flow during and after photodynamic therapy provides early assessment of therapeutic efficacy. *Clin. Cancer Res.* **2005**, *11*, 3543–3552. [CrossRef]
83. Roy, H.K.; Gomes, A.; Turzhitsky, V.; Goldberg, M.J.; Rogers, J.; Ruderman, S.; Young, K.L.; Kromine, A.; Brand, R.E.; Jameel, M.; et al. Spectroscopic microvascular blood detection from the endoscopically normal colonic mucosa: Biomarker for neoplasia risk. *Gastroenterology* **2008**, *135*, 1069–1078. [CrossRef]
84. Wang, H.-W.; Jiang, J.-K.; Lin, C.-H.; Lin, J.-K.; Huang, G.-J.; Yu, J.-S. Diffuse reflectance spectroscopy detects increased hemoglobin concentration and decreased oxygenation during colon carcinogenesis from normal to malignant tumors. *Opt. Express* **2009**, *17*, 2805–2817. [CrossRef]
85. Zonios, G.; Perelman, L.T.; Backman, V.; Manoharan, R.; Fitzmaurice, M.; Van Dam, J.; Feld, M.S. Diffuse reflectance spectroscopy of human adenomatous colon polyps in vivo. *Appl. Opt.* **1999**, *38*, 6628–6637. [CrossRef]
86. Dhar, A.; Johnson, K.S.; Novelli, M.R.; Bown, S.G.; Bigio, I.J.; Lovat, L.B.; Bloom, S.L. Elastic scattering spectroscopy for the diagnosis of colonic lesions: Initial results of a novel optical biopsy technique. *Gastrointest. Endosc.* **2006**, *63*, 257–261. [CrossRef] [PubMed]
87. Mourant, J.R.; Bigio, I.J.; Boyer, J.D.; Johnson, T.M.; Lacey, J.; Bohorfoush, A.G.; Mellow, M.H. Elastic scattering spectroscopy as a diagnostic tool for differentiating pathologies in the gastrointestinal tract: Preliminary testing. *J. Biomed. Opt.* **1996**, *1*, 192–200. [CrossRef] [PubMed]
88. Baltussen, E.J.M.; Brouwer De Koning, S.G.; Hendriks, B.H.W.; Jóźwiak, K.; Sterenborg, H.J.C.M.; Ruers, T.J.M. Comparing in vivo and ex vivo fiberoptic diffuse reflectance spectroscopy in colorectal cancer. *Transl. Biophotonics* **2019**, *1*, e201900008. [CrossRef]

89. De Koning, S.G.B.; Baltussen, E.J.M.; Karakullukcu, M.B.; Dashtbozorg, B.; Smit, L.A.; Dirven, R.; Hendriks, B.H.W.; Sterenborg, H.J.C.M.; Ruers, T.J.M. Toward complete oral cavity cancer resection using a handheld diffuse reflectance spectroscopy probe. *J. Biomed. Opt.* **2018**, *23*, 121611.
90. De Boer, L.L.; Molenkamp, B.G.; Bydlon, T.M.; Hendriks, B.H.W.; Wesseling, J.; Sterenborg, H.; Ruers, T.J.M. Fat/water ratios measured with diffuse reflectance spectroscopy to detect breast tumor boundaries. *Breast Cancer Res. Treat.* **2015**, *152*, 509–518. [CrossRef] [PubMed]
91. Soares, J.S.; Barman, I.; Dingari, N.C.; Volynskaya, Z.; Liu, W.; Klein, N.; Plecha, D.; Dasari, R.R.; Fitzmaurice, M. Diagnostic power of diffuse reflectance spectroscopy for targeted detection of breast lesions with microcalcifications. *Proc. Natl. Acad. Sci. USA* **2013**, *110*, 471–476. [CrossRef]
92. Spliethoff, J.W.; Evers, D.J.; Klomp, H.M.; van Sandick, J.W.; Wouters, M.W.; Nachabe, R.; Lucassen, G.W.; Hendriks, B.H.W.; Wesseling, J.; Ruers, T.J.M. Improved identification of peripheral lung tumors by using diffuse reflectance and fluorescence spectroscopy. *Lung Cancer* **2013**, *80*, 165–171. [CrossRef]
93. Evers, D.J.; Nachabe, R.; Hompes, D.; Van Coevorden, F.; Lucassen, G.W.; Hendriks, B.H.W.; van Velthuysen, M.-L.; Wesseling, J.; Ruers, T.J.M. Optical sensing for tumor detection in the liver. *Eur. J. Surg. Oncol.* **2013**, *39*, 68–75. [CrossRef]
94. Tanis, E.; Evers, D.J.; Spliethoff, J.W.; Pully, V.V.; Kuhlmann, K.; van Coevorden, F.; Hendriks, B.H.W.; Sanders, J.; Prevoo, W.; Ruers, T.J.M. In vivo tumor identification of colorectal liver metastases with diffuse reflectance and fluorescence spectroscopy. *Lasers Surg. Med.* **2016**, *48*, 820–827. [CrossRef]
95. Baltussen, E.J.M.; Snæbjörnsson, P.; De Koning, S.G.B.; Sterenborg, H.J.C.M.; Aalbers, A.G.J.; Kok, N.; Beets, G.L.; Hendriks, B.H.W.; Kuhlmann, K.F.D.; Ruers, T.J.M. Diffuse reflectance spectroscopy as a tool for real-time tissue assessment during colorectal cancer surgery. *J. Biomed. Opt.* **2017**, *22*, 106014. [CrossRef]
96. Baltussen, E.J.M.; Kok, E.N.D.; de Koning, S.G.B.; Sanders, J.; Aalbers, A.G.J.; Kok, N.F.M.; Beets, G.L.; Flohil, C.C.; Bruin, S.C.; Kuhlmann, K.F.D.; et al. Hyperspectral imaging for tissue classification, a way toward smart laparoscopic colorectal surgery. *J. Biomed. Opt.* **2019**, *24*, 16002. [CrossRef] [PubMed]
97. Baltussen, E.J.M.; de Koning, S.G.; Sanders, J.; Aalbers, A.G.J.; Kok, N.F.M.; Beets, G.L.; Hendriks, B.H.W.; Sterenborg, H.J.C.M.; Kuhlmann, K.F.D.; Ruers, T.J.M. Using Diffuse Reflectance Spectroscopy to Distinguish Tumor Tissue from Fibrosis in Rectal Cancer Patients as a Guide to Surgery. *Lasers Surg. Med.* **2019**, *52*, 604–611. [CrossRef] [PubMed]
98. Baltussen, E.J.M.; De Koning, S.G.B.; Sanders, J.; Aalbers, A.G.J.; Kok, N.F.M.; Beets, G.L.; Hendriks, B.H.W.; Sterenborg, H.J.C.M.; Kuhlmann, K.F.D.; Ruers, T.J.M. Tissue diagnosis during colorectal cancer surgery using optical sensing: An in vivo study. *J. Transl. Med.* **2019**, *17*, 333. [CrossRef] [PubMed]
99. Baltussen, E.J.M.; Sterenborg, H.J.C.M.; Ruers, T.J.M.; Dashtbozorg, B. Optimizing algorithm development for tissue classification in colorectal cancer based on diffuse reflectance spectra. *Biomed. Opt. Express* **2019**, *10*, 6096–6113. [CrossRef] [PubMed]
100. Langhout, G.C.; Spliethoff, J.W.; Schmitz, S.J.; Aalbers, A.G.J.; van Velthuysen, M.-L.; Hendriks, B.H.W.; Ruers, T.J.M.; Kuhlmann, K.F.D. Differentiation of healthy and malignant tissue in colon cancer patients using optical spectroscopy: A tool for image-guided surgery. *Lasers Surg. Med.* **2015**, *47*, 559–565. [CrossRef] [PubMed]
101. Langhout, G.C.; Spliethoff, J.W.; Aalbers, A.G.J.; Verwaal, V.J.; Hendriks, B.H.W.; Ruers, T.J.M.; Kuhlmann, K.F.D. Colorectal Cancer Identified Using Optical Spectroscopy. *Ann. Oncol.* **2014**, *25*, iv206. [CrossRef]
102. Kumashiro, R.; Konishi, K.; Chiba, T.; Akahoshi, T.; Nakamura, S.; Murata, M.; Tomikawa, M.; Matsumoto, T.; Maehara, Y.; Hashizume, M. Integrated endoscopic system based on optical imaging and hyperspectral data analysis for colorectal cancer detection. *Anticancer Res.* **2016**, *36*, 3925–3932.
103. Han, Z.; Zhang, A.; Wang, X.; Sun, Z.; Wang, M.D.; Xie, T. In vivo use of hyperspectral imaging to develop a noncontact endoscopic diagnosis support system for malignant colorectal tumors. *J. Biomed. Opt.* **2016**, *21*, 16001. [CrossRef]
104. Yuan, X.; Zhang, D.; Wang, C.; Dai, B.; Zhao, M.; Li, B. Hyperspectral Imaging and SPA–LDA Quantitative Analysis for Detection of Colon Cancer Tissue. *J. Appl. Spectrosc.* **2018**, *85*, 307–312. [CrossRef]
105. Ge, Z.; Schomacker, K.T.; Nishioka, N.S. Identification of colonic dysplasia and neoplasia by diffuse reflectance spectroscopy and pattern recognition techniques. *Appl. Spectrosc.* **1998**, *52*, 833–839. [CrossRef]
106. Rodriguez-Diaz, E.; Huang, Q.; Cerda, S.R.; O'Brien, M.J.; Bigio, I.J.; Singh, S.K. Endoscopic histological assessment of colonic polyps by using elastic scattering spectroscopy. *Gastrointest. Endosc.* **2015**, *81*, 539–547. [CrossRef] [PubMed]
107. Chen, H.; Lin, Z.; Wu, H.; Wang, L.; Wu, T.; Tan, C. Diagnosis of colorectal cancer by near-infrared optical fiber spectroscopy and random forest. *Spectrochim. Acta Part A Mol. Biomol. Spectrosc.* **2015**, *135*, 185–191. [CrossRef]
108. Chen, H.; Lin, Z.; Mo, L.; Tan, C. Identification of colorectal cancer using near-infrared spectroscopy and adaboost with decision stump. *Anal. Lett.* **2017**, *50*, 2608–2618. [CrossRef]
109. Chen, H.; Tan, C.; Wu, H.; Lin, Z.; Wu, T. Feasibility of rapid diagnosis of colorectal cancer by near-infrared spectroscopy and support vector machine. *Anal. Lett.* **2014**, *47*, 2580–2593. [CrossRef]
110. Ehlen, L.; Zabarylo, U.J.; Speichinger, F.; Bogomolov, A.; Belikova, V.; Bibikova, O.; Artyushenko, V.; Minet, O.; Beyer, K.; Kreis, M.E.; et al. Synergy of Fluorescence and Near-Infrared Spectroscopy in Detection of Colorectal Cancer. *J. Surg. Res.* **2019**, *242*, 349–356. [CrossRef]
111. Claridge, E.; Hidović-Rowe, D. Model based inversion for deriving maps of histological parameters characteristic of cancer from ex-vivo multispectral images of the colon. *IEEE Trans. Med. Imaging* **2013**, *33*, 822–835. [CrossRef]

112. Lee, L.C.; Liong, C.-Y.; Jemain, A.A. Partial least squares-discriminant analysis (PLS-DA) for classification of high-dimensional (HD) data: A review of contemporary practice strategies and knowledge gaps. *Analyst* **2018**, *143*, 3526–3539. [CrossRef] [PubMed]
113. Brereton, R.G.; Lloyd, G.R. Partial least squares discriminant analysis: Taking the magic away. *J. Chemom.* **2014**, *28*, 213–225. [CrossRef]
114. Gromski, P.S.; Muhamadali, H.; Ellis, D.I.; Xu, Y.; Correa, E.; Turner, M.L.; Goodacre, R. A tutorial review: Metabolomics and partial least squares-discriminant analysis–a marriage of convenience or a shotgun wedding. *Anal. Chim. Acta* **2015**, *879*, 10–23. [CrossRef]
115. ElMasry, G.; Nakauchi, S. Prediction of meat spectral patterns based on optical properties and concentrations of the major constituents. *Food Sci. Nutr.* **2016**, *4*, 269–283. [CrossRef]
116. Maruo, K.; Yamada, Y. Near-infrared noninvasive blood glucose prediction without using multivariate analyses: Introduction of imaginary spectra due to scattering change in the skin. *J. Biomed. Opt.* **2015**, *20*, 47003. [CrossRef] [PubMed]
117. Tromberg, B.J.; Shah, N.; Lanning, R.; Cerussi, A.; Espinoza, J.; Pham, T.; Svaasand, L.; Butler, J. Non-invasive in vivo characterization of breast tumors using photon migration spectroscopy. *Neoplasia* **2000**, *2*, 26–40. [CrossRef] [PubMed]
118. Wang, C.-Y.; Chen, C.-T.; Chiang, C.-P.; Young, S.-T.; Chow, S.-N.; Chiang, H.K. Partial least-squares discriminant analysis on autofluorescence spectra of oral carcinogenesis. *Appl. Spectrosc.* **1998**, *52*, 1190–1196. [CrossRef]
119. Nogueira, M.S.; Cosci, A.; Kurachi, C. Assessment of oxidative stress and metabolic rates in liver grafts using time-resolved fluorescence spectroscopy. In Proceedings of the Biophotonics: Photonic Solutions for Better Health Care VI, Strasbourg, France, 22–26 April 2018; Volume 10685. [CrossRef]
120. Nogueira, M.S.; Rosa, R.G.T.; Pratavieira, S.; D'almeida, C.D.P.; Kurachi, C. Assembly and characterization of a fluorescence lifetime spectroscopy system for skin lesions diagnostic. *Biophotonics S. Am.* **2015**, *9531*, 95313D. [CrossRef]
121. Almeida, C.D.P.D.; Campos, C.; Nogueira, M.S.; Kurachi, C. Time-resolved and steady-state fluorescence spectroscopy for the assessment of skin photoaging process. In Proceedings of the Biophotonics South America, Rio de Janeiro, Brazil, 23–25 May 2015; Volume 9531. [CrossRef]
122. Baker, M.J.; Byrne, H.J.; Chalmers, J.; Gardner, P.; Goodacre, R.; Henderson, A.; Kazarian, S.G.; Martin, F.L.; Moger, J.; Stone, N.; et al. Clinical applications of infrared and Raman spectroscopy: State of play and future challenges. *Analyst* **2018**, *143*, 1735–1757. [CrossRef] [PubMed]
123. Coelho, M.C.D.M.S.; Leal, L.B.; Nogueira, M.S.; Castro, P.A.; Peralta, F.; Zezell, D.M. Biochemical characterization of saliva of smoking and non-smoking patients by using Fourier-transform infrared spectroscopy. In Proceedings of the Biomedical Vibrational Spectroscopy 2022: Advances in Research and Industry, San Francisco, CA, USA, 22 January–28 February 2022; Volume 11957, p. 119570E. [CrossRef]
124. Pakiet, A.; Kobiela, J.; Stepnowski, P.; Sledzinski, T.; Mika, A. Changes in lipids composition and metabolism in colorectal cancer: A review. *Lipids Health Dis.* **2019**, *18*, 29. [CrossRef]
125. Bravo, J.J.; Paulsen, K.D.; Roberts, D.W.; Kanick, S.C. Sub-diffuse optical biomarkers characterize localized microstructure and function of cortex and malignant tumor. *Opt. Lett.* **2016**, *41*, 781–784. [CrossRef]
126. Kirkpatrick, N.D.; Brewer, M.A.; Utzinger, U. Endogenous optical biomarkers of ovarian cancer evaluated with multiphoton microscopy. *Cancer Epidemiol. Prev. Biomark.* **2007**, *16*, 2048–2057. [CrossRef]
127. Petrik, V.; Loosemore, A.; Howe, F.A.; Bell, B.A.; Papadopoulos, M.C. OMICS and brain tumour biomarkers. *Br. J. Neurosurg.* **2006**, *20*, 275–280. [CrossRef]
128. Georgakoudi, I.; Quinn, K.P. Optical imaging using endogenous contrast to assess metabolic state. *Annu. Rev. Biomed. Eng.* **2012**, *14*, 351–367. [CrossRef] [PubMed]
129. Slaby, O. Non-coding RNAs as biomarkers for colorectal cancer screening and early detection. In *Non-Coding RNAs in Colorectal Cancer*; Springer: Boston, MA USA, 2016; pp. 153–170.
130. Custodio, A.; Barriuso, J.; De Castro, J.; Martínez-Marín, V.; Moreno, V.; Rodríguez-Salas, N.; Feliu, J. Molecular markers to predict outcome to antiangiogenic therapies in colorectal cancer: Current evidence and future perspectives. *Cancer Treat. Rev.* **2013**, *39*, 908–924. [CrossRef] [PubMed]
131. Song, H.; Wang, L.; Liu, H.-L.; Wu, X.-B.; Wang, H.-S.; Liu, Z.-H.; Li, Y.; Diao, D.-C.; Chen, H.-L.; Peng, J.-S. Tissue metabolomic fingerprinting reveals metabolic disorders associated with human gastric cancer morbidity. *Oncol. Rep.* **2011**, *26*, 431–438. [PubMed]
132. Gadducci, A.; Guerrieri, M.E.; Greco, C. Tissue biomarkers as prognostic variables of cervical cancer. *Crit. Rev. Oncol. Hematol.* **2013**, *86*, 104–129. [CrossRef] [PubMed]
133. Beger, R.D. A review of applications of metabolomics in cancer. *Metabolites* **2013**, *3*, 552–574. [CrossRef] [PubMed]
134. Langhout, G.C.; Bydlon, T.M.; van der Voort, M.; Müller, M.; Kortsmit, J.; Lucassen, G.; Balthasar, A.J.R.; van Geffen, G.-J.; Steinfeldt, T.; Sterenborg, H.J.C.M.; et al. Nerve detection using optical spectroscopy, an evaluation in four different models: In human and swine, in-vivo, and post mortem. *Lasers Surg. Med.* **2018**, *50*, 253–261. [CrossRef]
135. Salomatina, E.; Yaroslavsky, A.N. Evaluation of the in vivo and ex vivo optical properties in a mouse ear model. *Phys. Med. Biol.* **2008**, *53*, 2797. [CrossRef]

Analyst

PAPER

View Article Online
View Journal | View Issue

Check for updates

Cite this: *Analyst*, 2024, **149**, 88

Diffuse reflectance spectroscopy for colorectal cancer surgical guidance: towards real-time tissue characterization and new biomarkers

Marcelo Saito Nogueira, *[a,b] Siddra Maryam, [a,b] Michael Amissah, [a,b] Shane Killeen, [c] Micheal O'Riordain [c] and Stefan Andersson-Engels [a,b]

Colorectal cancer (CRC) is the third most common and second most deadly type of cancer worldwide, representing 11.3% of the diagnosed cancer cases and resulting in 10.2% (0.88 million) of the cancer related deaths in 2020. CRCs are typically detected at the late stage, which leads to high mortality and morbidity. Mortality and poor prognosis are partially caused by cancer recurrence and postoperative complications. Patient survival could be increased by improving precision in surgical resection using accurate surgical guidance tools based on diffuse reflectance spectroscopy (DRS). DRS enables real-time tissue identification for potential cancer margin delineation through determination of the circumferential resection margin (CRM), while also supporting non-invasive and label-free approaches for laparoscopic surgery to avoid short-term complications of open surgery as suitable. In this study, we have estimated the scattering properties and chromophore concentrations based on 2949 DRS measurements of freshly excised *ex vivo* specimens of 47 patients, and used this estimation to classify normal colorectal wall (CW), fat and tumor tissues. DRS measurements were performed with fiber-optic probes of 630 μm source–detector distance (SDD; probe 1) and 2500 μm SDD (probe 2) to measure tissue layers ~0.5–1 mm and ~0.5–2 mm deep, respectively. By using the 5-fold cross-validation of machine learning models generated with the classification and regression tree (CART) algorithm, we achieved 95.9 ± 0.7% sensitivity, 98.9 ± 0.3% specificity, 90.2 ± 0.4% accuracy, and 95.5 ± 0.3% AUC for probe 1. Similarly, we achieved 96.9 ± 0.8% sensitivity, 98.9 ± 0.2% specificity, 94.0 ± 0.4% accuracy, and 96.7 ± 0.4% AUC for probe 2.

Received 16th February 2023,
Accepted 10th September 2023

DOI: 10.1039/d3an00261f

rsc.li/analyst

Open Access Article. Published on 05 October 2023. Downloaded on 5/1/2024 12:28:50 PM.
This article is licensed under a Creative Commons Attribution-NonCommercial 3.0 Unported Licence.

Introduction

Colorectal cancer (CRC) represented 11.3% of the diagnosed cancer cases and resulted in 10.2% (0.88 million) of the cancer related deaths in 2020.[1,2] High mortality and morbidity are caused by cancer recurrence, postoperative complications, and system complications typically associated with patients' health even prior to surgery.[3] The survival of patients tends to increase with complete resection enhanced by surgical guidance tools for real-time accurate intraoperative cancer margin delineation. In particular, tools for guidance of laparoscopic surgery (LS) could potentially reduce long-term surgical complications, as LS has already been shown to be an effective method to avoid short-term complications of open surgery (OS).[4] However, one of the main drawbacks of LS compared with OS is its impaired accuracy due to the lack of tactile feedback. This reduction could potentially improve long-term outcomes including metastasis, recurrence-free survival, disease recurrence, mortality, and overall survival.[4] Short-term outcomes already improved by LS include postoperative recovery parameters such as time-to-bowel function, time-to-food intake, time-to-mobilization and length of hospital stay and pain. Surgical parameters including size of surgical wound, positive tumor margin, blood loss, number of nodes removed, and duration of operation are also improved.[4] Surgical long-term outcomes can be improved by increasing the accuracy of circumferential resection margin (CRM) determination. Currently, surgical decisions rely on tissue structural information, while higher accuracies could potentially be obtained by using molecular-sensitive methods of tissue identification. Preference in developing such methods is given to automated methods for intraoperative real-time surgical guidance. In this context, surgeons can obtain real-time probability scores for tissue types probed. Next, surgeons can use these scores to take biopsies from the most suspected locations containing cancer cells after resection, and ensure complete resection of

[a]*Tyndall National Institute, Lee Maltings, Dyke Parade, Cork, T12 R5CP, Ireland. E-mail: marcelosaitonogueira@gmail.com, marcelo.nogueira@tyndall.ie*
[b]*Department of Physics, University College Cork, College Road, Cork, T12 K8AF, Ireland*
[c]*Department of Surgery, Mercy University Hospital, Cork, T12 WE28, Ireland*

This journal is © The Royal Society of Chemistry 2024

Open Access Article. Published on 05 October 2023. Downloaded on 5/1/2024 12:28:50 PM.
This article is licensed under a Creative Commons Attribution-NonCommercial 3.0 Unported Licence.

every patient. Some of the most promising real-time and molecular-sensitive tools are based on optical spectroscopy methods combined with machine learning models.[5] Our study uses diffuse reflectance spectroscopy (DRS).

DRS uses the diffuse reflected light travelling inside the tissue to extract tissue structural and biochemical information based on light scattering and absorption properties, respectively. Scattering properties include reduced scattering amplitude a', Mie scattering power b_{Mie}, and the percentage contribution of Rayleigh scattering f_{Ray} to the total Mie scattering in the tissue. These scattering properties can be associated with tissue microstructures including organelles (*e.g.*, mitochondria) and other structures (*e.g.*, cell and organelle membranes, collagen fibers and fibrils). Similarly, absorption properties consist of volume fractions of tissue chromophores (represented by $f_{chromophore}$) including β-carotene, bile (f_{bile}), bilirubin, ceroid, collagen, deoxyhemoglobin (f_{Hb}), oxyhemoglobin (f_{HbO_2}), methemoglobin (f_{metHb}), water (f_{water}), lipid (f_{lipid}), and melanin.[6,7]

Previous DRS and hyperspectral imaging studies on colorectal cancer detection focused on either endoscopic[8–15] or surgical[16–23] applications. Feasibility DRS studies have employed surgical guidance techniques based on machine learning (ML) approaches using either spectra collected from the outer surface of tissues through surface contact probes or spectra collected from interstitial tissues through needle-shaped probes.[16–23] However, previous studies have several limitations. First, these studies explored only small tissue volumes determined by small source-to-detector distances (SDDs) employed in the fiber-optic probes used. Second, the only study determining tissue chromophore concentrations and scattering properties[22] used analytical models based on the diffusion equation, which is known not to describe the reflectance at small SDDs well under the conditions in which DRS spectra were collected.[5,6,10,11,14,24] Third, DRS surgical guidance studies analyzed visible and near-infrared wavelengths ranging up to 1600 nm only. Finally, the number of measurements collected in DRS studies ranges from 117 to 1273 per dataset (*i.e.*, 117–1273 DRS measurements collected under the same conditions). Machine learning models considering thousands of wavelengths directly as predictors for validation in less than thousand measurements could lead to overfitting. Our study has overcome all of the above limitations.

In this study, we quantified tissue microstructural and biochemical parameters for potential clinical decision making in open surgery, laparoscopic surgery, and robotic surgery. Our study combined ML models with reflectance spectral fitting extraction of tissue chromophore concentrations and scattering properties from 2949 locations on fresh *ex vivo* tissue samples of 47 patients (1386 tissue locations with a 630 μm SDD probe and 1563 locations with a 2500 μm SDD probe). This extraction relied on a reflectance lookup table (LUT) built using MC simulations of light propagation in tissues[10,24] and covering a wide range of optical properties (absorption coefficient from 0.01 to 300 cm^{-1} and scattering coefficient varying from 0.1 to 1000 cm^{-1} with the anisotropy factor g = 0.9). To train these ML models, we used a classification and regression tree (CART) algorithm to estimate thresholds of scattering properties and chromophore concentrations to classify normal colorectal wall (CW), fat and tumor tissues. All DRS measurements were performed in the extended wavelength range between 350 and 1920 nm by using fiber-optic probes of 630 μm SDD (probe 1) and 2500 μm SDD (probe 2) to measure tissue layers ~0.5–1 mm and ~0.5–2 mm deep, respectively.[8]

Compared to our previous studies focusing on investigating the potential of DRS for colorectal tissue diagnostics,[8–10] this study is aimed at analyzing fat and CW tissues for LS and OS guidance applications instead of malignant and healthy surrounding tissues for endoscopic applications. With that in mind, please note that our study is novel based on the analysis of a different set of tissues for a completely different clinical application from those of our previous studies. We also emphasize that the analysis of this paper cannot be used to guide endoscopic microsurgery,[8–10] since tissues have been measured from outside the colon and/or rectum.

Materials and methods

Study protocol and clinical data collection

In our study, we included 47 patients undergoing bowel resection at the Mercy University Hospital, Cork, Ireland. All experiments were performed in accordance with the Guidelines approved by the Clinical Research Ethics Committee of University College Cork under approval numbers ECM 4 (n) 07/03/18 and ECM 3 (hhh) 18/06/19. Informed consent was obtained from human participants of this study. Table 1 shows the patient demographics of our study. In total, 47 tumors were investigated, among which 5 were in the pT1 stage, 7 were pT2, 26 were pT3 and 9 were pT4. In addition, local lymph node metastases were found in 28 out of 47 patients.[8–10]

We collected data from about 15 sites of freshly excised *ex vivo* CW tissues, 15 sites of fat tissues and 15 sites of tumor tissues on each colorectal specimen after surgical resection. To ensure sufficient representation of the tissue heterogeneity in our data collection, DRS measurements were performed over a typical area of 100 cm^2. The measurement protocol consisted of first removing the colorectal specimen from the patient and transporting it to a measurement bench for DRS measurements. Next, we gently rinsed the specimen with water and cleaned it to remove any residual stool and excess of blood. Before starting DRS measurements, we placed the specimen

Table 1 Patient demographics of our study

		Number of patients
Gender	Female	15
	Male	32
Age (years)	Mean (± standard deviation)	68 ± 11
	Range	40–89

Open Access Article. Published on 05 October 2023. Downloaded on 5/1/2024 12:28:50 PM.
This article is licensed under a Creative Commons Attribution-NonCommercial 3.0 Unported Licence.

on a measurement grid with the coordinates of the data collection locations. These locations were used to identify tissues based on demarcation by experienced surgeons and correlate tissue types with DRS spectra. On average, we took 40 minutes between specimen removal and the start of data collection, and about 1 hour after surgical resection for full data collection. We kept the tissue moist and preserved the physiological conditions to the best of our ability by putting a damp cloth on the specimen approximately every 7 measurements. Once we finished DRS data collection, we returned each specimen to the Pathology Department for processing and analysis according to standard protocols. The ground truth of our tissue types corresponding to our CRC DRS measurements was determined by histopathological analysis.

Diffuse reflectance spectroscopy (DRS) instrumentation

Our DRS system comprised a tungsten-halogen broadband light source with emission between 350 and 2400 nm (ref. 8) (HL-2000-HP, Ocean Optics, Edinburgh, United Kingdom), connected with fiber-optic probes of 630 μm SDD (probe 1) and 2500 μm SDD (probe 2) to send light from the source to the tissue and collect the tissue reflected light to be detected by two spectrometers. One spectrometer detected the reflected light intensity at the wavelength ranging between 350 and 1140 nm (QE-Pro, Ocean Optics, Edinburgh, United Kingdom) and another detected intensities in the wavelength range between 1090 and 1920 nm (NIR-Quest, Ocean Optics, Edinburgh, United Kingdom). We used the overlapping wavelengths between 1090 and 1140 nm to merge the two collected DRS spectra into one broadband (350–1920 nm) spectrum for each tissue site measured. More details of the instrumentation and data preprocessing are described elsewhere.[8] The depth probed by probes 1 and 2 (*i.e.*, ~0.5–1 mm and ~0.5–2 mm deep, respectively) was analyzed in detail in our earlier publications.[8] Briefly, the tissue depth was estimated by using forward Monte Carlo (MC) simulations of light transport in multi-layered tissues (MCML)[25] accelerated by a graphics processing unit (GPU).[26,27] We considered a wide range of optical properties[28,29] obtained from the analysis of our reflectance spectral fitting algorithm (described in detail elsewhere[10,24]) and in subsequent sections of this paper.

Optical data collection

We collected background and reference DRS spectra by placing each probe within a dark enclosed holder that avoided ambient light and backscattered light, and fixed the distance between our reflectance standard (FWS-99-01c, Avian Technologies LLC, New London, USA) and the fiber-optic probes. Background spectra were taken with our broadband light source turned off, while reference spectra were taken with the light source turned on, before tissue measurements. We avoided probe contamination by covering our probes with a polyvinyl chloride (PVC) film. In addition, we cleaned all probes with ethanol 70% after each set of data collection. In this study, we analyzed a total of 1386 spectra for probe 1 and 1563 for probe 2.

Data preprocessing

We obtained the tissue reflectance $R(\lambda)$ by subtracting the background ($I^{\text{Background}}$) of each spectrometer from tissue intensity measurements (I^{Tissue}). Next, the subtracted intensity was divided by the reference measurements $I^{\text{Reference}}$ taking into account its reflectivity:

$$R(\lambda) = \frac{1}{\text{Reference reflectivity}(\lambda)} \times \frac{I^{\text{Tissue}}(\lambda) - I^{\text{Background}}(\lambda)}{I^{\text{Reference}}(\lambda) - I^{\text{Background}}(\lambda)}. \quad (1)$$

To merge the reflectance spectra and correct for any slight reflectance mismatch between spectra collected from the two spectrometers, we used the overlapping spectral range between 1090 and 1140 nm to perform an interpolation by using the weighted sum of eqn (2):

$$R_{\text{experimental}}(\lambda) = \sum_{i=0}^{100} \frac{((100-i) \times R_{\text{vis}} + i \times R_{\text{NIR}})}{100}. \quad (2)$$

The resulting reflectance spectra $R_{\text{experimental}}(\lambda)$ were used for the estimation of chromophore concentrations and scattering parameters, as described in the next section.

Spectral fitting and extraction of biomolecule concentrations

The complete description of our reflectance spectral fitting algorithm can be found elsewhere.[10,24] Briefly, we used the obtained reflectance spectra $R_{\text{experimental}}(\lambda)$ to obtain the scattering properties α', b_{Mie}, and f_{Ray} and the tissue chromophore concentrations $f_{\text{chromophore}}$ of bile (f_{bile}), deoxyhemoglobin (f_{Hb}), oxyhemoglobin (f_{HbO_2}), methemoglobin (f_{metHb}), water (f_{water}), and lipid (f_{lipid}). Blood-related chromophore concentrations were used to calculate the tissue total hemoglobin percentage (THb), total hemoglobin concentration (THC), tissue blood oxygen saturation (StO_2) and the average blood vessel diameter R_{vessel} as indicated in the supplementary material of our previous publications.[10,24] THC was calculated by using the equation from Jacques,[29] which assumes the mass concentration within blood to be an average of 150 g L^{-1} and considers the molecular weight of 64 458 g mol^{-1}:

$$\text{THC}\left[\frac{\text{mol}}{\text{L}}\right] = \text{THb} \times \frac{150[\text{g L}^{-1}]}{64458[\text{g mol}^{-1}]}. \quad (3)$$

First, the spectral fitting used four types of input:

1. A measured reflectance spectrum $R_{\text{experimental}}(\lambda)$ to be fitted

2. The pure chromophore absorption spectra $\mu_{\text{a,chromophore}}(\lambda)$

3. Wavelength-dependence of tissue scattering $\mu'_{\text{s,tissue}}(\lambda)$ due to Rayleigh and Mie scattering (eqn (4))

4. A MC look-up table (LUT) of diffuse reflectance $R(\mu_a,\mu'_s)$ values generated with MC simulations

By associating the experimental reflectance of $R_{\text{experimental}}(\lambda)$ with a combination of ($\mu_{\text{a,tissue}}(\lambda)$, $\mu'_{\text{s,tissue}}(\lambda)$), we obtained $R_{\text{theoretical}}(\lambda)$ based on values of $R_{\text{MC}}(\mu_{\text{a,tissue}}, \mu'_{\text{s,tissue}})$ from the MC LUT. This association was only possible by using at least

This journal is © The Royal Society of Chemistry 2024

Open Access Article. Published on 05 October 2023. Downloaded on 5/1/2024 12:28:50 PM. This article is licensed under a Creative Commons Attribution-NonCommercial 3.0 Unported Licence.

as many wavelengths as fitting parameters and allowed the extraction of $f_{\text{chromophore}}$ by using the equation:

$$\mu_{\text{a,tissue}}(\lambda) = \sum_{\text{chromophore}} f_{\text{chromophore}} \times \mu_{\text{a,chromophore}}(\lambda), \quad (4)$$

where

$$\sum_{\text{chromophore}} f_{\text{chromophore}} = 1. \quad (5)$$

Similarly, the scattering properties α', b_{Mie}, and f_{Ray} were extracted by calculating the optimum $\mu'_{\text{s,tissue}}(\lambda)$

$$\mu'_{\text{s,tissue}}(\lambda) = \alpha' \times \left[(1 - f_{\text{Ray}})\left(\frac{\lambda}{\lambda_0}\right)^{-b_{\text{Mie}}} + f_{\text{Ray}}\left(\frac{\lambda}{\lambda_0}\right)^{-4}\right] \quad (6)$$

during the fitting procedure. Then, by iteratively estimating every $f_{\text{chromophore}}$ as well as α', b_{Mie}, and f_{Ray}, a combination of $\mu_{\text{a,tissue}}(\lambda)$ and $\mu'_{\text{s,tissue}}(\lambda)$ was used to calculate a theoretical reflectance spectrum $R_{\text{theoretical}}(\lambda)$ based on values of $R_{\text{MC}}(\mu_{\text{a,tissue}}, \mu'_{\text{s,tissue}})$ from the MC LUT. Finally, $R_{\text{theoretical}}(\lambda)$ was multiplied by a constant to make its scale comparable with that of $R_{\text{experimental}}(\lambda)$ and the difference $R_{\text{experimental}}(\lambda) - R_{\text{theoretical}}(\lambda)$ was minimized. In our study, there was no $-\log R_{\text{experimental}}(\lambda)$ transformation before fitting for the chromophore concentrations and scattering properties.

It is worth noting that the tissue may contain traces of bilirubin found in blood at ranges between 5.8 and 40% in humans (based on bilirubin blood serum levels that vary between 10 and 50 mg dL^{-1} (ref. 30) and the total hemoglobin blood levels that vary between 121 and 172 mg dL^{-1} (ref. 29)). We did not include bilirubin as a chromophore with a significant contribution in our spectral fitting so that there is no contamination between the estimation of f_{bile} and $f_{\text{bilirubin}}$. Furthermore, we emphasize that the use of the bilirubin absorption spectrum in our reflectance spectral fitting would narrow the wavelength range of our fitting, since the bilirubin absorption spectrum was not reported over the broadband wavelength range used in our DRS measurements. Similarly, met-hemoglobin (metHb) has been taken into account not to interfere with the quantification of other chromophores due to absorption spectrum overlap and potential metHb formation in *ex vivo* tissues.

Machine learning for tissue classification

We used the estimated tissue chromophore concentrations and scattering properties as predictors to classify normal colorectal wall (CW), fat and tumor tissues. This classification involved building a decision tree model based on thresholds of predictor values defined by the classification and regression tree (CART) algorithm.[10] We used 5-fold cross-validation to validate this model through its confusion matrix and evaluated classification performance metrics such as sensitivity, specificity, accuracy and area under the receiver operating characteristic curve (AUC). We also ensured that our tissue classification model was not overfitted by reporting the mean and standard deviation of the output of 20 iterations of 5-fold cross-validation with random sampling, as described in our previous publication.[10]

Finally, we removed StO_2 and f_{metHb} predictors with variations in *ex vivo* settings (and thus could not be translated to an *in vivo* setting from our study). Therefore, we considered only THb, R_{vessel}, f_{lipid}, f_{water}, f_{bile}, α', f_{Ray} and b_{Mie} as input predictors for tissue classification.

Statistical tests

Significant statistical differences between spectrally fitted parameters of CW, fat and tumor tissues were found by using one-way ANOVA with each fitted parameter. Every ANOVA test was performed with Tukey's honestly significant difference test (Tukey's HSD or Tukey–Kramer test) as the *post-hoc* test for pairwise comparison of means contributing to the overall significant difference. To evaluate the adequate use of one-way ANOVA, we assessed the normality of data distribution by using the Anderson–Darling normality test.

Results and discussion

Tissue scattering properties and chromophore concentrations

By using our reflectance spectral fitting method, we extracted relevant biochemical and microstructural parameters of tissues from superficial and deep tissue layers (~0.5–1 mm and ~0.5–2 mm deep, respectively). Fig. 1 and 2, and Table 2 show the THb, StO_2, R_{vessel}, f_{lipid}, f_{water}, f_{bile}, α', f_{Ray} and b_{Mie} from probe 1 (*i.e.*, the 630 μm source–detector distance probe) and probe 2 (2500 μm source–detector distance probe). As expected, fat tissues have higher f_{lipid} and StO_2, and lower f_{water} in data from both probes. Since our measurements have been performed in *ex vivo* tissues, it is expected that fat tissues have higher StO_2 since they have a lower metabolic rate compared to CW and tumor tissues and hence consume less O_2 which is now replenished at slower rates since the blood flow has stopped. When using the small SDD probe, fat contained higher f_{bile}, and exhibited larger R_{vessel} and lower b_{Mie} compared with CW and tumor tissues. When using probe 2, fat had slightly higher $\alpha'$and lower b_{Mie} compared to normal colorectal wall (CW) and tumor tissues and exhibited smaller R_{vessel} compared to tumor tissues. Based on the findings of both probes, bile and large diameter blood vessels were only found in superficial fat tissues, whereas particle sizes tend to be larger throughout fat tissues up to 2 mm deep.

When comparing CW and tumor tissues, tumor has higher R_{vessel}, α', and b_{Mie}, as well as slightly higher f_{water} and f_{bile}, and slightly lower f_{lipid}. These results are valid for both probes, being more pronounced for probe 2 (2500 μm SDD probe). In particular, for probe 2, one can see that THb is slightly higher and the difference between StO_2 of CW and tumor tissues is smaller compared to that in probe 1 (630 μm SDD probe). While this result may not be translated into *in vivo* colorectal tissues due to the study limitations described in subsequent sections,[8] our results suggest that superficial tissue probed with probe 1 might be more sensitive to tissue metabolic rates once blood flow has been ceased. The higher difference in StO_2 of *ex vivo* superficial tissues of the CW and tumor can be explained by the tumor higher metabolic rates leading to

Open Access Article. Published on 05 October 2023. Downloaded on 5/1/2024 12:28:50 PM.
This article is licensed under a Creative Commons Attribution-NonCommercial 3.0 Unported Licence.

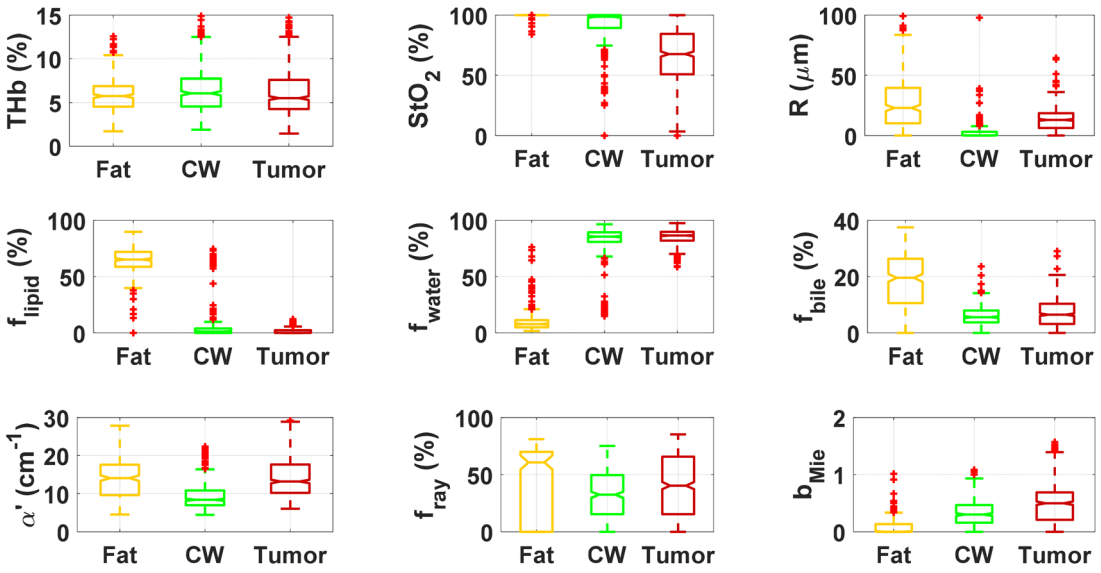


Fig. 1 Boxplots of relevant parameters for differentiation between superficial tissue layers of fat, normal colorectal wall (CW) and tumor tissues using the 630 μm source–detector distance probe (probe 1). Red points represent outliers (points at more than 1.5 times the interquartile range away from the bottom or top of the box).

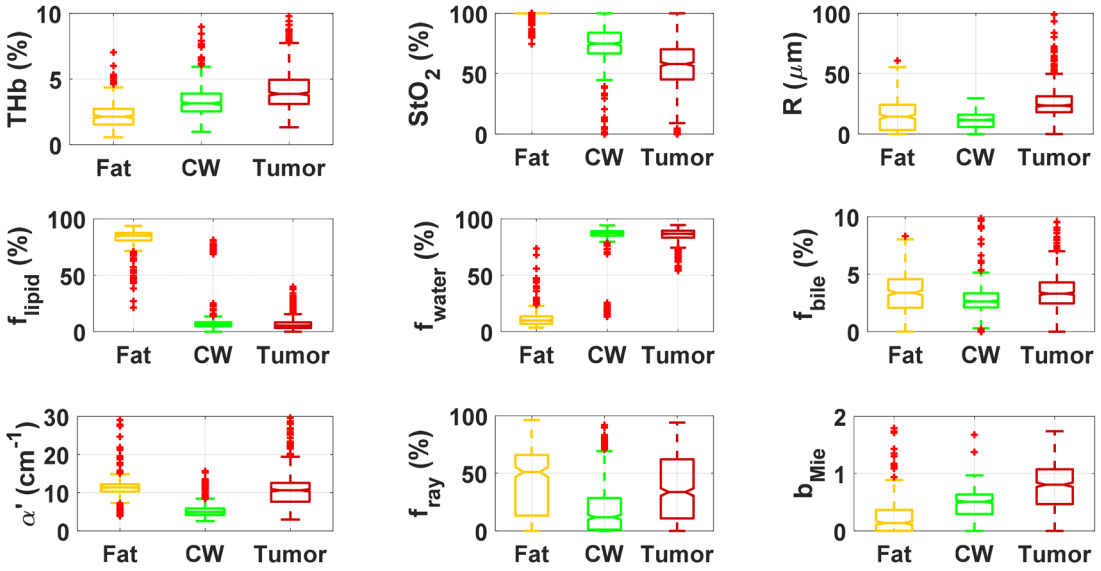


Fig. 2 Boxplots of relevant parameters for differentiation between deeper tissue layers of fat, normal colorectal wall (CW) and tumor tissues using the 2500 μm source–detector distance probe (probe 2). Red points represent outliers (points at more than 1.5 times the interquartile range away from the bottom or top of the box).

higher blood oxygen consumption, and the rates of replenishment of this oxygen through Hb exposure to atmospheric molecular oxygen forming HbO_2 are significantly smaller than the blood oxygen consumption rates in tumors. On the other hand, rates of this replenishment seem to be comparable with blood oxygen consumption rates in the CW. Still, one should note that both blood oxygen consumption rates and oxygen replenishment rates change over time, as tissue cells die and Hb is converted to met-Hb which cannot bind to O_2 molecules in its protein structure.

We found statistically significant differences between groups with one-way ANOVA $p < 0.05$ for all fitted parameters (Tables 3 and 4, column "All groups"). Pairwise comparison between groups did not show statistically significant differences ($p < 0.05$) between CW and tumor tissues by using the THb or THC of probe 1, between fat and tumor tissues by using R, f_{metHb}, α' of probe 2, and between CW and tumor tissues by using the f_{metHb} of probe 2. All other parameters indicated statistically significant differences with $p < 0.05$ for pairwise comparisons of Tukey's HSD.

This journal is © The Royal Society of Chemistry 2024

Open Access Article. Published on 05 October 2023. Downloaded on 5/1/2024 12:28:50 PM.
This article is licensed under a Creative Commons Attribution-NonCommercial 3.0 Unported Licence.

Table 2 Biochemical and microstructural parameters of fat, normal colorectal wall (CW) and tumor tissues investigated with the small source–detector distance probe (superficial tissue) and the large source–detector distance probe (deeper tissue layers)

	Small SDD probe (probe 1)			Large SDD probe (probe 2)		
Biochemical/microstructural parameters	Fat	Colorectal wall (CW)	Tumor	Fat	Colorectal wall (CW)	Tumor
THb (%)	5.9 ± 2.0	6.5 ± 3.0	6.6 ± 3.9	2.3 ± 1.0	3.3 ± 1.3	4.8 ± 1.9
THC (μmol L^{-1})	136.6 ± 46.0	151.8 ± 69.1	154 ± 90	52.6 ± 22.3	77.7 ± 30.7	111 ± 45
StO_2 (%)	99.8 ± 1.5	92.4 ± 13.7	66 ± 23	98.8 ± 3.7	73.3 ± 16.7	56 ± 18
R (μm)	29.8 ± 29.7	3.8 ± 14.8	14 ± 11	20.9 ± 75.7	11.3 ± 6.9	24 ± 13
f_{lipid} (%)	64.9 ± 11.6	5.5 ± 14.0	1.4 ± 2.2	82.3 ± 9.5	10.6 ± 16.3	4.8 ± 3.0
f_{water} (%)	10.4 ± 10.2	81.9 ± 15.4	84.9 ± 7.2	12.1 ± 9.0	83.1 ± 16.5	86.7 ± 4.0
f_{bile} (%)	18.8 ± 9.2	6.1 ± 3.5	7.0 ± 4.8	3.3 ± 2.0	2.9 ± 1.5	3.7 ± 2.5
f_{MetHb} (%)	1.4 ± 0.8	0.9 ± 0.6	1.1 ± 0.7	0.4 ± 0.2	0.3 ± 0.2	0.3 ± 0.5
α' (cm^{-1})	14.2 ± 6.6	9.5 ± 3.7	15.9 ± 10.1	12.9 ± 12.2	5.7 ± 3.4	12.0 ± 5.6
b_{Mie}	0.1 ± 0.1	0.3 ± 0.2	0.5 ± 0.3	0.2 ± 0.4	0.5 ± 0.3	0.9 ± 0.4
f_{Ray} (%)	45.5 ± 30.2	32.0 ± 21.1	40 ± 27	42.5 ± 26.9	18.9 ± 21.3	36 ± 28

Table 3 *P*-Values of the one-way ANOVA test and *post-hoc* test for each spectrally fitted parameter using probe 1 (630 μm-SDD probe)

			Pairwise (*post-hoc* test)		
One-way ANOVA		All groups	1 2	1 3	2 3
p-Value	THb (%)	0.002	0.018	0.002	0.843
	THC (μM)	0.002	0.018	0.002	0.843
	StO_2 (%)	<0.001	<0.001	<0.001	<0.001
	R (μm)	<0.001	<0.001	<0.001	<0.001
	f_{lipid} (%)	<0.001	<0.001	<0.001	<0.001
	f_{water} (%)	<0.001	<0.001	<0.001	<0.001
	f_{bile} (%)	<0.001	<0.001	<0.001	0.038
	f_{MetHb} (%)	<0.001	<0.001	<0.001	<0.001
	α' (cm^{-1})	<0.001	<0.001	0.007	<0.001
	b_{Mie}	<0.001	<0.001	<0.001	<0.001
	f_{Ray} (%)	<0.001	<0.001	0.004	<0.001

The *post-hoc* test used was the Tukey's honestly significant difference test (Tukey's HSD or Tukey–Kramer test). A statistically significant difference for $p < 0.001$ is represented in green color and a statistically significant difference for $0.001 < p < 0.05$ was represented in yellow color. Values not showing a statistically significant difference are displayed in red color.

Table 4 *P*-Values of one-way ANOVA test and *post-hoc* test for each spectrally fitted parameter using probe 2 (2500 μm-SDD probe)

			Pairwise (*post-hoc* test)		
One-way ANOVA		All groups	1 2	1 3	2 3
p-Value	THb (%)	<0.001	<0.001	<0.001	<0.001
	THC (μM)	<0.001	<0.001	<0.001	<0.001
	StO_2 (%)	<0.001	<0.001	<0.001	<0.001
	R (μm)	<0.001	<0.001	0.310	<0.001
	f_{lipid} (%)	<0.001	<0.001	<0.001	<0.001
	f_{water} (%)	<0.001	<0.001	<0.001	<0.001
	f_{bile} (%)	<0.001	0.010	0.007	<0.001
	f_{MetHb} (%)	0.017	0.018	0.539	0.094
	α' (cm^{-1})	<0.001	<0.001	0.184	<0.001
	b_{Mie}	<0.001	<0.001	<0.001	<0.001
	f_{Ray} (%)	<0.001	<0.001	<0.001	<0.001

The *post-hoc* test used was the Tukey's honestly significant difference test (Tukey's HSD or Tukey–Kramer test). Statistically significant difference for $p < 0.001$ is represented in green color and statistically significant difference for $0.001 < p < 0.05$ is represented in yellow color. Values not showing statistically significant difference are displayed in red color.

Tables 3 and 4 show the *p*-values corresponding to the one-way ANOVA test and *post-hoc* tests for all parameters listed in Table 2. These differences should be reliable for all parameters and tissue types, since all data distributions were considered normal by using the Anderson–Darling test (required for the reliability of the ANOVA test). It is worth noting that the choice of parameters for the most accurate tissue classification depends on the combination of parameters instead of the evaluation of each individual spectrally fitted parameter. With that in mind, such accuracy was evaluated by the CART analysis shown in the next section.

Tissue classification using decision trees

We built decision trees based on spectral fitting parameters of probes 1 and 2 in order to evaluate the accuracy of tissue identification in colorectal surgical applications and categorize tumors based on their particular ranges of chromophore concentrations and scattering properties.[10] Based on the categories of tumor, fat and normal colorectal wall (CW) tissues, Table 5 shows the percentage of classified observations (samples) normalized by the total number of observations (true class) for each tissue type. Our results suggest that probe 2 can be used for more accurate tissue classification compared to probe 1. This result is valid for DRS measurements with a reasonable signal-to-noise ratio (SNR), and one should consider that miniaturized DRS instruments may have a less SNR due to less powerful light sources and/or less costly detectors.

A lower SNR may lead to a higher decrease in the accuracy for probe 2 measurements than that for probe 1 measurements because the amplitude of the reflected intensity is lower for probe 2. Therefore, to reproduce the results of this study, The SNR should be as high as possible to the current state-of-the-art DRS instruments and investigation should be conducted to confirm whether our results are translatable for *in vivo* colorectal tissues.

Open Access Article. Published on 05 October 2023. Downloaded on 5/1/2024 12:28:50 PM.
This article is licensed under a Creative Commons Attribution-NonCommercial 3.0 Unported Licence.

Table 5 Confusion matrices for the differentiation of fat, normal colorectal wall (CW) and tumor tissues for laparoscopic applications using the small SDD probe (630 μm-SDD probe), the large SDD probe (2500 μm-SDD probe) and CART classification with the spectral fitting parameters THb, R_{vessel}, f_{lipid}, f_{water}, f_{bile}, α', f_{Ray} and b_{Mie} and b_{Mie} chosen as relevant parameters for *ex vivo* tissue classification

	Predicted class							
	Small SDD probe (probe 1)				Large SDD probe (probe 2)			
% of classified observations/ number of observations		Fat	Colorectal wall (CW)	Tumor		Fat	Colorectal wall (CW)	Tumor
True class	Fat (n = 318)	96.3 ± 0.9	3.7 ± 0.9	0.1 ± 0.3	Fat (n = 348)	96.3 ± 0.5	3.4 ± 0.5	0.4 ± 0.3
	CW (n = 434)	2.6 ± 0.5	86.2 ± 1.4	11.2 ± 1.3	CW (n = 493)	1.9 ± 0.6	92.7 ± 1.1	5.4 ± 1.0
	Tumor (n = 635)	0.3 ± 0.2	9.9 ± 0.6	89.8 ± 0.6	Tumor (n = 722)	0.3 ± 0.0	5.9 ± 0.5	93.8 ± 0.5

The SNR varies dramatically over the wide wavelength range between 350 nm and 1900 nm. For probe 1, the highest signal of a typical recorded spectrum is 1000 times stronger than the lowest signal, and the lowest signal is typically 10 times above the noise floor. Therefore, the dynamic range of the recorded spectra is 10 000 : 1. For probe 2, the highest signal is 100 times stronger than the lowest signal, and the lowest signal is typically twice above the noise floor for water-rich tissues (such as the CW and tumor), leading to a total dynamic range of 200 : 1. The given dynamic range and noise of our measurements gave rise to the variations in the fitting parameters reported in Table 2. It is worth noting that the poor SNR in probe 2 occurs only between 1400 nm and 1600 nm of the fitted wavelength range, and that the spectral fitting algorithm may tend to consider fitting for the water concentration based on the wavelength range between 900 nm and 1300 nm for water-rich tissues, as the signal at the water absorption peaks is typically 50–100 times above the noise floor.

Based on our experience on studies in colorectal tissues, we recommend having a bare minimum of 10 times higher reflectance signal compared to the noise (*i.e.*, approximately 13 dB in the power ratio) for analyzing wavelengths below 1400 nm. Further scientific evidence is needed for the calculation of minimum SNR requirements and the impact of the SNR on the performance of the spectral fitting algorithm (SFA). Such evidence requires meticulous calculation that is out of the scope of our study. The calculation of minimum SNR requirements depends on factors including the combination of (1) the spectral shape difference due to the contribution of tissue chromophores at a given fitted wavelength range, (2) the amplitude of the reflectance signal at such a range, and (3) the homogeneity of optical properties over the tissue depth probed with light at each wavelength.

Our SFA will be more accurate when the sharper and more specific chromophore spectral features are at the selected wavelength range. Accuracy is also enhanced when the more homogeneous tissue layers are in terms of optical properties at the probed depth defined by the probe geometry (*e.g.*, source–detector distance) and light wavelength used. If tissue is sufficiently homogeneous and has spectral features that can distinguish the contribution of each chromophore *via* spectral shape, the SNR helps to improve accuracy by facilitating the identification of chromophore spectral features. Future studies will explore the impact of the SNR on the performance of our SFA.

Fig. 3 and 4 show the two separate branches of a decision tree with parameters leading to the most accurate classification between fat (n = 318), CW (n = 434) and tumor (n = 634) tissues by using probe 1. These parameters were THb, R_{vessel}, f_{lipid}, α', and b_{Mie}. By using the 5-fold cross-validation, we

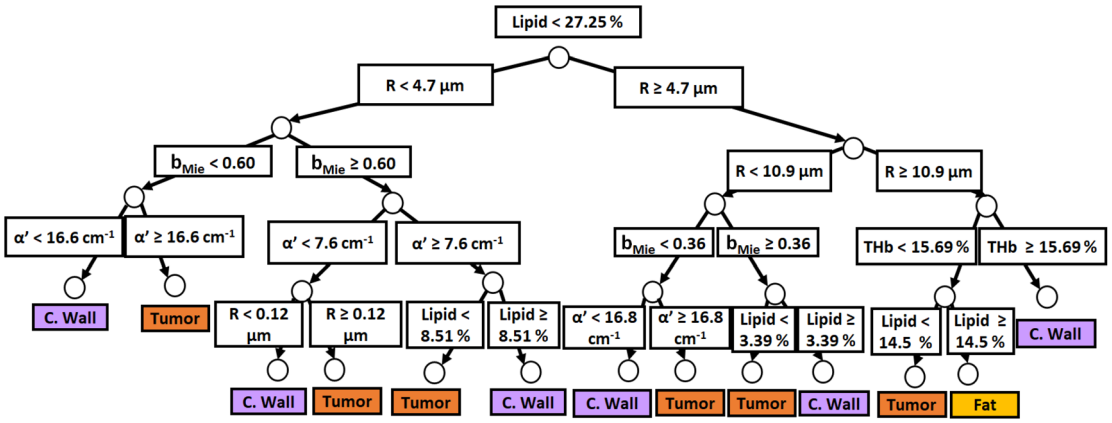


Fig. 3 Classification decision tree of fat, colorectal wall and tumor tissues based on parameter threshold values of probe 1 (630 μm-SDD probe) for f_{lipid} < 27.25%.

This journal is © The Royal Society of Chemistry 2024

Open Access Article. Published on 05 October 2023. Downloaded on 5/1/2024 12:28:50 PM.
This article is licensed under a Creative Commons Attribution-NonCommercial 3.0 Unported Licence.

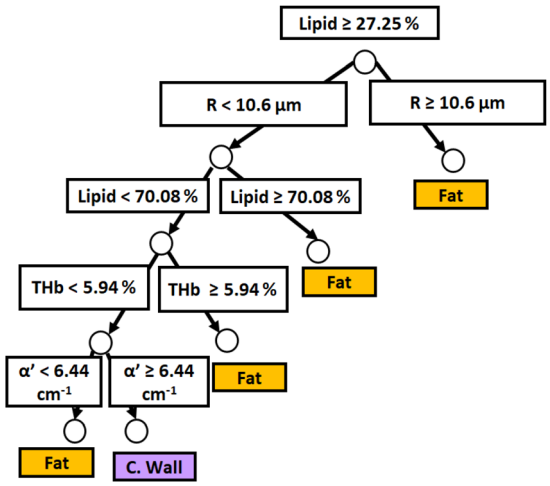


Fig. 4 Classification decision tree of fat, colorectal wall and tumor tissues based on parameter threshold values of probe 1 (600 μm-SDD probe) for $f_{lipid} \geq 27.25\%$.

achieved 95.9 ± 0.7% sensitivity, 98.9 ± 0.3% specificity, 90.2 ± 0.4% accuracy, and 95.5 ± 0.3% AUC. Also, it is important to remember that parameters appearing close to the top of the decision trees (Fig. 3–6) are the most important for tissue classification. With this in mind, the parameters appearing at the top two layers of splits for probe 1 (Fig. 3 and 4), *i.e.*, f_{lipid}, R_{vessel}, and b_{Mie} can be important parameters for laparoscopic CRC detection when using the 630 μm-SDD probe.

Similar to probe 1, Fig. 5 and 6 show that the two separate branches of a decision tree with parameters leading to the most accurate classification between fat (n = 348), CW (n = 493) and tumor (n = 722) tissues by using probe 2. These parameters were THb, R_{vessel}, f_{lipid}, f_{bile}, α', and b_{Mie}. By using 5-fold cross-validation, we achieved 96.9 ± 0.8% sensitivity, 98.9 ± 0.2% specificity, 94.0 ± 0.4% accuracy, and 96.7 ± 0.4% AUC. The parameters which appear on the top two layers of splits from probe 2 (f_{lipid}, R_{vessel}, α', and b_{Mie}) were similar to those from probe 1. Since THb does not appear on the two layers of splits for neither probe, THb may not be an important parameter for classification of fat, CW and tumor tissues. Still, f_{lipid}, R_{vessel}, and b_{Mie} appear as important parameters for both probes and may be explored in future studies for laparoscopic CRC detection. These findings need to be confirmed by *in vivo* tissue measurements to overcome the limitations of data collection of *ex vivo* tissues.

Relevance of our work

Compared to previous studies with the intention to guide CRC resections, we have (1) extended the wavelength range of the collected DRS spectra to 350–1920 nm, (2) unveiled the tissue biochemistry and microstructure of superficial and deeper tissue layers (~0.5–1 mm and ~0.5–2 mm deep, respectively) with a real-time and non-invasive method, (3) collected more DRS measurements per dataset (2949 DRS spectra in total, 1386 with probe 1 and 1563 with probe 2) and (4) extracted tissue scattering properties and chromophore concentrations using probabilistic Monte Carlo models not restricted by the limitations of the diffusion theory used in previous studies.

In a practical perspective, our study is the first step to overcome the limitations of prior DRS research on surgical CRC detection. By incorporating DRS into a flexible fiber-optic probe that can be either passed down a laparoscope working channel, or used with robotic surgery instruments, DRS surgical guidance can potentially increase the accuracy of surgical procedures, improve rates of complete resection and thereby decrease colorectal cancer (CRC) recurrence and mortality. If a side-firing fiber-optic probe[31] can be directly integrated into the fingertip of a surgeon, open surgery could also be made more accurate.

In a research perspective, our work identified CRC categories based on the thresholds of biomarkers that may be associated with CRC recurrence and/or with patient prognosis. Prediction of treatment outcomes can potentially be achieved by future *in vivo* studies correlating surgical outcomes with

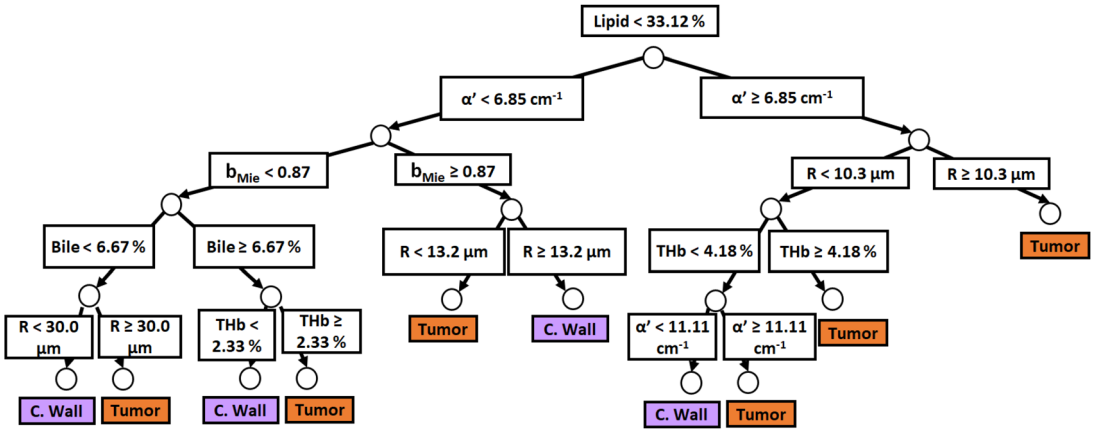


Fig. 5 Classification decision tree of fat, colorectal wall and tumor tissues based on parameter threshold values of probe 2 (2500 μm-SDD probe) for $f_{lipid} < 33.12\%$.

Open Access Article. Published on 05 October 2023. Downloaded on 5/1/2024 12:28:50 PM.
This article is licensed under a Creative Commons Attribution-NonCommercial 3.0 Unported Licence.

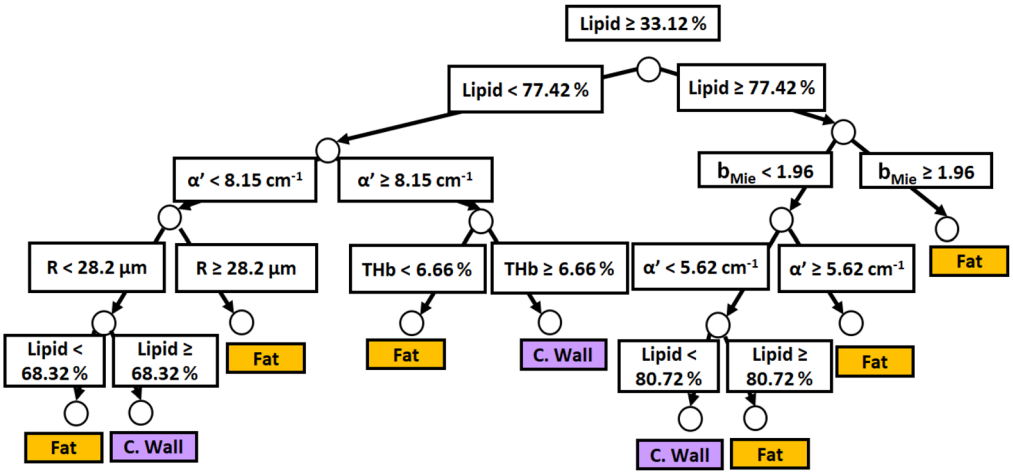


Fig. 6 Classification decision tree of fat, colorectal wall and tumor tissues based on parameter threshold values of probe 2 (2500 μm-SDD probe) for $f_{lipid} \geq 33.12\%$.

CRC categories based on chromophore concentrations and scattering properties.

It is important to note that our approach combining spectral fitting with machine learning has a different purpose compared with approaches using only machine learning methods to identify colorectal cancer directly from reflectance spectral data. Our spectral fitting provides interpretable parameters with biological relevance while enabling tissue classification and future patient stratification based on parameters that can potentially be associated with other biochemical analysis of laboratory samples. Previous approaches using only machine learning methods used *k*-nearest neighbors (kNNs), support vector machines (SVMs), artificial neural networks, decision trees, and linear discriminant analysis (LDA) as methods to identify colorectal cancer in real-time without biologically/biochemically interpretable parameters.[21] Future studies will include work on complementary approaches to ours including feature selection by excluding uncorrelated variables through ensembles of random forest classifiers (*i.e.*, importance testing) and/or the maximum relevance minimum redundancy (MRMR).[32]

Validity and limitations of our study

Due to variations present in contact measurements and *ex vivo* tissues, our study has several limitations. First, the measured CRC locations were demarcated based on the palpation and naked eye feedback by experienced surgeons prior to confirmation with histopathology results. It is worth noting that this demarcation does not decrease the validity of our dataset and structural/biochemical analysis, as our dataset is sufficiently large to incorporate tissue spectral variations at larger areas (~100 cm^2) and within several time periods after surgery (which results in variation of tissue dehydration, blood concentration and blood oxygenation). In addition, we attempted to avoid dehydration by keeping tissue moist with damp cloth at every 7 DRS measurements.

Our *ex vivo* measurements also could not control blood oxygenation, which could potentially be modeled by using data such as time after specimen excision, pH, and pCO_2, among others in future studies. Still, in a pilot *ex vivo* observation of the DRS signal in 3 patients, we observed no significant variations in the average Hb and HbO_2 of CRC tissues at 7 locations during the first 15 minutes of our measurements (data not shown).[8–10] We are aware that, according to Baltussen *et al.*[33] f_{water} may decrease, and THb and StO_2 may increase in *ex vivo* tissues compared to *in vivo* tissues within 1 hour after resection. Still, StO_2 trends are controversial, since Salomatina *et al.*[34] reported decreased StO_2 in mouse ear tissues between 5 and 10 minutes after excision (*ex vivo*) of tissue and after 24 and 72 hours of storage. It is important to note that variations in THb, StO_2 and f_{water} did not affect the results of our study because these parameters were not used to classify tissues.

We did not include non-cancer pathology in our study. Future inclusion of non-cancer pathologies such as inflammatory bowel disease, radiation-induced fibrosis, and scarring following local excision of cancers may change the classification performance of our CART model and categories of CRC to be considered on long-term follow up studies. It is worth noting that the lack of non-cancer pathology does not affect our tissue biochemical/structural parameters. Our analysis is valid and robust, considering that our dataset includes intra- and inter-patient variations (1386 + 1563 spectra of 47 patients) of both superficial and deeper tissue layers.

Also, our spectral fitting assumes homogeneous media to extract the average tissue chromophore concentrations and scattering properties. Inaccuracies may arise if the heterogeneity on the optical properties deviates significantly from the average properties estimated by assuming that tissue is homogeneous. These inaccuracies are only significant if the heterogeneity over tissue layers probed at each wavelength λ changes the spectral shape of $R_{experimental}(\lambda)$ at wavelength ranges perti-

 This journal is © The Royal Society of Chemistry 2024

Open Access Article. Published on 05 October 2023. Downloaded on 5/1/2024 12:28:50 PM.
This article is licensed under a Creative Commons Attribution-NonCommercial 3.0 Unported Licence.

nent to distinguish the contribution of different chromophores (*e.g.*, heterogeneity at tissue probed between 520 nm and 560 nm when fitting primarily for Hb and HbO_2). However, our results suggest that overfitting is not an issue in our study because uncertainties of fitted parameters are much smaller than uncertainties due to tissue heterogeneity.

For homogeneous medium simulating tissue optical properties, the typical coefficient of variation (COV, *i.e.*, the ratio of the standard deviation to the mean) of each fitted parameter is about 1–10% of the true value of each parameter, except for b_{Mie}, which has typical standard deviations around 10–30% for tissue optical properties. When comparing COV in homogeneous media with COV values taken from Table 2, we can see that the average COV over all tissue types varies between 18% and 174%. The only parameters with a lower COV are StO_2 (COV ranging from 2% and 35% with a mean of 18% over all tissue types) and water (COV ranging from 5% and 98% with a mean of 37% over all tissue types).

Further evidence indicating that fitted parameters may not be overfitted is that trends on lower COV values occur in the same tissue type, even when measured with different probes and using a different Monte Carlo Look-up Table for spectral fitting. We observed lower COV values only for StO_2(%) in fat tissues and f_{water} (%) in tumor tissues, independent of the probe (or source–detector distance; SDD) used. Consistently lower COV values for independent spectral fitting procedures and probes suggest there was no overfitting even when COV values were approximately the minimum expected from the spectral fitting algorithm (SFA). Therefore, the uncertainty in the fitted parameters as evaluated by their COV should not affect our tissue classification.

In addition, StO_2(%) and f_{water} (%) were not included in the list of the most important parameters for tissue classification and thus did not influence such a classification. This non-inclusion suggests that the tissue classification already excluded the contribution of fitted parameters with uncertainty comparable to the minimum expected from the SFA (*i.e.*, parameters with potentially most of their uncertainties coming from the SFA instead of the tissue heterogeneity). Hence, only fitted parameters with uncertainty dictated primarily by tissue heterogeneity were considered as the most important parameters. With that in mind, our results suggest that the uncertainty on the fitted parameters did not influence our tissue classification.

Finally, previous studies have shown that reflectance measurements can accurately estimate optical properties based on the fitted parameters.[35,36] A detailed study on the uncertainty on fitted parameters upon variations in reflectance is not within the scope of our study.

Conclusions

In this study, we evaluated the most important structural and biochemical parameters for surgical CRC delineation through broadband diffuse reflectance spectroscopy (DRS), as well as the categories of CW, fat and tumor tissues based on thresholds of these parameters. These parameters were f_{lipid}, R_{vessel}, α', and b_{Mie}, since they appeared on the top of both decision trees of probe 1 and probe 2. Differences between probe 1 (for superficial tissues 0.5–1 mm deep) and probe 2 (for deeper tissue layers 0.5–2 mm deep) mainly rely on α' being more important than R_{vessel} for tissue classification using probe 2. We have shown that classification performance metrics for tissue identification can be as high as 95.9 ± 0.7% sensitivity, 98.9 ± 0.3% specificity, 90.2 ± 0.4% accuracy, and 95.5 ± 0.3% AUC for probe 1, and 96.9 ± 0.8% sensitivity, 98.9 ± 0.2% specificity, 94.0 ± 0.4% accuracy, and 96.7 ± 0.4% AUC for probe 2. Future studies should validate these metrics for *in vivo* DRS and/or hyperspectral imaging during laparoscopy, open surgery and robotic surgery. Benefits of laparoscopic surgery and robotic surgery include real-time and accurate tissue identification when tactile feedback is not available to surgeons. Another benefit is the precise localization of cancer to obviate the need for multiple biopsies and accurately delineate cancer margins through personalized determination of the circumferential resection margin (CRM). The latter benefit also extends to open surgery.

Author contributions

M. S. N.: conceptualization, methodology, software, validation, formal analysis, investigation, resources, data curation, writing – original draft, writing – review & editing, visualization, supervision, project administration; S. M.: investigation; M. A.: investigation; S. K.: investigation, resources, data curation; M. O. R.: conceptualization, methodology, investigation, resources, writing – review & editing, supervision, project administration, funding acquisition; S. A. E.: conceptualization, methodology, resources, software, investigation, writing – original draft, writing – review & editing, supervision, project administration, funding acquisition.

Conflicts of interest

There are no conflicts to declare.

Acknowledgements

We acknowledge Eduardo Moriyama for the advice and logistics of the project associated with this manuscript, Shree Krishnamoorthy for the discussions on the same project, Huihui Lu for the help with clinical research ethics documentation, Haiyang Li for the design and assembly of the holder of the DRS system, Noel Lynch and Andrew McGuire for the specimen retrieval of patients of this study and all the logistics related to it, and Vivienne Curran, Aoife Foyle, Una McAuliffe, Evelyn Flanagan, Shauni Fitzgerald, and Edmund Manning for all the logistics of clinical procedures, research ethics documents, and search for patient information. Shauni Fitzgerald

Open Access Article. Published on 05 October 2023. Downloaded on 5/1/2024 12:28:50 PM. This article is licensed under a Creative Commons Attribution-NonCommercial 3.0 Unported Licence.

and Edmund Manning were funded by the Mercy Hospital Foundation. This study received financial support from the Science Foundation Ireland (SFI): grant ID SFI/15/RP/2828.

References

1 F. Bray, J. Ferlay, I. Soerjomataram, R. L. Siegel, L. A. Torre and A. Jemal, *Ca-Cancer J. Clin.*, 2018, **68**, 394–424.
2 J. Ferlay, M. Ervik, F. Lam, M. Colombet, L. Mery, M. Piñeros, A. Znaor, I. Soerjomataram and F. Bray, *Global cancer observatory: cancer today*, international agency for research on cancer, Lyon, France, 2018.
3 H. Pak, L. H. Maghsoudi, A. Soltanian and F. Gholami, *Ann. Med. Surg.*, 2020, **55**, 13–18.
4 M. M. Reza, J. A. Blasco, E. Andradas, R. Cantero and J. Mayol, *Br. J. Surg.*, 2006, **93**, 921–928.
5 M. S. Nogueira, R. Matthews, S. Killeen, M. O'Riordain and S. Andersson-Engels, *Colorectal cancer detection based on the extraction of scattering properties and biochemical concentrations from fluorescence spectroscopy measurements*, Clinical and Translational Biophotonics, Optica Publishing Group, 2022, p. TS2B–5.
6 M. S. Nogueira, M. Raju, J. Gunther, K. Grygoryev, K. Komolibus, H. Lu and S. Andersson-Engels, in Proceedings of SPIE 10685 Biophotonics: Photonic Solutions for Better Health Care VI, 2018, vol. 10685, p. 106853G.
7 C. T. de Andrade, M. S. Nogueira, S. C. Kanick, K. Marra, J. Gunn, J. Andreozzi, K. S. Samkoe, C. Kurachi and B. W. Pogue, in Proceedings of SPIE 9694 Optical Methods for Tumor Treatment and Detection: Mechanisms and Techniques in Photodynamic Therapy XXV, 2016, vol. 9694, p. 969410.
8 M. S. Nogueira, S. Maryam, M. Amissah, H. Lu, N. Lynch, S. Killeen, M. O'Riordain and S. Andersson-Engels, *Sci. Rep.*, 2021, **11**, 798, 1–17.
9 M. Saito Nogueira, S. Maryam, M. Amissah, A. McGuire, C. Spillane, S. Killeen, S. Andersson-Engels and M. O'Riordain, *Cancers*, 2022, **14**, 5715.
10 M. S. Nogueira, M. Raju, J. Gunther, S. Maryam, M. Amissah, H. Lu, S. Killeen, M. O'Riordain and S. Andersson-Engels, *J. Phys. D: Appl. Phys.*, 2021, **54**, 454002.
11 M. S. Nogueira, M. Raju, J. Gunther, S. Maryam, M. Amissah, H. Lu, S. Killeen, M. O'Riordain and S. Andersson-Engels, Proc. SPIE 11943, Photonics West, 11943-4.
12 M. S. Nogueira, S. Maryam, M. Amissah, N. Lynch, S. Killeen, H. Lu, M. O'Riordain and S. Andersson-Engels, Proc. SPIE 11954, Photonics West, 11954-15.
13 M. S. Nogueira, S. Maryam, M. Amissah, N. Lynch, S. Killeen, M. O'Riordain and S. Andersson-Engels, in *European Conference on Biomedical Optics*, 2021, pp. EW4A–16.
14 M. S. Nogueira, M. Raju, J. Gunther, S. Maryam, M. Amissah, S. Killeen, M. O'Riordain and S. Andersson-Engels, in *European Conference on Biomedical Optics*, 2021, pp. ETu3A–1.
15 M. S. Nogueira, M. Amissah, S. Maryam, N. Lynch, S. Killeen, M. O'Riordain and S. Andersson-Engels, in *European Conference on Biomedical Optics*, 2021, pp. EW4A–17.
16 E. J. M. Baltussen, P. Snæbjörnsson, S. G. B. De Koning, H. J. C. M. Sterenborg, A. G. J. Aalbers, N. Kok, G. L. Beets, B. H. W. Hendriks, K. F. D. Kuhlmann and T. J. M. Ruers, *J. Biomed. Opt.*, 2017, **22**, 106014.
17 E. J. M. Baltussen, E. N. D. Kok, S. G. B. de Koning, J. Sanders, A. G. J. Aalbers, N. F. M. Kok, G. L. Beets, C. C. Flohil, S. C. Bruin, K. F. D. Kuhlmann, *et al.*, *J. Biomed. Opt.*, 2019, **24**, 16002.
18 E. J. M. Baltussen, S. G. de Koning, J. Sanders, A. G. J. Aalbers, N. F. M. Kok, G. L. Beets, B. H. W. Hendriks, H. J. C. M. Sterenborg, K. F. D. Kuhlmann and T. J. M. Ruers, *Lasers Surg. Med.*, 2020, **52**, 604–611.
19 E. J. M. Baltussen, S. G. B. De Koning, J. Sanders, A. G. J. Aalbers, N. F. M. Kok, G. L. Beets, B. H. W. Hendriks, H. J. C. M. Sterenborg, K. F. D. Kuhlmann and T. J. M. Ruers, *J. Transl. Med.*, 2019, **17**, 1–10.
20 G. C. Langhout, T. M. Bydlon, M. van der Voort, M. Müller, J. Kortsmit, G. Lucassen, A. J. R. Balthasar, G.-J. van Geffen, T. Steinfeldt and H. J. C. M. Sterenborg, *Lasers Surg. Med.*, 2018, **50**, 253–261.
21 E. J. M. Baltussen, H. J. C. M. Sterenborg, T. J. M. Ruers and B. Dashtbozorg, *Biomed. Opt. Express*, 2019, **10**, 6096–6113.
22 G. C. Langhout, J. W. Spliethoff, S. J. Schmitz, A. G. J. Aalbers, M.-L. van Velthuysen, B. H. W. Hendriks, T. J. M. Ruers and K. F. D. Kuhlmann, *Lasers Surg. Med.*, 2015, **47**, 559–565.
23 G. C. Langhout, J. W. Spliethoff, A. G. J. Aalbers, V. J. Verwaal, B. H. W. Hendriks, T. J. M. Ruers and K. F. D. Kuhlmann, *Ann. Oncol.*, 2014, **25**, iv206.
24 M. S. Nogueira, M. Raju, K. Komolibus, K. Grygoryev and S. Andersson-Engels, *J. Phys. D: Appl. Phys.*, 2021, **54**, 374003.
25 L. Wang, S. L. Jacques and L. Zheng, *Comput. Methods Programs Biomed.*, 1995, **47**, 131–146.
26 E. Alerstam, W. C. Y. Lo, T. D. Han, J. Rose, S. Andersson-Engels and L. Lilge, *Biomed. Opt. Express*, 2010, **1**, 658–675.
27 E. Alerstam, T. Svensson and S. Andersson-Engels, *J. Biomed. Opt.*, 2008, **13**, 60504.
28 T. Valery, *Tissue Optics: Light Scattering Methods and Instruments for Medical Diagnosis*, SPIE Press, Bellingham, Washington, 2007.
29 S. L. Jacques, *Phys. Med. Biol.*, 2013, **58**(11), R37–R61.
30 J. F. L. Cobbold and J. A. Summerfield, in *Handbook of Liver Disease*, Elsevier, 2012, pp. 297–307.
31 F. Geldof, M. Witteveen, H. J. C. M. Sterenborg, T. J. M. Ruers and B. Dashtbozorg, *Biomed. Opt. Express*, 2023, **14**, 128–147.
32 J. Ollesch, M. Zaczek, H. M. Heise, O. Theisen, F. Grosserueschkamp, R. Schmidt, K. Morgenroth,

 This journal is © The Royal Society of Chemistry 2024

Open Access Article. Published on 05 October 2023. Downloaded on 5/1/2024 12:28:50 PM.
This article is licensed under a Creative Commons Attribution-NonCommercial 3.0 Unported Licence.

S. Philippou, M. Kemen and K. Gerwert, *Vib. Spectrosc.*, 2017, **91**, 99–110.

33 E. J. M. Baltussen, S. G. Brouwer De Koning, B. H. W. Hendriks, K. Jóźwiak, H. J. C. M. Sterenborg and T. J. M. Ruers, *Transl. Biophotonics*, 2019, **1**, e201900008.

34 E. Salomatina and A. N. Yaroslavsky, *Phys. Med. Biol.*, 2008, **53**, 2797.

35 G. M. Palmer and N. Ramanujam, *Appl. Opt.*, 2006, **45**, 1062–1071.

36 R. J. Hennessy, S. L. Lim, M. K. Markey and J. W. Tunnell, *J. Biomed. Opt.*, 2013, **18**, 37003.

1 Safety considerations of the use of light and ultrasound in medical solutions

The combination of acoustic waves and optical radiations for biological imaging and therapy or diagnostics require some safety considerations. In the context of acousto-optics and its applications, these considerations would be the limits of illumination by both forms of radiations. Clinical use of ultrasound and lasers is guided by decades of biophysical research and international standards. Safety indices like the thermal index (TI) and mechanical index (MI) are displayed on modern ultrasound scanners to inform users of the relative risk of thermal and mechanical bioeffects [125]. Likewise, laser devices are classified (Class 1 to 4) based on the accessible emission limit (AEL) that correlates with potential hazard. Regulatory bodies such as the U.S. Food and Drug Administration (FDA) and international committees (IEC – International Electrotechnical Commission; ICNIRP – International Commission on Non-Ionizing Radiation Protection; ANSI – American National Standards Institute) have published guidelines to cap output levels and define safe operating conditions.

Safe use of ultrasound and laser systems relies on quantitative metrics that predict the likelihood of bioeffects. These metrics are rooted in the physics of wave-tissue interactions. In ultrasound, the key indices are the Mechanical Index (MI) and Thermal Index (TI), which are dimensionless numbers calculated in real-time on most diagnostic machines. In laser safety, the fundamental quantity is the Maximum Permissible Exposure (MPE), from which device-specific Accessible Emission Limits (AELs) are derived. The following sections define each metric and these are general information about safety that could be sourced from Wikipedia as well.

1.1 Ultrasound Mechanical Index (MI)

The MI is defined to reflect the risk of non-thermal (mechanical) effects of ultrasound, particularly the potential for cavitation. Mathematically, MI which is unitless is the ratio of the peak rarefaction pressure (in MPa) to the square root of the ultrasound's center frequency (in MHz):

$$MI = \frac{P_r}{C_{MI}\sqrt{f_c}}, \tag{.1}$$

where P_r is the peak rarefactional pressure of the ultrasound wave, C_{MI} is a normalization factor = $1MPa\ MHz^{-1/2}$ and f_c is the center frequency. By normalizing pressure to frequency, MI encapsulates the likelihood of cavitation: a higher MI indicates greater chance that the negative pressure will form vapor bubbles in tissue fluids. An MI of 1, for example, $MI \approx 1.9$ at 190 W/cm^2 for a 1 MHz wave and as a result, the FDA regulatory limits usually cap MI below 2. It is generally considered that $MI < 0.3$ has no detectable biological effects, whereas at higher MI the probability of effects rises. The

MI concept assumes worst-case conditions (for example, the presence of microbubbles); thus it provides a conservative safety indicator. It is noted that MI specifically addresses mechanical bioeffects: these include cavitation (bubble collapse shock waves) and acoustic radiation force phenomena like microstreaming. For example, the presence of gas bodies (lung alveoli, or microbubble contrast agents) dramatically lowers the cavitation threshold, making a given MI more significant in those contexts [125].

1.2 Ultrasound Thermal Index (TI)

The TI is intended as an approximate indicator of thermal effects from ultrasound absorption. It is defined as the ratio of the current acoustic power output to the estimated power required to raise tissue temperature by $1°C$ [125]. In concept, TI of 1 means the ultrasound exposure is predicted to cause a steady-state temperature rise on the order of $1°C$ in the tissue, if sustained. Mathematically,

$$TI = \frac{W_{acoustic}}{W_{\text{deg}}}, \tag{.2}$$

where $W_{acoustic}$ is the acoustic power being emitted (in Watts) and W_{deg} is the power needed to produce a $1°C$ temperature increase in a standard model tissue [125]. The latter is determined by mathematical models of heat deposition and thermal diffusion in tissue. There are actually three variants of TI, corresponding to different assumptions about where heating is most likely: TIS (soft-tissue thermal index) assumes only soft tissue in the beam path (no bone involvement); TIB (bone thermal index) assumes bone is present at or near the ultrasound focus, causing increased absorption there (applicable for example, in second or third trimester fetal scanning when bone is in the beam's focal region); TIC (cranial bone thermal index) assumes the transducer is very close to bone, such as in adult transcranial ultrasound or neonatal brain scanning through fontanelle. Each TI is computed with a different W_{deg} appropriate to those scenarios (bone absorbs more ultrasound and can heat faster than soft tissue). The TI is also unitless. A TI value is a rough estimate: TI = 2 does not guarantee a $2°C$ rise, but suggests a higher risk of a few degrees rise than TI = 1. It is a conservative indicator rather than a precise thermometer reading. The rationale is to give sonographers a quick sense of thermal risk so they can adjust exposure or limit scan time accordingly. The equations for TI come from models of acoustic absorption and heat transfer; their derivation is detailed in standards (IEC 62359) and [126]. In practice, if an ultrasound scanner shows $TI \approx 1.0$, it implies the machine's output is at the threshold of raising tissue by by $1°C$ in a worst-case assumption (for example, bone at focus for TIB). Values of TI in diagnostic ultrasound usually range from <0.1 up to about 1–2 under normal imaging settings, but Doppler or high-intensity modes can push TI higher.

1.3 Maximum Permissible Exposure (MPE) for Lasers

In laser safety, the MPE is a fundamental quantitative limit. It is defined as the highest level of laser radiation (power or energy density) to which a person may be exposed without harmful effects. The MPE is usually given either as an irradiance (W/cm^2) for continuous exposures or as a radiant exposure (J/cm^2) for pulsed exposures. It depends critically on the laser wavelength, exposure duration, and the tissue (eye or skin) involved. The MPE is set to include a margin of safety which is typically about one-tenth of the actual threshold for damage determined in lab experiments. For example, if 10 J/cm^2 causes a retinal lesion in 50% of cases, the MPE might be ≈ 1 J/cm^2 for that exposure time and wavelength. Regulatory standards (ANSI Z136.1, IEC 60825-1) provide detailed tables and formulas for calculating MPE. The derivations consider damage mechanisms: photochemical injury (relevant in the blue-ultraviolet for eye, where effects accumulate over time) vs thermal injury (relevant for most lasers, where power causes heating). For the eye, the worst-case focusing by the lens of the eye is assumed, meaning the MPE at the cornea is set such that even if that light is focused on the retina, it is below retinal damage levels. For instance, visible or near-infrared lasers that can focus on the retina have stricter MPE limits (because a tiny retinal spot can get very high energy density) compared to far-infrared light that is absorbed in the cornea. The MPE also accounts for the aversion response for bright light: for visible lasers, an exposure up to 0.25 seconds is assumed to be naturally limited by a person's blink reflex or head movement. The MPE for a continuous visible laser is therefore set around the level that would cause injury if the beam was viewed for the maximum 0.25 s aversion time. By contrast, for infrared wavelengths > 1400 nm which do not reach the retina, the limiting concern is corneal or skin heating, and the MPE can be higher. As a concrete example, according to ANSI for a single pulse on skin, the MPE might be 20 mJ/cm^2 for wavelengths 400–700 nm and around 100 mJ/cm^2 for near-infrared around 1064 nm [127]. These values come from empirical thresholds where above these energies, transient reddening or burns were observed in skin. We will detail such exposure limits further in a dedicated section. In summary, MPE provides a time- and wavelength-dependent cap on laser exposure to avoid injury, based on known bioeffect thresholds with safety factors. It is the yardstick for laser safety calculations.

1.4 Accessible Emission Limit (AEL)

While MPE is about exposure of a person, the AEL is a property of a laser device used for classification. The AEL for a given laser class (1, 1M 2, 2M, 3R, 3M, or 4) is essentially the maximum output that the laser can emit and still be considered in that safety class. Importantly, AEL is derived from MPE by accounting for viewing conditions. Specifically, AEL = MPE × area of the limiting aperture. The limiting aperture is a standardized area (often related to a pupil size, for example 7 mm for the eye) over which the emission is averaged for classification purposes. For example, a Class 2 laser (visible, safe via blink reflex) has an AEL of 1 mW for a continuous beam, corresponding to the 1 mW average power that is below the 0.25 s MPE for the eye. A Class 1 laser has an AEL such that even a

worst-case exposure would not exceed the MPE; in practice this means very low power or fully enclosed beams. The derivation of AEL involves worst-case assumptions about how the laser could be viewed. A small-diameter beam is considered fully entering the eye (aperture or pupil size), whereas a very large or highly divergent beam might only partly enter. Classes like 1M and 2M are defined for extended-source lasers where direct naked-eye viewing is still safe but dangerous if optics are used to collect the beam. The mathematical relationship between AEL and MPE ensures that any laser of a given class, under reasonably foreseeable use, should not expose a person above the MPE. In effect, regulatory standards take MPE (a safe exposure limit) and multiply by an area and time factors to set AEL (a safe emission for a product).

In addition to these primary metrics, a few other technical parameters are important: for ultrasound, intensities are often given as spatial-peak temporal-average (SPTA) or spatial-peak pulse-average (SPPA). SPTA is the intensity averaged over time (accounting for duty cycle) at the location of peak intensity, relevant to thermal effects. SPPA (or ISPPA.3 when derated) is the peak intensity during the pulse, relevant to instantaneous mechanical effects. They relate to TI and MI respectively. For lasers, one often computes the Nominal Ocular Hazard Distance (NOHD) which is the distance at which the beam is just at the MPE for the eye (especially for Class 4 lasers), but this is more for safety planning than a fundamental limit.

In conclusion, the safe use of ultrasound and lasers is a success story of modern medicine – by respecting the physics-based limits and guidelines developed from rigorous research, clinicians can leverage these technologies and their benefits with minimal risk. Diagnostic ultrasound can provide critical information from a fetus or an organ with essentially no known harm when used properly. Medical lasers can achieve precise cutting or tumor destruction while sparing surrounding tissue, as long as the beam is controlled. By following the best practices, healthcare providers and researchers can continue to expand the frontiers of imaging and therapy safely, maintaining the trust that patients place in these technologies.